DESIGN, DEVELOPMENT AND CHARACTERISATION OF A PASSIVE ACTIVE MULTIJUNCTION RF LAUNCHER COMPATIBLE WITH ADITYA –UPGRADE TOKAMAK

By

JAIN YOGESH MITHALALJI

ENGG06201504001

Institute for Plasma Research, Gandhinagar

A thesis submitted to the

Board of Studies in Engineering Sciences

In partial fulfilment of requirements

for the Degree of

DOCTOR OF PHILOSOPHY

of

HOMI BHABHA NATIONAL INSTITUTE

February, 2021

Homi Bhabha National Institute

Recommendations of the Viva Voce Board

As members of the Viva Voce Board, we certify that we have read the dissertation prepared by JAIN YOGESH MITHALALJI entitled "Design, Development and Characterisation of a Passive Active Multijunction RF launcher compatible with ADITYA –Upgrade tokamak" and recommend that it maybe accepted as fulfilling the dissertation requirement for the Degree of Doctor of Philosophy.

______________________________ Date: 05 / 02 / 2021

Chairman - Prof. Subroto Mukherjee

______________________________ Date: 05 / 02 / 2021

Guide/Convener - Dr. Promod Kumar Sharma

(James Raju)

______________________________ Date: 05 / 02 / 2021

External Examiner - Prof. K. C. James Raju

______________________________ Date: 05 / 02 / 2021

Co-Guide - Dr. Surya Kumar Pathak

______________________________ Date: 05 / 02 / 2021

Member - Dr. Mainak Bandyopadhyay

______________________________ Date: 05 / 02 / 2021

Member - Dr. Harish V. Dixit

Final approval and acceptance of this dissertation is contingent upon the candidate's submission of the final copies of the dissertation to HBNI.

I hereby certify that I have read this dissertation prepared under my direction and recommend that it may be accepted as fulfilling the dissertation requirement.

Date: 05 / 02 / 2021

Place: IPR, Gandhinagar

Guide: Dr. Promod Kumar Sharma

STATEMENT BY AUTHOR

This dissertation has been submitted in partial fulfillment of requirements for an advanced degree at Homi Bhabha National Institute (HBNI) and is deposited in the Library to be made available to borrowers under rules of the HBNI.

Brief quotations from this dissertation are allowable without special permission, provided that accurate acknowledgement of the source is made. Requests for permission for extended quotation from or reproduction of this manuscript in whole or in part may be granted by the Competent Authority of HBNI when in his or her judgement the proposed use of the material is in the interests of scholarship. In all other instances, however, permission must be obtained from the author.

Jain Yogesh Mithalalji

DECLARATION

I, hereby declare that the investigation presented in the thesis has been carried out by me. The work is original and has not been submitted earlier as a whole or in part for a degree/diploma at this or any other Institution/University.

Jain Yogesh Mithalalji

CERTIFICATION ON ACADEMIC INTEGRITY

1. I, Jain Yogesh Mithalalji, HBNI Enrolment No. ENGG06201504001, hereby undertake that, the Thesis titled "***Design, Development and Characterisation of a Passive Active Multijunction RF launcher compatible with ADITYA –Upgrade tokamak***" is prepared by me and is the original work undertaken by me and free of any plagiarism. That the document has been duly checked through a plagiarism detection tool and the document is plagiarism free.

2. I am aware and undertake that if plagiarism is detected in my thesis at any stage in future, suitable penalty will be imposed as per the applicable guidelines of the Institute/UGC.

Signature of Student

Endorsed by the thesis Supervisor:

(I certify that the work done by the Researcher is plagiarism free)

Signature

Name: Dr. Promod Kumar Sharma

Designation: Scientific Officer - G, Division Head

Department/Centre: Lower Hybrid Current Drive (LHCD)

Name of CI/OCC: Institute for Plasma Research, Gandhinagar

List of Publications from this thesis

a) Journal Publications

1. **Yogesh M. Jain**, P. K. Sharma et al., "**RF Design of Passive Active Multijunction (PAM) Launcher for LHCD System of ADITYA –Upgrade Tokamak.**", *Fusion Engineering and Design, Elsevier*, 134 (2018): pp. 109-117.

2. P. K. Sharma, **Yogesh M. Jain** et al., "**Recent Activities on SST-1 and ADITYA – U Tokamaks.**", *Plasma and Fusion Research, The Japan Society of Plasma Science and Nuclear Fusion Research*, 13 (2018): pp. 3502100.

3. **Yogesh M. Jain**, P. K. Sharma et al., "**Multiphysics Analysis of Passive Active Multijunction (PAM) Launcher for LHCD System of ADITYA –Upgrade Tokamak.**", *Fusion Engineering and Design, Elsevier*, 147 (2019).

b) Other Publications : Conferences/Symposium

1. **Yogesh M. Jain**, P. K. Sharma, Jagabandhu Kumar, Aviraj R. Jadhav, Harish V. Dixit, K. K. Ambulkar, P. R. Parmar, C. G. Virani, "**Conceptual design of PAM antenna for Aditya –U Tokamak.**", *Proceedings of the 10th Asia Plasma and Fusion Association (APFA) Conference*, India, 2015.

2. **Yogesh M. Jain**, P. K. Sharma, P. R. Parmar, K. K. Ambulkar, "**Design of Test Kits for the RF Characterization of the PAM Antenna of LHCD System for ADITYA –Upgrade Tokamak.**", *32nd National Symposium on Plasma Science and Technology*, Gandhinagar, 2017.

3. **Yogesh M. Jain**, P. K. Sharma, "**Design and Performance Studies of Passive Active Multijunction (PAM) Antenna for ADITYA –Upgrade Tokamak.**", *32nd National Symposium on Plasma Science and Technology*, Gandhinagar, 2017.

4. **Yogesh M. Jain**, P. K. Sharma, Jagabandhu Kumar, Harish V. Dixit, Aviraj R. Jadhav, "**Multiphysics design of a high power CW mode converter at 3.7 GHz for tokamak applications.**", *Asia Pacific Microwave Conference (APMC)*, Kuala Lumpur, Malaysia, 2017, *IEEE*.

5. **Yogesh M. Jain**, P. K. Sharma, Harish V. Dixit, Aviraj Jadhav, Pramod Parmar, "**Design and multiphysics analysis of a high power RF window for LHCD system of tokamaks.**", *Progress in Electromagnetics Research Symposium-Fall (PIERS-FALL)*, Singapore, 2017, *IEEE*.

6. **Yogesh M. Jain**, P. K. Sharma, P. R. Parmar, K. K. Ambulkar, Harish V. Dixit, "**Development and Qualification of Passive Active Multijunction (PAM) Launcher for LHCD system of ADITYA –Upgrade Tokamak.**", *Fusion Energy Conference*, Gandhinagar, India, 2018.

7. **Yogesh M. Jain**, P. K. Sharma, P. R. Parmar, K. K. Ambulkar, "**RF Characterization of the Passive Active Multijunction (PAM) Launcher for LHCD system of ADITYA –Upgrade Tokamak.**", *33rd National Symposium on Plasma Science and Technology*, New Delhi, 2018.

8. **Yogesh M. Jain**, P. K. Sharma, K. K. Ambulkar, "**Profile Measurement of the Passive Active Multijunction (PAM) Launcher for LHCD system of ADITYA –Upgrade Tokamak.**", *34th National Symposium on Plasma Science and Technology*, VIT Chennai, 2019.

9. **Yogesh M. Jain**, P. K. Sharma, P. R. Parmar, K. K. Ambulkar, Harish V. Dixit, "**Multiphysics Analysis of a High Power RF Window using COMSOL.**", *COMSOL conference*, Bangalore, India, 2019. (**Best Poster award**).

10. **Yogesh M. Jain**, "**Design and Development of a Passive Active Multijunction (PAM) Launcher for LHCD system of ADITYA –Upgrade Tokamak.**", *EMPRA*, BITS Hyderabad, 2020. (**Best Poster award**).

ACKNOWLEDGEMENTS

A Ph.D. degree not only leads to an academic advancement of the person but also helps in an overall improvement in his/her personality. The degree is bestowed upon a single person, but the Ph.D. work and the corresponding thesis is a collective effort of some extremely knowledgeable, hardworking and helpful people. This becomes even more important considering the Multiphysics nature of the work where slack in a single aspect can put the efforts of all in jeopardy. Throughout my journey, I have been fortunate to have worked with many such experts and this acknowledgement is to express my sincere gratitude to each of them. In foresight, I would like to apologise if I have unknowingly forgotten to mention anyone who has contributed to this work.

Foremost, I would like to express my gratitude to my supervisor, Dr. P. K. Sharma, who has been a pillar of support and understanding. His guidance helped me to sail over numerous technical problems encountered during this work. The discussions with him related to the thesis work have been extremely fruitful. I would like to thank him for his incessant encouragement and for being extremely patient with me throughout this period. I consider myself fortunate to work under his guidance.

I want to thank my co-supervisor, Dr. S. K. Pathak, whose insightful suggestions in the design of the PAM launcher has improved its overall engineering aspect. His suggestions pertaining to the RF measurements have been very useful. I would like to express my sincere thanks to Dr. Subroto Mukherjee, Chairman of my doctoral committee, for always suggesting the most practical approach to a problem. His suggestions have greatly helped in shaping the thesis well. I would like to thank Dr. Mainak Bandyopadhyay, whose ever so inspiring presence in my doctoral committee was necessary for me to strive for better performance. I thank him for his invaluable critiquing opinions. I am highly indebted to Dr. Harish V. Dixit, who has been extremely patient, inspiring, helpful and supportive through more than a decade. I would like to thank him for introducing me to the beauty of RF and microwave. His insightful and invaluable suggestions have immensely shaped my Ph.D. work and thesis.

I am grateful to Dr. Sudip Sengupta, Academic Dean, and the Academic committee members for helping me in navigating through academic affairs smoothly.

I am thankful to the members of my LHCD group who have been very kind with their help and support and lending every bit of their expertise. The discussions with Mr. K. K. Ambulkar pertaining to RF measurements and klystron operations have been very helpful. I would like to thank Mr. P. R. Parmar who has been of great help in the design, fabrication and testing of the launcher. The launcher would not have been fabricated had it not been for his expertise in translating the design to mechanical drawings. I am thankful to Mr. Chetan Virani, Mrs. Shefali Dalakoti, Mr. Arvind L. Thakur, Jagabandhu Kumar, Chandra Sekhar Singh for their help throughout my Ph.D and making the lab a great place to work.

The sailing of this ship (read: thesis), would have been extremely rough if not for the help and support of Aviraj Jadhav. His patience and untiring help has been immense and not limited just to my Ph.D. tenure but for more than a decade. His support professionally and personally has made things a lot easier for me and I am grateful to him endlessly.

I express my sincere gratitude towards Dr. Joydeep Ghosh and the ADITYA –U tokamak team for extending their complete support and expertise throughout the design, development and testing phase of the PAM launcher. The discussions with Mr. S. B. Bhatt, Mr. Kumarpalsinh Jadeja and Mr. Kaushal Patel have been very useful in the development and testing of the launcher.

I am grateful to the High Temperature Technology Division (HTTD) for their support in the development and testing of the RF window. I would like to thank Mr. Sunil M. Belsare and Mr. Prakash K. Mokaria for their help during the vacuum furnace operations and Mr. Kedar Satish Bhope for carrying out the ultrasonic testing of the window. I would like to thank Dr. Santosh Pandya for lending his expertise during the temperature measurements of the RF window using the IR camera.

I would like to thank Dr. R. Ganesh, Head of the Computer Centre, Mr. Prashant Kumar, Mr. Deepak Aggarwal and the complete computer centre staff for extending their support wholeheartedly. They were always ready to solve my problems related to COMSOL, CST studio and the UDAY and ANTYA cluster.

I am thankful to Mr. Vishnu Prajapati and the complete staff of the Drafting section for helping me in preparing the mechanical drawings of my design. I have spent a lot of time in the drafting section during my tenure and they have been very prompt, efficient and extremely friendly.

I am grateful to Mr. Vijay Patel and the Workshop staff for their precise fabrication of all my designs. I express my sincere gratitude towards the Library, Stores and Administration for their kind support during my Ph.D. I would like to thank all the helpers at IPR, without whom working on my half ton system would have been very difficult.

I am thankful to Mr. Upendra Loriya and his team for their help in the fabrication of the PAM launcher and other components. Mr. Dharmesh Purohit has helped me enthusiastically in the profile measurement setup. Further, I am also grateful to the ECRH group for lending the RF measurement translator. Mr. Dharmendra Rathi deserves a special mention for his constant advice throughout my Ph.D.

I would like to thank my friends at IPR, Dipshikha Borah, Devshree Mandal, Ayushi Vashistha, Tanmay Macwan, Pawandeep Kaur, Soumen De Karmakar, Hariprasad MG, Jay Joshi, Montu Bhuva, Prabhakar Srivastava, Sagar Sekhar, Gaurav Singh, Arun Pandey, Ajay Pandey, Sanjeev Pandey, Sanket Chaudhary who have not only helped me technically but have been extremely kind and have created a friendly ambience around me.

I want to thank the most important people in my life, my mother, Mrs. Vasanti Jain and my sisters, Rupal and Jayshree, who have always supported and encouraged me with immense patience. Their hard work and sacrifices have not only made me capable of writing this thesis but also motivated me. I will always be grateful to my father, Late Shri. Mithalal Jain, who has always inspired me.

Contents

List of Figures

List of Tables

Chapter 7

Conclusion and Future Scope of Work

As the milestones for International Thermonuclear Experimental Reactor (ITER) at Cadarache are coming closer, it becomes important for member nations to be abreast and equipped with the developments in relevant technologies so as to rapidly capitalise on the results obtained from ITER. It was with this motivation that the objective of this thesis was to carry out studies on the design and development of the Passive Active Multijunction (PAM) launcher for the ADITYA –U tokamak.

Although PAM launchers have been designed, deployed and tested in a few tokamaks before, its design and performance vary from tokamak to tokamak on account of different port and plasma constraints. This thesis, therefore, presents the studies on the design and development of a PAM launcher for the ADITYA –U tokamak. Another focus of this thesis was to carry out studies relevant to the design and development of a high power pill box type RF vacuum window.

The salient contributions of this thesis are as follows:-

1 **Design, Development and testing of a PAM launcher:** The design, development and low power testing of a PAM launcher capable of handling 250 kW/1 s of RF power at 3.7 GHz are carried out. Due to the available port size, the launcher had

a smaller number of active and passive waveguides. The PAM concept was thus realised in a smaller size satisfactorily.

2 Low Power profile measurement technique: A new method to evaluate the performance of the PAM launcher, in air, at low power before installing it on the machine is proposed. This method gives the $N_{\|}$ spectra; the power spectrum of the wave launched from the launcher and demonstrates the steering of the waves. The results obtained agreed excellently with simulation.

3 Design, Development, Low and High power testing of the RF window: A novel mechanical design of a pill box type RF vacuum window capable of handling 125 kW of RF power for 1 s at 3.7 GHz is proposed. Further, its Multiphysics analysis, fabrication and low and high power testing is carried out. The novel structure enables the brazing of two joints involving two dissimilar materials (metallised alumina and copper, SS304L and copper) in a single brazing cycle. Thus, there is a fifty percent reduction in the brazing efforts and costs involved in developing the window.

4 Novel Mode Converter design: A new mode converter structure is proposed which does not utilise a post to match the input. In this work, a few steps are added to the broader side of the mode converter (where the E-field is zero) at the output. This method reduces the concentration of the E-field locally near the post and thereby increases the power threshold for RF breakdown.

The salient characteristics of the developed PAM launcher and RF window which confirms its compatibility with the ADITYA –U tokamak are as follows:-

1 Parallel Refractive index ($N_{\|}$): The developed PAM launcher can launch RF waves with a parallel refractive index ($N_{\|}$) ranging from 1.875 to 2.625. This variation can be achieved by varying the external phase shift between the two toroidal modules. The central $N_{\|}$ value of 2.25 is achieved when an external phase shift of 165° is applied. These measurements were reported in Chapter 5. The $N_{||}$ of the launched wave is found to be as desired and is consistent with various plasma parameters of the ADITYA –U tokamak

2 Size of the port: The cross-sectional dimension of the mouth of the PAM launcher after fabrication is 288 mm × 127 mm. This is consistent with the allocated ADITYA –U port size of 490 mm × 190 mm. Thus, the launcher can be installed with all the relevant diagnostics.

3 Footprint: The RF (Chapter 3) and mechanical (Chapter 4) design of the PAM launcher conforms to all the space constraints imposed by the support structure of the ADITYA –U tokamak. Fig. 7.1 shows the depiction of the PAM launcher connected to its tokamak port. The position of the PAM launcher in the tokamak along with various existing support structures can also be observed.

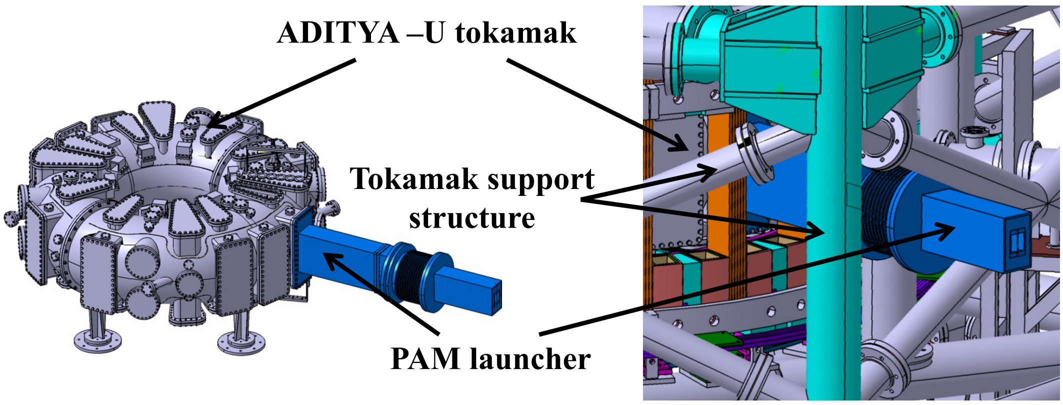

Figure 7.1: Position of the PAM launcher in the tokamak illustrating that the launcher conforms to all the space constraints.

4 Disruption: As elaborated in chapter 3, the PAM launcher was designed and further developed such that it could withstand the stress exerted on it due to thermal and plasma disruption effects. The total stress exerted on the launcher is ~53 MPa.

5 HLD, Baking and UHV: The complete PAM structure was tested for its leak rate (maximum leak rate < 1×10^{-9} mbarl/s), baking (up to a temperature of ~ 180°C) was employed to release the trapped gases and impurities and a vacuum level of

1.3×10^{-8} mbar was achieved. The leak rate obtained, maximum baking temperature applied and the vacuum level achieved satisfy the ADITYA –U tokamak's requirement before installation.

6 **RF vacuum window:** The fabricated window was able to withstand a differential pressure of 3 bars which it would encounter in real-time during high power operations. The HLD test of the window revealed a leak rate of less than 1.11×10^{-9} mbar-l/s confirming its UHV compatibility. The high power test of the window was conducted at 150 kW (20% higher than the design value of 125 kW) for 1 s. The design, development and all the qualification tests performed are elaborated in chapter 6

Future Scope of Work

1 **Investigation for CW operation:** The PAM launcher was designed for pulsed operation. In case the launcher is to be utilised for SST-1 tokamak (operating in CW mode for 1000 s), thermal, mechanical and plasma disruption studies would have to be carried out. The evaluation of the total stress acting on the launcher due to thermal load and plasma disruption would be important after the addition of cooling pipes at critical locations.

2 **Design of RF vacuum window for CW operation:** The use of a PAM launcher for SST-1 tokamak would warrant the need to design a pill box type RF vacuum window capable of operating in CW mode. During steady-state operation, the ceramic is usually unable to dissipate the heat away from its centre to periphery due to which it expands. This causes the ceramic to crack at various fixed boundaries. Thus, considerable research effort would have to be expended in selecting an appropriate ceramic material, cooling mechanism and thereby designing the RF window.

ABSTRACT

The Lower Hybrid Current Drive (LHCD) is a robust and reliable mechanism employed in many tokamaks worldwide to drive plasma current non-inductively. A grill launcher was commissioned on the LHCD system of ADITYA tokamak to launch 125 kW of RF power at 3.7 GHz. The grill is a phased array waveguide launcher that requires a complex waveguide feed network to launch the wave with an appropriate parallel refractive index ($N_{\|}$). It also suffers from other disadvantages, such as poor reflection characteristics and need of a higher density at the mouth of the launcher during operations. Thus, the upgrade of the ADITYA tokamak to ADITYA -Upgrade gives an opportunity to upgrade its LHCD system and replace the grill launcher with a more advanced and robust Passive Active Multijunction (PAM) launcher.

Although the concept of PAM launcher is an established one, its design and development do not follow a cookbook approach as it is based on several plasma and space constraints, which are often unique to a particular tokamak. Hence, it is the objective of this thesis to carry out studies which would ultimately culminate in the design, development and characterisation of a PAM launcher compatible with the ADITYA -U tokamak. The PAM launcher would also require a pillbox type RF window to be installed to isolate the vacuum and pressurised section of the transmission line. This thesis also discusses a novel design of such a window and further reports its development and testing.

The design of the PAM launcher is often governed by the available port size, parallel refractive index ($N_{\|}$) and frequency of the wave to be launched from it. The available port size on the ADITYA -U tokamak is 490 mm $\times$ 190 mm, which is the smallest in comparison with other tokamaks where the PAM launcher has been commissioned. The design and development of a launcher capable of launching around 250 kW of RF power via such a small port size coupled with other space constraints without encountering RF breakdown would be a challenge. An issue, post the development of a PAM launcher,

is its characterisation to validate its performance without installing it on the tokamak. As the tokamak is a very complex machine with several interdisciplinary activities associated with it, there is a need for a method to characterise the PAM launcher without waiting for the machine to be ready. Another issue that is frequently encountered while commissioning any high power RF system is the availability of a pill box window which is used to isolate the pressurised and the vacuum sections of a transmission line. The design and development of a pill box type RF window; although simple in principle, pose several complex engineering challenges such as brazing of dissimilar materials, thermal and mechanical performance for 1 s of operation et cetera.

It is thus, the objective of this thesis to overcome the above challenges and propose the design and thereafter develop and characterise a Passive Active Multijunction (PAM) launcher and a pill box type RF window to launch 250 kW of RF power at 3.7 GHz into the tokamak.

The major contributions of this work vis-à-vis existing literature are,

1. The design, development and low power testing of a PAM launcher capable of launching 250 kW of RF power for 1 s at 3.7 GHz is carried out. Due to the available port size, the launcher had a fewer number of active and passive waveguides. The PAM concept was thus realised for a small size launcher system satisfactorily.

2. An experimental method to evaluate the performance of the PAM launcher at low power, in air, before installing it onto the tokamak is proposed. This method gives the power spectrum ($N_{\parallel}$ spectrum) of the wave launched by the launcher and also demonstrates the steering of the waves. The results obtained agreed excellently with the simulation.

3. The design, development, along with the low and high power testing of a pill box type RF vacuum window capable of handling 125 kW/1 s of RF power at 3.7 GHz is carried out. The pill box window has a novel structure that enables brazing of two

joints involving two dissimilar materials (metallised alumina and copper, SS304L and copper) in a single brazing cycle.

4. A new mode converter structure is proposed which does not utilise a post to match the input impedance. In this work, a few steps are added to the broader dimension of the waveguide (where the E-field is zero) near the output. This method reduces the concentration of the E-field locally, thereby increasing the power threshold for breakdown.

The PAM launcher exhibited a return loss of ~27 dB, equal power division and desired phase differences between the output waveguides during low power measurement. The main peak $N_{\|}$ value of the wave launched from the launcher was measured in free space to be 2.25 (as desired) with the help of a novel measurement technique proposed in this thesis. As the launcher would operate close to cutoff density, this method gives a reasonable estimate of the $N_{\|}$ spectrum of the wave that would be launched in the tokamak. The pill box window exhibited a return loss of ~36 dB and an insertion loss of ~0.01 dB during the low power measurements and could satisfactorily handle power of 125 kW for durations up to 1 s during the high power tests. The novel mechanical structure of the window proposed in this work facilitated in-house development of the window with a 50% reduction in the brazing costs and efforts.

Keywords: **PAM, Tokamak, High Power, Pill Box Window, Plasma, Measurement.**

Chapter 1

Introduction

Rapid industrialisation among the developing countries has led to a large scale increase in carbon emissions due to the dependence on coal, oil and natural gas for energy sources. This dependence on fossil fuels for energy has resulted in the fast depletion of sources, thus creating a precarious situation for future energy requirements. Given that the urbanisation among the developing countries will only increase, it is important to work on the development and realisation of safer and cleaner energy sources for sustainable development. Although renewable sources like solar and wind energy are good alternatives, they can only be used to supplement the energy requirement and not as primary sources due to inconsistencies in environmental conditions and the problems of their storage. Hence, it is important to look at scenarios that may generate energy on the scale of a modern power plant but which are cleaner, safer, emission-free and sustainable. One process which fits all these parameters is *Nuclear Fusion*.

Nuclear fusion is a mechanism by which two light atoms like deuterium and tritium fuse together to create a heavier atom like helium. During this process, a huge of amount of energy is created (of the order of 17.6 MeV for one atom of deuterium and tritium) owing to the difference in the mass of the heavier atom and the two light atoms. The fusion process mainly occurs naturally in the stars and the Sun, thus powering them for years. However, there are several technological and scientific challenges before this process is recreated on earth in a controlled environment. The major issue is the inherent coulombs force of repulsion between the two light atoms which prevent them from fusing. However, if conditions are created where the nuclear binding force would surpass the electrostatic force of repulsion, then atoms may fuse, thus releasing energy. Such conditions are created when deuterium and tritium are densely confined and heated to more than 100 million degrees Celsius (comparable to that of the Sun). At these temperatures, the matter gets transformed into its fourth state- plasma (a mixture of unbounded electrons and ions [10]). Even if one may be able to heat this plasma, it is impossible for a container to contain it at such high temperatures. It is synonymous with creating a Sun first and then creating a box to hold the Sun. There is no known material that can withstand such extreme environments. One way to overcome this problem is to confine the plasma magnetically such that it does not touch the container. A very established way to achieve this is the *Tokamak* concept.

A tokamak is a device that has a donut shaped helically twisted magnetic fields due to a special arrangement of toroidal and poloidal magnetic fields. These fields create a magnetic cage and confine the plasma such that the plasma remains within this virtual cage. There have been worldwide efforts to establish and realise the tokamak concept. Several tokamaks have been built and/or are in operation, such as the Joint European Torus (JET) in UK [11], Frascati Tokamak Upgrade (FTU) in Italy [12, 13], Korea Superconducting Tokamak Advanced Research (KSTAR) in South Korea [14, 15], Experimental Advanced Superconducting Tokamak (EAST) in China [16, 17], Tungsten Environment in Steady-state Tokamak (WEST) and International Thermonuclear Experimental Reactor (ITER) in France [18–20], Tokamak Fusion Test Reactor (TFTR) and Alcator C-Mod in USA [21, 22], Japan Torus (JT-60) and Japan Torus-60 Super Advanced (JT-60SA) in Japan [23–25] and Steady-state Superconducting Tokamak (SST-1) and ADITYA -U in India [26–29]. These tokamaks have contributed to several interesting studies on plasma physics relevant to fusion research.

As mentioned earlier, to confine plasma in a tokamak configuration, toroidal and poloidal magnetic fields are necessary. The toroidal magnetic field is generated by toroidal magnetic coils. With the advent of large scale superconducting technology; superconducting coils based toroidal magnetic coils are employed in modern-day tokamaks for continuous operation. However, to generate a poloidal magnetic field, one has to drive the plasma current non-inductively to realize steady-state operation of a tokamak. One of the efficient methods to drive plasma current non-inductively relies on Lower Hybrid Current Drive (LHCD) scheme.

The LHCD system technology is proven on several tokamaks since the early eighties and is considered to be the most robust and matured technology. LHCD scheme involves the launching of directional waves carrying megawatts of power around a frequency of (1-5) GHz into the tokamak. There are several different types of launchers that may be used to launch these waves, namely Grill, Multijunction and Passive Active Multijunction. Conventionally, grill launcher was used worldwide and hence the LHCD system on ADITYA Tokamak employed the grill launcher. However, with the upgradation of the ADITYA Tokamak, it was decided to replace this grill launcher with a Passive Active Multijunction (PAM) launcher. The design, simulation studies, development and testing of this PAM launcher and its associated components form the subject of this thesis.

1.1 Rationale

The grill launcher is an array of phased waveguides which couples the RF power to the plasma. Although conceptually simple, it suffers from very poor reflection characteristics at the grill-plasma interface when density near the mouth of the launcher reduces. A reflection of more than 30% was observed on the erstwhile grill launcher installed on the ADITYA tokamak. On the other hand, the PAM launcher consists of an array of alternate passive (without excitation) and active (with excitation) waveguides. This arrangement reduces the reflection and hence couples more RF power to the plasma even at very low edge densities. This allows the launcher to be placed far away from the plasma edge. Cooling channels can be drilled through the thick walls behind the passive waveguides, thereby providing efficient thermal management of the launcher. Also, these walls aid in neutron shielding and increase the mechanical robustness of the structure. The PAM launcher is more compact and does not require a separate network of waveguides to feed RF power to its input. Hence, it was decided to develop a PAM launcher compatible with the ADITYA -U tokamak.

Although the PAM launcher has been designed and developed at JET, FTU, Tore Supra, EAST and KSTAR, it is critical to carry out its design studies separately for the ADITYA –Upgrade tokamak. This is because the design and development of the launcher do not follow a cook-book approach and is unique on account of different operating plasma parameters (like electron/ion density, electron/ion temperature, plasma current et cetera), tokamak parameters (like major radius, minor radius, the strength of the toroidal magnetic field et cetera) and space constraints (like port size, clearance from the support structure of the tokamak et cetera). This complex design requires extensive academic and research studies pertaining to its RF, thermal, disruption and plasma coupling performance, which are further verified using 3D simulation studies. After its design, the fabrication of the launcher is highly challenging as it demands several dedicated and precise fabrication techniques which are otherwise closely guarded. Thus, the design and realisation of the PAM launcher for the ADITYA -U tokamak involves considerable research and is therefore the focus of this thesis.

A survey of the literature (reviewed in detail in the next chapter) revealed a few lacunae, which are described below:

1. The PAM concept has been tested for launchers, which could accommodate a large number of active waveguides. For ADITYA –U tokamak, the port size constraint demands a smaller and compact launching system with fewer active waveguides.

The effectiveness of this concept for smaller and compact launcher systems with only three poloidal sections and two toroidal modules at 3.7 GHz has not been reported.

2. There is no mention of an experimental method to evaluate the performance of the PAM launcher in terms of the parallel refractive index ($N_{||}$) spectrum of the launched wave or the directionality of the wave at low power level, in air, before installing the launcher onto the tokamak.

3. The design and development of a 3.7 GHz RF window (to isolate the tokamak's Ultra High Vacuum (UHV) environment from the pressurised medium of the feeding waveguides) is a major concern for the proposed PAM launcher. The techniques reported in the open literature to fabricate the window involve multiple brazing cycles to braze two joints involving two dissimilar materials.

4. The mode converter structure, which forms a part of the transmission line network, uses a post to match the input impedance. The inclusion of this post is a bottleneck in the attempt to increase the power handling capacity of the transmission line network. This is because the E-field would get more concentrated near the post, thereby reducing the breakdown threshold.

1.2 Objectives and Major Contributions

It is the objective of this work to overcome these lacunae so that a PAM launcher and its associated components may be designed and developed for the ADITYA -U tokamak. The earlier grill launcher was being operated by 3.7 GHz klystron based RF source and hence PAM launcher should operate at a frequency of 3.7 GHz and must satisfactorily work for 1 s. The major contributions of this thesis are as follows:

1. The design, development and low power testing of a PAM launcher capable of

launching 250 kW/1 s of RF power at 3.7 GHz is carried out. Due to the available port size, the launcher had a fewer number of active and passive waveguides. The PAM concept was thus realised for a small size launcher system satisfactorily.

2. An experimental method to evaluate the performance of the PAM launcher at low power, in air, before installing it onto the tokamak is proposed. This method gives the power spectrum ($N_{\|}$ spectrum) of the wave launched by the launcher and also demonstrates the steering of the waves. The results obtained agreed excellently with the simulation.

3. The design, development along with the low and high power testing of a pill box type RF vacuum window capable of handling 125 kW/1 s of RF power at 3.7 GHz is carried out. The pill box window has a novel structure that enables brazing of two joints, each involving two dissimilar materials (metallised alumina and copper, SS304L and copper) in a single brazing cycle.

4. A new mode converter structure is proposed, which does not utilise a post to match the input impedance. In this work, a few steps are added to the broader dimension of the waveguide (where the E-field is zero) near the output. This method reduces the concentration of the E-field locally, thereby increasing the power threshold for breakdown.

1.3 Outline of the thesis

The remainder of the thesis is organised as follows:

Chapter 2 presents a review of the available literature and identifies the lacunae in them from the point of view of the work proposed in this thesis. The academic challenges involved while carrying out the work and the corresponding research highlight of the work is reported.

In **Chapter 3**, the design of the PAM launcher is presented considering various plasma, tokamak, space and RF constraints. The analyses of the proposed launcher in terms of its RF, thermal and mechanical performance are further reported. A novel mode converter design with a higher power handling capacity than the conventional mode converter is proposed and a comparative analysis between the two designs is reported.

In **Chapter 4**, the challenges involved in the mechanical design and fabrication of the PAM launcher are reported. Further, the methodologies devised and precise techniques identified/developed for the fabrication of the PAM launcher are presented.

Chapter 5 reports the RF characterisation of the PAM launcher in terms of its S-parameters. Further, a novel methodology used to measure the characteristics of the wave launched from the launcher is described.

Chapter 6 reports the design, development and low and high power testing of the RF vacuum window.

Finally, **Chapter 7** discusses the compatibility of the developed PAM launcher with the ADITYA –U tokamak, summarises the complete thesis and finally gives a short note on the future scope of the work.

Appendix A discusses the procedure employed for the benchmarking of the disruption analysis in COMSOL Multiphysics. The theoretical estimate of the disruption forces acting on a circular disc is calculated and further compared with the simulation results.

Appendix B presents the mechanical drawing of the PAM launcher.

Appendix C discusses the fabrication procedure employed for the realisation of the PAM section and the RF window. Further, the qualification tests carried out are described and their corresponding results are reported.

The design, development and RF characterisation of the test kits are discussed in **Appendix D**. These kits are used for the S-parameters measurement of the PAM launcher and its individual components.

Appendix E presents the post-processing methodology used to obtain the S-parameters of the launcher component from the measured combined (component + test kit(s)) S-parameters.

Chapter 2

Literature Review

2.1 Nuclear Fusion

Advances in high energy plasma physics have shown that nuclear fusion (which is the energy source of the Sun and the stars) may provide a sustainable source of energy for the future. If realised, such nuclear fusion based power plants would be safe, environment friendly and an almost unlimited source of energy [30–32]. Another advantage of a nuclear fusion based power plant is the minimal nuclear radiation associated with it. Also, the radioactive waste would not place a major burden on future generations [33–35]. A report [36] mentions that the cost associated with fusion power plants are only marginally higher as compared to that of the fission and coal power plants.

All matter around us is made up of atoms consisting of a positively charged nucleus surrounded by a negatively charged electron cloud [37]. Nuclear fusion is a reaction wherein two light nuclei fuse together to form a heavier nucleus and the mass difference manifests itself in the form of energy. One example of such a reaction is when deuterium and tritium (isotopes of hydrogen) react under favourable circumstances to give helium and neutrons, as shown in Eq. 2.1 [35],

$$ {}^{2}_{1}H + {}^{3}_{1}H \rightarrow {}^{4}_{2}He + {}^{1}_{0}n + 17.59\,MeV \tag{2.1} $$

To force the two nuclei to fuse, it is required that the repulsive Coulomb's forces are overcome. One could impart a very high kinetic energy (through heating) to the nuclei to bring them together within the separation of 10^{-15} m and overcome this Coulomb's force, thereby fusing the nuclei. At these high temperatures (in the range of few million degrees Kelvin (8620 - 17240 eV)), matter exists in plasma state. The temperature of the plasma and the Lawson parameter (product of the plasma density and the energy confinement time) determines the probability of fusion. In equilibrium, the ratio of the total plasma energy to the total power input to the plasma is the energy confinement time. The Lawson parameter should be greater than 10^{14} cm^{-3}s and the plasma temperature must be greater than ~2×10^{8} K [10].

There is no known material that can contain the plasma at such high temperatures. Magnetic confinement of plasma is considered to be the best option out of the various plasma confinement techniques. There exist different configurations to confine the plasma magnetically, which include the Stellarator [38, 39], the Magnetic mirror [40], the Z-pinch [41–43] and the Tokamak [44]. The most promising configuration as of date has been the Tokamak and is being studied rigorously worldwide. Thus, only the magnetic confinement via tokamak would be discussed further.

2.2 Magnetic Confinement via Tokamak

2.2.1 Principle

The tokamak, first commissioned in the Soviet Union (present-day Russia), is a torus shaped vacuum vessel inside which the plasma is confined. The vacuum in the tokamak is maintained with the help of external pumps. It has a toroidal magnetic field, produced by a set of toroidal field coils encircling the vacuum vessel, and a poloidal magnetic field, produced by the plasma current as shown in Fig. 2.1. When current is passed through the Inner poloidal field coils (Ohmic coils), it induces toroidal electric field in to the plasma vessel due to the transformer action. The central Ohmic coil acts as the primary winding (Primary transformer circuit), while the plasma acts as the single turn secondary winding (Secondary transformer circuit), as shown in Fig. 2.1. Small puffs of gas are let in the vessel and the toroidal electric field induced by the Ohmic coil breaks down the gas forming the plasma (and hence the plasma electric current). The plasma current produced by this technique is proportional to the rate of change of the flux in the Ohmic coil and is thus pulsed in nature. This plasma current further induces a poloidal magnetic field. The vector addition of the toroidal and the poloidal magnetic fields results into field lines that twist helically around the tokamak and helps in confining the plasma [45]. Fig. 2.1 depicts the structure of the tokamak along with all the other mentioned components [46].

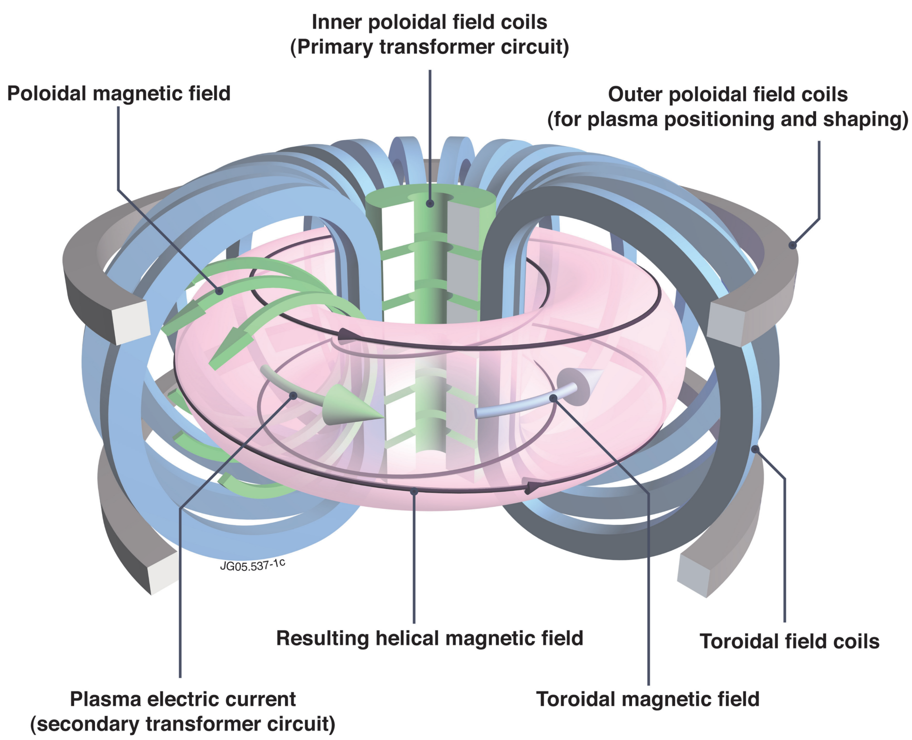

Figure 2.1: Structure of the tokamak [46].

2.2.2 International Efforts

Worldwide, efforts are underway to confine the plasma for longer durations and realise fusion power. In this quest, many countries have built and operated tokamaks. Some of the tokamaks around the world are mentioned in Chapter 1.

A major upcoming reactor, International Thermonuclear Experimental Reactor (ITER) at Cadarache, France, is funded by a consortium of seven countries, namely, European Union (EU), China, India, Japan, Russia, South Korea and USA. The main goal of ITER is to generate ten times more energy (Q = 10) than what is fed into it and produce a self-sustaining reaction for periods up to 480 seconds. Table 2.1 summarises the important parameters of these tokamaks, while Fig. 2.2 shows these tokamaks.

Table 2.1: Parameters of the major tokamaks around the world [47].

Name	**Country**	**(Major, Minor) radius (m)**	**Toroidal Field, TF (T)**	**Configuration**	**LHF (GHz)**	**LH power (MW)**
JET	EU	2.96, 0.96	4	D-shaped	3.7	7
FTU	Italy	0.93, 0.3	8	Circular	8	2.5
KSTAR	South Korea	1.8, 0.5	3.5 SC*	D-shaped	5	3
EAST	China	1.75, 0.43	5 SC*	D-shaped	2.45	4
Tore Supra (WEST)	France	2.25, 0.7	4.5 SC*	Circular	3.7	5
ITER	International	6.2, 2	5.3 SC*	D-shaped	5	40 planned
Alcator C-Mod	USA	0.67, 0.22	8	D-shaped	4.6	2.5
JT-60U	Japan	3.4, 1	4.2	D-shaped	Around 2	8-12

*SC: Superconducting

2.2.3 National Efforts

In India, indigenous tokamaks - ADITYA (operating since 1989 and now upgraded to ADITYA –Upgrade) and Steady-state Superconducting Tokamak-1 (SST-1) (operating since 2013) [48–50] have been commissioned at the Institute for Plasma Research, Gandhinagar.

The ADITYA was the first indigenously designed and fabricated tokamak in India which

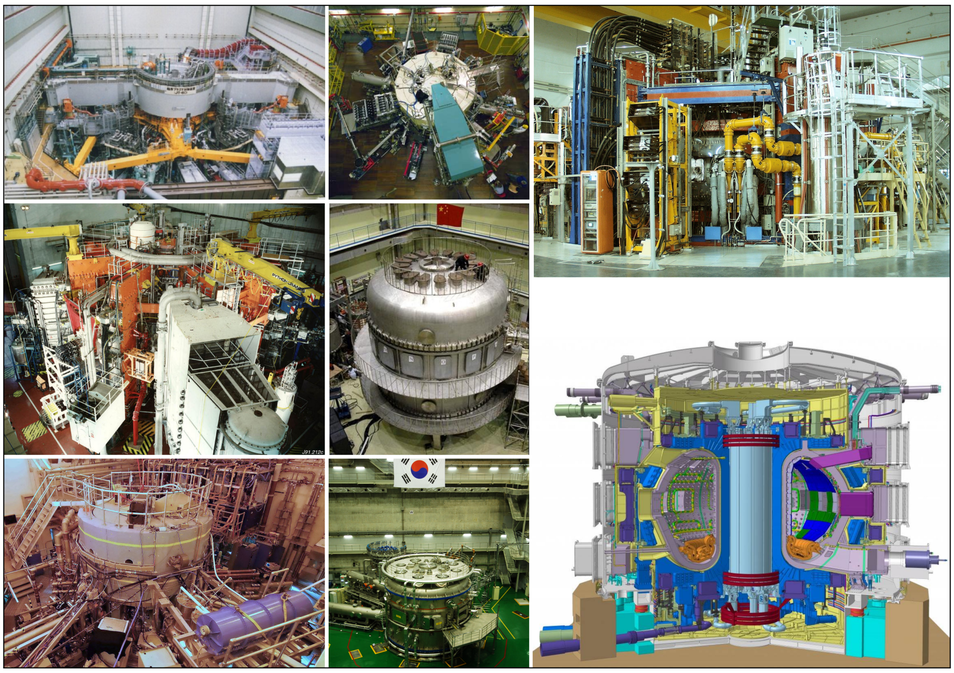

Figure 2.2: Tokamaks around the world (top to bottom, left to right): JT-60U, JET, Alcator C-Mod, FTU, EAST, KSTAR, Tore Supra, ITER [47].

operated in pulsed mode. The ADITYA tokamak is upgraded to ADITYA –Upgrade tokamak to operate at enhanced plasma parameters. This upgrade includes the installation of diverters, integration of more diagnostics and auxiliary heating systems. The ADITYA –Upgrade tokamak has a major and minor radius of 0.75 m and 0.25 m, respectively, with a toroidal magnetic field of 1.5 T at the plasma center.

The SST-1 is a Steady-state Superconducting Tokamak aiming at a discharge of 1000 s. It has a major radius of 1.1 m and a minor radius of 0.2 m with a toroidal magnetic field of 3 T at the plasma center.

To realise steady-state tokamak plasma, the plasma current is required to be driven non-inductively. There are various methods proposed in the literature to heat the plasma and drive the plasma current using RF electromagnetic waves, relativistic beam electrons, phased injection of frozen hydrogen pellets and oscillating magnetic fields [51–56]. These systems are called the auxiliary heating and current drive systems. The Lower Hybrid Current Drive (LHCD) scheme is one of the RF electromagnetic waves methods which is used for the driving the plasma current non-inductively and is discussed below.

2.3 Lower Hybrid Current Drive (LHCD)

The LHCD is the most popular and robust scheme which has successfully demonstrated non-inductive plasma current drive experimentally in low density regime. The plasma current is driven by the injection of high power electromagnetic travelling waves toroidally in a preferred direction. The launched waves undergo non-collisional Landau damping with the resonant particles and transfer momentum to them, leading to a non-inductive current drive.

Following Stix [57, 58] notation for slab geometry of the plasma; wherein, the plasma has been modelled as a dielectric material possessing anisotropy because of the toroidal magnetic field. The plasma density varies in the x-direction, the toroidal magnetic field is along the z-direction and the y-axis corresponds to the poloidal direction, as shown in Fig. 2.3.

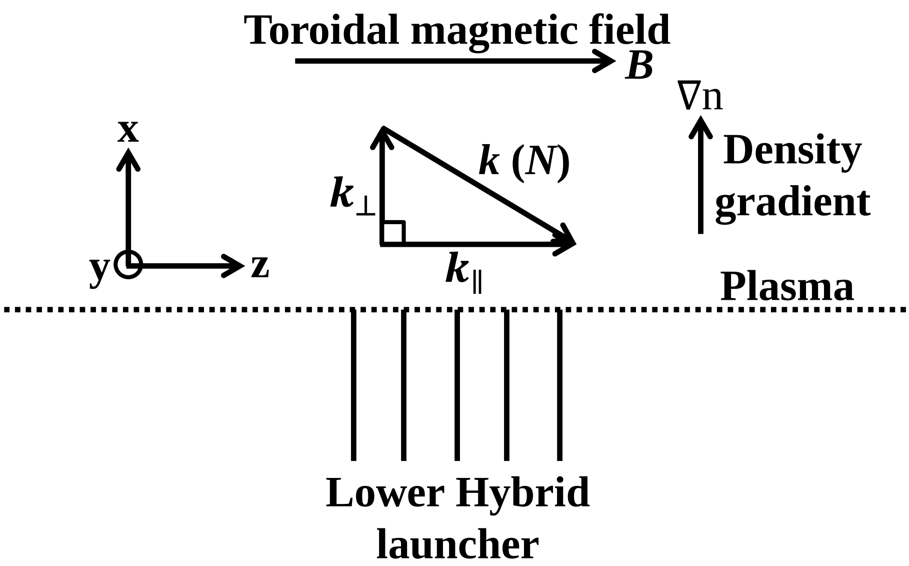

Figure 2.3: Pictorial representation of slab geometry of the plasma.

The propagation of the electromagnetic wave in this plasma (dielectric) medium follows Maxwell's equation (after Fourier analysis in time and space) and the wave may be written as,

$$\boldsymbol{k} \times \boldsymbol{k} \times \boldsymbol{E} + \frac{\omega^2}{c^2}\boldsymbol{\varepsilon} \cdot \boldsymbol{E} = \boldsymbol{0} \tag{2.2}$$

where,

$\boldsymbol{\varepsilon}$ is the dielectric tensor and can be written as,

$$\boldsymbol{\varepsilon} = \begin{bmatrix} S & -iD & 0 \\ iD & S & 0 \\ 0 & 0 & P \end{bmatrix} \tag{2.3}$$

Typically, lower hybrid waves lie in the range, $\omega_{ci}^2 \ll \omega^2 \ll \omega_{ce}^2$, and hence the tensor elements S, D and P may be written as,

$$S = 1 + \left(\frac{\omega_{pe}^2}{\omega_{ce}^2}\right) - \left(\frac{\omega_{pi}^2}{\omega^2}\right) \tag{2.4}$$

$$D = \frac{\omega_{pe}^2}{\omega\,|\omega_{ce}|} \tag{2.5}$$

$$P = 1 - \frac{\omega_{pe}^2}{\omega^2} \tag{2.6}$$

The wave equation shown in Eq. 2.2 may also be written in terms of the refractive index ($\boldsymbol{N}$) as,

$$\boldsymbol{N} \times \boldsymbol{N} \times \boldsymbol{E} + \frac{\omega^2}{c^2}\boldsymbol{\varepsilon} \cdot \boldsymbol{E} = \boldsymbol{0} \tag{2.7}$$

Further, θ is the angle between the toroidal magnetic field, $\boldsymbol{B} = \mathrm{B}_0\boldsymbol{z}$ (z-direction) and $\boldsymbol{N}$, as shown in Fig. 2.3. Assuming, $\boldsymbol{N}$ lying in the x-z plane, the equation in the matrix form becomes,

$$\begin{bmatrix} S - N_{\|}^2 & -iD & N_{\perp}N_{\|} \\ iD & S - N^2 & 0 \\ N_{\perp}N_{\|} & 0 & P - N_{\perp}^2 \end{bmatrix} \begin{bmatrix} E_x \\ E_y \\ E_z \end{bmatrix} = 0 \tag{2.8}$$

where,

$N_{\|} = |\boldsymbol{N}|\cos(\theta)$

$N_{\perp} = |\boldsymbol{N}|\sin(\theta)$

For arbitrary electric field, the natural modes of plasma may be obtained by setting the determinant in Eq. 2.8 equal to zero which results in a biquadratic equation in $N_{\perp}^2$ (dispersion relation) as shown in Eq. 2.9,

$$AN_{\perp}^{4} + BN_{\perp}^{2} + C = 0 \tag{2.9}$$

where,

$A = S$

$B = (P + S)(N_{\parallel}^{2} - S) + D^{2}$

$C = P[(N_{\parallel}^{2} - S)^{2} - D^{2}]$

In general, the roots of the above dispersion relation shown in Eq. 2.9 can be written as,

$$N_{\perp}^{2} = \frac{-B \pm \left(B^{2} - 4AC\right)^{1/2}}{2A} \tag{2.10}$$

These roots have distinct behaviour depending on the value of $N_{\parallel}$. There exists a threshold value of $N_{\parallel}$, known as critical accessibility ($N_{\parallel}^{acc}$), which is defined in [58, 59] as,

$$N_{\parallel}^{acc} = \frac{\omega_{pe}}{\omega_{ce}} + \sqrt{1 + \left(\frac{\omega_{pe}}{\omega_{ce}}\right)^{2} - \left(\frac{\omega_{pi}}{\omega}\right)^{2}} \tag{2.11}$$

One root represents the fast wave (smaller $N_{\perp}$) while the other represents the slow wave (larger $N_{\perp}$). Now we discuss the three possible cases of $N_{\parallel}$ and the behaviour of the slow and fast waves with the help of the three graphs given in Fig. 2.4. The figure is a typical plot of the value of the $N_{\perp}^{2}$ with respect to the plasma density. From the graph, it is obvious that both slow wave and fast wave cannot propagate into the plasma until the density is above a critical density known as cutoff density (n_{sc} and n_{fc}). The cutoff for the slow wave is lower than the cutoff for the fast wave.

(a) $N_{\parallel} < N_{\parallel}^{acc}$: In this case, the slow wave propagates into the plasma beyond its cutoff density (n_{sc}) and gets converted to a fast wave at some density (say n_1). Here, the slow wave is inaccessible to the densities above n_1 from the low density side of the plasma. However, the slow wave can also propagate at a higher density (say n_2) to access the lower hybrid resonance layer. It shows that there exists a gap where slow

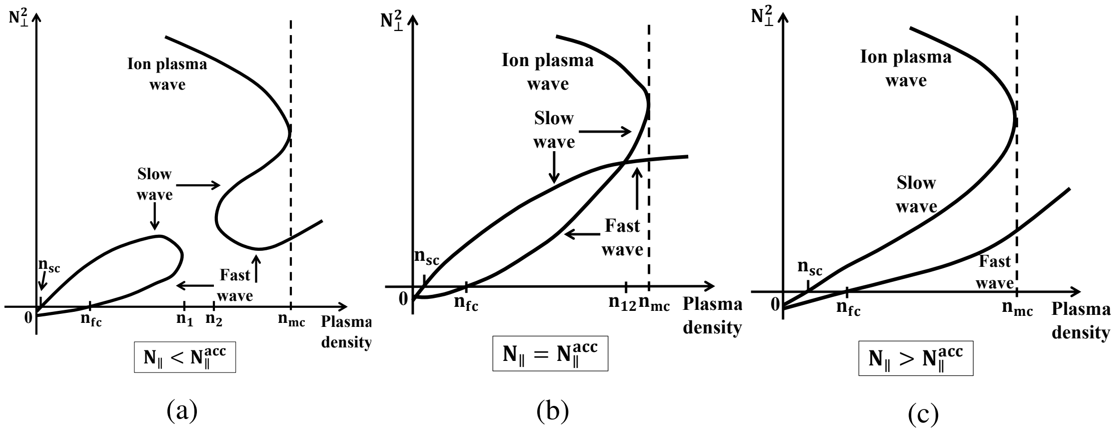

Figure 2.4: Perpendicular refractive index v/s Plasma density for constant parallel refractive index [59]

wave cannot propagate (between n_1 and n_2). This scenario is depicted in Fig. 2.4a.

(b) $N_\parallel = N_\parallel^{acc}$: Under this condition, the gap mentioned in the above case is reduced to a single point (say n_{12}). At this density, the slow wave may propagate further as a slow wave or mode convert into a fast wave, as shown in Fig. 2.4b.

(c) $N_\parallel > N_\parallel^{acc}$: In this case, no mode conversion is observed. It means the characteristics of slow wave are maintained until it reaches the lower hybrid resonance layer as shown in Fig. 2.4c.

It should be noted that the above analysis is with respect to slab geometry of the plasma. However, the same analysis may be applied in toroidal geometry to a good approximation, and it would still provide a good understanding of the wave propagation in tokamak plasmas [10]. As we are interested in driving plasma current using slow waves into the tokamak, the above cases suggest that slow wave can propagate deep into the plasma if $N_\parallel > N_\parallel^{acc}$ and can drive plasma current provided they do not encounter lower hybrid resonance layer inside the plasma. Therefore, it should be ensured that we choose a source frequency for which lower hybrid resonance layer should not exist in tokamak plasma.

The lower hybrid frequency can be evaluated using the equation given by Eq. 2.12 in [58, 59],

$$\omega_{lh} = \frac{\omega_{pi}}{\sqrt{1 + \frac{\omega_{pe}^2}{\omega_{ce}^2}}} \tag{2.12}$$

where,

ω_{pi} is the ion plasma frequency given by $0.4\pi\sqrt{\text{n}}$.

ω_{pe} is the electron plasma frequency given by $18\pi\sqrt{\text{n}}$.

ω_{ce} is the electron cyclotron frequency given by 1.76×10^{11}B.

Here, n is the density in m^{-3} and B is the magnetic field in Tesla.

For the ADITYA –Upgrade tokamak, f_{lh} ($\omega_{lh}/2\pi$) is of the order of GHz. Hence, the operating frequency is selected from the commercially available high power source as 3.7 GHz.

2.4 Slow Wave Launching

Slow waves may be excited toroidally into the plasma by feeding an array of narrow waveguides (grill launcher) with the fundamental mode in such a way that E-field is parallel to the narrower side (which is also parallel to the toroidal magnetic field) and the adjacent waveguides are phased relatively [60–64]. The resultant E-field in the plasma would then have an $N_{\|}$ spectrum with successive peaks at [6, 65, 66],

$$N_{\|m} = \frac{\delta\phi}{k\Delta} + \frac{2\pi m}{k\Delta}, m = 0, \pm1, \pm2, ... \tag{2.13}$$

With a fixed frequency of operation ($k = 2\pi$f/c) and geometry and variable phasing between the adjacent waveguides, one can launch travelling waves having different $N_{\|}$ with $\delta\phi$ between 0-π leading to directional waves and current drive while $\delta\phi$ between π-2π would lead to current drive in the opposite direction. The condition $\delta\phi = \pi$ would create symmetric slow waves leading to heating [6].

The coupling of these excited LH waves takes place at the edge of the plasma when the launcher is immersed in the plasma with density above cutoff. As discussed earlier, for a given LH frequency (3.7 GHz in our case), this cutoff density may be evaluated by equalising the local plasma frequency (ω_{pe}) to the launching LHW frequency (ω) as shown in Eq. 2.14 [58, 59],

$$\omega_{pe}^2 = \omega^2 = \frac{n_c \times e^2}{m_e \times \varepsilon_0} \tag{2.14}$$

where,

n_c is the cutoff density corresponding to the launching LHW frequency (ω) (m^{-3}).

e is the charge on the electron (C).

m_e is the mass of the electron (kg).

Rearranging the terms in Eq. 2.14, the cutoff density is given by Eq. 2.15,

$$n_c = \frac{\omega^2 \times m_e \times \varepsilon_0}{e^2} \tag{2.15}$$

The cutoff density corresponding to 3.7 GHz turns out to be 1.7×10^{17} m^{-3}.

Waves excited with $N_{\parallel}^2 > 1$ can tunnel through the evanescent region and propagate towards higher density, while those launched with $N_{\parallel}^2 < 1$ are reflected back [57, 61, 67]. As the coupling is determined by the electron density at the launcher's mouth, matching the impedance of the LH waves in the edge plasma and the launching structure is important. This can be achieved by shaping the front of the launcher to fit the plasma surface and by correctly positioning the launcher into the tokamak. The positioning of the PAM launcher is controlled via a bellow [68].

Systems which are used to generate these LH waves typically consist of RF power sources (usually solid-state drivers followed by high gain klystrons), transmission lines, RF windows and phased waveguide arrays. A vast amount of literature is available on the launcher of these systems [2, 3, 69–71]. These systems employ launchers which can majorly be classified as the GRILL [60, 61], the Multijunction and the PAM proposed in 1980's [72–74]. Along with these, loop antennas [75, 76], Fully Active Multijunction (FAM) [2], Quasi-optical grill [77–79] were also used, albeit rarely to launch the LH waves. The next section chronologically details the development of the LH launcher concept.

2.5 LHCD launchers

Fisch first proposed the lower hybrid current drive to maintain plasma discharges for a longer period [52, 56]. Thereafter, many experiments have successfully demonstrated its capability to maintain steady-state current without the help of an ohmic heating transformer [5, 80–90]. To ensure good coupling of RF energy to the plasma, Puri and Tutter [91] proposed to launch the wave directly in the toroidal vessel by using the classical waveguide in such a manner that the wave index $N_{\|}$ is lower but close to one. In this grazing incidence approach, the author shows that good RF coupling may occur when $\omega_{pe}^2/\omega_{ce}^2$ at resonance is less than 0.05. However, this method requires high RF fields in vacuum, which may lead to a possible breakdown. Thus, it is applicable for only low density plasmas. Another method proposed by Stix [58] is to slow down the phase velocity of the wave in the magnetic field direction. The parallel wave index ($N_{\|}$) must now be larger than the critical one ($N_{\|}^{acc}$).

P Lallia [60] first proposed the GRILL structure for the JET tokamak in 1974. The dimensions of the GRILL antenna are so selected that good impedance matching is obtained between it and plasma. To determine these dimensions of the GRILL antenna, a methodology was first reported by Brambilla in 1976 [61]. A computer code to determine the characteristics of the GRILL antenna, for a given design, was popularised by Boley [92] in his GRILL code. The GRILL antenna has been installed successfully in many tokamaks around the world [1, 86, 93–101] and the reflection of considerable percentage (20-50)% has been reported.

Further, Nguyen and Moreau [73, 74] proposed a simpler structure viz. a multijunction GRILL, which offered a lower reflection coefficient compared to the GRILL launcher at the cost of purity of the launched spectrum. In this, a terminal part of the waveguide is divided into several subsidiary waveguides by means of dividers. This provides a more compact arrangement. Although multiple schemes may accomplish this division [102] [103], generally, E-plane bijunctions are used [104]. In a multijunction launcher, choice of the input phase is important and helps in bringing forth the self-matching property which is the important aspect of the Multijunction [104]. This Multijunction property causes a recycling effect due to multiple reflections between the launcher mouth and the E-plane junction discontinuity, where the reflected power is sent back to the plasma. This reduces the reflection coefficient. The phase which may achieve this property is 90° in case of a Bijunction and 60° or 120° in case of a Trijunction.

The PAM concept was proposed in the mid 90's [105, 106], though some references to it may be found in the literature of the early 1980's [72, 73]. It's capability for steady-state operation was actively explored from the mid 90's [105, 106]. The PAM launcher is derived from a multijunction and can be viewed as a multijunction having a passive waveguide interposed between two active waveguides forming an alternate active and passive structure. The passive waveguides act as reflectors radiating back a majority of the power reflected from the plasma. The intense cross-coupling between the active and passive waveguides results in better coupling with the plasma even at very low plasma density (typically around cutoff density) at the mouth of the launcher [6].

For reactor-grade plasma, the amount of power required to be injected at the lower hybrid frequency is greater than 50 MW. The thermal management and the mechanical robustness at such a large power level then becomes an issue. Thus, an array of waveguides where only alternate waveguides are fed (active), which are separated by a short (passive), may be used. Cooling lines maybe drilled through the passive elements which may facilitate thermal management and mechanical stability. Further, if the depth of the passive short is adjusted so that the electric field in the passive waveguide is coherent with the active one a highly directive power spectrum with small reflection can be achieved. This is the basic concept behind the Passive Active Multijunction Antenna that was proposed by Motley and Hooke [72], Bibet [105, 106]. It is worth mentioning, for the sake of convenience, a Bijunction PAM usually uses 270° while a Trijunction based PAM uses 240°.

It is necessary to maintain amplitude and phase coherence for the appropriate current drive. This is usually achieved when the depth of the passive waveguide is approximately a quarter of the wavelength. This maximizes the E-field and causes the phase difference between the active and passive waveguide to be equal to half the phase difference between the two active waveguides. However, in practise it is required to optimise the depth of the passive waveguides carefully. Coupling codes such as Advanced LOwer Hybrid Antenna (ALOHA) [107] may be used to achieve this.

The PAM launcher was first deployed on the FTU Tokamak [85]. The power density achieved in almost steady-state condition has been 85 MW/m^2. This validated the PAM concept as proposed by [72, 105, 106]. Further, a PAM launcher was also installed on the Tore Supra tokamak which exhibited low reflection close to cutoff density. It consisted of 16 modules mounted in 2 rows and 8 columns. Each module comprised of two active and two passive waveguides. The passive waveguide was quarter wavelength long. An active cooling arrangement was employed so that long pulse operation can be achieved. Very low reflection (less than 2%) has been achieved with a coupling power of 2.7 MW during the pulse duration of 78 seconds. This demonstrated the capability of the PAM concept for ITER operations.

The RF modelling of the ITER antenna is presented in [108]. This is capable of delivering 20 MW/CW power at 5 GHz. This paper reported the design of individual components of PAM launcher thus building the overall confidence on the PAM concept.

2.6 RF Vacuum Window

The PAM launcher would be in ADITYA –U tokamak's UHV conditions while the transmission lines feeding the launcher would be pressurised with nitrogen to prevent RF breakdown. A high power RF vacuum window is required to mechanically isolate the vacuum and the pressurised sections and remain transparent to the RF power with minimum insertion loss [109–112]. The PAM launcher has two inputs and is designed for a total input power of 250 kW. Each of the two klystrons (rated at 0.5 MW/CW) would be required to inject 125 kW of RF power into separate transmission lines connected to these two inputs. Hence, a pill box window, capable of sustaining RF waves at a power level of 125 kW at 3.7 GHz with desired return and insertion loss, is required on each of the two transmission lines. The design and low power testing of an alumina based RF window, designed at 5 GHz, was reported in [109], however the high power performance was not reported. A BeO window was reported in [110] which could handle about 500 kW power for short pulse durations at 5 GHz, while a sapphire based window was reported [111], which could handle a power of 220 kW up to 3 seconds at 3.7 GHz. Fabrication and performance of high power RF windows for the PEP-II B factory energy collider were reported in [113, 114]. These windows could sustain a power level of 270 kW at 476 MHz for CW operations.

2.7 Relevance and salient contributions

The literature survey described in the above sections presents various efforts in the quest to continually improve the methods to launch the LH power into the plasma. The contributions of this thesis are now compared vis-à-vis the existing literature to highlight the salient features of this work and are reported in Table 2.2.

Table 2.2: Salient contributions vis-à-vis existing literature.

No.	Contribution	Source	Description	Remark
1.	Design and development of the PAM launcher compatible with the ADITYA –U tokamak.	[5, 6, 115]	PAM launcher has been designed/installed in various tokamaks like Tore Supra, FTU, JET et cetera. These PAM structures include multiple modules in toroidal and poloidal directions.	The PAM launcher at FTU tokamak had 4 modules in the poloidal and 3 modules in the toroidal direction. For ADITYA –U tokamak, these number of modules could not be accommodated due to port size constraints. Thus, an even smaller launcher system is required. PAM concept has not been demonstrated in a smaller size antenna with a limited number of modules/number of active waveguides.
		This work (Ch.3 and Ch.4).	A PAM launcher has been designed with 3 poloidal sections and 2 toroidal modules due to lower frequency, limitations in port size, and space constraints. Multi-junction effect has been successfully incorporated even with this limitation with a power level compatible with ADITYA –U tokamak.	Even in a smaller size, the proposed structure demonstrated a directivity of 65% with a power handling capacity of 250 kW for durations up to 1 sec.

2.	A method to measure the $N_{\parallel}$ spectrum and 2D profile of the launcher.	[116]	The characterisation of lower hybrid wave spectrum using metamaterial load to mimic the plasma is reported.	As per the best knowledge of the author, there is no report in the open literature on the experimental technique to measure the $N_{\parallel}$ spectrum and the 2D profile of the PAM launcher, in air, at low power level.
		This work (Ch.5).	A novel technique to measure the $N_{\parallel}$ spectrum and 2D profile of the waves launched by the PAM launcher, in air, at low power is proposed to validate the design.	The measurement results obtained from the proposed technique are consistent with those obtained from CST Studio suite software and the ALOHA codes. This technique helps to validate the launcher before installing it onto the tokamak.
3.	A novel pill box type RF vacuum window.	[109–111, 113, 114]	Windows utilising BeO and sapphire are presented.	The designs presented are such that multiple brazing cycles would be required for their development.
		This work (Ch.6).	A novel structure in which two joints involving two dissimilar materials (metallised alumina and copper, SS304L and copper) can be brazed in one brazing cycle.	Pill box window was successfully fabricated using this technique. A reduction of brazing cost and effort by a factor of two was achieved.

4.	A novel Mode Converter.	[117, 118]	Most mode converters (TE_{10} to TE_{m0}) use a post for RF impedance matching.	The inclusion of post increases the concentration of the E-fields, leading to a reduced power handling capacity.
		This work (Ch.3).	The proposed mode converter uses a step in lieu of the post to provide a capacitive reactance to match the input of the mode converter.	The steps are provided along the broader side of the waveguide where the E-field is zero. The absence of the matching post increases the power handling capacity by ~97.2%.

Further, considerable technology development and know how was generated in the development of the PAM launcher and the alumina based pill box window to further the cause of indigenous technology development.

2.8 Summary

The focus of this thesis is the design and development of the Passive Active Multijunction launcher for the ADITYA –U tokamak. Although these launchers have been designed and developed in a few other tokamaks, newer launcher design efforts are particularly encouraged in the fusion community as the design and performance of the launcher varies from tokamak to tokamak. The design and development of the PAM launcher and the associated waveguide components are focussed on in this thesis. The interaction of the wave with plasma must be first studied to determine the optimum launcher dimensions, after which its RF design can be carried out. The next chapter focuses on this aspect and presents detailed design and simulation results of the proposed PAM launcher.

Chapter 3

Design and Simulation Results

As discussed in Chapter 2, a Passive Active Multijunction (PAM) launcher compatible with the ADITYA –U tokamak is to be designed and developed at 3.7 GHz. Further, the performance of the designed launcher is to be evaluated in terms of its plasma coupling properties using open source code like ALOHA. Commercial solvers like COMSOL Multiphysics and CST studio are used to study the multiphysics performance of the launcher. A high power RF system, based on the 3.7 GHz, 500 kW/CW klystrons, is currently being used to feed the existing Lower Hybrid (LH) system of SST-1 tokamak [49]. It is worth mentioning that the same system would feed the PAM launcher.

In this chapter, a basic design of the PAM launcher, based on the plasma parameters and space constraints of the ADITYA –U tokamak, is proposed. The behaviour of the designed launcher is analysed for various density and density gradient combinations at the mouth of the launcher, launcher mouth dimensions and relative phasing between the adjacent active waveguides. Further, the performance of the design is studied using 3D simulations in terms of its RF, RF breakdown, thermal and disruption constraints to gauge its efficacy. The results shown in this chapter have been published in peer reviewed journals [8, 9]

3.1 PAM design considering operating densities

The parallel refractive index ($N_{\|}$) of the waves to be launched by the PAM launcher is the most important and also the first parameter which is to be considered before commencing the design of the launcher. The $N_{\|}^{acc}$ (accessibility $N_{\|}$) plays an important role in deciding the $N_{\|}$ as discussed in Chapter 2. A graph of $N_{\|}^{acc}$ versus the electron density for a toroidal magnetic field (B_t) of 1.5 T at the plasma axis (maximum B_t for ADITYA –Upgrade tokamak), is plotted in Fig. 3.1 using Eq. 2.11. The operating density for the ADITYA –U tokamak is in the range of (0.8-3) $\times$ 10^{19} m^{-3} and the end limits are marked in the graph with the vertical dark yellow dash-dot lines. It can be observed from the figure that the corresponding values of $N_{\|}^{acc}$ are 1.75 and 2.75 (marked with the horizontal dark yellow dash-dot lines). Thus, the RF waves could be launched with a parallel refractive index ($N_{\|}$) in the range of 1.75 to 2.75 (2.25 ± 0.5) to access the plasma centre. Also, the PAM launcher should be designed such that it is capable of incorporating these variations in the main peak $N_{\|}$ value of the launched wave spectrum.

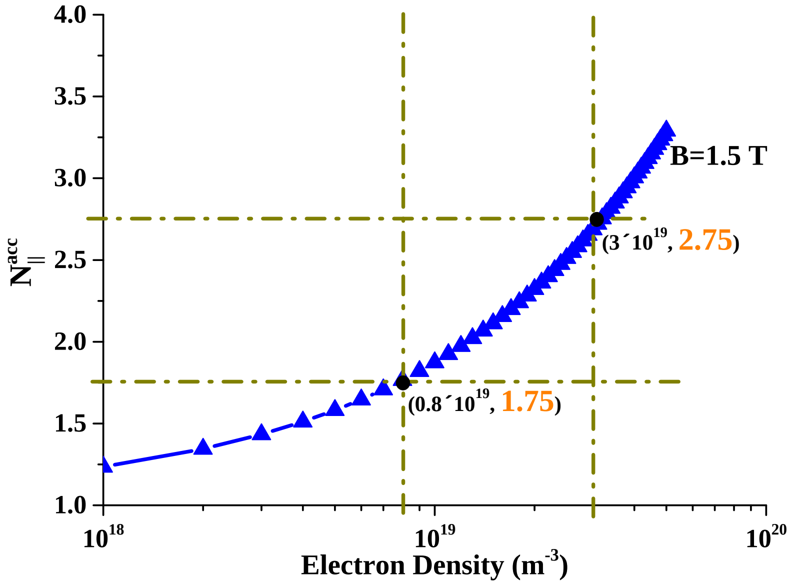

Figure 3.1: A plot of $N_{\|}^{acc}$ versus the electron density for a toroidal magnetic field (B_t) of 1.5 T. Vertical dark yellow lines (dash-dot) mark the densities 0.8 $\times$ 10^{19} m^{-3} and 3 $\times$ 10^{19} m^{-3} and the horizontal dark yellow lines (dash-dot) mark the corresponding $N_{\|}^{acc}$ values of 1.75 and 2.75, respectively.

3.2 PAM design considering port size constraint

This section discusses the basic design of the mouth of the PAM launcher considering the available port size dimensions and the desired $N_{||}$. The top view of a typical Passive Active Multijunction scheme is shown in Fig. 3.2. It has active (marked as “A”) and passive (marked as “P”) waveguides juxtaposed to form the mouth of the launcher. The active waveguides are the ‘radiators’ which radiate the RF waves (in the dominant mode (TE_{10}) of the rectangular waveguide) fed to them from the input lines. The passive waveguides are slots, grooved to a depth of $d_p = \lambda_g/4$ (typically, where, λ_g is the guided wavelength in the passive waveguide), between two adjacent active waveguides at the mouth. They act as reflectors and recirculate the reflected power (from the plasma) back to the plasma. This is of importance; particularly, when the density at the mouth of the launcher is close to the cutoff density leading to significant reflection from the plasma edge. The distance between the centres of the two adjacent active waveguides is referred as periodicity (δ) and plays an important role in deciding the $N_{||}$ of the launcher.

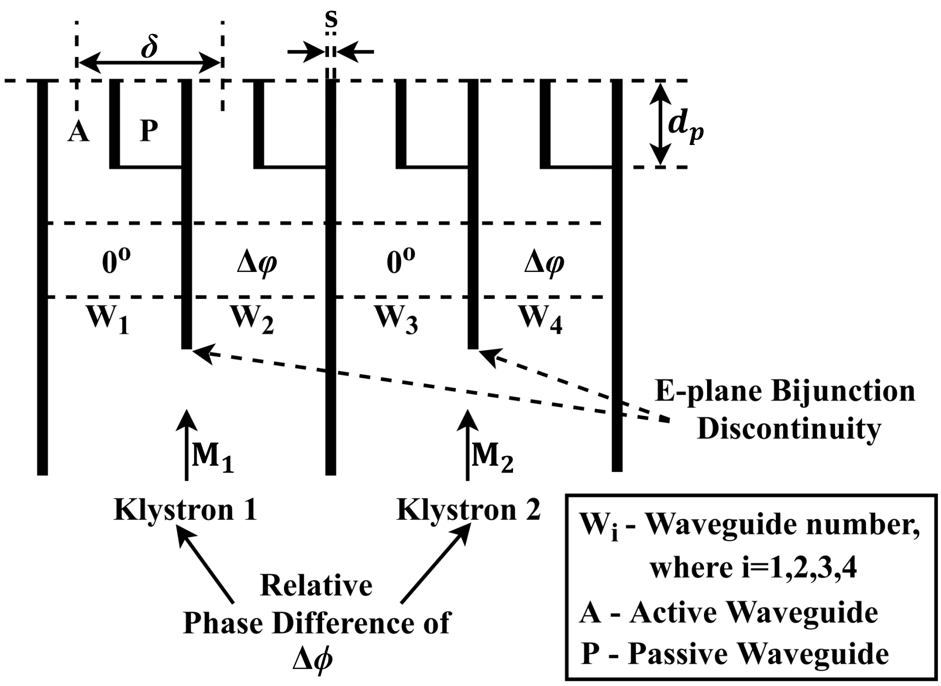

Figure 3.2: Top view of a typical Passive Active Multijunction scheme illustrating critical design parameters.

Another important parameter that governs the $N_{\parallel}$ of the launched wave is the phasing between the two adjacent active waveguides ($\Delta\varphi$). In Fig. 3.2, the phase shift of $\Delta\varphi$ is marked in waveguides W_2 and W_4 with dotted lines and it denotes the presence of a fixed phase shifter. Also, the phase shift of 0° is marked in waveguides W_1 and W_3 with dotted lines and it denotes the presence of straight waveguides of lengths equal to that of the fixed phase shifters. Similar notations are used in the figures henceforth. To provide flexibility to the $N_{\parallel}$ spectrum, the PAM launcher should comprise of an array of relatively phased ($\Delta\phi$) modules (denoted as M_1 and M_2). A group of active and passive waveguides in the toroidal direction is called a "module". Each module of the PAM launcher consists of an equal number of waveguides.

The main peak $N_{\parallel}$ value of the launched spectrum in terms of the parameters shown in Fig. 3.2 may be written as [119],

$$N_{\parallel} = \frac{\Delta\varphi}{k\delta} + \frac{\Delta\phi - \pi}{k\delta N_{wgd}} \tag{3.1}$$

where,

- $\Delta\varphi$ is the fixed internal phase shift between the adjacent active waveguides of a module and is measured with reference to the waveguide on the left.
- k is the wave number.
- δ is the periodicity of the PAM launcher (distance between the centres of the two adjacent active waveguides).
- $\Delta\phi$ is the variable external phase shift between the adjacent modules in the toroidal direction and is measured with reference to the module on the left.
- N_{wgd} is the number of active waveguides in a module.

The above equation has two terms; the first term helps to evaluate the main peak $N_{\parallel}$ value, which in our case is 2.25, whereas the second term gives the variation in this value. This variation can be achieved by changing the phase shift ($\Delta\phi$) between the adjacent modules.

For the design frequency of 3.7 GHz, the wave number (k) is constant and is 0.0775 rad/m. The first term in Eq. 3.1 is fixed to 2.25, as discussed in Section 3.1. Thus, the ratio of the fixed internal phase shift ($\Delta\varphi$) and the periodicity (δ) is constant. For a fixed internal phase shift of 90°, the periodicity obtained is 9 mm; whereas, for 270° the periodicity is 27 mm. The periodicity incorporates widths of one active waveguide, one passive waveguide and two septa thicknesses (s), as shown in Fig. 3.2. In the first case (90°), with a periodicity of 9 mm, the width of the active waveguides (radiators) would be very small, resulting in a higher probability of RF breakdown as compared to the second case (270°) which has a periodicity of 27 mm. Thus, it is decided to have a periodicity of 27 mm, resulting in a fixed internal phase shift ($\Delta\varphi$) of 270° between the two adjacent active waveguides of a module. The fixed internal phase shift of 270° is measured with reference to the waveguide on the left.

It is worth noting that the periodicity of the PAM launcher is higher as compared to that of the grill launcher due to the presence of the passive waveguides between the active waveguides. Thus, the excitation of a desired $N_{\|}$ power spectrum requires a higher relative phase shift between the adjacent active waveguides of the PAM launcher as compared to that of the grill launcher.

As discussed above, the periodicity (27 mm) incorporates widths of one active waveguide, one passive waveguide and two septa thicknesses. With two septa each of 2 mm, the total available width for the active and passive waveguides is 23 mm. It is desired to have an almost equal width for both the waveguides to avoid RF breakdown. Thus, the width of the active waveguide is decided to be 12 mm, while that of the passive waveguide is decided to be 11 mm. The width of the active waveguide is 1 mm greater than the width of the passive waveguide since the active waveguide (during transmission) would generally handle more RF power as compared to the passive waveguide (during recirculation). The height (broader dimension) of the waveguides is chosen to be 76 mm to ensure the propagation of only the dominant TE_{10} mode at 3.7 GHz.

The ADITYA –Upgrade tokamak has an available port size of 490 mm (height) × 190 mm (width) for the LH launcher. The possible combinations of the number of toroidal modules and number of active waveguides in each of these modules (for a fixed periodicity of 27 mm) which could be accommodated in the available width of 190 mm is shown in Table 3.1.

Table 3.1: Possible combinations of the number of toroidal modules and number of active waveguides in each of these modules.

Case	**No. of toroidal modules (x)**	**No. of active waveguides in each module (y)**	**Total width ($27 \times y \times x$) (in mm)**
A	2	2	108 (<190)
B	2	4	216 (>190) **discarded**
C	2	3	162 (<190)

From the above table, case (B) is automatically discarded, while case (C) is not chosen since it provides an additional space of only 28 mm for mechanical strength and diagnostics installations. Therefore, case (A), which has two modules in the toroidal direction with each module having two active and two passive waveguides, is the best available option and is finalised for our design.

Fig. 3.3 shows a schematic of the module configuration in the toroidal direction. There are two modules in the toroidal direction (marked in green and red rectangles) with each module consisting of two passive (shaded as grey) and two active (shaded as white) waveguides. The dimensions of these waveguides are illustrated in the figure. An additional passive waveguide is added to the left to make sure each of the active waveguides has two adjacent passive waveguides and to minimize edge electric effects [49]. There are two septa, each of 2 mm, at either end of the launcher mouth. Thus, the total launcher width is 123 mm (2 × 54 mm (two modules in the toroidal direction) + 11 mm (an additional passive waveguide on the left) + 2 × 2 mm (two septa on either side of the launcher mouth).

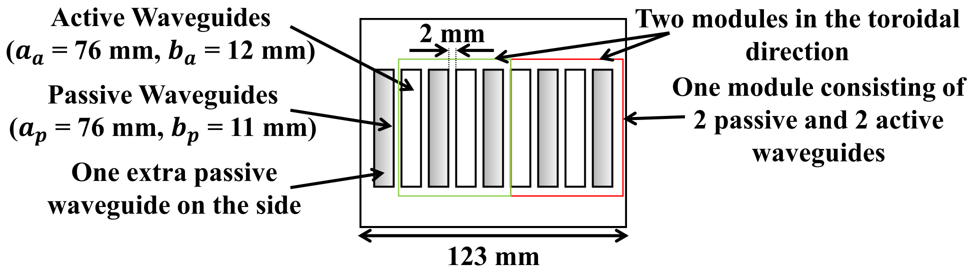

Figure 3.3: Schematic of the module configuration in the toroidal direction.

The second term of Eq. 3.1 evaluates the variation in the main peak $N_{\parallel}$ value. With a constant wave number (k), fixed periodicity (δ) and two active waveguides in a module (N_{wgd} = 2), the external phase shift ($\Delta\phi$) between the two adjacent modules of the PAM launcher primarily governs this variation. For an external phase shift of 180°, the second term is 0 and thus, the main peak $N_{\parallel}$ value is 2.25. For an external phasing of 90° and 270°, the main peak $N_{\parallel}$ values are 1.875 (2.25 - 0.375) and 2.625 (2.25 + 0.375), respectively. Thus, a variation ranging from -0.375 to +0.375 can be achieved by varying the external phase shift from 90° to 270°. It should be noted that the maximum variation which could be achieved in main peak $N_{\parallel}$ value is up to ±0.5 for the ADITYA –U operating densities, as discussed in Section 3.1. However, the launcher mouth dimensions limit this variation range up to ±0.375.

The total RF power injected into the plasma can be increased by increasing the number of PAM sections (depicted in Fig. 3.3) in the poloidal direction (vertical). Considering the height of the ADITYA –U port (490 mm), the thickness required between each of the poloidal sections for mechanical strength, the requirement of sufficient space for the movement of the launcher in and out of the tokamak and diagnostics, only three sections in the poloidal direction can be easily accommodated. The RF power is fed to these three sections with the help of TE_{10} to TE_{30} mode converters (discussed in subsection 3.6.1). The total height of the PAM launcher is 288 mm (3 × 76 mm (height of the waveguides in each section) + 2 × 15 mm (spacing between each poloidal section) + 2 × 15 mm (SS plates at the top and bottom of the launcher mouth to increase the mechanical strength)).

In summary, the proposed design of the PAM launcher consists of two modules in the toroidal direction and three sections in the poloidal direction. Each toroidal module consists of two active and two passive waveguides. Each of the three poloidal sections consists of four active waveguides and five passive waveguides. The complete schematic of the mouth of the PAM launcher illustrating the modular structure and all the relevant dimensions, as discussed in the above paragraphs, is shown in Fig. 3.4a and Fig. 3.4b, respectively. It can be observed that the mouth of the launcher has a cross-section of 288 mm × 123 mm. The remaining space of the port is utilised to install Langmuir probes and a reflectometry system to measure the temperature and edge density of the plasma.

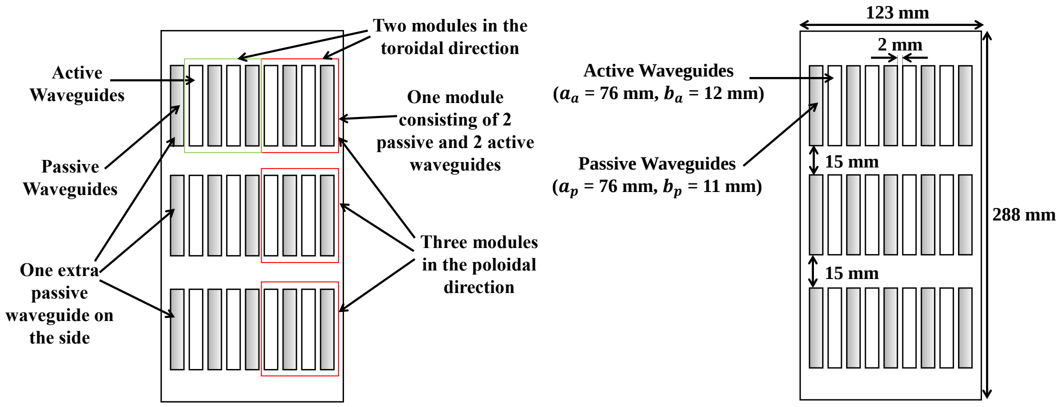

(a) Module structure. (b) Relevant dimensions.

Figure 3.4: Schematic of the mouth of the PAM launcher.

3.3 PAM design considering power constraints

The 8-waveguide grill launcher of the LHCD system was designed to launch 120 kW of RF power into the ADITYA tokamak [1, 68]. Each of these waveguides had a cross-sectional dimension of 76 mm × 7 mm. The ADITYA –U PAM launcher has 12 active waveguides, with each having a cross-sectional dimension of 76 mm × 12 mm. The width (narrower dimension) of the active waveguides of the proposed PAM launcher is greater than that of the grill launcher resulting in a higher RF breakdown threshold. Thus, with 12 active waveguides of the PAM launcher (as against 8 waveguides of the grill launcher), more RF power could be launched into the ADITYA –U tokamak. It is desired that the launcher is able to launch maximum RF power without the need for extensive conditioning (lower power flux at the mouth). To study this trade-off, a plot of the power flux versus f^2b is shown in Fig. 3.5. Here, the power flux is the ratio of the total RF power launched to the total cross-sectional area of the radiating waveguides and b is the narrow dimension of the radiating waveguide. The figure depicts three operating regions of the LH launcher, namely, Weak conditioning region, Extensive conditioning region and RF breakdown region. The operating point of the LH launchers, installed on various tokamaks around the world, are indicated in the Fig. 3.5 [101]. The data for the PAM launchers of Tore Supra [5], HL-2A [120, 121] and FTU [122] is included for easy comparison. The ADITYA –U PAM launcher is intended to launch 250 kW of RF power (more than twice of that launched by the earlier grill launcher) at 3.7 GHz. This corresponds to a power flux of ~2.3 kW/cm^2 and f^2b of ~16.4 GHz^{2}cm at the launcher mouth. With this data point incorporated in the figure, it can be observed that the proposed launcher can be easily operated without any requirement of extensive conditioning. Also, during high power operations, no RF breakdown is envisaged. Thus, the whole launcher is capable of launching a total RF power of 250 kW into the plasma through its 12 active waveguides.

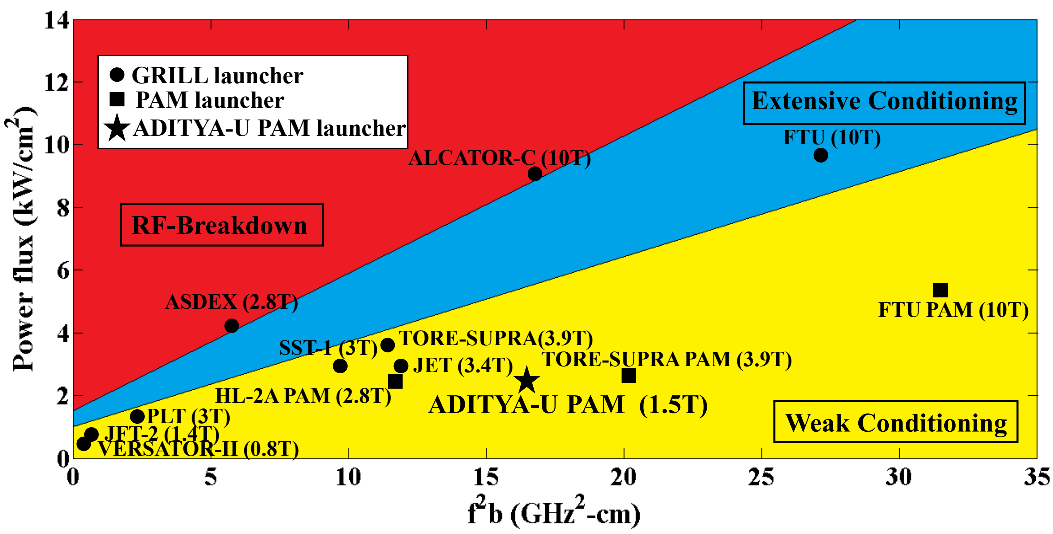

Figure 3.5: A plot of the power flux versus f^2b depicting the three operating regions of the LH launcher. The operating point of the LH launchers, installed on various tokamaks around the world, is indicated [101].

3.4 Coupling studies of the PAM launcher

The mouth of the PAM launcher is designed as discussed in the above sections. However, before finalising it, the behaviour of the launcher while facing the ADITYA –U tokamak plasma is to be studied. This section discusses the plasma coupling performance studies of the proposed PAM launcher and evaluates its efficiency by using the Advanced LOwer Hybrid Antenna (ALOHA) coupling code before proceeding to the RF design [107, 123]. The code is based on the linear coupling theory [124], where the plasma density varies linearly from the launcher mouth towards the plasma centre. It is assumed that there is no gap between the launcher mouth and the plasma edge. The plasma is modelled for three cases of edge densities (n_{e0}) at the launcher mouth; namely, (2, 5 and 20) $\times 10^{17}$ m^{-3}. The variation of the density from the mouth of the launcher to the last closed surface of the plasma, in simulations, is governed by the scrape-off length (λ_n, ratio of the edge density and the density gradient (∇n_{e0})). The different cases of the scrape-off lengths; namely, (1, 5, 10, 15 and 20) mm are considered in simulation studies. A typical plot illustrating the linear variation of the plasma density for one of the edge density and scrape-off length combination (here, 2×10^{17} m^{-3} and 1 mm) is shown in Fig. 3.6. The x-axis represents the distance from the launcher mouth (placed at the origin) towards the last closed surface.

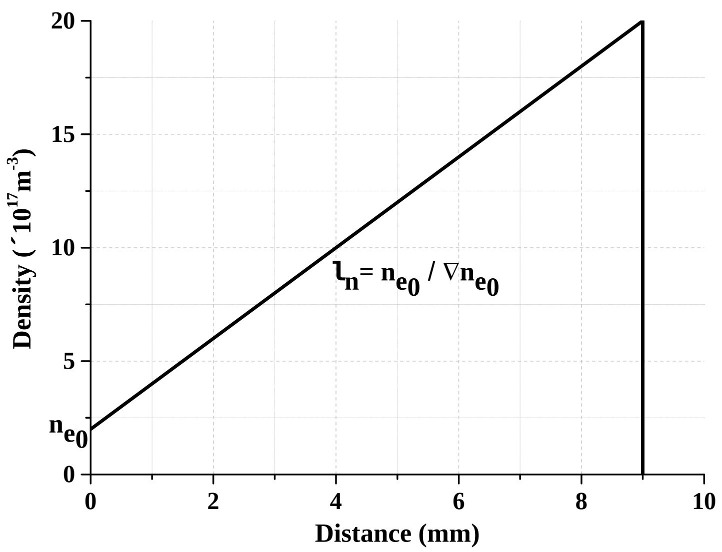

Figure 3.6: A typical plot illustrating the linear variation of the plasma density from the launcher mouth towards the last closed surface

3.4.1 Effect of electron density

The change in the electron density at the mouth of the PAM launcher primarily affects the cross-coupling coefficient between the adjacent waveguides [106]. It is desired that the amplitude of the cross-coupling is high as it would aid in the recirculation of power back to the plasma by the passive waveguides. The performance of the proposed launcher is studied by varying the electron density (in the range of (1-25) $\times 10^{17}$ m^{-3}) at the launcher mouth for different scrape-off lengths (1 mm, 5 mm, 10 mm, 15 mm and 20 mm). The amplitude of the cross-coupling coefficient, thereby obtained, is plotted as shown in Fig. 3.7. The amplitude drops sharply for densities below 2.5×10^{17} m^{-3} (marked with the dark yellow dash-dot line) as expected. This is because the performance of the launcher degrades below the cutoff density. The studies further reveal that the cross-coupling between the active and the passive waveguides is maximum when the density at launcher mouth (for λ_n = 5-20 mm) is around 2-3 times the cutoff density (marked with the orange dash-dot line). This is in good agreement with the experimental results reported in [5].

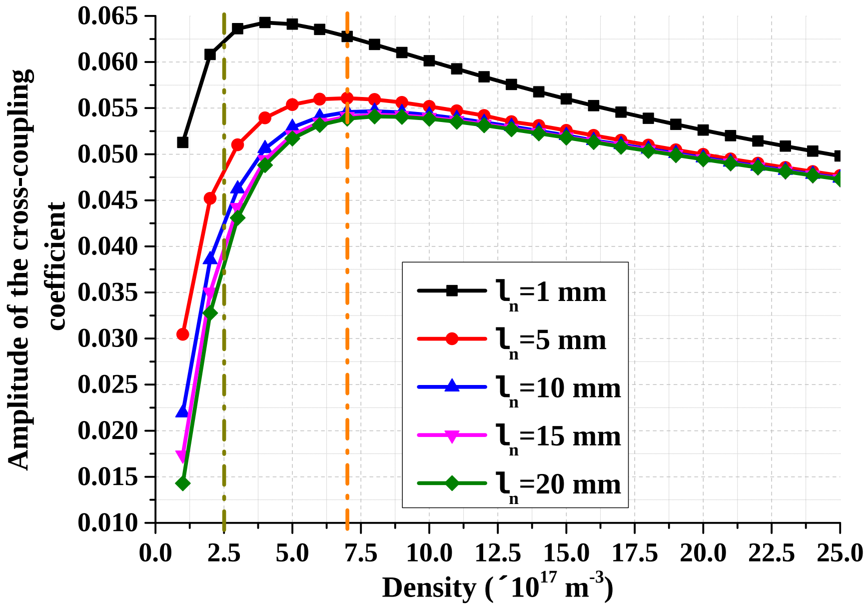

Figure 3.7: Amplitude of the cross-coupling co-efficient of the launcher versus the electron density at the launcher mouth. The dark yellow dash-dot line indicates the density (2.5×10^{17} m^{-3}) below which the amplitude drops sharply. The orange dash-dot line indicates the density corresponding to the maximum amplitude of the cross-coupling co-efficient.

The effect of the change in the electron density on the average reflection coefficient and directivity of the launcher is studied and subsequently plotted in Fig. 3.8a and Fig. 3.8b, respectively. The average reflection coefficient increases steeply and there is a sharp fall in the directivity of the launcher below the density value of 2.5×10^{17} m^{-3} (marked with the dark yellow dash-dot line) for reasons discussed above. It is observed that the reflection coefficient is minimum in the density range wherein the cross-coupling coefficient is maximum (2-3 times the cutoff density (marked with the orange dash-dot line)). This is because a higher cross-coupling coefficient results in more RF power being recirculated back to the plasma and less power returning back to the input of the launcher. The amplitude of the cross-coupling coefficient degrades gradually at higher densities, thereby, degrading the average reflection co-efficient and directivity at these densities.

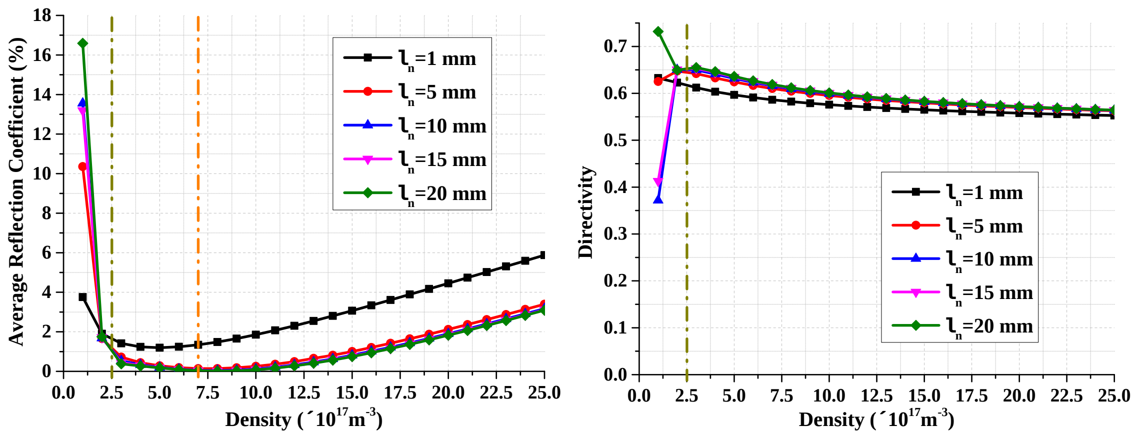

(a) (b)

Figure 3.8: (a) Average reflection co-efficient, (b) Directivity of the launcher versus the electron density at the mouth of the launcher. Dark yellow dash-dot line indicates the density (2.5×10^{17} m^{-3}) below which the performance of the launcher degrades. Orange dash-dot line indicates the density at which the average reflection coefficient is minimum.

Thus, to achieve the optimum performance of the PAM launcher, the density near the mouth of the launcher should be around 2-3 times the cutoff density. Further, the results clearly show the advantage of the PAM launcher (reflection < 5%) over the other conventional launchers (reflection > 20%) when the density at the mouth is near the cutoff density. This confirms one of the intrinsic properties of the PAM launcher that is to be able to couple more power into the plasma at lower densities [5, 106].

3.4.2 Effect of passive waveguide depth

The depth of the passive waveguide plays an important role in maintaining the coherence of the E-field at the launcher mouth. Ideally, the depth should be $\lambda_g/4$ [106] to recirculate maximum RF power (which was reflected from the plasma) back to the plasma. However, during experiments, the depth of the passive waveguide, required for optimum performance, would deviate from the ideal value. A study is carried out to optimise the depth for better RF coupling (lower reflection coefficient) and maximum directivity of the launcher. In this study, the depth of the passive waveguide is varied from $\lambda_g/8$ to $\lambda_g/2$ while the density at the mouth of the launcher and the scrape-off lengths are varied as discussed earlier. The performance of the launcher is studied for these variations.

Fig. 3.9a and Fig. 3.9b are typical plots of the reflection coefficient obtained for varying depths of the passive waveguide.

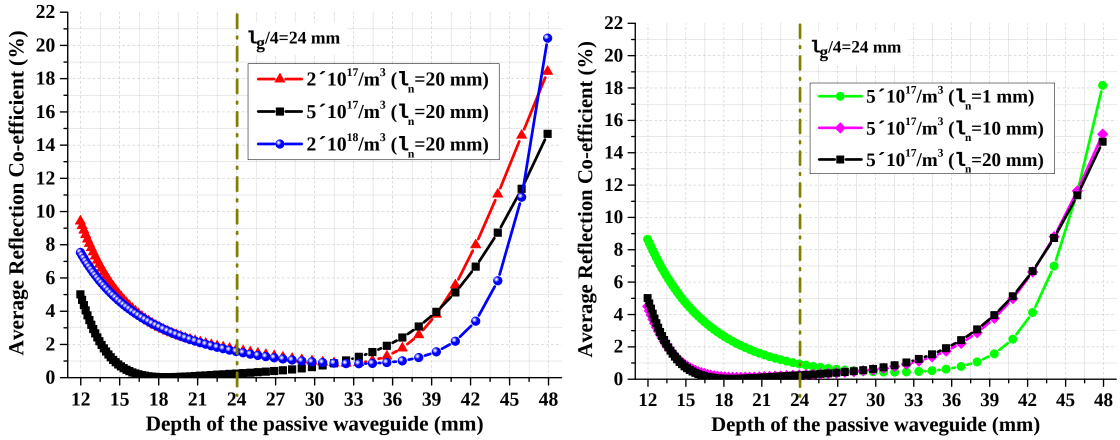

(a) (b)

Figure 3.9: Average reflection coefficient versus the depth of the passive waveguide for (a) different densities ($2 \times 10^{17}\,\mathrm{m}^{-3}$, $5 \times 10^{17}\,\mathrm{m}^{-3}$, $2 \times 10^{18}\,\mathrm{m}^{-3}$) and a scrape-off length 20 mm, (b) a density of $5 \times 10^{17}\,\mathrm{m}^{-3}$ but different scrape off lengths (1 mm, 10 mm, 20 mm). The dark yellow dash-dot line indicates the ideal value of 24 mm ($\lambda_g/4$).

Fig. 3.9a is a plot showing the trend of the reflection coefficient for three edge densities ($2 \times 10^{17}\,\mathrm{m}^{-3}$, $5 \times 10^{17}\,\mathrm{m}^{-3}$, $2 \times 10^{18}\,\mathrm{m}^{-3}$) and a constant scrape-off length of 20 mm. It can be observed that for a density of $5 \times 10^{17}\,\mathrm{m}^{-3}$ (around three times the cutoff density), the reflection coefficient is minimum for depths in the range of (15-27) mm. The ideal value of 24 mm ($\lambda_g/4$, marked with a dark yellow dash-dot line) lies within this range. On either side of this range, the reflection coefficient increases steeply as the coherence of the E-field at the mouth is not maintained. The reflection coefficient for this density is further investigated for different scrape-off lengths (1 mm, 10 mm and 20 mm) and is plotted in Fig. 3.9b. It can be observed that for scrape-off lengths of 10 mm and 20 mm (gradual variation of density), the reflection coefficient is minimum in the range of (15-27) mm (as concluded from Fig. 3.9a).

Further, the directivity of the launcher is investigated for varying depths of the passive waveguide, edge density and scrape-off length combinations as mentioned above. Fig. 3.10a is a typical plot showing the trend of the directivity for different edge densities and scrape-off length of 20 mm, while Fig. 3.10b shows the same for an edge density of 5×10^{17} m^{-3} and scrape-off lengths of 1 mm, 10 mm and 20 mm.

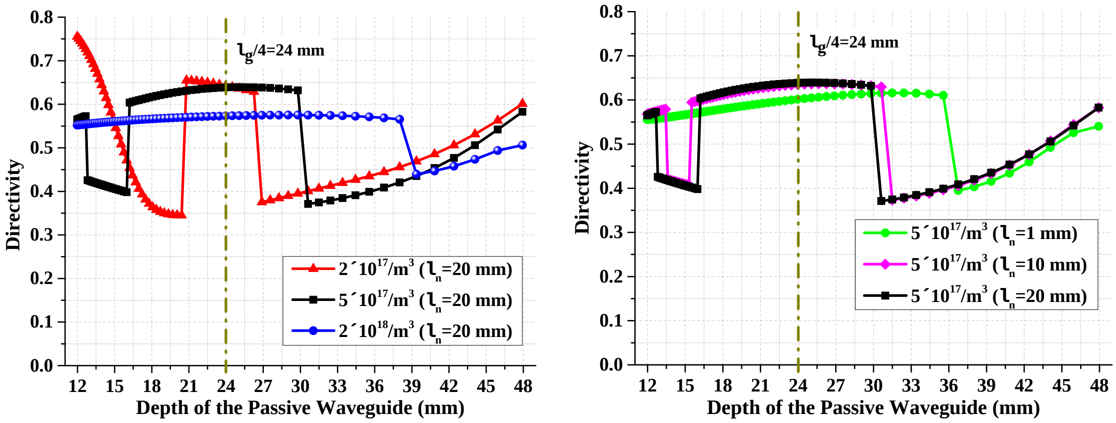

(a) (b)

Figure 3.10: Directivity versus the depth of the passive waveguide for (a) different densities (2×10^{17} m^{-3}, 5×10^{17} m^{-3}, 2×10^{18} m^{-3}) and a scrape-off length 20 mm, (b) a density of 5×10^{17} m^{-3} but different scrape off lengths (1 mm, 10 mm and 20 mm). Dark yellow dash-dot line indicates the ideal value of 24 mm ($\lambda_g/4$).

It can be observed from Fig. 3.10a that maximum directivity (∼66%) is obtained for edge densities of 2×10^{17} m^{-3} and 5×10^{17} m^{-3} for the depths of the passive waveguide in the range of (21-24) mm thereby narrowing down the optimum range obtained above. The directivity reduces on either side of this range. Further studying the edge density of 5 $\times$ 10^{17} m^{-3} for different scrape-off lengths concludes the same as shown in Fig. 3.10b.

Thus, the depth is decided to be the average of this range that is 22.5 mm, which is in good agreement with the theoretical value of 24 mm ($\lambda_g/4$).

3.4.3 Effect of external phase shift

The external phase shift between the two toroidal modules of the launcher primarily changes the main peak value of the $N_{||}$ spectrum as discussed in Section 3.2. The main peak $N_{||}$ value of 2.25 is obtained theoretically for an external phasing of 180° (see Eq. 3.1). In the event of a change in the external phase shift to obtain a particular main peak $N_{||}$ value, its effect on the performance of the launcher is required to be studied.

The external phase shift is varied from 90° to 270° in the ALOHA simulation studies for different densities ($2 \times 10^{17}\,\mathrm{m^{-3}}$, $5 \times 10^{17}\,\mathrm{m^{-3}}$, $2 \times 10^{18}\,\mathrm{m^{-3}}$) and scrape-off lengths (1 mm, 10 mm and 20 mm). Fig. 3.11a is a typical plot of the change in the average reflection coefficient. It can be observed that the maximum and minimum values of the reflection coefficient are 4.5% and 0.2%, respectively, across all the combinations of densities and scrape-off lengths. Thus, it can be concluded that the external phase shift has a marginal effect on it. The small change in the directivity of the launcher (maximum value of 65%, minimum value of 55%) with respect to the external phase shift for all the combinations of densities and scrape-off lengths is depicted in Fig. 3.11b. Thus, varying the external phase shift does not hamper the performance of the launcher significantly.

Further, the $N_{||}$ spectra for all the density, scrape-off length and external phase shift combinations are obtained from the above studies. A typical $N_{||}$ spectrum for density and scrape-off length of $5 \times 10^{17}\,\mathrm{m^{-3}}$ and 10 mm, respectively, is shown in Fig. 3.12. It is observed that the main peak $N_{||}$ value of 2.25 is obtained for an external phase shift of 170°. The figure is further populated with the $N_{||}$ spectrum obtained for external phase shifts of 150° and 190° to illustrate the shift in its main peak. The main peak shifts to the right of the spectrum (value of the main peak $N_{||}$ increases) with the increase in the external phase shift. This is further verified experimentally and is discussed in Chapter 5. The other peaks in the spectrum are 60% of the main peak.

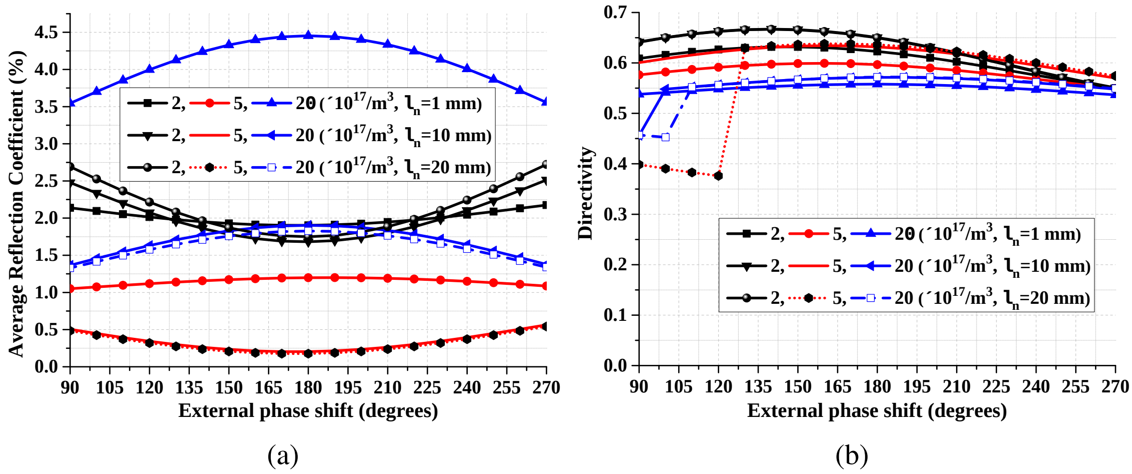

Figure 3.11: (a) Reflection coefficient, (b) Directivity versus External phase shift ranging from 90° to 270° for different densities (2×10^{17} m^{-3}, 5×10^{17} m^{-3}, 2×10^{18} m^{-3}) and scrape off lengths (1 mm, 10 mm and 20 mm).

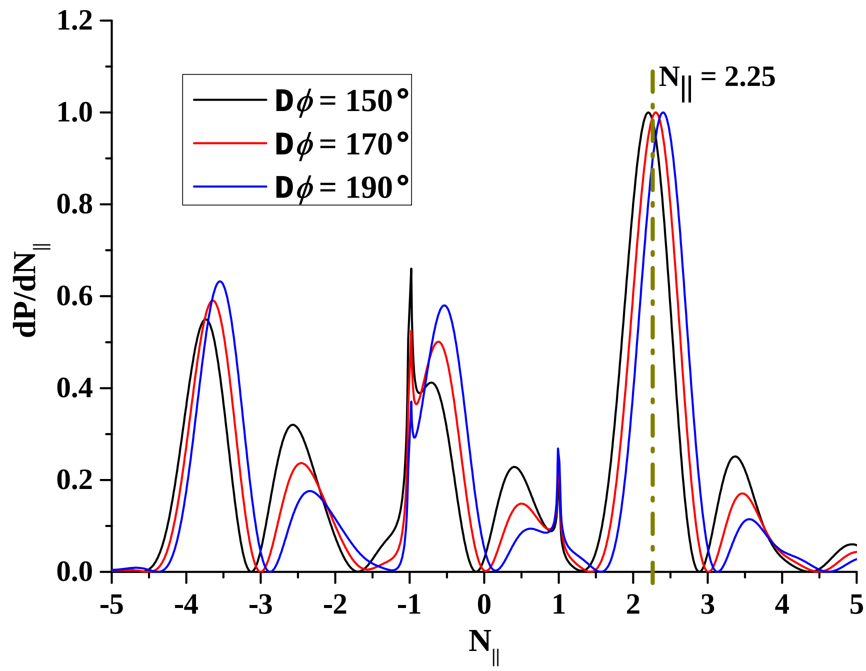

Figure 3.12: Typical $N_{\|}$ spectra for density and scrape-off length combination of 5×10^{17} m^{-3} and 10 mm and external phase shifts of 150°, 170° and 190° illustrating the right shift in the main peak of the $N_{\|}$ spectrum with the increase in the external phase shift.

3.5 Design of the PAM section

The mouth of the PAM launcher is designed after rigorous analysis based on the ALOHA simulations as discussed above. The passive active multijunction section is to be designed such that a fixed internal phase shift of 270° between adjacent active waveguides and multijunction effect could be incorporated. The top view of the proposed PAM section with two modules in the toroidal direction is depicted in Fig. 3.13. It is to be noted that the figure is only for the purpose of illustration and RF power is not fed directly by the klystrons but via the transmission lines and the transmission line components. Each module is fed by a separate klystron with an effective phase difference of 180° between them (for $N_{||} = 2.25$). This external phase shift (phase difference between the adjacent toroidal modules) is kept variable, thereby providing control over the main peak value of $N_{||}$ spectrum (from Eq. 3.1). The desired phase difference between the adjacent active waveguides is obtained by placing 90° fixed step phase shifters (represented by dotted lines) at appropriate positions, as discussed in section 3.2. The dotted lines in the active waveguides having 0° relative phase shift represent straight waveguides of length equal to that of the step phase shifters.

The RF power fed to each module is divided into 2 equal parts at the E-plane bijunction discontinuity and transmitted to the 90° step phase shifter and a straight waveguide. It is important to note that all the phase shifts indicated in Fig. 3.13 are relative. The 90° step phase shifters and straight waveguides are placed such that there is a relative phase shift of 270° in a particular waveguide with respect to the waveguide to its left. All the internal (position of the 90° step phase shifters and straight waveguides) and external (180° phase shift between the two modules) phase shifts result in one of the phase sequences of 180°, 270°, 0°, 90° (from right to left) at the launcher mouth as shown in the figure. There is a progressive phase shift of 90° from right to left. This results in the steering of RF power towards the right and thereby driving the plasma current in the opposite direction.

The passive waveguides (marked as "P") in Fig. 3.13 make the design robust and can be utilized for neutron shielding in future reactor grade plasmas. Cooling ducts can be drilled at the back of the thick walls of passive waveguides for efficient thermal management. The passive waveguides radiate back a consistent fraction of the total power which was reflected back to the launcher by the plasma.

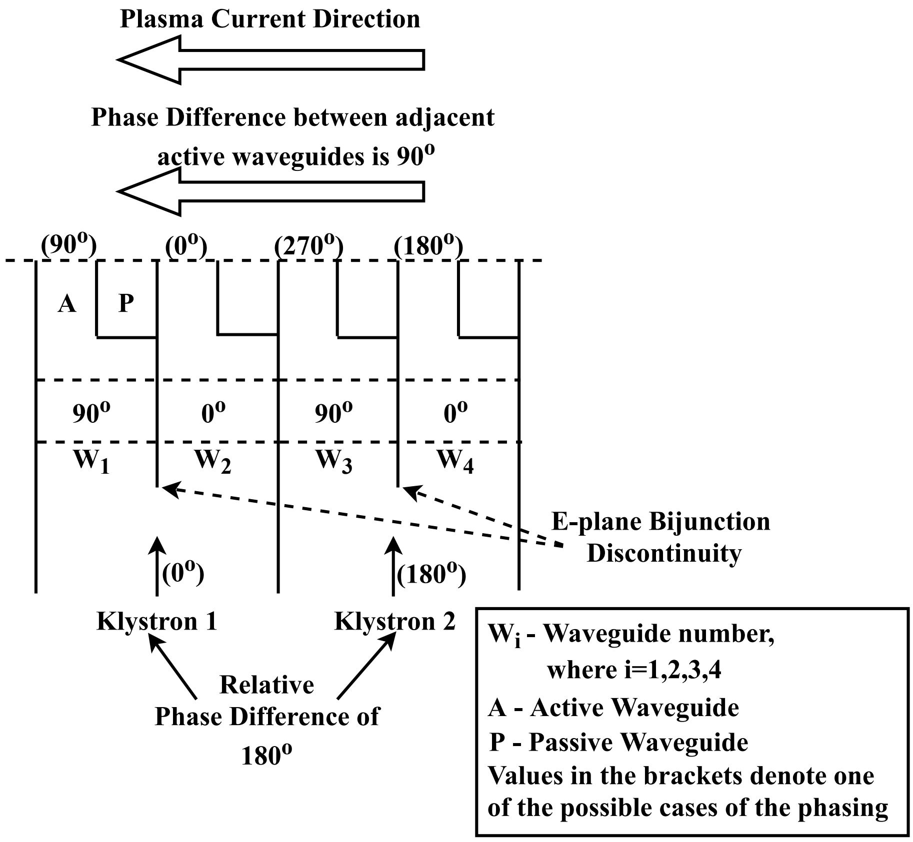

Figure 3.13: Top view of the proposed PAM section illustrating the two modules in the toroidal direction, one of the phase sequences at the launcher mouth, steering of RF waves to the right resulting into driving of the plasma current to the left.

Fig. 3.14 shows the top view profile of the PAM section. It illustrates the passage of the RF waves into the plasma (marked by the red arrow) and the role of passive waveguides in reflecting the RF waves (reflected from the plasma (marked by the black arrow)) back to the plasma (marked by the blue arrow).

The most prominent feature of the PAM launcher is its multijunction effect. This multijunction feature incorporated in the proposed launcher design, despite its small size, is explained in detail in Fig. 3.15 through four stages (A, B, C and D).

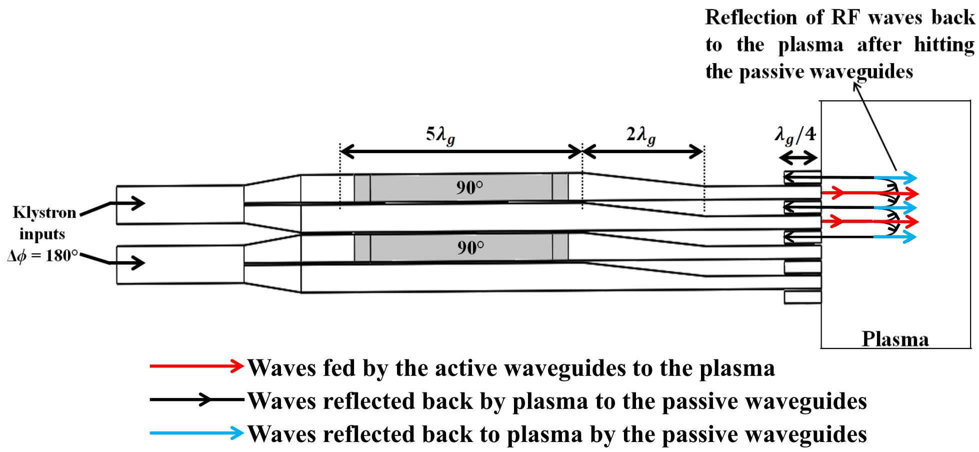

Figure 3.14: Top view profile of the PAM section illustrating the role of the passive waveguides in recirculation of the RF power.

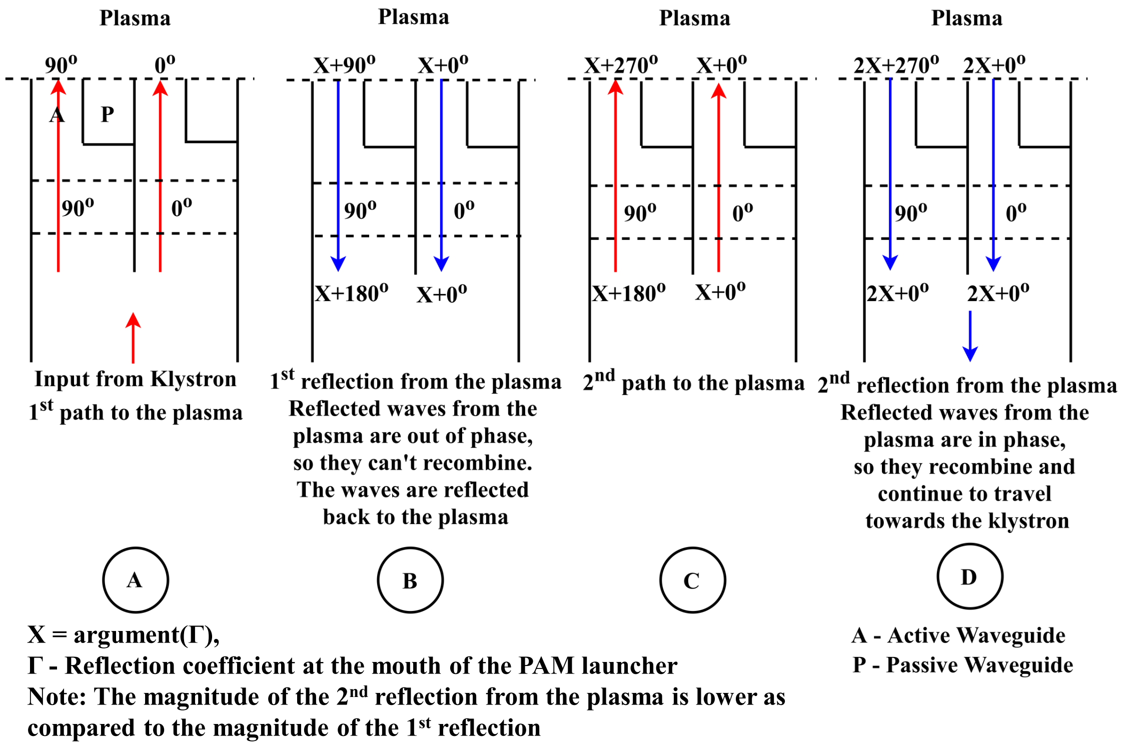

Figure 3.15: A schematic illustrating the Multijunction effect incorporated in the PAM launcher design.

Initially, the input from the klystron is transmitted through active waveguides and fed to plasma as shown in stage A. The active waveguides incorporate the step phase shifter and straight waveguide section leading to a relative phase shift of 90°, with respect to the right (or 270° with respect to the left), between the two adjacent active waveguides of a single module. In the event of reflection from the plasma (stage B, first reflection from plasma), with a reflection phase of X° (assume), the waves travel back through the active waveguides and are again subjected to step phase shifter and straight waveguide section. The two waves reaching the bijunction are 180° out of phase ((X+180)° and (X+0)°) and are, thus, reflected back to the plasma. The first reflection from the plasma is reflected back and does not reach the input of the launcher. These waves travel through the two active waveguides again and the resulting wave phases at the launcher mouth are (X+270)° and (X+0)° (stage C). In case they are further reflected from the plasma (second reflection from plasma), the waves travel back and reach the bijunction in phase ((2X+0)° and (2X+0)°) (step (D)). These waves combine at the bijunction and further travel towards the klystron. However, the magnitude of these secondary reflected waves are very small and would not hamper the performance of the launcher significantly. This is because, the magnitude of the reflected waves reduces on successive reflections since the plasma is well matched to the launcher mouth.

As discussed earlier, 90° step phase shifters are to be employed to obtain the desired phase sequence at the mouth of the launcher. These phase shifters are implemented using the quarter wavelength transformer technique such that the phase difference between the transformer incorporated active waveguide and straight active waveguide of same length is 90°. The 2D schematic with all the critical dimensions and the 3D structure of the step phase shifter is shown in Fig. 3.16.

The procedure to design a step phase shifter is explained in detail in [125]. The step phase shifter is symmetrical and has a total length of $4\lambda_{g1}$(here, λ_{g1} is the guided wavelength in a waveguide having broader dimension a_1). A MATLAB routine, based on the equations given in [125], is employed to obtain the analytical values of all the dimensions of the step phase shifter illustrated in Fig. 3.16a. These values are further optimised in COMSOL Multiphysics for higher return loss and 90° phase shift. The optimised dimensions of the step phase shifter are $(a_1, a_2, a_3, l_1, l_2, l_3)$ = (72.14, 68.3, 62.8, 24.5, 25.5, 297) mm.

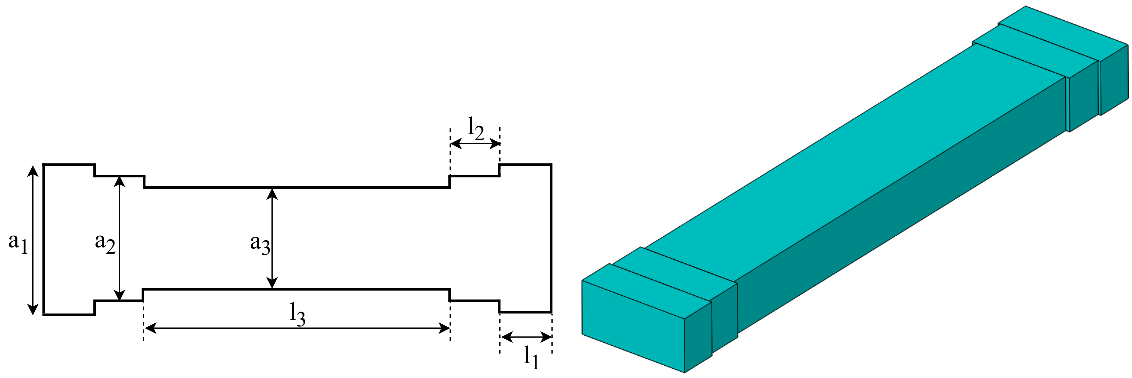

(a) (b)

Figure 3.16: (a) 2D schematic, (b) 3D structure of the step phase shifter.

The step phase shifter and a straight waveguide of the same length ($4\lambda_{g1}$) are thus designed and analysed for their RF performance in COMSOL. Fig. 3.17 illustrates the electric field profile of the phase shifter section. It can be observed that the inputs of the straight waveguide (A) and the 90° step phase shifter (B) are in the same phase, while the phase difference between the output of the phase shifter (D) and that of the straight waveguide (C) is 90°.

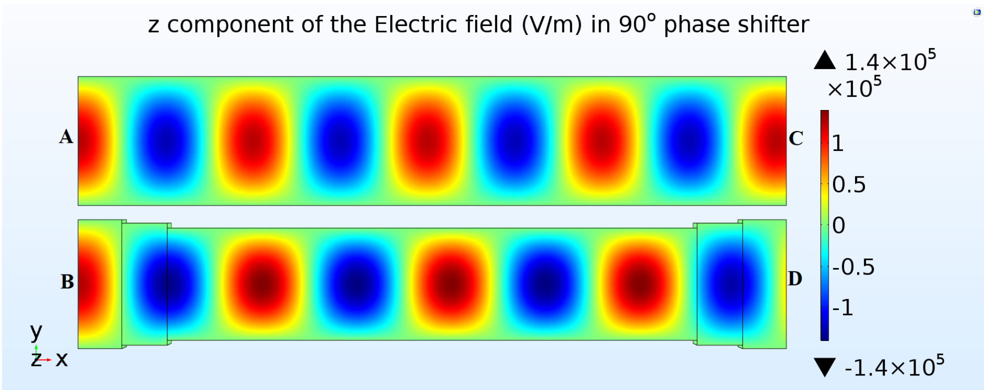

Figure 3.17: Electric field (V/m) profile of the phase shifter section comprising of the step phase shifter and a straight waveguide of the same length.

Fig. 3.18 shows the frequency response of the step phase shifter. It depicts that the difference between the output phase of the waves (having the same input phase) travelling in the step phase shifter and the straight waveguide of the same length remains almost constant over the desired bandwidth (Klystron bandwidth of ±5 MHz centred around 3.7 GHz). Further, a return loss of more than 50 dB is obtained in simulation.

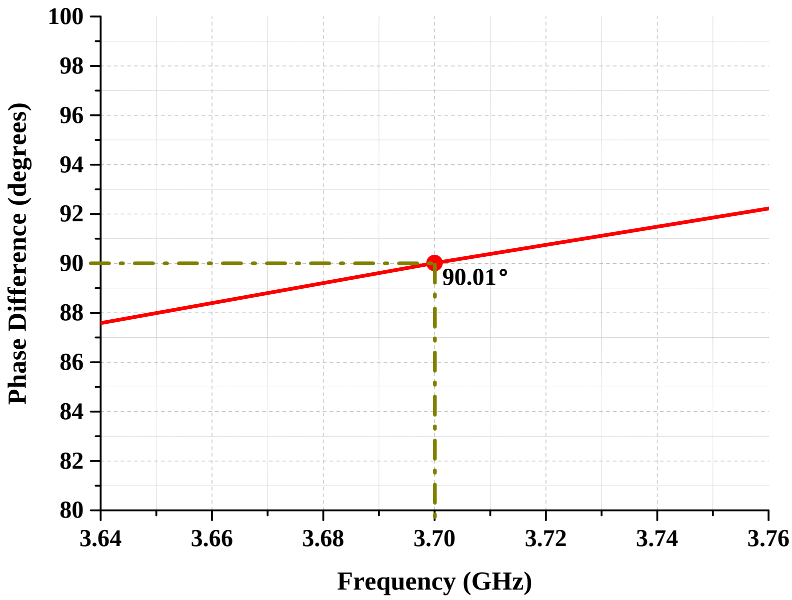

Figure 3.18: Frequency response of the step phase shifter.

3.6 Design of the transmission line network

The PAM launcher has two toroidal modules and three poloidal sections as discussed in the previous sections. Thus, an appropriate transmission line network needs to be designed such that equal RF power could be transmitted to each of the active waveguides of these modules/sections.

RF power from two klystrons would be fed to the two inputs of the PAM launcher (via waveguide based transmission line system). The relative phase shift between these two inputs is variable. A mode converter is first employed to convert the input power, which is in the dominant TE_{10} mode, to TE_{30} mode in order to feed the three poloidal sections. A tapered divider is used to transform the output impedance of the mode converter to the input impedance of the PAM section gradually. Also, it helps in dividing the power equally between the two toroidal modules.

The design of the various transmission line components is described in detail in the following sections.

3.6.1 Mode Converter

A TE_{10} to TE_{30} mode converter, required to feed the three poloidal sections of the PAM launcher, is designed using the perturbation method [126]. In this method, the broader dimension of the waveguide is perturbed to excite the desired mode and suppress the undesired modes. In theory, if an appropriately perturbed rectangular waveguide is excited with an odd mode (TE_{i0}, where i = 1, 3, 5 and so on), then the whole input power is coupled only to odd modes. The output of the perturbed waveguide comprises of only the input odd mode and all the other successfully propagated odd modes. All the even modes, if excited, are subjected to high insertion loss and do not propagate through the structure. A similar argument can be given for perturbed waveguides excited with even modes. The TE_{10} to TE_{30} mode converter, for the PAM launcher, is designed such that all the input power (in the dominant TE_{10} mode) is coupled only to the desired TE_{30} mode. The complete design procedure of the mode converter is discussed below.

Fig. 3.19 depicts the top view schematic of the mode converter. The broader dimension (width) of the mode converter is perturbed cosinusoidally along its length (z-direction) to achieve the desired TE_{10} to TE_{30} mode conversion [126].

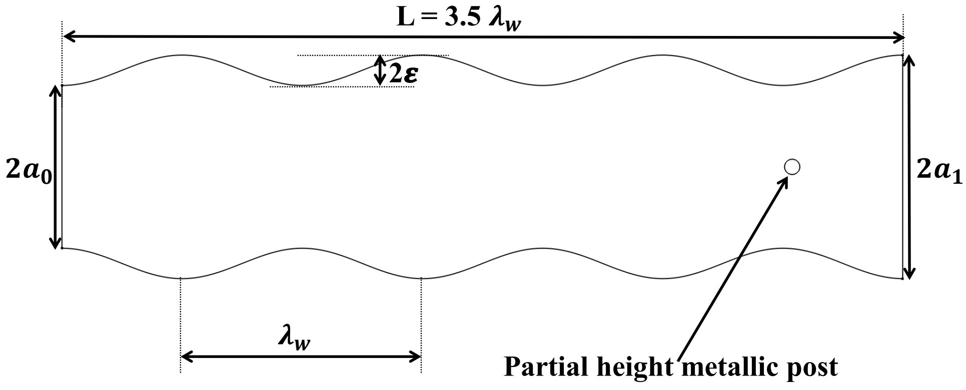

Figure 3.19: Top view schematic of the mode converter.

The expression for the cosinusoidal perturbation profile along the length is given by,

$$a(z) = a_0 + \varepsilon\left(1 - \cos\left(\frac{2\pi z}{\lambda_w}\right)\right) \tag{3.2}$$

where,

$a(z)$ is the change in the width of the mode converter.

a_0 is half the width of the input of the mode converter.

ε is the amplitude of the perturbation.

λ_w is the uniform geometrical wavelength of the perturbation.

The total length (L) of the mode converter depends on λ_w and is given by,

$$L = N\lambda_w \tag{3.3}$$

where,

N is the number of times the perturbation is repeated (here $N = 3.5$).

The broader dimension of the input of the mode converter is oversized ($2a_0 \geq 121.7$ mm) so as to support the propagation of TE_{30} mode. The mode converter is excited by the odd TE_{10} mode. Thus, the possibility of the generation of even modes (TE_{20}, TE_{40} et cetera) is negligible owing to the symmetrical nature of the structure [127]. The broader dimension of the output of the mode converter ($2a_1 = 2(a_0 + 2\varepsilon)$) is less than 202.7 mm to ensure that the TE_{50} mode is cutoff. Thus, at 3.7 GHz, only TE_{10} and TE_{30} modes exist in the mode converter.

Further, the values of a_0, ε and λ_w are optimised numerically by solving a set of differential equations. These differential equations describe the evolution of the amplitudes (A) of the forward and backward waves with respect to the axial location z in a ripple wall waveguides and can be written as Eq. 3.4 and Eq. 3.5 [118],

$$\frac{dA_n^{\pm}}{dz} = \mp j\beta_n A_n^{\pm} - \frac{1}{2}\frac{d(\ln Z_n)}{dz}A_n^{\mp} + \kappa_{nm}^{\pm}A_m^{+} + \kappa_{nm}^{\mp}A_m^{-} \tag{3.4}$$

$$\frac{dA_m^{\pm}}{dz} = \mp j\beta_m A_m^{\pm} - \frac{1}{2}\frac{d(\ln Z_m)}{dz}A_m^{\mp} + \kappa_{mn}^{\pm}A_n^{+} + \kappa_{mn}^{\mp}A_n^{-} \tag{3.5}$$

Here, subscripts m and n refer to TE_{m0} and TE_{n0} modes, respectively. These equations are based on the coupled wave theory for two modes (TE_{n0} and TE_{m0}) in the above mentioned ripple wall waveguides. The boundary conditions applied to these differential equations are,

$$A^{+}|_0 = (1,0)\,,\; A^{-}|_L = (0,0) \tag{3.6}$$

The wave impedance (Z_n) of the input mode TE_{n0} is given by,

$$Z_n = \frac{\omega\mu}{\beta_n},\; \beta_n = \sqrt{k^2 - \left(\frac{x_n}{a}\right)^2} \tag{3.7}$$

It is important to note that β_n is dependent on frequency as well as z while x_n/a is the cutoff wavenumber. The coupling coefficients ($k^{\pm}_{nm}$) required for the smooth change in the width of the mode converter are derived by Unger [128] and can be written as,

$$k^{\pm}_{nm} = \frac{x_n x_m}{x_m^2 - x_n^2} \frac{d\,(\ln a)}{dz} \frac{(\beta_n \pm \beta_m)}{\sqrt{\beta_n \beta_m}} \tag{3.8}$$

The superscripts + and – in the above equation correspond to the two modes having phase velocities in the same and opposite directions, respectively. Also, these coefficients satisfy the following conditions,

$$k^{-}_{nm} = k^{-}_{mn},\; k^{+}_{mn} = -k^{+}_{nm} \tag{3.9}$$

The mode converter design analysis is based on the Equations (3.4) to (3.9). The input broader dimension of the mode converter is decided using Eq. 3.2. This enables the estimation of the allowable range of ε such that only two desired modes exist in the mode converter. Further, Equations (3.4) to (3.6) are solved numerically, using a MATLAB code, to obtain the values of L (655 mm) and ε (23.6 mm) for which maximum mode conversion is achieved.

The code also provides information regarding the power distribution along the length of the mode converter which is illustrated in Fig. 3.20. It can be observed that the input of the mode converter (x = 0) is excited by a pure TE_{10} mode (blue curve). As the wave travels along the length, the power in TE_{10} mode is transferred to that in TE_{30} mode (red curve). A 99.52% conversion to TE_{30} mode is achieved at a length (L) of 655 mm ($3.5\lambda_w$).

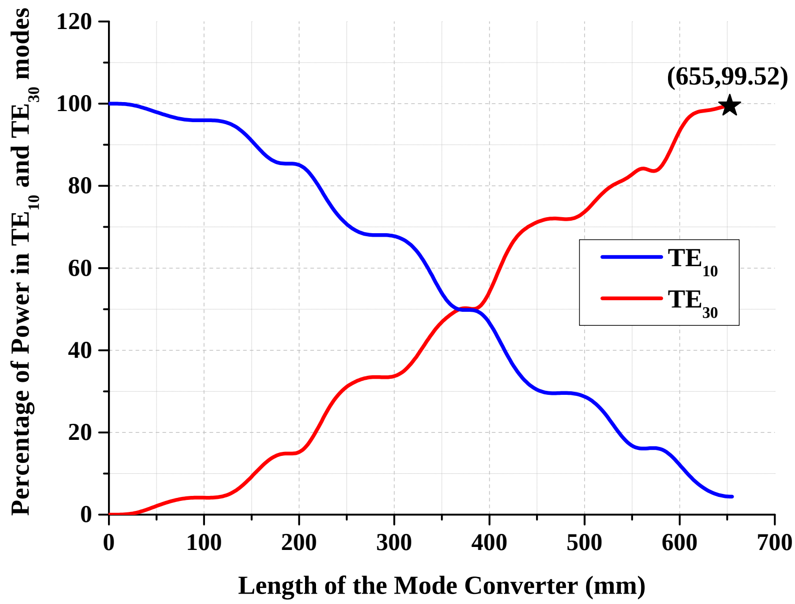

Figure 3.20: Power distribution along the length of the mode converter illustrating 99.52% mode conversion efficiency.

A small amount of power, in both the modes, is reflected along the length of the mode converter, as shown in Fig. 3.21. A comparatively higher amount of power (~5.6%) is reflected in TE_{30} mode at the output. This is due to the simplification of the boundary conditions given in Eq. 3.6.

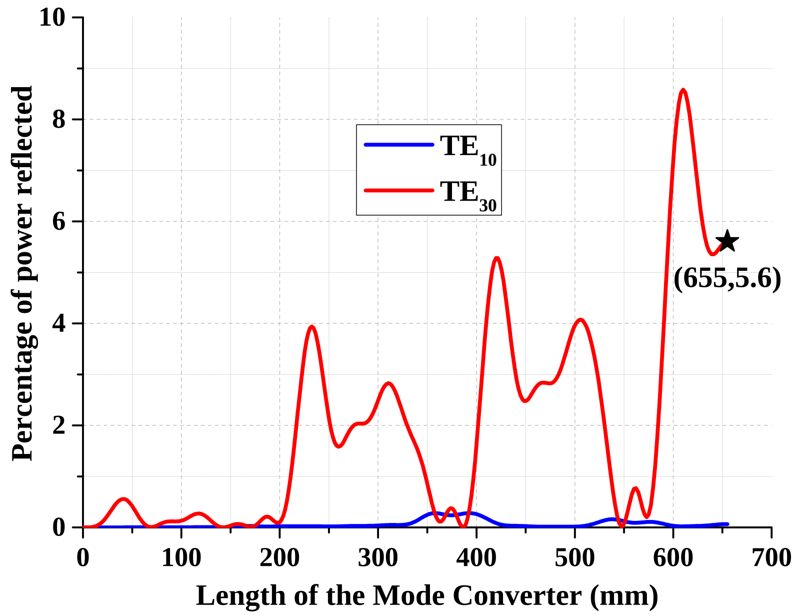

Figure 3.21: Reflected power distribution along the length of the mode converter.

The MATLAB code used in the above analyses provides the preliminary design of the mode converter, which is further verified and tuned in COMSOL multiphysics.

A metallic post is incorporated in the mode converter to match its input impedance while still keeping the mode conversion efficiency close to 100%. The diameter, height and the axial position of the post are optimised in COMSOL Multiphysics to obtain a higher return loss. Fig. 3.22 shows the frequency response of the mode converter. It can be observed that the simulated return loss, in the desired bandwidth of ±5 MHz (bandwidth of the input klystron), is better than 32.5 dB and is ~35.6 dB at the centre frequency of 3.7 GHz.

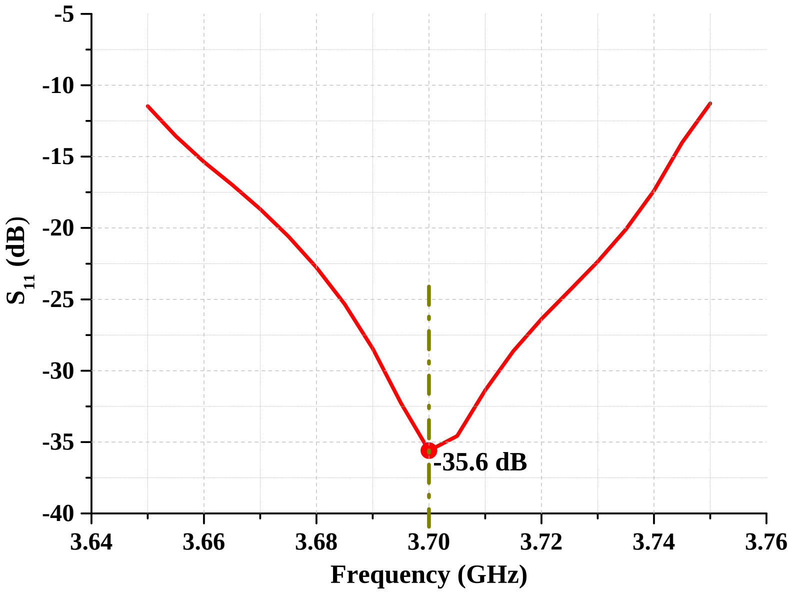

Figure 3.22: Frequency response of the mode converter.

Further, the mode conversion efficiency is evaluated in COMSOL and is depicted in Fig. 3.23. The efficiency has dropped to 98.5% (at 3.7 GHz) as compared to that obtained using MATLAB codes (99.52%) due to the addition of the metallic post. The total surface loss due to the usage of Stainless Steel (SS304L) material is 0.5% of the total input power.

The optimised dimensions of the mode converter and the metallic post as obtained from the MATLAB and COMSOL Multiphysics simulations are summarised in Table 3.2.

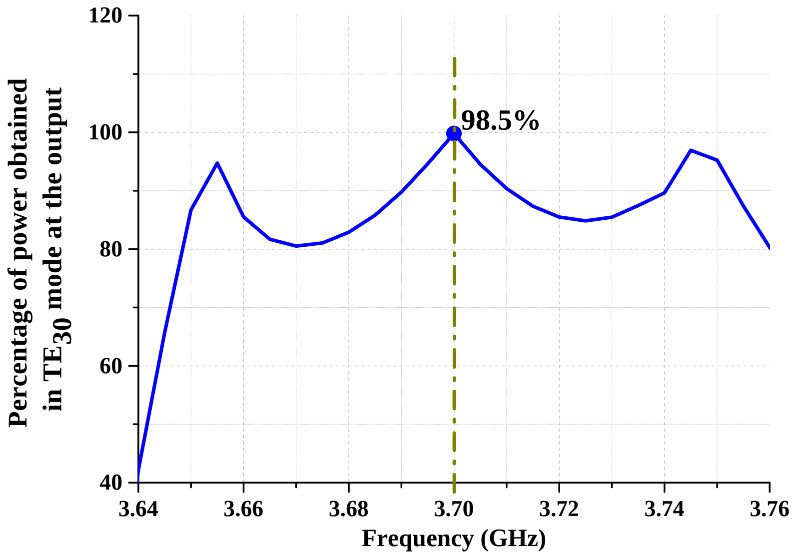

Figure 3.23: Mode conversion efficiency as evaluated in COMSOL Multiphysics.

Table 3.2: Optimised dimensions of the mode converter and the metallic post.

Dimension	Value
Length of the mode converter	655 mm
Input dimension	126.4 mm × 34.04 mm
Output dimension	173.6 mm × 34.04 mm
Perturbation amplitude	23.6 mm
Diameter of the post	12 mm
Height of the post	6.65 mm
Axial position of the post	578.1 mm

A linear taper is designed and incorporated at the input of the mode converter to transform the standard rectangular WR284 cross-section of the input of the launcher to the optimised and oversized input dimensions of the mode converter. It is designed such that the generation and transmission of modes other than TE_{10} mode are suppressed.

The mode converter along with the linear taper, is simulated in COMSOL for an input RF power of 125 kW (half of the total input power of the PAM launcher) to obtain the E-field profile. A peak electric field of 565 kV/m is observed near the post, as shown in Fig. 3.24, which is much below the breakdown electric field. It can be observed that if the output of the mode converter (TE_{30} mode) is divided into three equal parts to obtain three TE_{10} modes, the middle section would be 180° out of phase. This does not affect the performance of the launcher which can be further seen in Chapter 5.

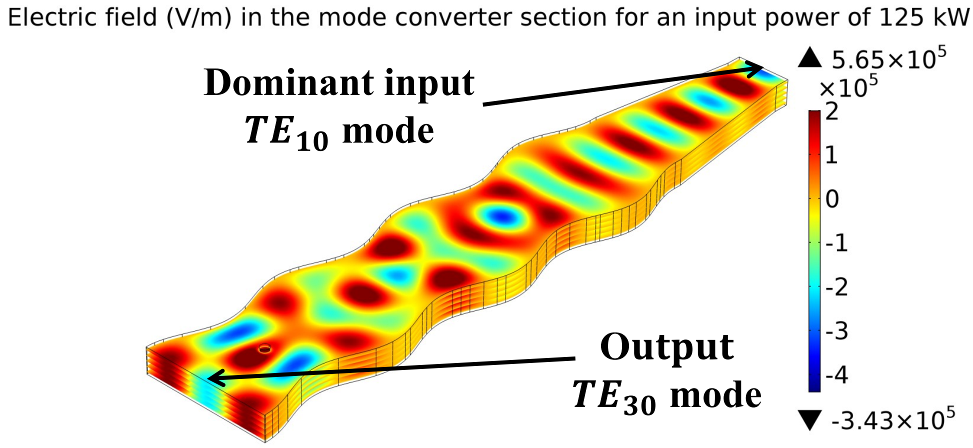

Figure 3.24: E-field (V/m) profile in the mode converter section illustrating a peak electric field of 565 kV/m near the matching post.

3.6.2 Mode converter design with stepped transformer

A metallic post is generally used in conventional mode converters to match the converter's input impedance and thereby obtain a higher return loss. It reduces the height of the structure locally, resulting in the concentration of E-field near it and thereby lowering the RF breakdown threshold of the overall structure. The mode converter with a post (discussed in Section 3.6.1) is adopted for the ADITYA –U PAM launcher since the design value of its RF power is lower (125 kW for each mode converter). However, for future PAM launchers (for SST-1 tokamak), the mode converter maybe required to handle RF power up to 500 kW/CW. The peak electric field obtained for the conventional mode converter at 500 kW is 4.2×10^6 V/m and is at the location of the post as shown in Fig. 3.25. This increases the possibility of RF breakdown during high power operations. Hence, the mode converter would act as a bottleneck as it would reduce the RF breakdown threshold of the complete structure.

In this work, a novel mode converter is proposed which employs a step transformer (as discussed in Section 3.5) instead of a matching post as shown in Fig. 3.26. The changing

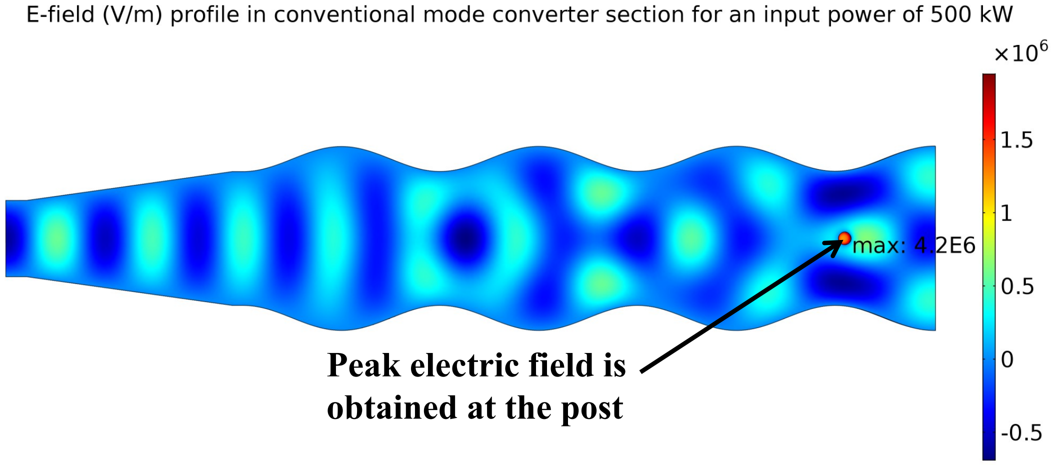

Figure 3.25: E-field (V/m) profile in the conventional mode converter section for an input RF power of 500 kW.

width of the step transformer adds a reactance and thereby matches the impedance of the mode converter. The step transformer only changes the broader dimension of the structure while the height is intact. Thus, the E-field is not concentrated locally and the structure could withstand higher power RF signals.

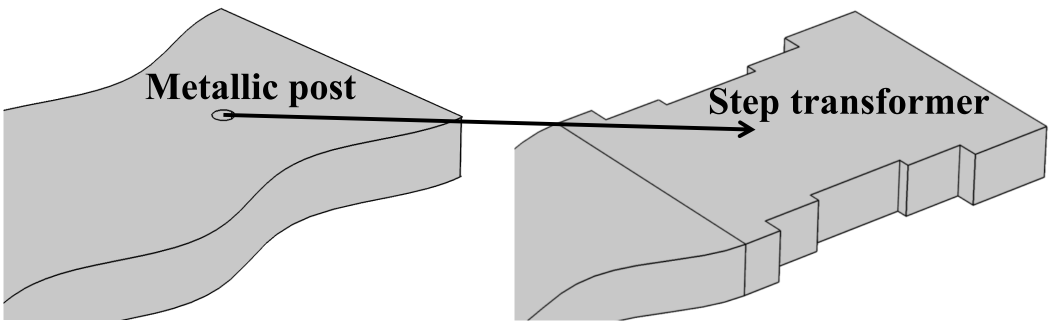

Figure 3.26: Novel mode converter structure employing a step transformer instead of a metallic post.

The step transformer replaces the last λ_w section of the conventional mode converter. Thus, the lengths of the new mode converter and the conventional mode converter are equal. The design of the step transformer is similar to that discussed in Section 3.5. The preliminary values of (a_1, a_2, a_3) and (l_1, l_2, l_3) are obtained from a MATLAB routine, which is used to perform the analytical calculations discussed in [125]. These values are further optimised in COMSOL Multiphysics to obtain maximum mode conversion efficiency and a higher return loss. A mode conversion efficiency and return loss of 98.5%

and 43 dB, respectively, are obtained, thereby confirming that the introduction of the step transformer does not hamper the mode converter's RF performance. The values of the important dimensions of the step transformer are (a_1, a_2, a_3) = (173.6 mm, 146.4 mm, 131.6 mm) and (l_1, l_2, l_3) = (25.5 mm, 39.4 mm, 67 mm). Fig. 3.27 shows the E-field profile of the novel mode converter structure, as obtained from COMSOL Multiphysics, for an input power of 500 kW. It can be observed that the peak E-field obtained is 7×10^5 V/m. This value is almost one order lower than that obtained in the conventional mode converter (see Fig. 3.25). Thus, the novel structure has a higher RF breakdown threshold as compared to the conventional mode converter.

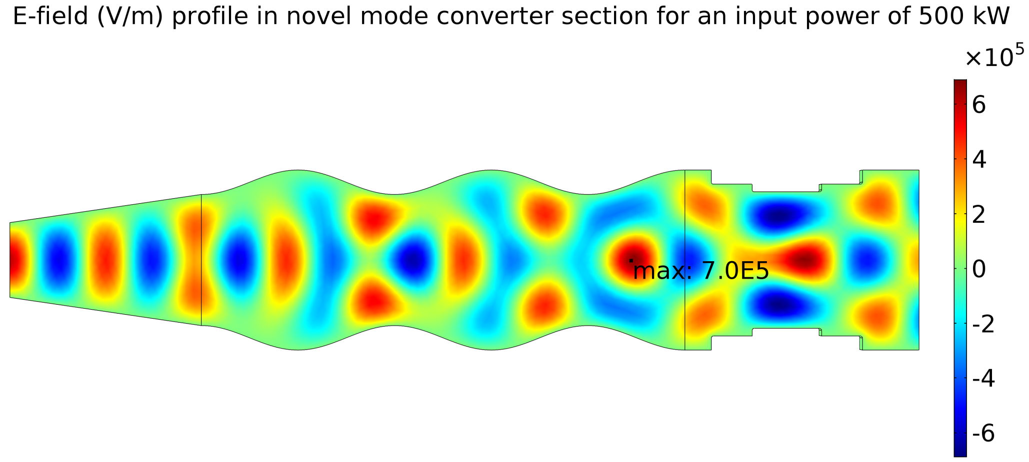

Figure 3.27: E-field (V/m) profile in the novel mode converter structure for an input RF power of 500 kW.

This novel design of the mode converter with enhanced RF breakdown characteristics is not reported in the literature. It can be adopted for the future PAM launcher of the SST-1 tokamak.

3.6.3 Tapered Divider

A tapered divider, illustrated in Fig. 3.28, is designed by virtue of optimisation for its RF performance. The divider introduces an E-plane discontinuity into each of the three outputs of the mode converter, thereby generating three E-plane bijunctions. Thus, the tapered divider is a 3 × 2 matrix of six waveguides, each tapering in both the lateral dimensions along their length. It translates the three outputs of the mode converter into six inputs (two in each poloidal module) of the PAM section. These six inputs further form six active waveguides. Each of them carries about $(1/6)^{th}$ (-7.78 dB) of the output power of one klystron. The simulated return loss is ~45 dB at the centre frequency and better than 42 dB in the desired bandwidth. A peak E-field value of 1.5 kV/m is observed in the tapered divider.

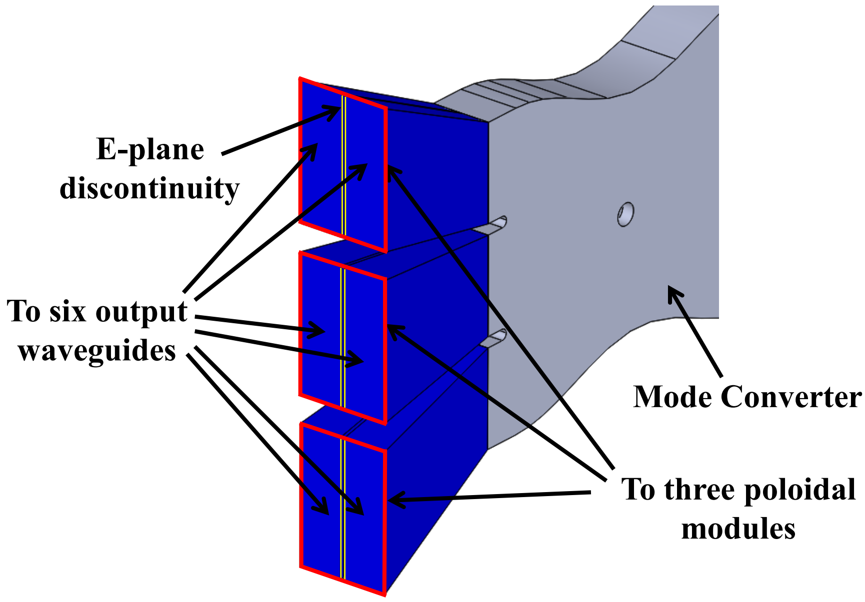

Figure 3.28: Inner profile of the Tapered divider.

3.7 RF analysis of the PAM launcher and the transmission line components

Fig. 3.29 depicts the complete 3D structure of the proposed PAM launcher along with its transmission line components [8]. It is to be noted that the figure depicts only the inner profile of the structure and thus, the 15 mm thickness on the top and bottom and the 2 mm thickness on the sides of the structure is not shown. Thus, the cross-section of the launcher mouth is 258 mm × 119 mm, as shown in the figure.

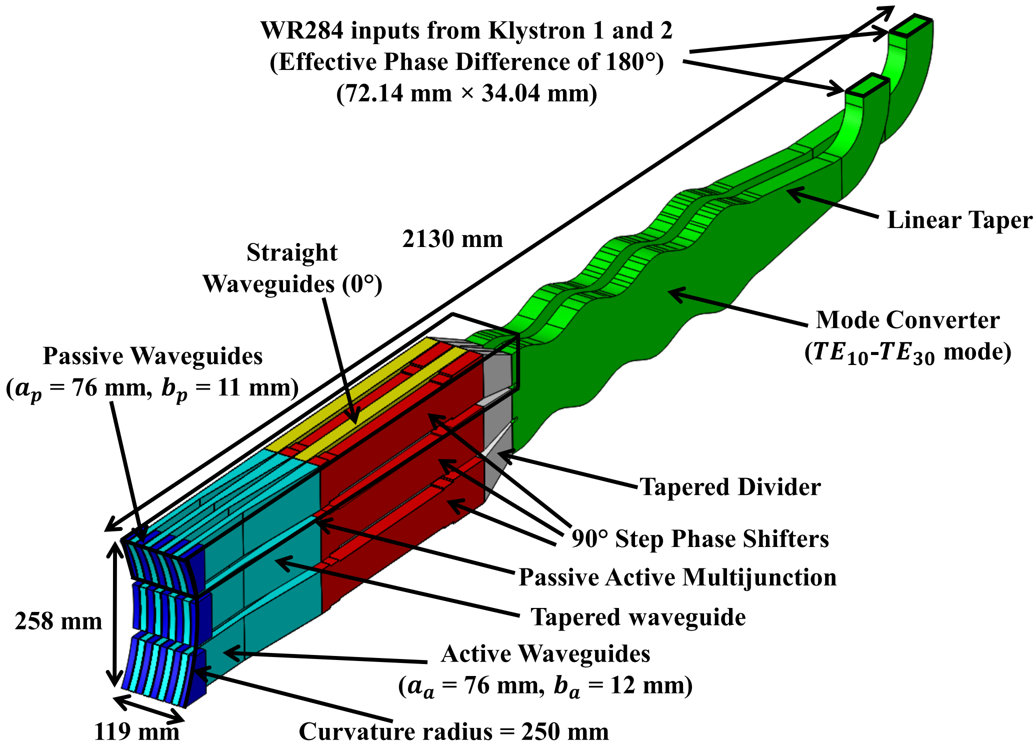

Figure 3.29: Complete 3D structure of the proposed PAM launcher along with its transmission line components.

Two independent klystrons feed the two inputs of the launcher via WR284 waveguides. Pill box type RF windows (not shown in the figure) are required in each of the input lines to mechanically isolate the UHV in the structure and the pressurised transmission lines (up to 3 bars relative) feeding it. The bend at the input of one of the modules is offset by a distance of $2\lambda_g$ with respect to the other module to avoid any physical interference during the launcher integration, installation and operation. The input dominant TE_{10} mode is converted to TE_{30} mode and further fed to the three poloidal sections using a combination of linear taper, mode converter and tapered divider. 90° step phase shifters are used to provide appropriate phase shifts between the adjacent active waveguides and thereby steer the wave in the desired direction. The step phase shifters/straight waveguides are followed by tapered (length $\sim 2\lambda_g$) and active (length $\sim 1.5\lambda_g$) waveguides. A tapered waveguide transforms the output narrower dimension (25 mm) of the step phase shifter/straight waveguide to the input narrower dimension (12 mm) of the active waveguide. The RF wave is launched into the plasma through the active waveguides. The surface of the launcher mouth is contoured to the plasma surface (poloidal radius of 250 mm) in order to geometrically match the two surfaces and provide identical plasma impedance to all the waveguides. In the toroidal direction, the surface is almost linear since the width of the launcher is very small (119 mm) as compared to the radius of 1 m (major radius of 750 mm + minor radius of 250 mm).

The PAM launcher is constructed using stainless steel (SS304L) material. This is because the higher electrical resistivity of steel as compared to that of copper induces a lower current in the SS based launcher (as compared to the copper based launcher) in the event of plasma disruption (discussed in Section 3.11.2). Subsequently, the SS based launcher is subjected to lower disruption forces and corresponding stress. Further, the inherent good mechanical stiffness of the thick walls of SS counteracts these disruption forces efficiently. The downside of having a higher resistivity is that the RF losses in SS would be higher as compared to that in copper. However, the pulsed nature of the launcher's operation ensures that the heat dissipation in it is not much of a concern.

The RF performance of the proposed PAM launcher is analysed in COMSOL Multiphysics. The structure spans over 258 mm × 119 mm × 2130 mm and extensive computing resources are required for its simulation. The two toroidal modules of the PAM launcher are identical except for the input feeding structure. Thus, the RF simulation of only one module is presented. The passive waveguides are not considered during analysis as they are inconsequential in the RF simulations with matched output ports. The input of the toroidal module under analysis is excited with the dominant TE_{10} mode. The skin depth in SS is resolved using the 'impedance boundary' feature available in COMSOL. A tetrahedral mesh size of $\lambda_g/10$ is used, where, λ_g is the guided wavelength in the respective material. A peak electric field of 630 kV/m is obtained at the location of the post in the mode converter for an input power of 125 kW as shown in Fig. 3.30. The computed return loss of the structure is ~33.7 dB at the centre frequency, as shown in Fig. 3.31. It is better than 32.5 dB in the desired bandwidth of ±5 MHz centred around 3.7 GHz.

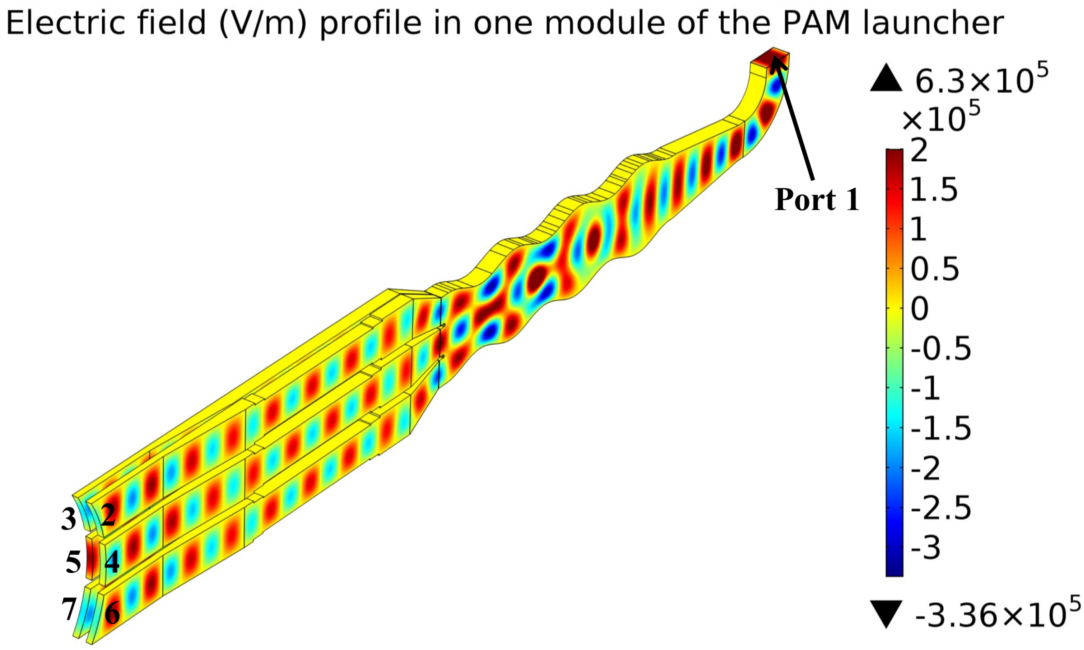

Figure 3.30: E-field (V/m) profile in one module of the PAM launcher.

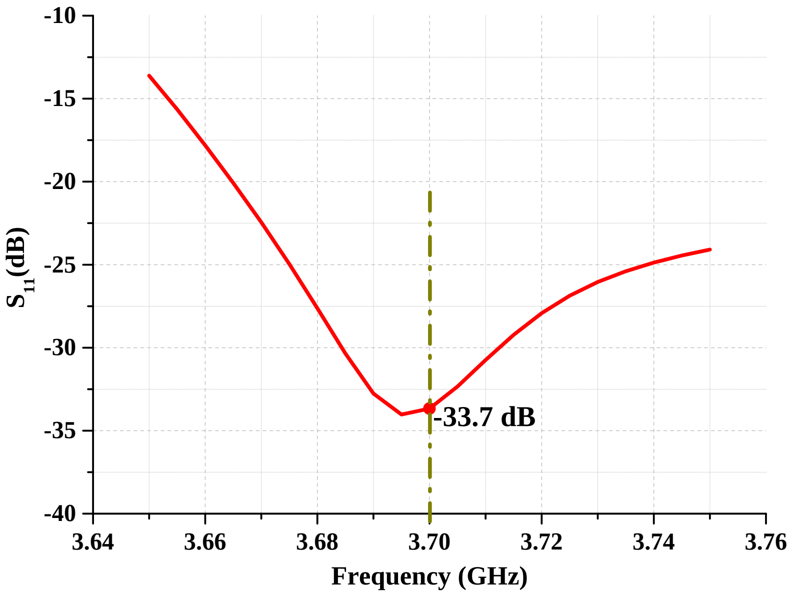

Figure 3.31: Computed return loss of the PAM launcher.

The input power of 125 kW is equally divided between all the 6 active waveguides of a toroidal module. The port numbers (assigned during simulation) and the labelling (used during the low power testing later) for each of these active waveguides of a toroidal module are shown in Fig. 3.32. The total surface loss in one module of the PAM launcher alongwith the transmission line components is evaluated by integrating the surface loss density and is obtained to be ~8 kW. Thus, the power transmitted to each of the active waveguides is ~19.5 kW (S_{n1} ~-8.1 dB, where, (n = 2 to 7)) as shown in Fig. 3.33a. The phase of an active waveguide (for example '3, Upper right') with respect to the one on its left ('2, Upper left'), leads by 270° (−90°, as desired) and is illustrated in Fig. 3.33b.

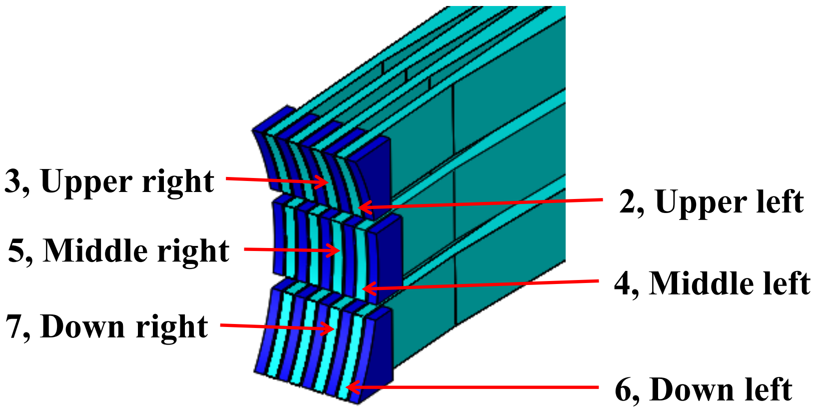

Figure 3.32: 3D figure illustrating the output port numbers (assigned during simulation) and the labelling (used during the low power testing) for each of the active waveguides.

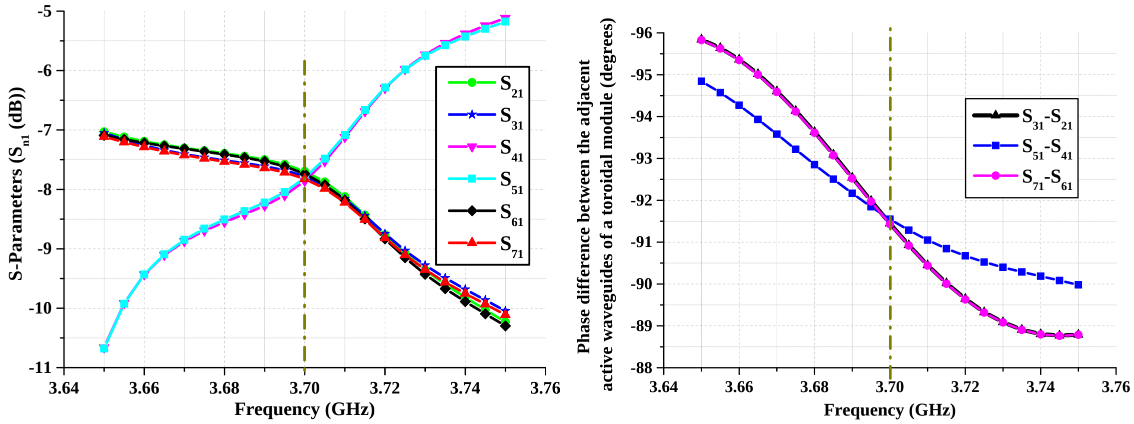

(a) (b)

Figure 3.33: (a) Power transmitted to each of the active waveguides, (b) Phase difference between the adjacent active waveguides.

The total surface loss of the complete structure is ~16 kW, while that of only the PAM section is ~7 kW [8]. The insertion loss of one module of the launcher is ~0.3 dB.

3.8 Multipaction Analysis

The PAM launcher, operating in UHV (10^{-8} mbar) of the tokamak, would be subjected to high E-fields (as high as 630 kV/m). This would lead to the emission of secondary electrons from the surface of the launcher. The exponential growth of these electrons may cause RF breakdown. Therefore, it is necessary to evaluate and study the secondary electron growth in the SS304L based PAM launcher.

A multipaction analysis is carried out, which evaluates the number of secondary electrons emitted in response to a given E-field configuration. The surface parameter of the material (such as emissivity) also plays an important role in determining the secondary electron growth behaviour in the structure. The multipactor modelling of the structure is based on an averaged version of Furman's Secondary Electron Yield (SEY) model [129] and the analysis is performed in CST Particle studio [130].

Initially, 1000 electrons are introduced in the PAM launcher as 'seed electrons'. The launcher is excited with different values of input RF power and the number of secondary electrons emitted with time is computed for each case to obtain the threshold above which multipaction (exponential growth of electrons) occurs. Fig. 3.34 is a typical plot depicting the secondary electron growth in the launcher for different values of input RF power.

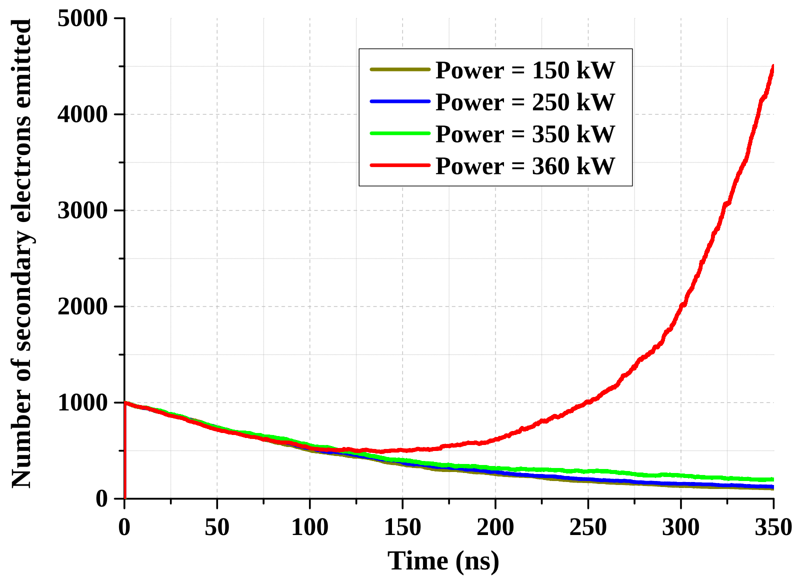

Figure 3.34: Number of secondary electrons emitted with time in the PAM launcher for power levels of 150 kW, 250 kW, 350 kW and 360 kW.

It can be observed that, for input power lower than 350 kW, the number of secondary electrons reduces with time. An exponential growth in the number of electrons is observed when the launcher excited with a total input power of 360 kW.

It can thus be concluded that the launcher may be operated at or below an input RF power of 350 kW. The data provided in [131] gives an idea about the threshold limit for multipactor breakdown. The simulation results obtained are consistent with this data.

3.9 Thermal analysis of the PAM launcher

The PAM launcher is designed for a total input power of 250 kW at 3.7 GHz. The corresponding power flux at the mouth of the launcher is ~2.3 kW/cm^2. The two major sources of heat generation in the launcher are the surface losses in the waveguides and the radiation heat from the plasma. The launcher has thick walls behind the passive waveguides, which helps to conduct the heat away efficiently and reduce the bulk temperature during high power operations. The following subsections discuss each of these sources in detail. Further, analytical calculations are performed to estimate the first order thermal behaviour of the launcher, which is later compared with the simulation results [9].

3.9.1 Thermal load due to RF losses

The analytical estimation, pertaining to the RF losses in the PAM section, is carried out in this section. The inner profile of the PAM section, alongwith some of its critical dimensions, is illustrated in Fig. 3.35. The PAM section is a 3×4 matrix of 12 waveguides with each waveguide comprising of three parts; namely,

(a) Step phase shifter/Straight waveguide (L_{sps} = ~$4\lambda_g$)

(b) Tapered waveguide (L_{tap} = ~$2\lambda_g$)

(c) Active waveguide (L_{act} = ~$1.5\lambda_g$)

The details of these parts are tabulated in Table 3.3.

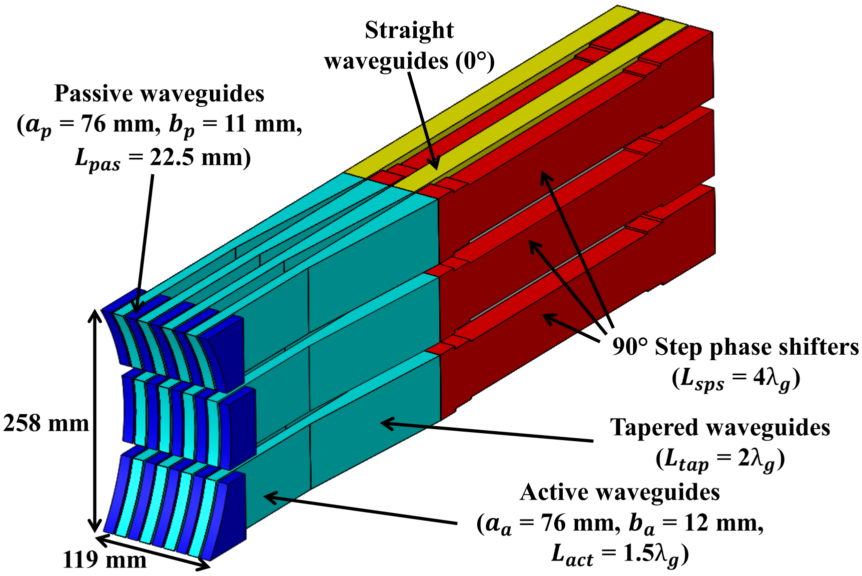

Figure 3.35: PAM section with some critical dimensions.

Table 3.3: Details of the PAM section components.

Component (no.)	**Feature**	**Broader dimension**	**Narrower dimension**
Step phase shifter (6)	Varying broader dimension in steps along the length	76 mm (approximated)	25 mm
Straight waveguide (6)	Constant cross-sectional dimensions	76 mm	25 mm
Tapered waveguide (12)	Linearly varying narrower dimension along the length	76 mm	18.5 mm (average of 25 mm and 12 mm)
Active waveguide (12)	Constant cross-sectional dimensions	76 mm	12 mm

The propagation of RF power through the 12 waveguides of the PAM section would result into continuous dissipation of power and corresponding generation of heat along the length. The attenuation constant (α_c, in Np/m) due to conductor (surface) losses in a rectangular waveguide is obtained by using Eq. 3.10 [132],

$$\alpha_c = \frac{R_s}{a^3 b\beta k\eta}\left(2b\pi^2 + a^3k^2\right) \tag{3.10}$$

where,

R_s is the Surface resistivity of the conductor and is given by $\sqrt{\frac{\omega\mu}{2\sigma}}$ (Ohms).

ω is the frequency of operation (rad/s).

μ is the permeability of the material (H/m).

σ is the electrical conductivity of the material (here SS304L) (S/m).

$\beta = \sqrt{k^2 - \left(\frac{\pi}{a}\right)^2}$ (rad/m), for TE_{10} mode in a rectangular waveguide.

k is the wave number (rad/m).

η is the characteristic impedance of a vacuum filled waveguide (120π) (Ohms).

a, b are the cross-sectional dimensions of a waveguide (m).

The surface resistivity of the SS304L walls ($\sigma = 1.4 \times 10^6$ S/m) at 3.7 GHz is 0.102 Ω. The attenuation constant for the step phase shifter/straight waveguide, tapered waveguide and active waveguide is evaluated using Eq. 3.10 and are 0.13 dB/m, 0.17 dB/m and 0.25 dB/m, respectively. The surface loss in the PAM section, for a total input power of 250 kW, is evaluated by using the length and the attenuation constant of each part and is obtained as ~6.7 kW. This is in good agreement with the surface loss obtained through COMSOL simulations (~7 kW).

The heat generated due to this surface loss is diffused up to a thickness d, which is evaluated by using Eq. 3.11,

$$d = \sqrt{D\tau} \tag{3.11}$$

where,

D is the diffusion constant and is given by $\frac{k}{\rho C_p}$.

k is the thermal conductivity (W/mK).

ρ is the density of the material (kg/m^3).

C_p is the specific heat capacity of the material (J/kgK).

τ is the duration of operation (seconds).

The thermal properties of SS304L material and the subsequently evaluated diffusion constant (D) and thickness (d) is reported in Table 3.4.

Table 3.4: Thermal properties of SS304L material and calculated values of diffusion constant (D) and thickness (d).

Property	Value
Thermal conductivity	15 W/mK
Density	8000 kg/m^3
Specific heat capacity	500 J/kgK
Diffusion constant (D)	3.75×10^{-6} m^2/s
d	2 mm

The diffusion of heat in the inner surface of the PAM section waveguides results in a rise in the overall temperature of the PAM launcher. This bulk temperature rise (ΔT) for up to a few seconds (not steady-state) can be evaluated by using Eq. 3.12,

$$\Delta T = \frac{Qt}{\rho C_p V} \tag{3.12}$$

where,

Q is the RF surface losses (W).

t is the duration of operation (seconds).

ρ is the density of the material (kg/m^3).

C_p is the specific heat capacity of the material (J/kgK).

V is the volume of the material (m^3).

For one second of operation and a heat load of ~6.7 kW (evaluated above), the bulk temperature rise obtained is 0.13°C.

The thermal response of the PAM launcher is determined by carrying out a coupled RF-thermal analysis in COMSOL Multiphysics. The surface loss obtained from the RF simulations further act as heat load during the thermal analysis of the launcher. Since the launcher would be in tokamak vacuum during high power operations, a radiation boundary condition, wherein the generated heat is radiated to the surrounding vacuum, is required to be modelled. This is achieved by defining the surface emissivity of the inner and outer SS walls of the launcher as 0.07. The complete temperature profile of the launcher, for an input RF power of 250 kW after 1 s, as obtained from the thermal analysis is shown in Fig. 3.36. The bulk temperature rise obtained is ~0.18°C, which is in good agreement with the analytical estimate. The peak temperature rise is 18.5°C and is at the location of the post in the mode converter.

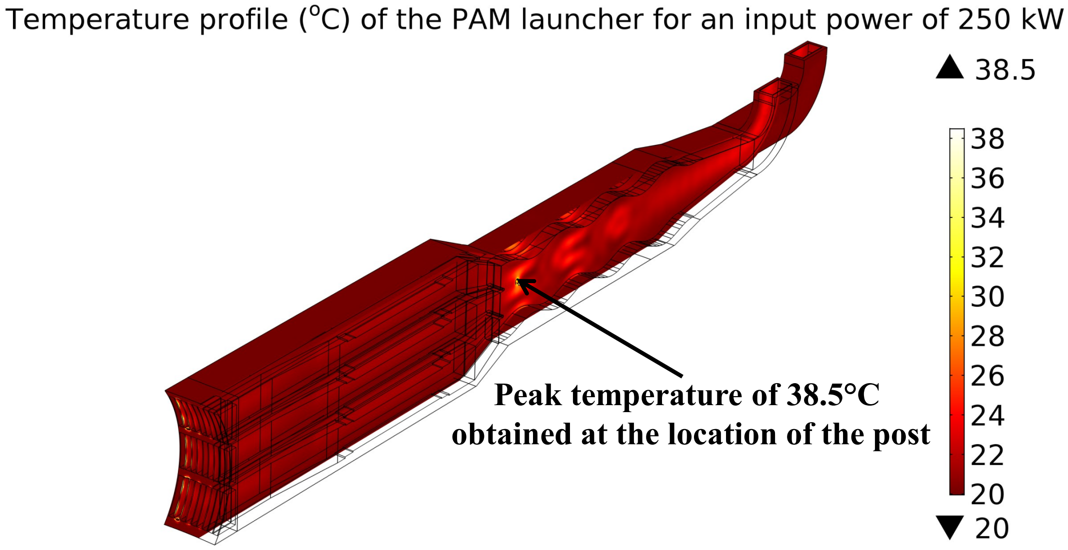

Figure 3.36: Temperature profile (°C) of the launcher for an input power of 250 kW, 1 s.

The thermal response is further studied for a total duration of 150 s to gauge the maximum temperature rise (when the source is on) and the cooling time (after the source is switched off) required by the launcher to reach a steady-state temperature. The temporal evolution of the maximum temperature of the launcher, for different input power levels, is depicted in Fig. 3.37. It can be observed that after reaching a maximum temperature of ~38.5°C (for an input power of 250 kW) just after 1 s, the launcher attains a steady state temperature of ~25°C within six seconds.

3.9.2 Thermal load due to radiation losses

The total power injected into the ADITYA –U tokamak through all the heating and current drive systems would never exceed 1 MW. The power radiated from the plasma to the outer plasma facing wall is assumed to be ~25% of the total power. Thus, the total power falling

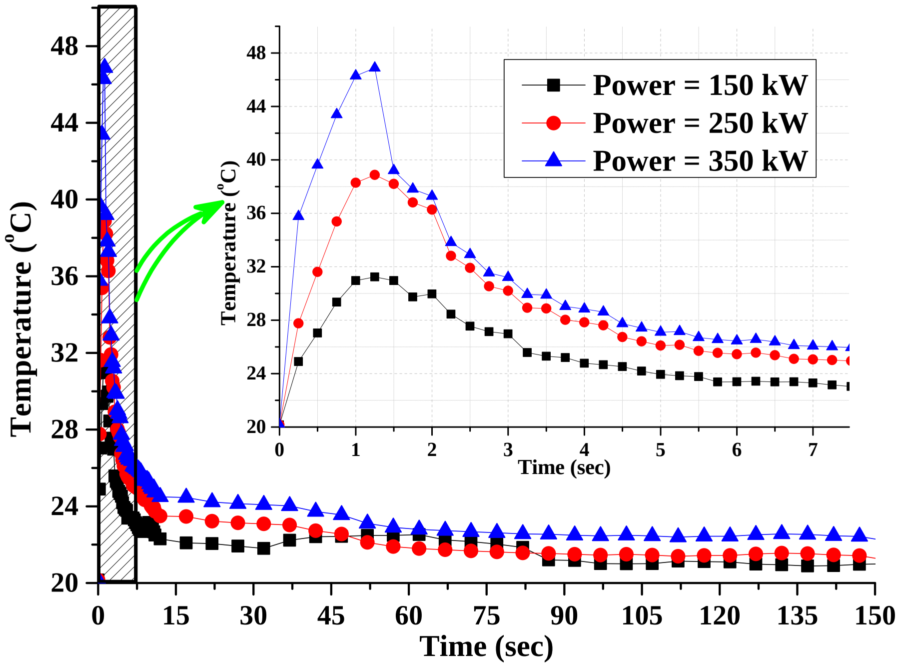

Figure 3.37: Temporal evolution of the maximum temperature of the PAM launcher for input power levels of 150 kW, 250 kW and 350 kW

on the launcher mouth would typically be ~2 kW. The radiation loss is less than (1/8)th of the RF surface loss. Further, the mouth of the launcher will be protected against it by graphite tiles (discussed in Chapter 4). Thus, the contribution of the radiation loss to the total temperature rise of the launcher is negligible.

3.10 Stress analysis

In this section, the various stresses and forces generated due to temperature rise and plasma disruption are discussed. The thermal stress is evaluated analytically and further compared with the simulation results. The forces and the corresponding stress generated in the launcher due to plasma disruption are evaluated using COMSOL Multiphysics [9].

3.10.1 Thermal stress

The rise in the overall temperature of the launcher due to heat dissipation generates thermal stress. The launcher undergoes deformation due to this stress during high power operations. Since the peak temperature rise is not alarmingly high, the thermal stress generated is not substantial and can be estimated by Eq. 3.13,

$$Thermal\ Stress = \alpha \Delta T Y \tag{3.13}$$

where,

α is the coefficient of thermal expansion (/K).

ΔT is the bulk temperature rise (K).

Y is the Young's modulus (Pa).

A thermal stress of 74 MPa is estimated for SS304L's Young's modulus (200 GPa) and coefficient of thermal expansion (20 μ/K).

The Solid Mechanics module of COMSOL Multiphysics is employed to couple the heat load, obtained from the thermal analysis, with the structural analysis. A von Mises stress profile obtained from the simulation results is shown in Fig. 3.38. It can be observed that a maximum von Mises stress of 50 MPa is generated, which is in good agreement with the theoretical estimate. This maximum stress is at the same location (near the mode converter post) as that of the maximum temperature.

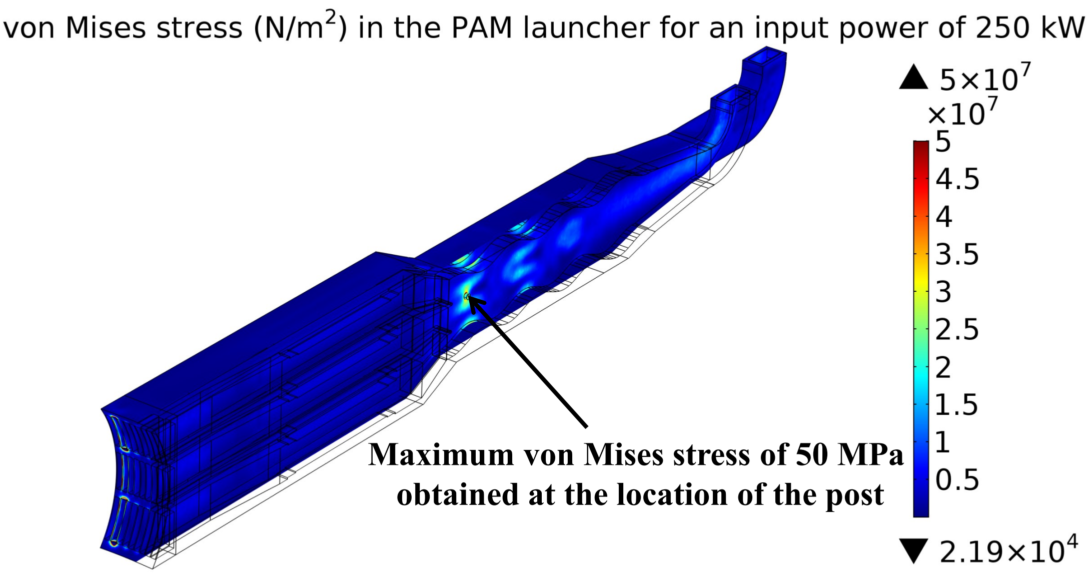

Figure 3.38: von Mises stress (N/m^2) profile in the PAM launcher due to thermal load for a total input power of 250 kW.

The peak von-Mises stress generated in the launcher is well below the Yield stress of SS304L material (215 MPa). The launcher would thus be subjected to deformations well within the acceptable limits, as shown in Fig. 3.39.

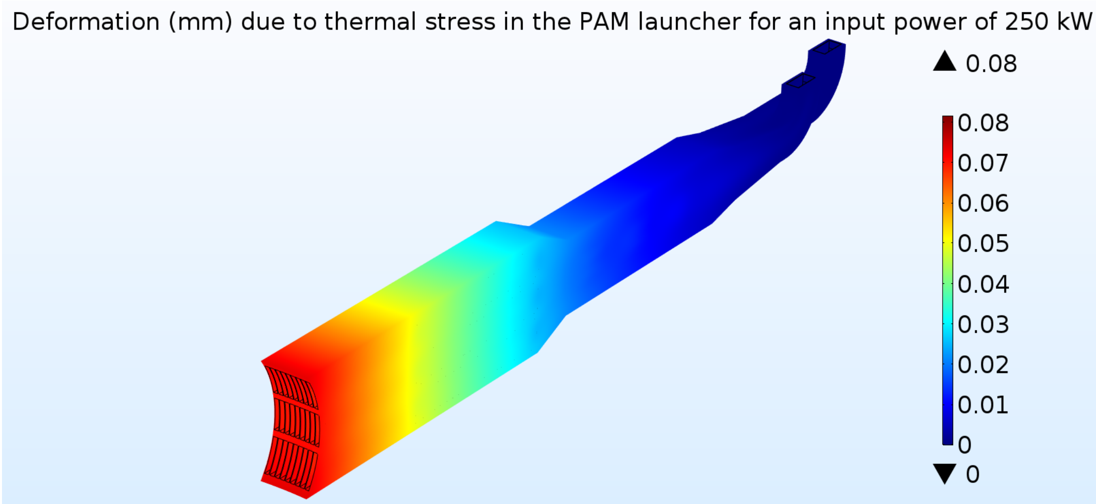

Figure 3.39: Deformation (mm) in the PAM launcher due to thermal stress.

3.10.2 Disruption stress

Plasma disruption (sudden decay of plasma current) generates mechanical stress in the PAM launcher. Fig. 3.40 depicts a pictorial representation of this phenomenon. The plasma current decay induces a varying magnetic field (represented by the green arrows in Fig. 3.40a) by Ampere's law. This further induces a loop voltage and hence a loop current (represented by the red arrow loop) on the top and bottom plates of the launcher. The toroidal magnetic field of the tokamak crosses with this loop current density and generates $\boldsymbol{J} \times \boldsymbol{B_T}$ disruption forces, as shown in Fig. 3.40b. These forces are equal, opposite and act on the opposite ends of the plates, thereby causing a rotational motion (torque) about the radial axis. The launcher is fixed to the tokamak at the port flange. Thus, the torque translates into mechanical stress in the launcher. One way of reducing this stress is to reduce the induced loop current density, which is a major variable component of these disruption forces. The use of a fabrication material having lower electrical conductivity would lead to a lower induced current density. This is one of the reasons for using SS304L instead of OFHC copper for fabrication.

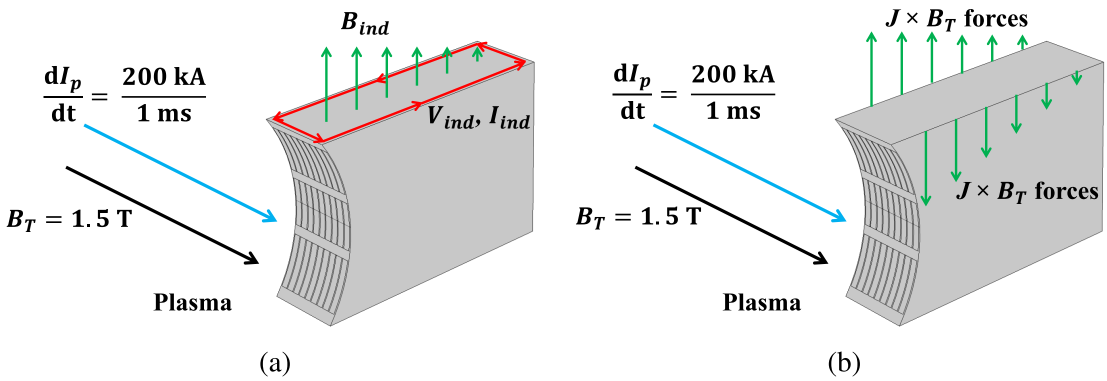

Figure 3.40: A pictorial representation of the phenomenon of generation of disruption forces (a) Loop voltage and loop current induced on the top and bottom plates of the launcher (b) Equal and opposite forces generated at the opposite ends of the plates.

The disruption analysis of the PAM launcher is carried out in COMSOL Multiphysics. To verify the simulation results, the theoretical estimation of the disruption forces is required, which is not feasible to evaluate for complex structures such as the PAM launcher. These estimations for a circular disc, instead, are feasible and simple. Thus, simulation studies are carried out in COMSOL to obtain the disruption forces acting on a circular disc, which are further verified with the theoretical estimates. The results obtained were in close agreement and are reported in Appendix A. This helps in benchmarking the modelling considerations used in the analysis. Further, the circular disc is replaced by the PAM section in the model and the desired disruption forces are obtained.

The launcher dimensions are small as compared to that of the tokamak as depicted by the schematic shown in Fig. 3.41. Thus, the plasma current can be modelled as a single, straight, uniform current density conductor in COMSOL Multiphysics. A typical plasma current profile with respect to time is taken into consideration from the ADITYA –U experimental shot to model its shape.

Fig. 3.42 shows the plasma current profile; wherein, it is assumed to rise from 0 to 200 kA in 10 ms and fall from 200 kA to 0 in 1 ms. A flat top of 200 kA is maintained for 189 ms.

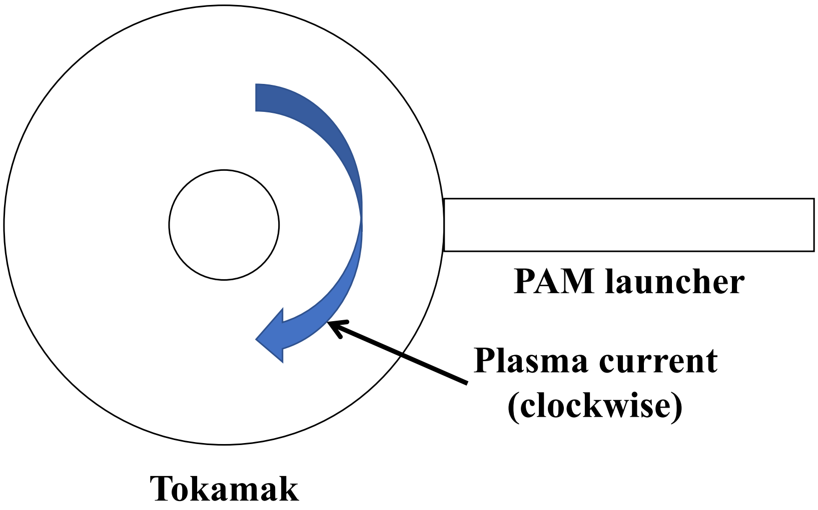

Figure 3.41: Stick diagram illustrating small launcher dimensions as compared to that of the tokamak.

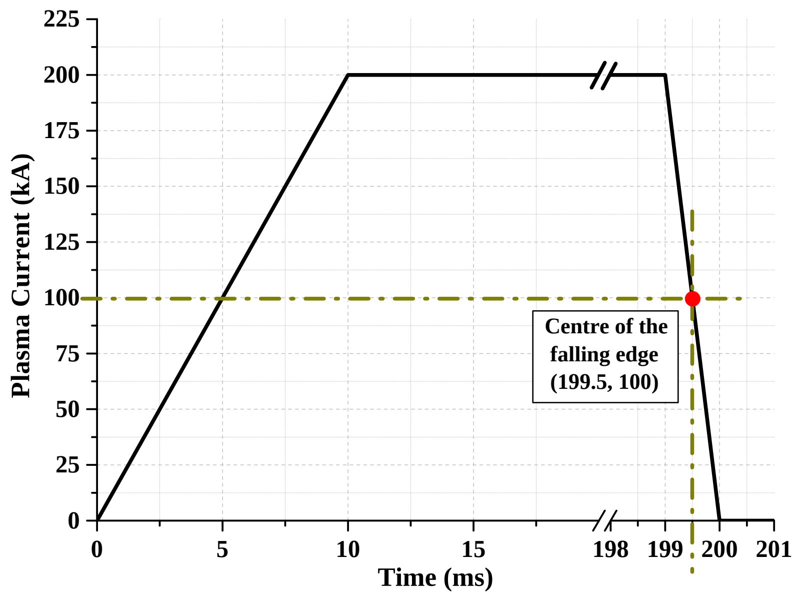

Figure 3.42: A typical plasma current profile in the ADITYA –U tokamak experimental shot.

The falling edge of the plasma current causes a $\frac{dB_{pol}}{dt}$ of ~0.16 T/s. The plots presented and explained below are at the time instant of 199.5 ms. Fig. 3.43 shows the induced loop current density on the top plate of the PAM section. The resulting $\boldsymbol{J} \times \boldsymbol{B_T}$ forces is illustrated in Fig. 3.44. The red and blue colours in the colour scheme, representing the peak positive and negative values, respectively, are on the opposite ends of the plate. The red arrows, in Fig. 3.43, reveal the direction of the induced current and further confirm that it forms concentric loops on the top plate. It is maximum (represented by longer arrows) on the edges of the plate and closer to the mouth of the launcher. In Fig. 3.44, the red arrows represent the direction of $\boldsymbol{J} \times \boldsymbol{B_T}$ forces, which are equal and opposite on either side of the top plate and maximum near the mouth of the launcher.

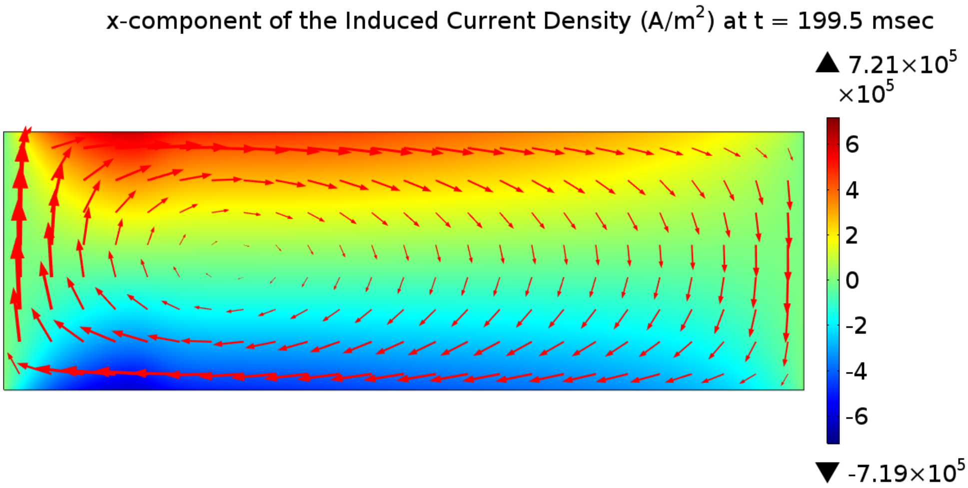

Figure 3.43: Induced loop current density (A/m^2) on the top plate of the PAM launcher at t = 199.5 ms.

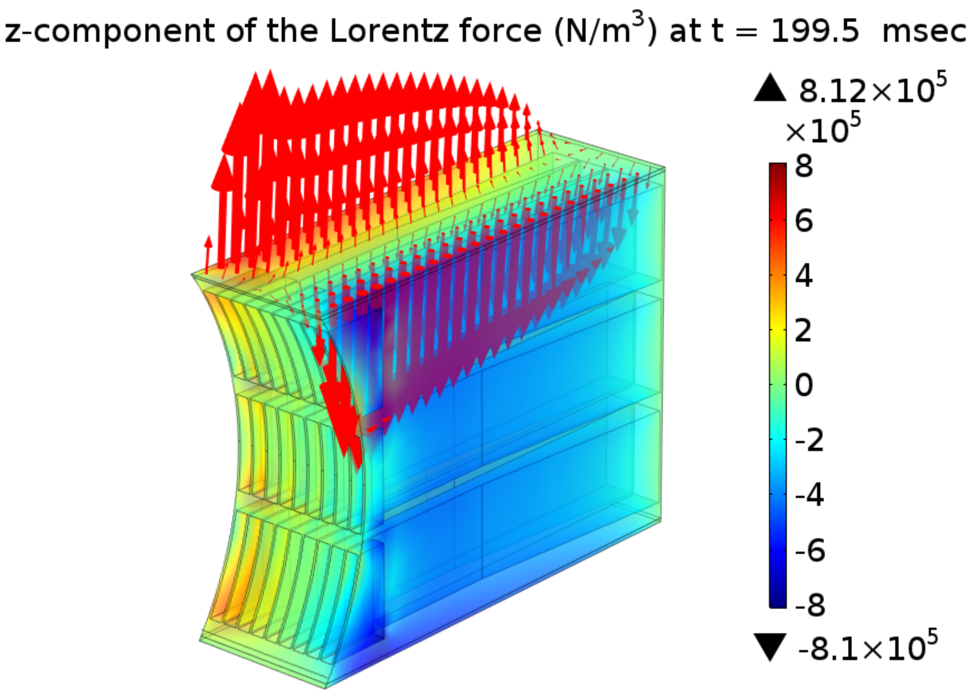

Figure 3.44: $\boldsymbol{J} \times \boldsymbol{B_T}$ forces (N/m^3) acting on the top plate of the PAM launcher at t = 199.5 ms.

The disruption forces translate to stress on the PAM launcher. The temporal evolution (in steady-state and fall phases of the plasma current) of the von Mises stress generated and the resulting deformation (in mm) of the PAM section is illustrated Fig. 3.45. The deformation is exaggerated for easy visualisation. The figure reveals that, as the plasma current decays from 200 kA to 0, the stress generated and the corresponding deformation in the launcher increases with the maximum obtained at the end of the decay. A peak von Mises stress and maximum deformation of ~2.21 MPa and 9.73 μm, respectively, is obtained at 200 ms.

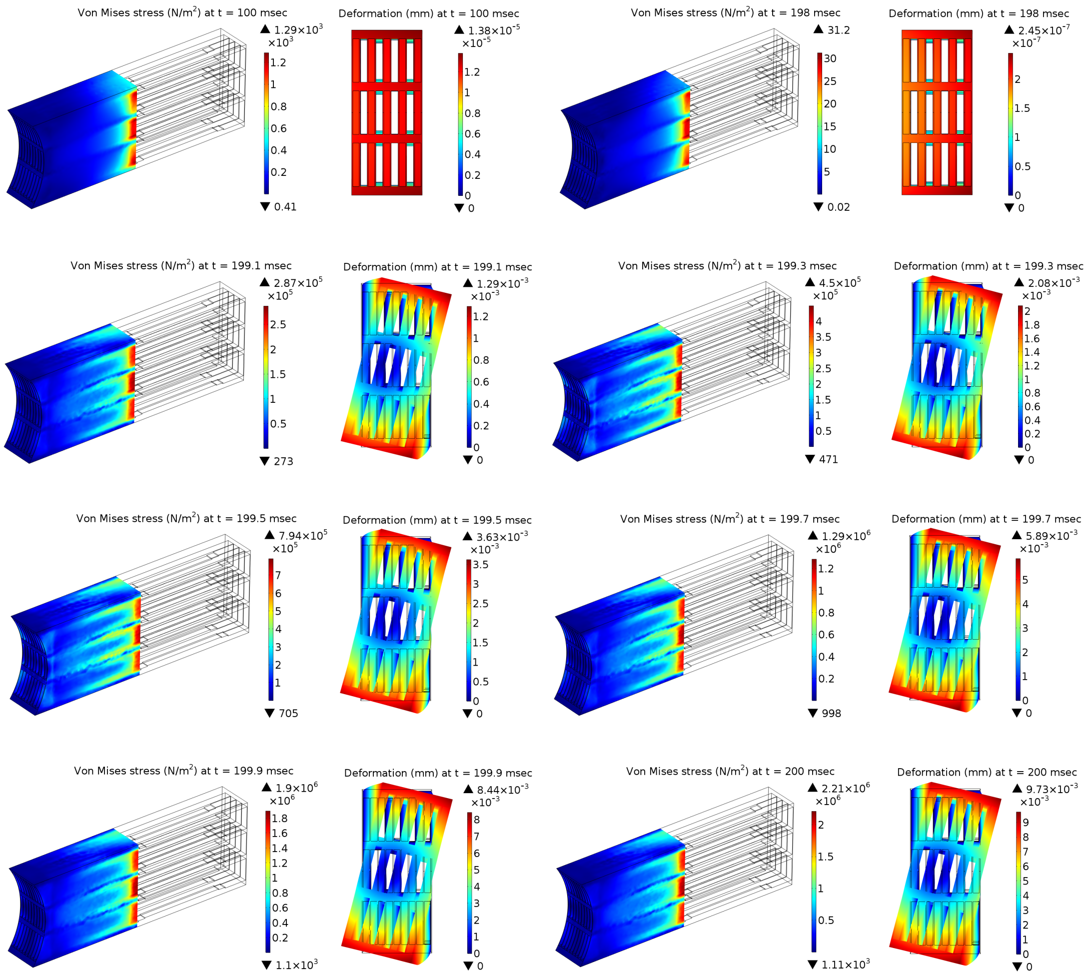

Figure 3.45: Temporal evolution of the von Mises stress (N/m^2) and deformation (mm) in the PAM launcher.

The results obtained from the thermal and stress analysis of the PAM launcher is summarised in Table 3.5. It compares the theoretical estimates and the simulation results.

Table 3.5: Analytical and simulation results of the thermal and stress analysis.

	Analytical values	**COMSOL simulation results**
Surface loss in PAM launcher	6.5 kW	7 kW
Bulk temperature rise	~0.13°C	~0.18°C
Thermal stress	24 MPa	50 MPa

As per the standard operating practises, the dimensional changes are required to be within 100 microns for the RF performance to remain unhampered. The overall deformation of the launcher is within this acceptable limit.

3.11 Summary

This chapter presents the design of a Passive Active Multijunction (PAM) launcher for the ADITYA –U tokamak. The proposed PAM launcher incorporated the multijunction effect in spite of the limited space available owing to the port size constraint. A new type of mode converter was also proposed, which does not require a metallic post for impedance matching. Various multiphysics coupled simulations were also carried out to evaluate the thermal and mechanical performance of the PAM launcher. The launcher exhibited good RF, thermal and mechanical performance in these simulations which increased the confidence level to proceed towards the fabrication of the structure. The next chapter presents the methodologies developed for fabricating the launcher. New methodologies were required to be developed owing to the limitations in fabrication expertise and the critical nature of the design.

Chapter 4

Methodologies for the Development of the PAM Launcher

The translation of a design from its CAD model to a physical entity needs a detailed and critical analysis of fabrication methods and engineering aspects involved with it. This is more so true in the case of a PAM launcher. The PAM launcher would be placed in ADITYA –U tokamak, which requires UHV environment compatibility with a required ultimate vacuum level of 10^{-8} mbar. Thus, fabrication techniques should be appropriately and uniquely identified and established so that the developed PAM launcher meets the desired vacuum specifications. Further, to achieve this level of vacuum, the PAM launcher should be able to withstand baking conditions up to ~180°C. This means that there exist additional constraints on the choice of development/fabrication techniques, which should withstand high temperature baking. Although RF design and analysis carried out in the earlier chapter provided encouraging results in terms of return/insertion loss, the selection of improper and incompatible fabrication techniques would lead to arcing and other undesirable effects. Hence, it is imminent to undertake studies on techniques and methods to fabricate the PAM launcher.

The fabricated launcher should meet the critical requirements such as UHV compatibility, withstanding baking at elevated temperatures, ADITYA –U port constraints, RF compatibility, easy radial movement of the launcher, DC isolation et cetera.

This chapter discusses the challenges and further presents the techniques and methodologies developed to facilitate the fabrication of the PAM launcher. Further, it describes various components incorporated in the mechanical design of the launcher to meet the above mentioned critical requirements.

4.1 Choice of material

As mentioned earlier, the tokamak plasma is confined by magnetic surfaces formed by toroidal/poloidal coils and plasma current. The use of any magnetic material would distort the plasma confinement magnetic surfaces. Therefore, all the components of the PAM launcher are fabricated using Stainless Steel SS304L material because of its non-magnetic properties, vacuum compatibility and high mechanical strength. It can withstand higher baking temperature (as compared to copper) which would eventually help in degassing at a higher temperature and achieve desired UHV conditions. Further, it provides good weldability to realise a UHV compatible structure.

Several critical tests carried out on the SS304L raw material are listed below:

(a) Inter Granular Corrosion (IGC) Practice 'E' test as per the American Society for Testing and Materials (ASTM), A262-2015 (to detect any IGC-fissures or cracks in the material)

(b) Ultrasonic test (to test the material for any objectionable flaw).

(c) Chemical composition of the material (using the Spectroscopy-OES method).

(d) Rockwell hardness and tensile strength test (to determine the mechanical properties of the raw material)

The test results suggest that the raw material conform to material standards and can be used for fabrication. The highlights of the fabrication technique, depicting its uniqueness, used for some of the components of the launcher are briefly discussed below. It is to be noted that the detailed drawings having all the critical dimensions and tolerances of the launcher are attached in Appendix B.

4.2 PAM section

The inner profile of the PAM section is shown in Fig. 4.1. As discussed in Chapter 3, it consists of alternate 90° step phase shifters (marked in red) and straight waveguides (marked in yellow), followed by the tapered waveguides, which finally terminate into active waveguides. The passive waveguide pockets are present at the mouth of the launcher between the adjacent active waveguides.

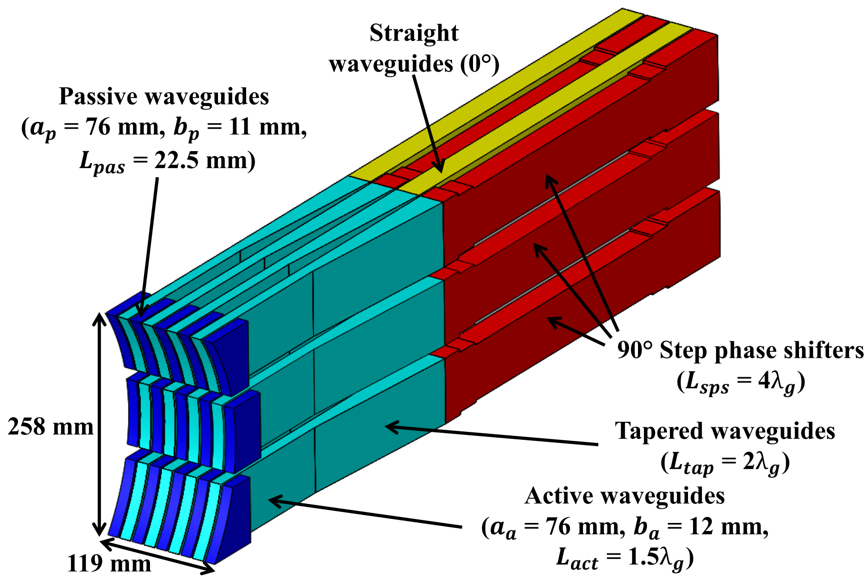

Figure 4.1: Inner profile of the PAM section.

The fabrication technique, capable of realising the waveguide arrangement shown in Fig. 4.1, is required to be identified. The pros and cons of various techniques which can be employed are now discussed.

The Electrical Discharge Mechanism (EDM) wire cutting technique can be used to realise a waveguide structure from a single metal block. The corresponding fabricated waveguide has no issues pertaining to poor metallic contact, rough surface finish and RF losses. Also, the chances of arcing are very low. However, the waveguide pockets in the PAM section are long, uneven and thus cannot be realised using EDM.

Another technique that could be employed is by stacking several metallic plates together. These plates would have a waveguide profile scooped out of thick metal. Employing this technique by using a single bolting mechanism would result in poor metallic contact between the intermediate plates and further increase the insertion loss. The gaps between the plates would also lead to arcing during high power operations.

Brazing or welding of these plates may lead to large dimensional distortions, thereby hampering the overall RF performance in terms of insertion and return loss. The rough and uneven joints caused by these procedures deteriorate the surface finish of the profiled plates leading to arcing during high power operations. Further, these joints increase the overall insertion loss in the PAM section.

A novel methodology is proposed in which the plates are stacked in a sequential manner. Here, the second plate is bolted to the first plate at the alternate tapped holes (of the first plate). The third plate is bolted to the stacked combination of the first and second plates and so on. This process is repeated until the entire structure is realised. The stacking scheme with reference to the actual plates and the fabrication procedure employed is explained in detail in Appendix C. The input and output side of the final assembled PAM section is shown in Fig. 4.2 and Fig. 4.3, respectively.

4.3 Tapered Divider

As discussed in Chapter 3, the tapered divider is a 3×4 matrix of 12 tapered rectangular waveguides. It is fed by the mode converter, which has 6 output waveguides, each having

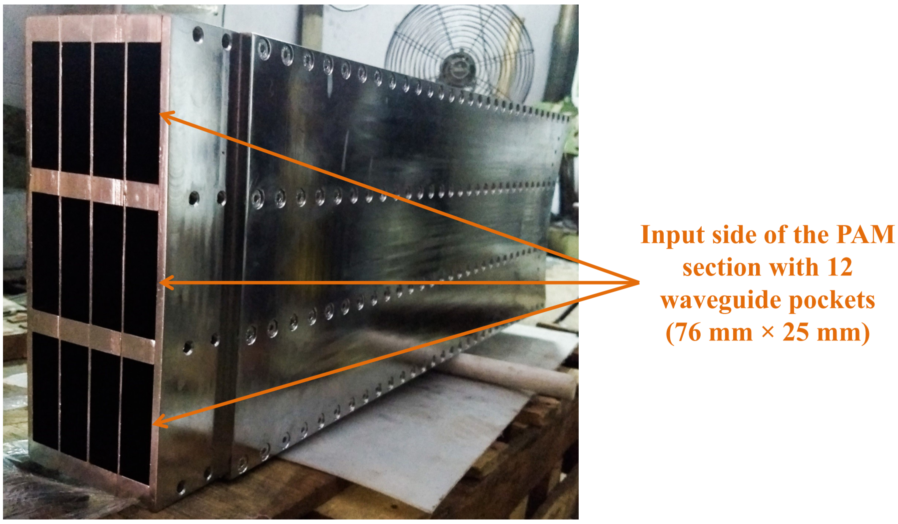

Figure 4.2: Input side of the PAM section.

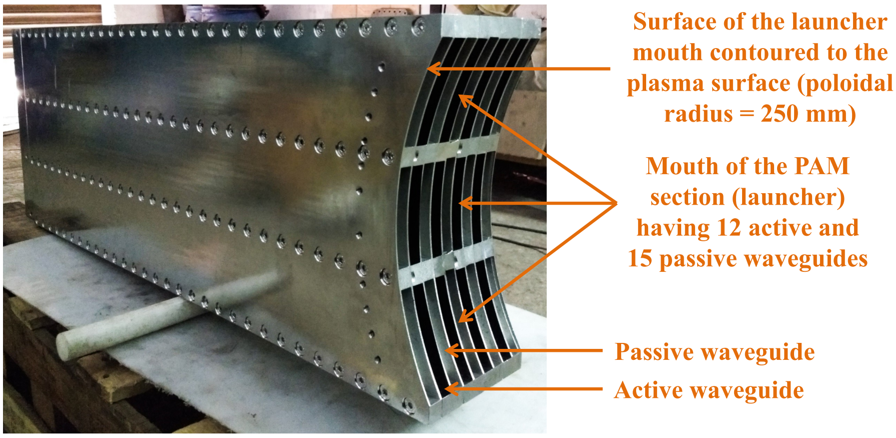

Figure 4.3: Mouth of the PAM section.

a cross-sectional dimension of 53.87 mm × 34.04 mm. The tapered divider transmits RF power from the 6 outputs of the mode converter to the 12 inputs of the PAM section. The cross-sectional dimensions of the input and the output waveguides of the tapered divider are 53.87 mm × 16 mm and 76 mm × 25 mm, respectively, as shown in Fig. 4.4.

The tapered divider is flared in both the lateral dimensions, along its length, with a precise tapering angle of 11.4°. Hence, a 5-axis wire Electrical Discharge Machining (EDM) technique is best suited for its fabrication. The divider, along with its input and output flanges, is fabricated from a single SS304L block. The most critical part is to realise the inclined rectangular waveguides as the EDM wire cuts the raw material in a vertical direction only. Thus, the raw material block is held with a precise tilt (as per the tapering

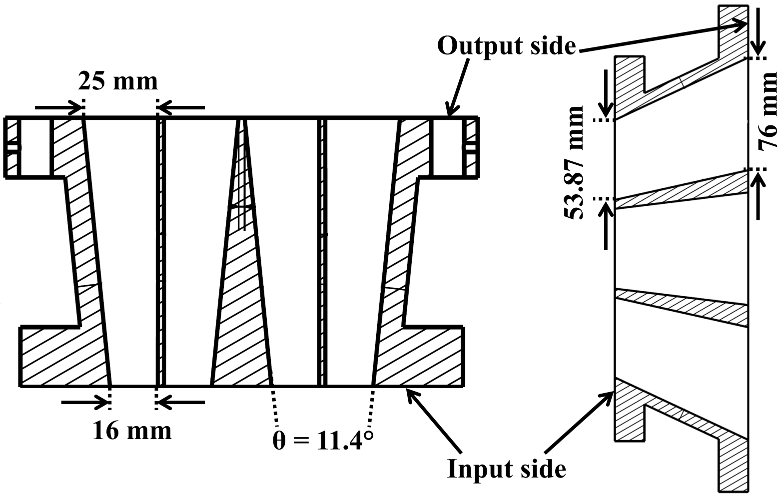

Figure 4.4: A schematic of the Tapered divider.

angle), for every waveguide pocket, using specially designed jigs and fixtures. The input flange (output flange) has dowel pin holes for accurate alignment of the divider's input (output) waveguide cross-section with the output (input) waveguide cross-sections of the mode converter (PAM section). Fig. 4.5a and Fig. 4.5b show the input and the output side of the fabricated tapered divider, respectively.

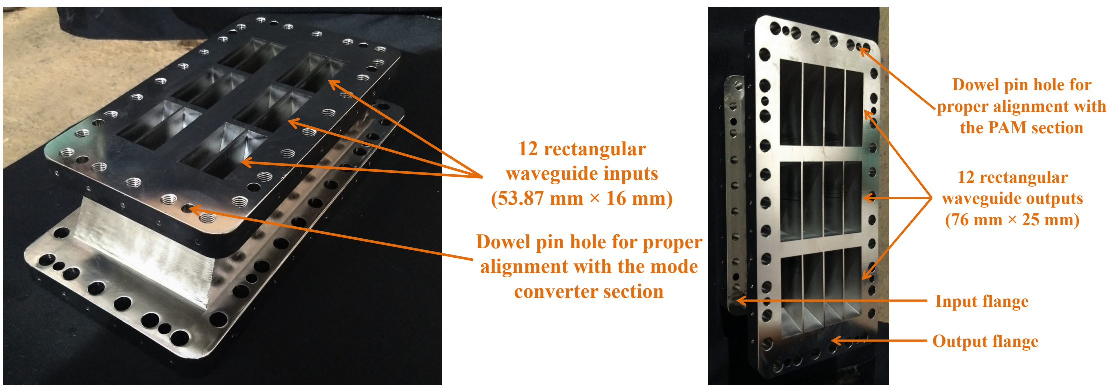

(a) (b)

Figure 4.5: Fabricated tapered divider.

4.4 Mode Converter section

The cosinusoidal profile is the most challenging feature of the mode converter from the fabrication point of view. There are two mode converter sections, each consisting of the mode converter and the linear taper, as shown in Fig. 4.6. Each of them has a 90° bend at its input. One of the mode converters is longer than the other by $2\lambda_g$ to ease the integration of the mode converter inputs with the RF windows.

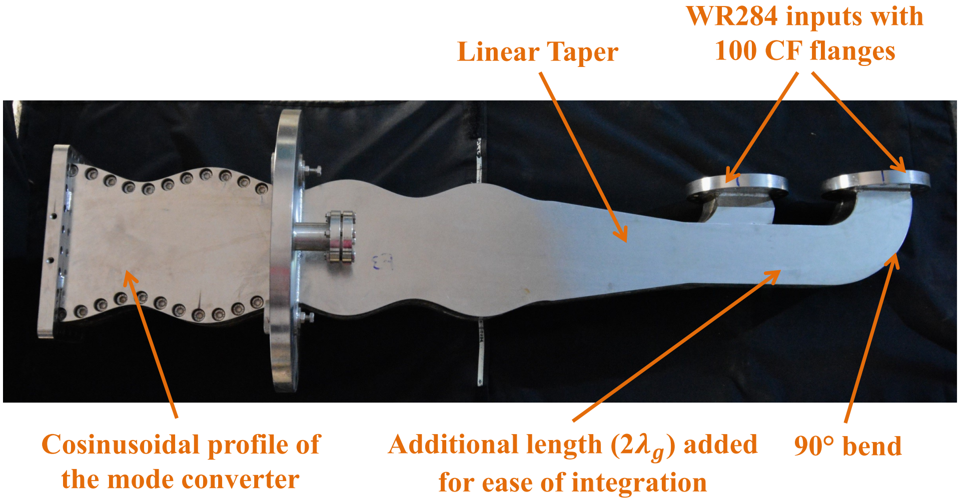

Figure 4.6: Mode converter section illustrating the cosinusoidal and linear taper profile.

The basic scheme in fabricating the mode converter section is to have two plates of different lengths (1255 mm × 255 mm × 50 mm, 1070 mm × 255 mm × 50 mm), profiled cosinusoidally (using the VMC machine) to the desired depth of 34.04 mm. A third plate (1260 mm × 255 mm × 25 mm) is machined so as to sandwich it between the two profiled plates, as shown in Fig. 4.7. The middle plate has a final thickness of 20 mm and is partially welded (near the input) and partially bolted (near the output).

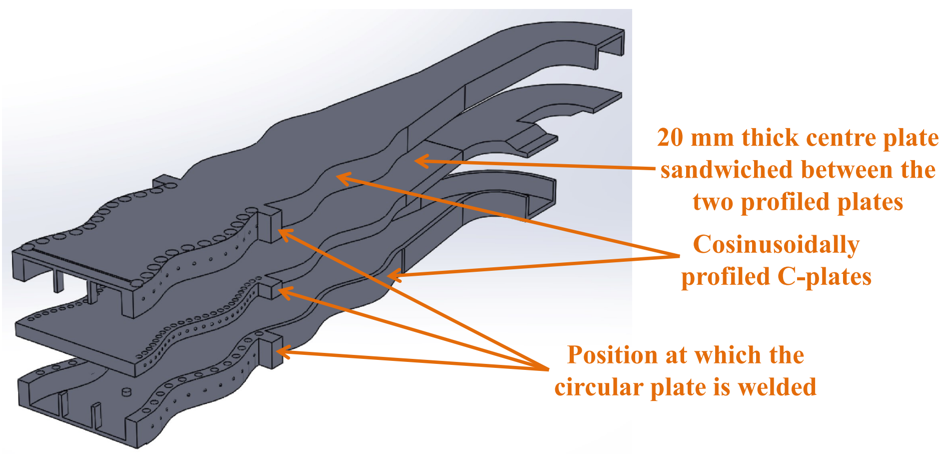

Figure 4.7: Exploded view of the mode converter section depicting the arrangement of the profiled and centre plates.

Owing to the ADITYA –U tokamak space constraints, the mode converter section is partially placed in a vacuum enclosure while the rest of the section lies in atmosphere. The part within the vacuum enclosure is nut bolted as welding cannot be carried out from the inside (to avoid trapped volume) as per UHV norms. The part lying in the atmosphere is welded as using bolts is not a feasible solution to maintain vacuum inside the structure. The most challenging part of the fabrication is to ensure UHV compatibility as the partial welding and partial bolting of the structure are prone to leaks. Thus, the three plates are tightly held together during welding using jigs and fixtures as shown in Fig. 4.8.

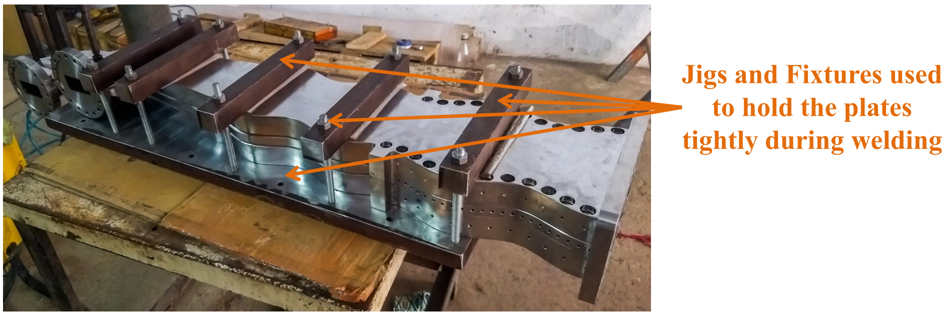

Figure 4.8: Welding setup for the mode converter section. Jigs and fixtures are used to hold the plates tightly during welding.

A circular plate is welded between the bolted and welded section for easy UHV compatible assembly of the launcher as shown in Fig. 4.9. Also, this plate helps in holding the swivel flange, which is incorporated to connect the mode converter to the bellow.

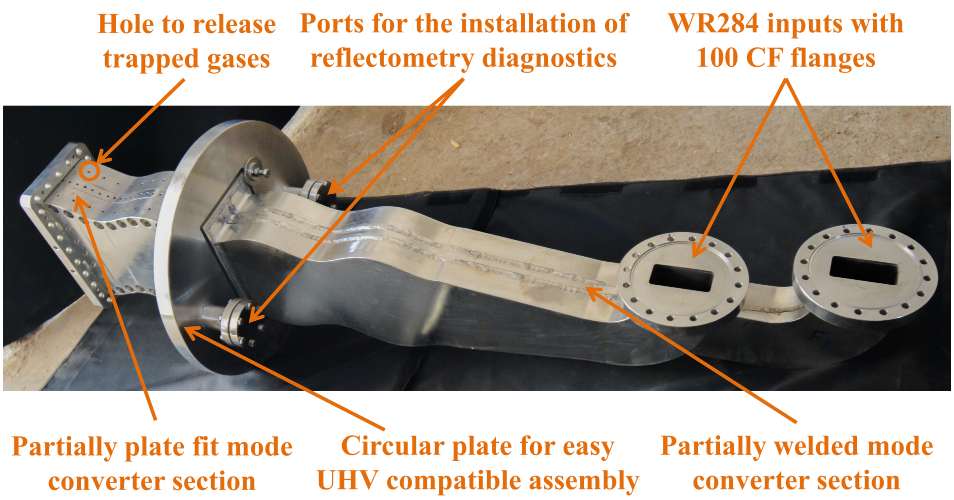

Figure 4.9: Complete mode converter section.

The input of the mode converter section has a cross-section of 72.14 mm × 34.04 mm with a 100 CF circular flange. It has 6 non-standard rectangular waveguide outputs (see Fig. 4.10), which are further connected to the input of the tapered divider. The output flange has dowel pin holes for proper alignment with the tapered divider.

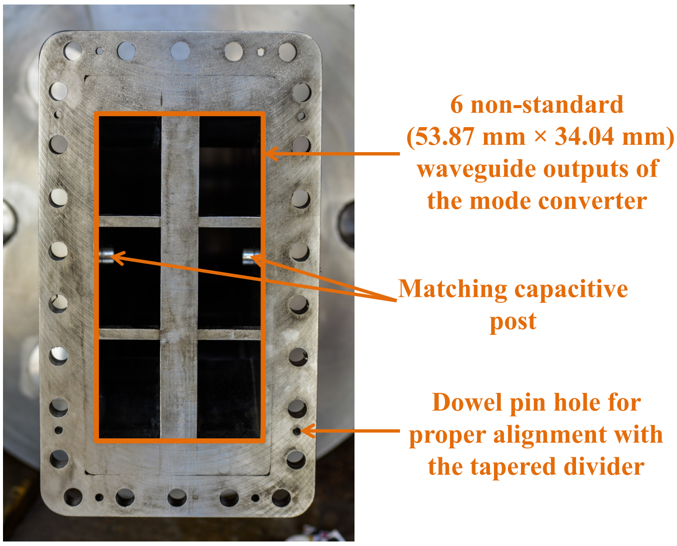

Figure 4.10: Output cross-section of the mode converter section.

4.5 Others Components

4.5.1 Enclosure

An enclosure, shown in Fig. 4.11 is fabricated (by bending and welding of plates) to enclose the PAM launcher in the UHV environment. Also, it is desired to have a smooth radial movement of the launcher. Thus, a rolling support is fixed on the inner side of the enclosure and the PAM section is placed over it. The support is made up of PolyEther Ether Ketone (PEEK) material to provide the required electrical isolation between the launcher and the enclosure. The enclosure has a circular CF flange welded at one end and a port flange at the other. The circular flange is connected to the bellow (helps in the radial movement of the PAM launcher) while the port flange would be connected to the ADITYA –U tokamak port. A 100 CF, 63 CF and 35 CF ports are incorporated for pumping, gauge installation and diagnostic purposes.

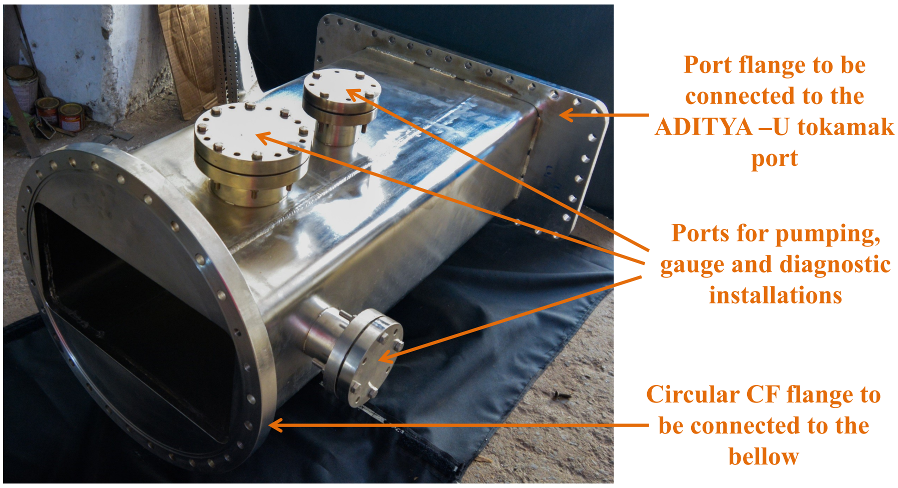

Figure 4.11: Fabricated Enclosure.

4.5.2 Intermediate Flange

An intermediate flange is fabricated to enable vacuum compatible joint and DC isolation. As Viton O-ring is used for DC isolation, the flange has two groves (for two Viton O-rings) on one side as shown in Fig. 4.12. The space between the two O-rings is maintained at an intermediary vacuum through a hole. This hole terminates to a 16 KF port at the periphery of the flange.

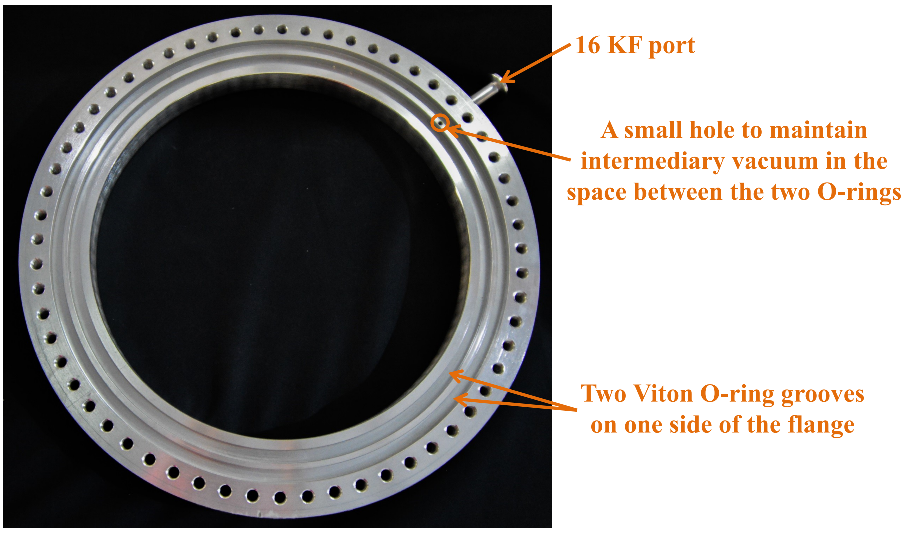

Figure 4.12: Intermediate flange with double Viton O-ring grooves.

4.5.3 Graphite tiles

Graphite tiles are placed around the periphery of the launcher mouth, as shown in Fig. 4.13, to protect the launcher from heat flux during plasma operations.

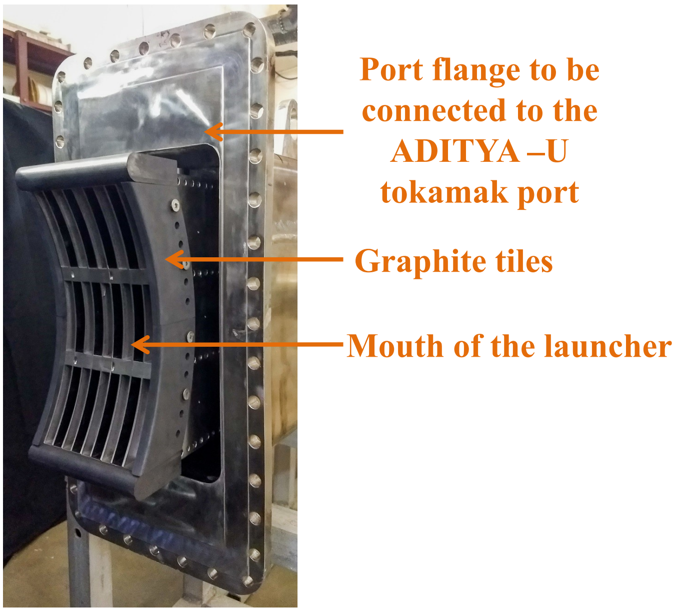

Figure 4.13: Graphite tiles placed around the mouth of the launcher.

4.6 Complete Assembly

The plate-fit PAM section, tapered divider and the mode converter sections are assembled to form the PAM structure, which would launch the RF waves into the tokamak. Fig. 4.14 shows the PAM structure with all the important components labelled.

Fig. 4.15 shows the complete PAM launcher with the enclosure, bellow, intermediate flanges and the graphite tiles integrated and having a total length of 2185 mm.

The ultrasound cleaning method is used to remove any impurities, oil, machinery coolant, et cetera, introduced in the structure during the fabrication process. The inner and end surfaces of each component of the structure require a surface finish of 3 delta for good RF performance. This is achieved using electropolishing.

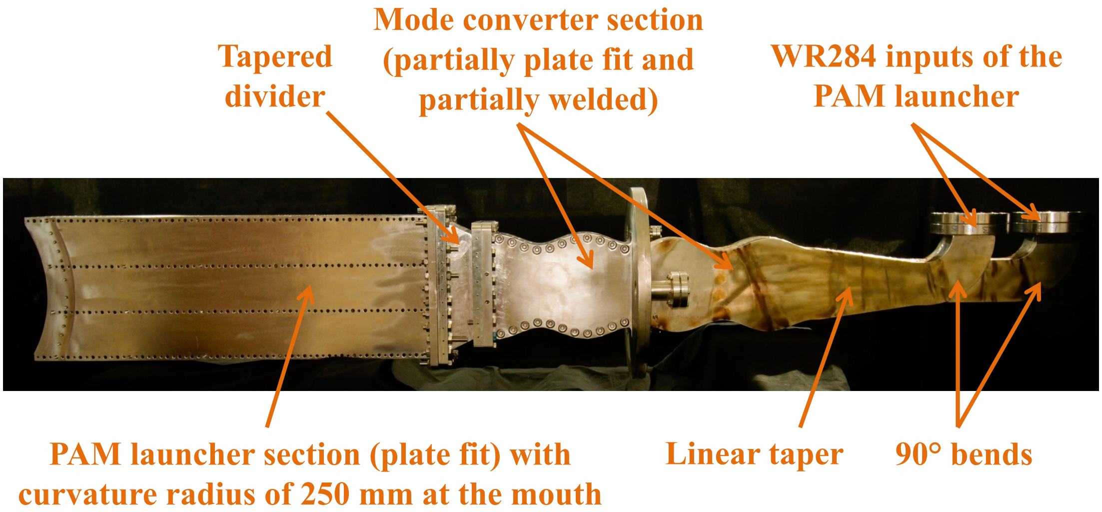

Figure 4.14: PAM structure comprising of the plate-fit PAM section, tapered divider and the mode converter section.

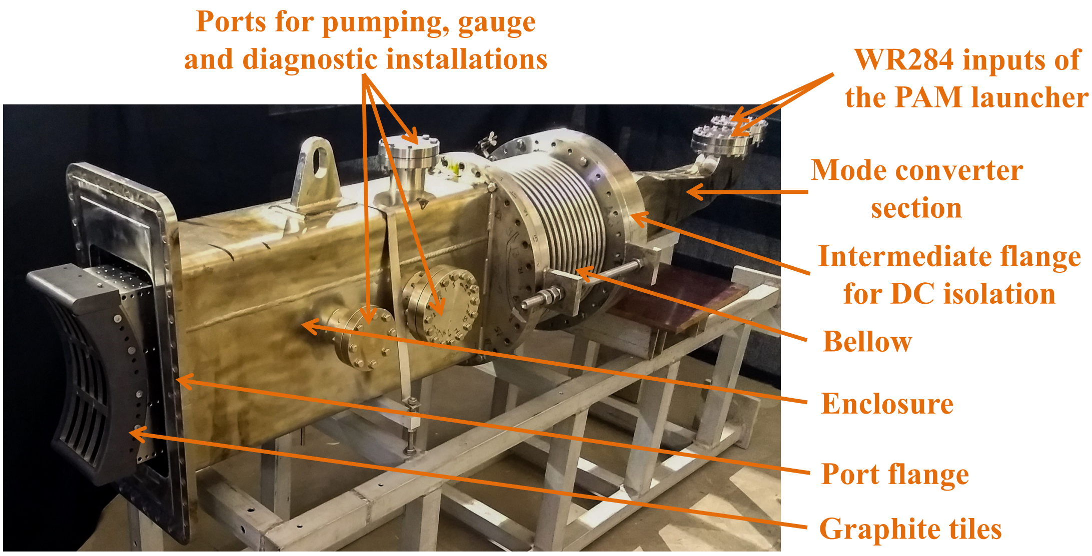

Figure 4.15: Complete PAM launcher.

4.7 Summary

Considering various technical constraints, the choice of material for the PAM launcher is identified. A summary of various methodologies developed, in order to fabricate the PAM launcher such that it conform to the various constraints, are presented in this chapter. These methodologies were further established by developing prototypes in order to facilitate the fabrication of the launcher. The detail of the fabrication techniques and the corresponding photographs/drawings are presented in the appendices for the sake of completeness. Various mechanical components are added to the launcher to address the issues of compatibility with the ADITYA –U tokamak without compromising on the RF design. The details of each of these components are discussed. The next chapter presents the measurement results obtained from experiments conducted on the developed PAM launcher.

Chapter 5

Measurement Results of the PAM Launcher

The PAM launcher, after its fabrication, is subjected to several qualification tests to evaluate its mechanical and RF performance and ensure its compatibility with ADITYA –U tokamak. The launcher is also tested for its UHV compatibility as it would be in the UHV environment of the tokamak after installation. Once its mechanical and vacuum compatibilities are established, the RF characterisation of the launcher is carried out.

This chapter presents the RF characterisation, in terms of the S-parameters, of the individual sections and the complete structure of the PAM launcher. They are compared with the simulation results discussed in Chapter 3 to ascertain its behaviour. Finally, a novel method to evaluate the $N_{||}$ spectrum, power spectrum density and the directionality of the launcher, for RF power launched in air, is reported. This method helps to evaluate the performance of the launcher in free space before installing it on the machine, thereby increasing the degree of confidence on the design of the PAM launcher.

5.1 RF Characterisation

The RF performance of the launcher is characterised by measuring the S-parameters using a Vector Network Analyser (VNA). The S-parameters of the complete PAM structure is measured in a phased manner. Initially, the mode converter section is characterised for its RF performance, followed by the PAM section. Finally, the S-parameters of the complete structure is measured. This is done to study each of the important parts of the structure. The output dimensions of the mode converter section and the PAM section are non-standard, as discussed in Chapter 3. Thus, the VNA measurements demand the design of customised test kits for a smooth transition between the output of the mode converter (and the PAM launcher) and the VNA adapters (standard WR284 dimensions). These test kits are designed as per the desired transition and simulated in COMSOL Multiphysics to evaluate their performance. Further, they are fabricated and their S-parameters are measured. The test kit designs and their simulated and measured RF results are presented in Appendix D. The measured RF results of the test kits are used in the post-processing of the data obtained from the measurements discussed below.

5.1.1 Mode converter section

The mode converter section consists of two mode converters and their corresponding linear tapers. The S-parameters of each of the mode converter-linear taper units are measured separately using the mode converter test kits. The complete measuring setup is shown in Fig. 5.1. The input cross-section of the mode converter section is the standard WR284 which is connected to the standard WR284 VNA adapter. The output of the mode converter is divided into three parts each accommodating $(1/3)^{rd}$ of the output TE_{30} mode. A customised three input three output test kit is used to transform the non-standard cross-section (53.87 mm × 34.04 mm) of each of the output part to standard WR284 cross-section. The 3 inputs of the test kit match the three closely placed outputs of the mode converter. The test kit has three arms (Upper, Middle and Lower) and each arm carries each part of the mode converter output from its input to three different directions. This eases the integration of the VNA adapters. The transformation of the non-standard to standard WR284 cross-section is done individually at the output of the three arms of the test kit using a step transformer. The three outputs of the mode converter are thus obtained at the three arms of the test kit. Each arm is connected to the VNA, at a time, while the others are connected to low power waveguide absorbers and the S-parameters are measured. The obtained S-parameters are the combined S-parameters of the mode converter section and the test kit. The combined S-parameters are further post-processed in MATLAB (see Appendix E for the post-processing steps) to obtain the S-parameters of the mode converter section. Although each mode converter section has two sets of S-parameters corresponding to the two test kits, only one set of S-parameters for one of the mode converter section is shown below as the results obtained in all the cases are similar.

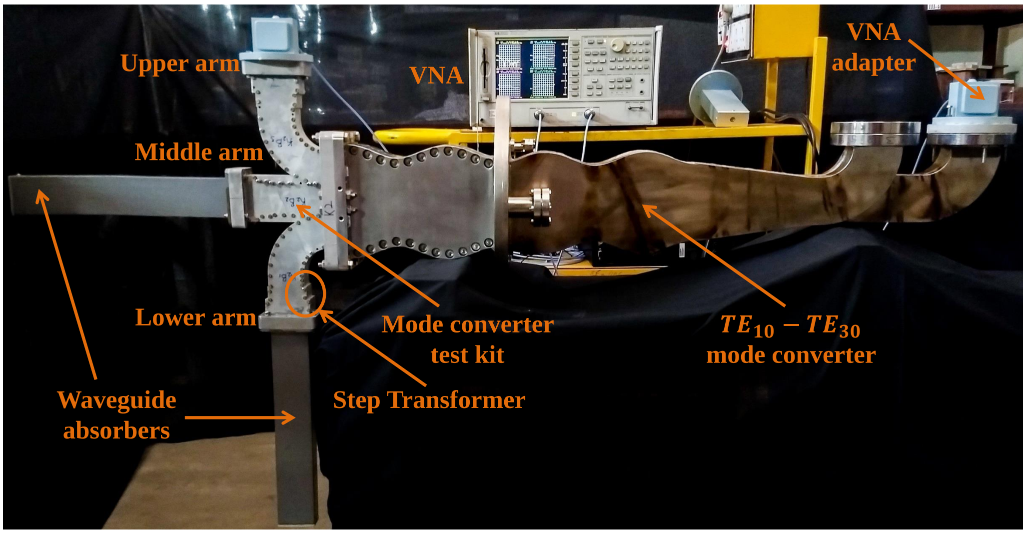

Figure 5.1: Complete setup for low power RF characterisation of the mode converter-linear taper section using a VNA.

Fig. 5.2 shows the frequency response (return loss) obtained for one of the mode converter sections. The simulated return loss obtained from COMSOL Multiphysics, as discussed in Chapter 3, is incorporated in the figure for easy comparison. It can be observed that there is a shift in the minima of the S_{11} of the measured results with respect to that of the simulated results. This shift can be attributed to the non-ideal mechanical joints between the mode converter output flange and the test kits. Also, the test kits are not fabricated using advanced VMC machining, thereby leading to fabrication errors. However, the value of S_{11} obtained at the desired frequency of 3.7 GHz is still acceptable from an operational point of view (<-25 dB).

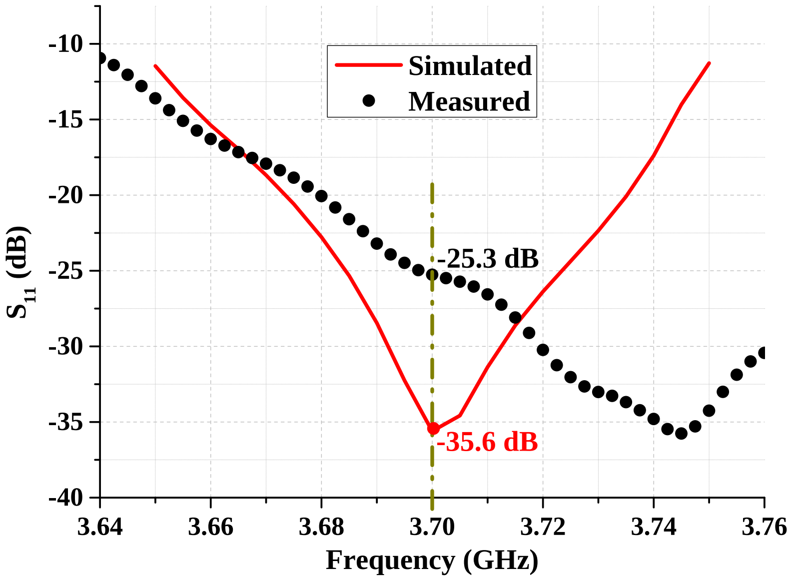

Figure 5.2: Measured and simulated frequency response (return loss) of one of the mode converter sections.

The output of the mode converter section is divided into three equal parts. Fig. 5.3 shows the measured power division between the three arms of the mode converter. They are labelled as Upper, Middle and Lower arms, as shown in Fig. 5.1. It is observed in the figure that each arm has a S_{n1} of ~-5 dB (±0.1 dB), which is in close agreement to the desired S_{n1} of -4.77 dB (ideal, marked by the dark yellow dash-dot line). The deviation of the measured results from the simulated results can be attributed to the surface losses in the mode converter and fabrication tolerances of the test kits. It can be observed that the S-parameter profile of the middle arm is opposite to that of the other two. This is because the E-field profile in the middle arms is 180° phase shifted as compared to that in the other two arms of the mode converter.

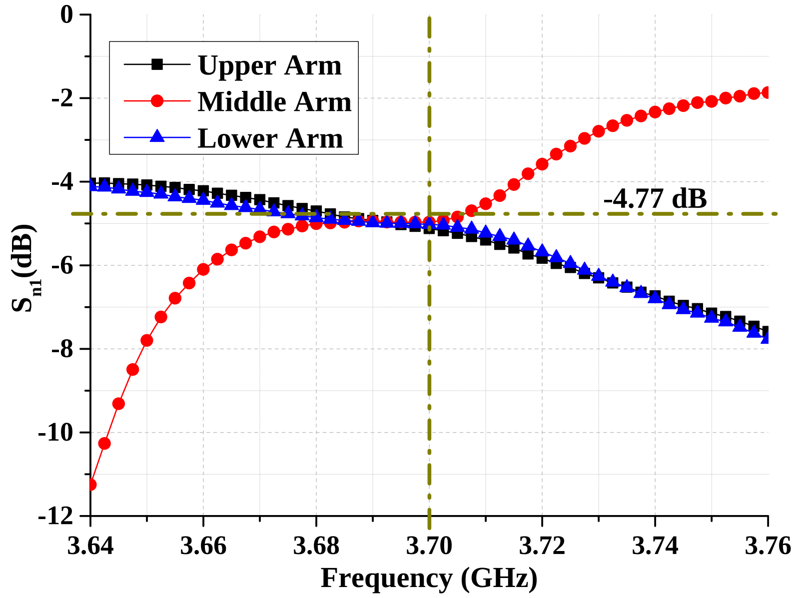

Figure 5.3: Measured power division between the three arms of the mode converter section. The dark yellow dash-dot horizontal line represents the ideal value of -4.77 dB (1/3).

5.1.2 PAM section (with tapered divider)

The PAM section is a 3 × 4 matrix of rectangular waveguide sections with the input of each of the waveguide sections having a cross-sectional dimension of 76 mm × 25 mm as shown in Fig. 5.4. A combination of step phase shifters and straight waveguides followed by the active and passive waveguides constitute each waveguide section, as discussed in Chapter 3.

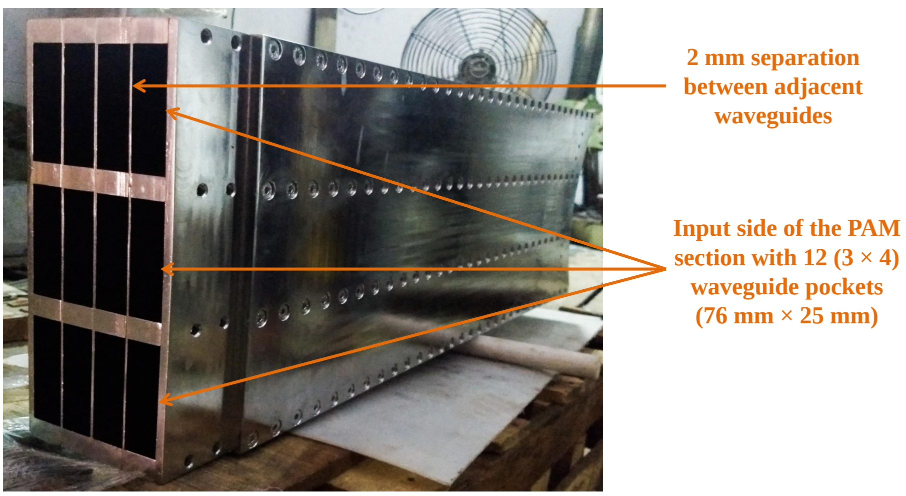

Figure 5.4: Input side of the PAM section.

It can be observed from Fig. 5.4 that there is a separation of only 2 mm (septa thickness) between the adjacent waveguide sections. The standard WR284 VNA adapters cannot be connected directly at the input of the PAM section due to the non-standard cross-sectional dimension of the waveguides and very thin septa. Thus, the tapered divider is connected at the input of the PAM section to facilitate VNA measurements. As the input would now be given to the tapered divider, the mode converter test kit, which is used in Section 5.1.1 (at the mode converter output), can be connected at the input of the overall structure as shown in Fig. 5.5. This is because the profiles of the input of the tapered divider and the output of the mode converters are the same. The mode converter test kit thus provides a standard cross-section and ease of integration to connect the VNA adapters. In this configuration, the S-parameters of one toroidal module are measured at a time, as shown in Fig. 5.5.

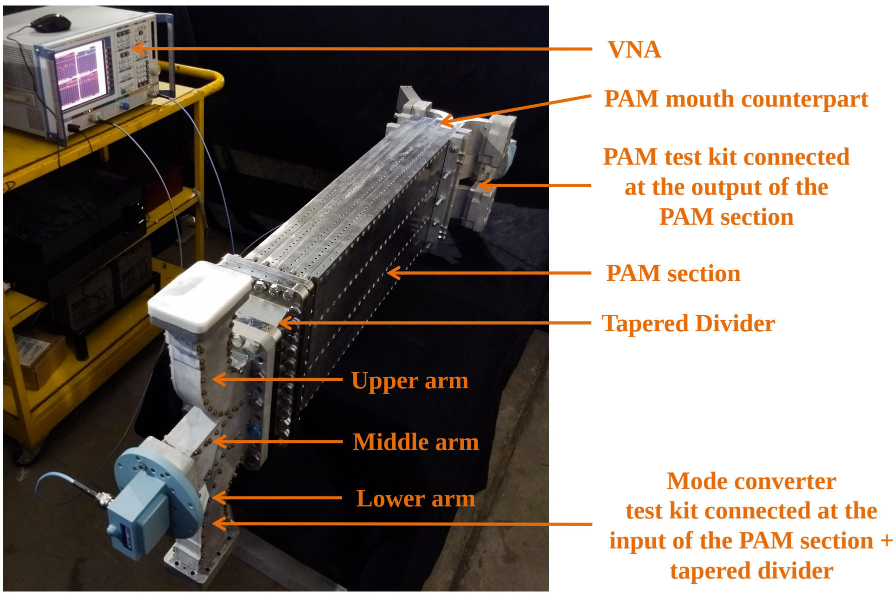

Figure 5.5: Input side of the setup employed for low power RF characterisation of the PAM section.

The output of the PAM section, that is the mouth of the PAM launcher, is contoured to match the plasma surface with a poloidal radius of 250 mm, as shown in Fig. 5.6. Also, the output has non-standard active (76 mm $\times$ 12 mm) and passive waveguides (76 mm $\times$ 11 mm), as discussed in Chapter 3.

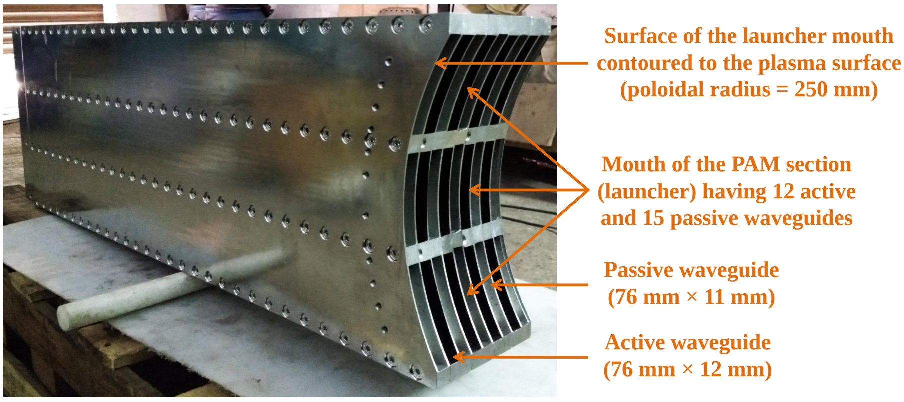

Figure 5.6: Output side of the PAM section.

The curved surface of the launcher mouth and the non-standard cross-sections of the output active waveguides are the two major challenges in connecting the VNA adapters to the launcher output for RF measurements. The solution to the curved surface problem is to connect the counterpart of the launcher output obtained during fabrication and is shown in Fig. 5.7. This helps in converting the curved surface to a flat surface keeping intact the active and passive configuration. The counterpart is connected to the launcher using specially designed jigs and fixtures.

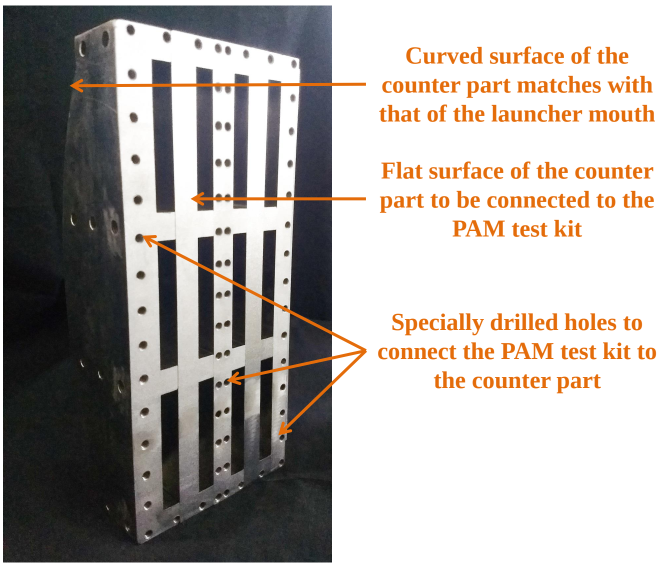

Figure 5.7: PAM mouth counterpart.

As discussed earlier, the mode converter test kit is connected at the input such that the RF characterisation of one toroidal module is carried out at a time. A special 6 input 6 output waveguide PAM test kit is designed to transform the 6 active waveguides at the output of one of the toroidal modules to the standard WR284 waveguides and also ease the integration of the VNA adapters. The input of the test kit is a flat surface having a matrix of 3×2 waveguides (one half of the PAM output/one toroidal module) and it matches with the counterpart as shown in Fig. 5.8. The test kit input is connected to this counterpart using the specially drilled holes shown in Fig. 5.7. The six arms of the test kit transmit the RF power from its six inputs to different directions, thereby providing easy integration of adapters. A quarter-wave step transformer is employed at the output of each arm to transform the active waveguide cross-sectional dimension to standard WR284 waveguide dimension.

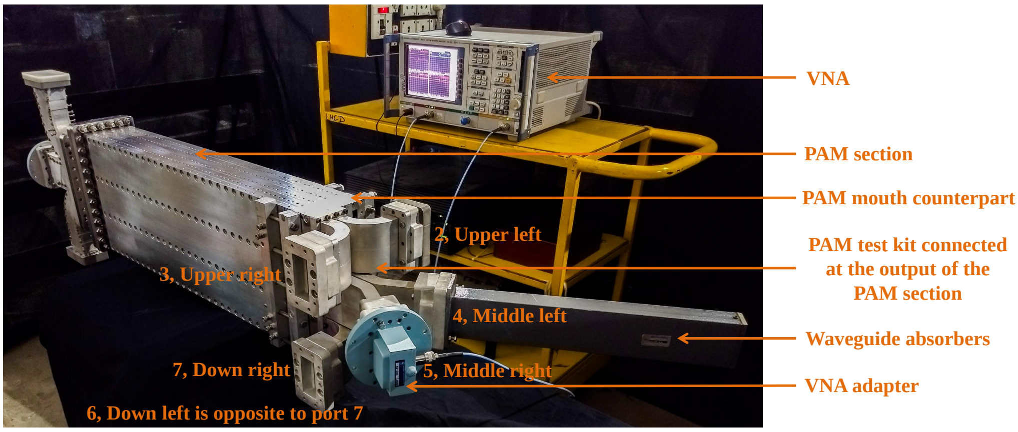

Figure 5.8: Output side of the setup employed for low power RF characterisation of the PAM section.

The arms of the PAM test kit (or the output waveguides of the launcher) are numbered and labelled as Upper left, Upper right, Middle left, Middle right, Down left and Down right as shown in Fig. 5.8. The upper (middle, lower) arm of the mode converter test kit at the input will transmit power to the Upper (Middle, Lower) left and Upper (Middle, Lower) right arms of the PAM test kit. The input of the VNA is connected to one of the three arms of the mode converter test kit and the corresponding two outputs of the PAM test kit are connected to the VNA adapter while the others are connected to the low power waveguide absorbers as shown in Fig. 5.9. Thus, the power is divided into two equal parts with an ideal division of -3 dB.

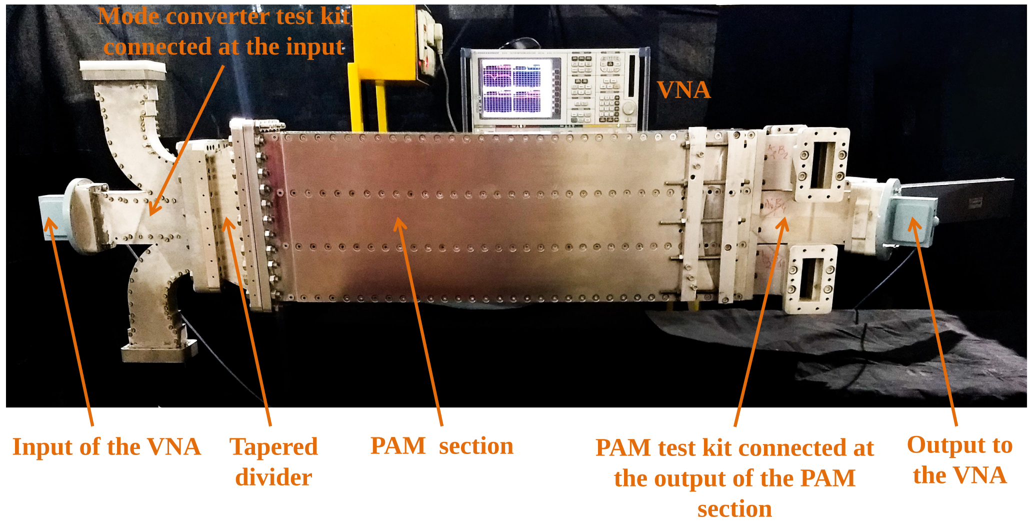

Figure 5.9: Complete setup for low power RF characterisation of the PAM section.

The measured S-parameters are the combined S-parameters of the PAM section, tapered divider and the two test kits. These parameters are post-processed in MATLAB to obtain the S-parameters of the PAM section. Here, the effect of the addition of the test kits on the S-parameters is nullified using their average S-parameters. The RF characterisation of the PAM section aids in confirming the phase shifts obtained by the step phase shifters. Fig. 5.10 reports the phase difference between the two adjacent active waveguides (for example, Upper right and Upper left waveguides) to be ~-90° for all three poloidal sections.

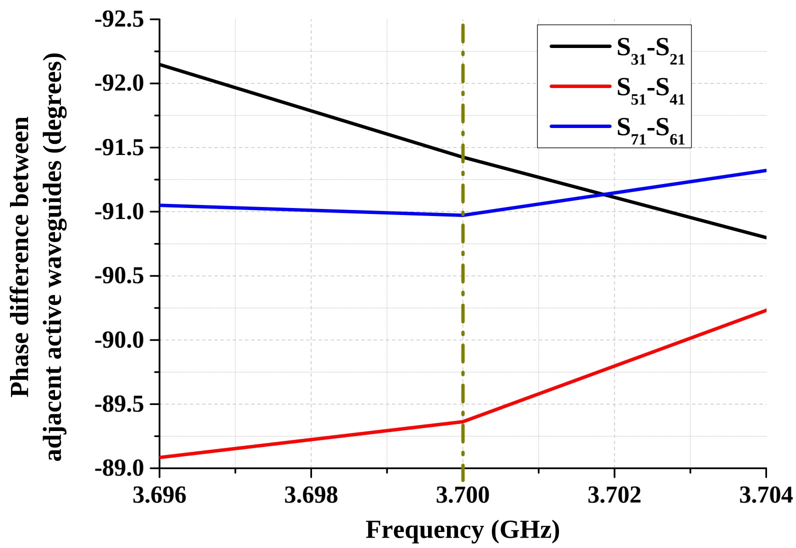

Figure 5.10: Measured phase difference between the two adjacent active waveguides of each of the three poloidal sections.

The return loss obtained at 3.7 GHz is ~33 dB and within the operationally acceptable limit (<-25 dB) as shown in Fig. 5.11. The results obtained for both the toroidal modules are similar and thus, those of only one is reported below.

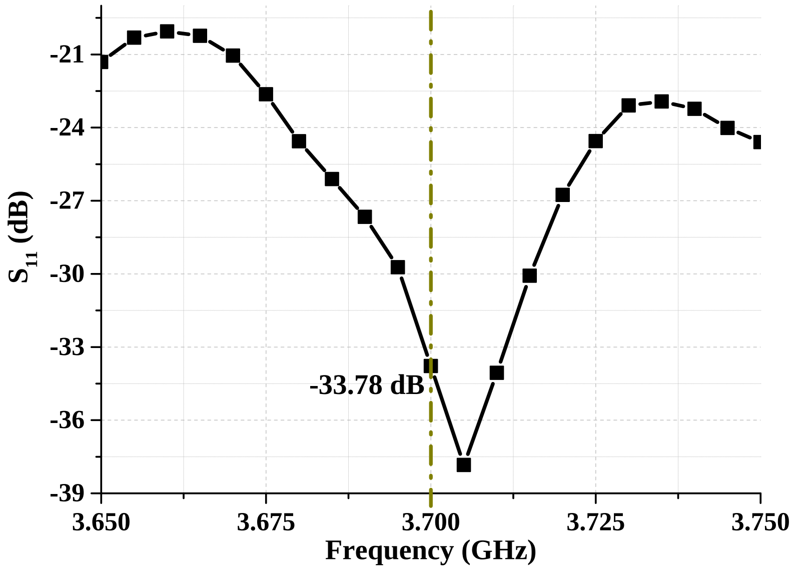

Figure 5.11: Measured frequency response (return loss) of the PAM section.

5.1.3 Complete PAM launcher

The S-parameters of the complete PAM launcher are measured and further compared with the simulation results reported in Chapter 3. The two WR284 rectangular cross-section inputs of the launcher are connected to the VNA using the standard WR284 VNA adapters. The output of the launcher (PAM launcher mouth) is connected to the counterpart followed by the PAM test kit as discussed in Section 5.1.2 and shown in Fig. 5.8. The S-parameters for all the six active waveguides are measured by connecting the VNA adapter to one of the six output arms of the test kit at a time while the others are terminated by low power waveguide absorbers. Fig. 5.12 shows the low power RF measurement setup of the complete PAM launcher. The PAM launcher has two toroidal modules and the RF measurement of each module is done separately. The S-parameters obtained for both the modules are similar and thus, that of only one module (after post-processing in MATLAB) is discussed below.

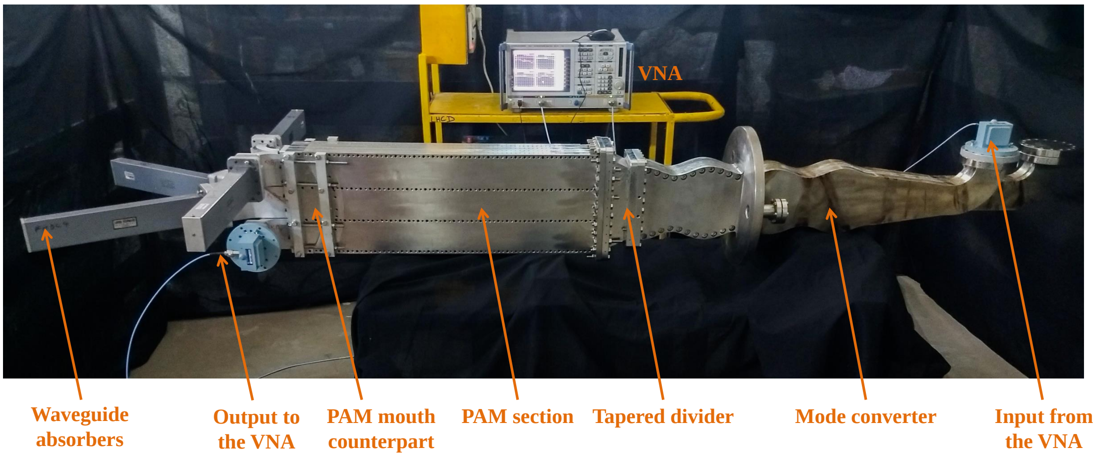

Figure 5.12: Low power test setup of the complete PAM launcher.

The single input of the PAM launcher transmits RF power to the six output active waveguides of a toroidal module equally. It can be observed from Fig. 5.13 that the measured S_{n1} (in dB) for all the output waveguides is ~-8.25 dB (±0.5 dB) at 3.7 GHz, which is in close agreement with the desired result of ~-8.1 dB (see Section 3.7).

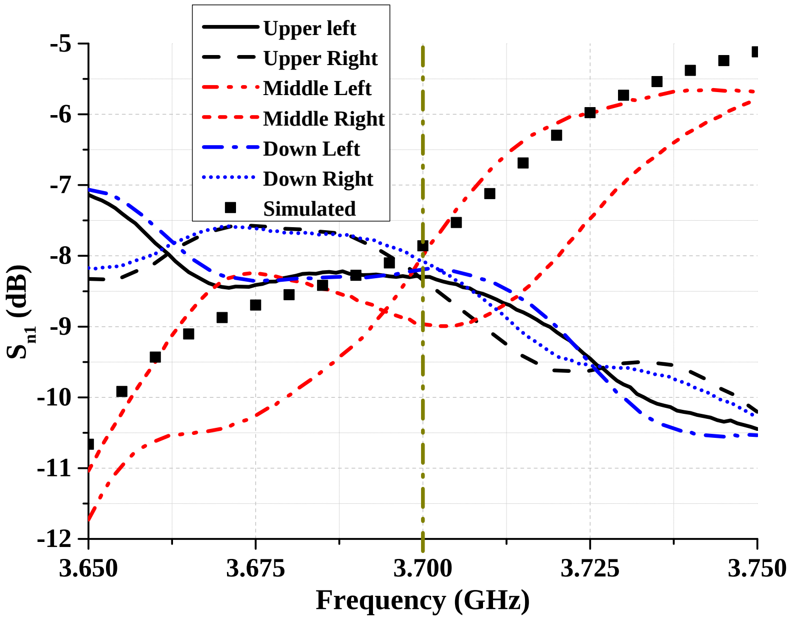

Figure 5.13: Power transmitted (in dB) to the output active waveguides of a single toroidal module.

The measured phase difference between the adjacent active waveguides is ~-88° (~-90° by design) as shown in Fig. 5.14. The mechanical joint between the test kit, counterpart and the launcher is not ideal, thereby resulting in a slightly poor value of S_{n1}.

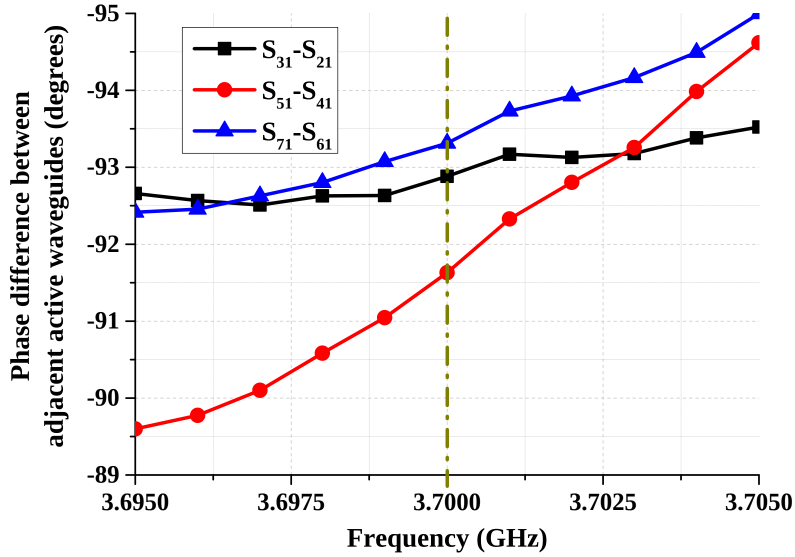

Figure 5.14: Measured phase difference between the adjacent active waveguides of a toroidal module.

The measured and simulated (obtained in Section 3.7) return loss is plotted in Fig. 5.15. The measured return loss is better than 25 dB in the desired bandwidth of ±5 MHz and is ~27.4 dB at the desired centre frequency of 3.7 GHz. The measured results obtained are in close agreement with the simulation results discussed in Chapter 3.

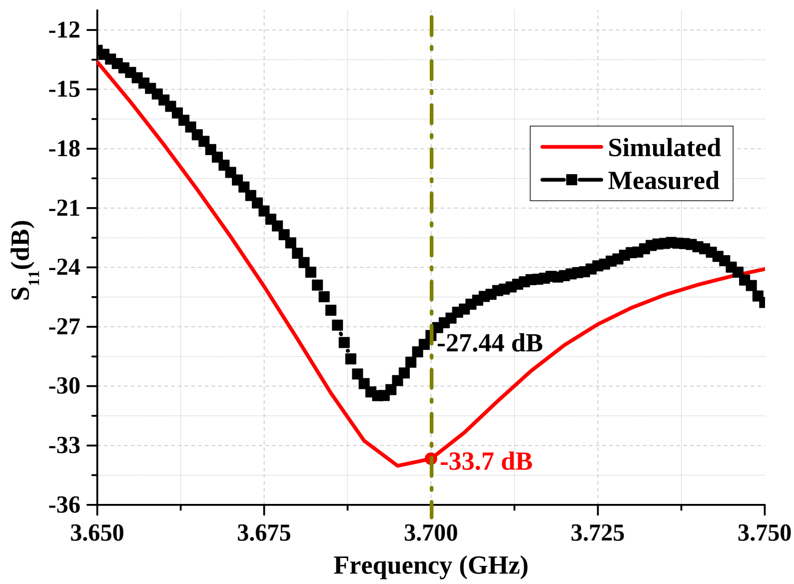

Figure 5.15: Measured and simulated return loss obtained for the complete PAM launcher.

5.2 Profile Measurement

To understand the spectrum launched by the PAM launcher, its configuration, when placed inside the tokamak, should be well understood. The PAM launcher consists of several waveguides stacked together in horizontal as well as in vertical direction. The horizontal direction is almost parallel to the ambient toroidal magnetic field of the tokamak and is often referred to as parallel direction. When these horizontally stacked waveguides are relatively phased (here at 270°), they launch spectrum in the parallel direction with an $N_{||}$ (centred at 2.25), where $N_{||}$ is the refractive index of the launched wave in parallel (or horizontal) direction and hence this nomenclature.

The conventional RF characterisation of the launcher, discussed in Section 5.2, does not reveal about the performance of the launcher in terms of its directivity and the parallel refractive index ($N_{||}$) spectrum of the wave launched by it. The characterisation of lower hybrid wave spectrum, using metamaterial load to mimic plasma, is reported in [116]. A new technique is proposed and developed to evaluate these parameters of the launched wave, in air, at low RF power without installing the launcher onto the tokamak.

In air, the propagation of wave may be defined by,

$$\sim e^{jk_\perp x} \tag{5.1}$$

where,

$k_\perp$ is the propagation vector emanating out of the PAM launcher, often referred to as perpendicular direction.

Further, it is known that,

$$k_\perp = \sqrt{k_0^2 - k_{||}^2} \tag{5.2}$$

Rearranging Eq. 5.2 and substituting $k = \frac{N\omega}{c}$ ($N = 1$, for k_0),

$$k_\perp = \frac{j\omega}{c}\sqrt{N_{||}^2 - 1} \tag{5.3}$$

Thus, the propagation of the wave in perpendicular direction becomes,

$$\sim e^{-\frac{\omega x}{c}\sqrt{N_{||}^2 - 1}} \tag{5.4}$$

It can be observed that the waves become evanescent in the perpendicular direction when it has finite $N_{||}$. For $N_{||} \sim 2.25$ and $\omega = 2\pi \times 3.7 \times 10^9$ rad/s, $k_\perp$ turns out to be ~156.2 rad/m, while the radial characteristic decay scale length is ~6.4 mm [133]. This means that the parallel spectrum may be maintained within this characteristic length. Therefore, the measurement is carried out very close to the PAM launcher mouth at around (1-3) mm to infer the spectrum of the wave launched by the launcher.

This technique helps in evaluating the $N_{||}$ spectrum, 2D power spectrum profile of the waves launched and also demonstrates the steering of the waves (directionality).

5.2.1 Measurement of $N_{||}$ spectrum

In this technique, the RF signal profile is measured at the mouth of the launcher (signal with respect to the distance across the mouth). The spatial Fourier transform of the measured signal transforms the signal into k-space which after post-processing gives the $N_{||}$ spectrum ($N = ck/\omega$) of the launched wave. Fig. 5.16 shows the experimental setup used for the measurement and the corresponding schematic of the setup.

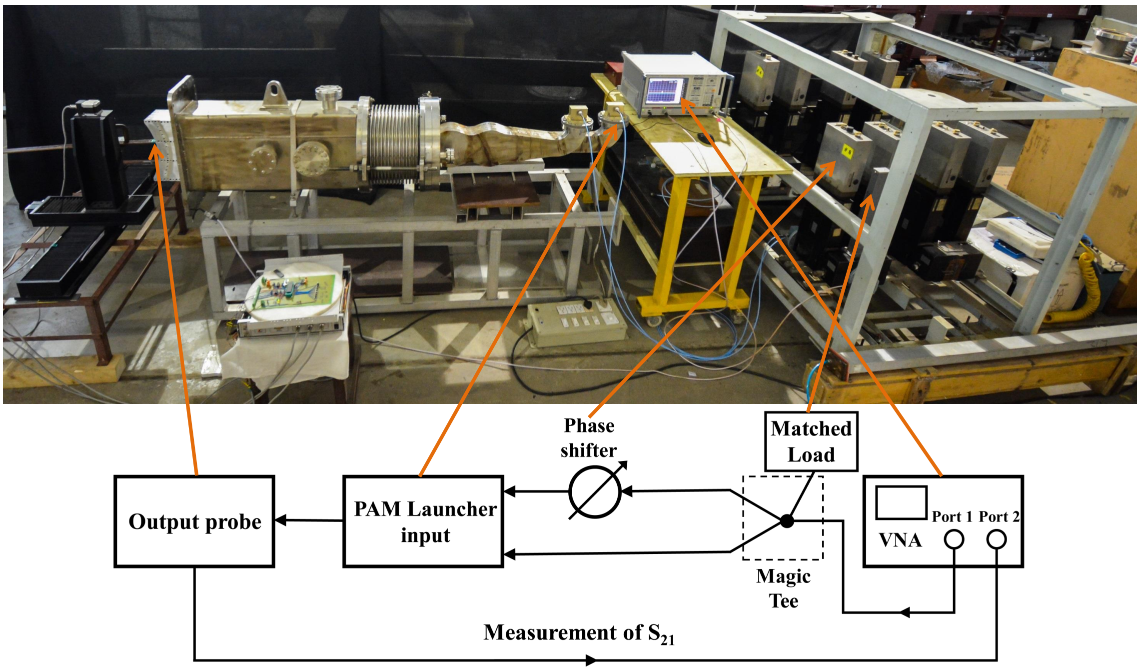

Figure 5.16: Experimental setup used to measure $N_{||}$ spectrum. The schematic of the setup at the bottom helps to identify the components of the setup.

The major components required for the measurement are a VNA, waveguide based phase shifting network and a probe. The probe is a simple coaxial cable with the outer shielding removed at the tip (up to 1 mm) as shown in Fig. 5.17.

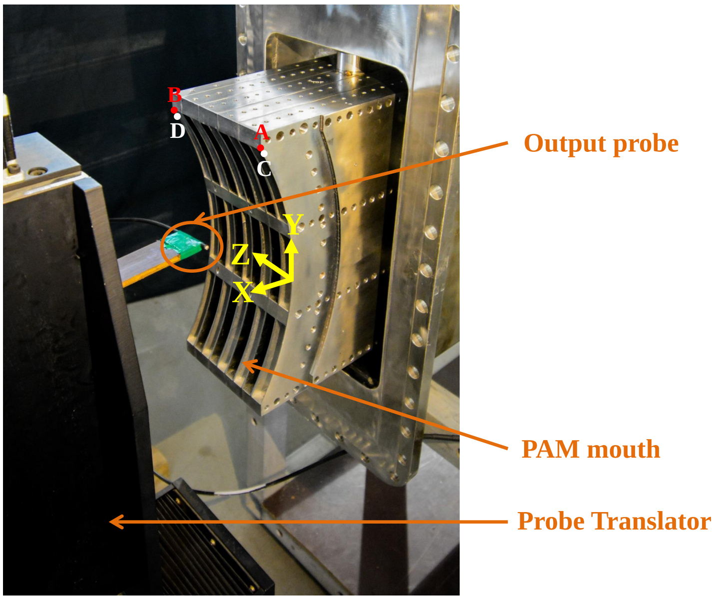

Figure 5.17: Coaxial cable based probe used for the measurement of the E-field at the mouth of the launcher.

The VNA acts as a source as well as a measuring instrument. The N-type input from the VNA (Port 1) is fed to a waveguide based magic tee via a WR284 adapter. The four port magic tee divides the input into two in-phase equal parts. The out of phase arm of the magic tee is terminated by a low power waveguide absorber. Fig. 5.18 shows the magic tee isolated from the complete setup. The two equal parts are fed to a waveguide based phase shifter section wherein the absolute phase of each part can be set manually.

Initially, the two outputs of the phase shifter section are fed to the two ports of the VNA and the phase difference between them is observed. After setting the desired phase difference, the two outputs are disconnected from the VNA and fed to the two inputs of the PAM launcher. Thus, the launcher inputs are excited by RF signals which are equal in magnitude and have the desired phase difference ($\Delta\phi$) between them. The input RF power propagates through the launcher and is launched from the active waveguides at the output. The probe is placed in front of the launcher mouth (almost touching the mouth)

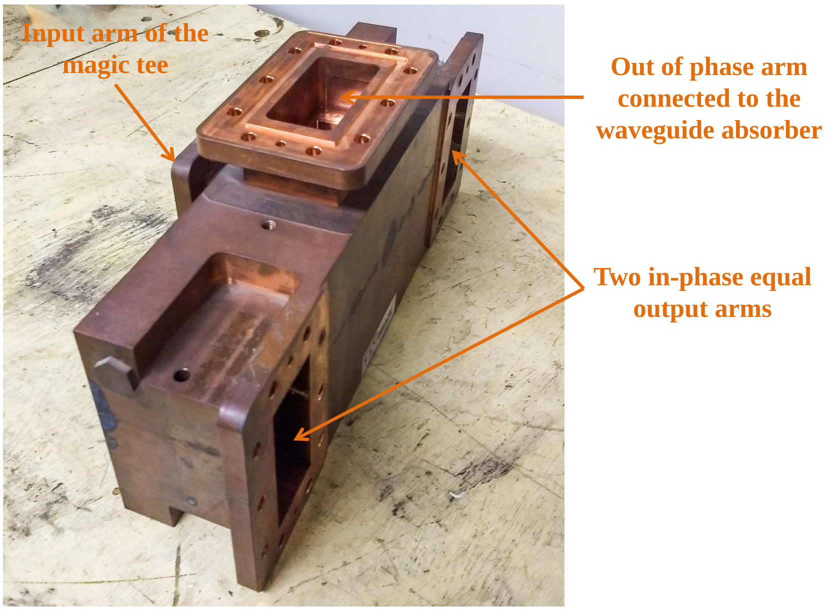

Figure 5.18: Four port waveguide based magic tee.

and the exposed part of the probe is aligned to the dominant E-field of the launched wave as shown in Fig. 5.17. It is moved across the centre of one of the poloidal sections (to obtain the maximum value of the E-field) at the mouth using a translator as shown in Fig. 5.16. The speed of the translator and the number of data points in the VNA are set in such a way that the width of the launcher mouth (127 mm) is scanned with a resolution of 5 μm. The other end of the probe is an N-type connector which is directly connected to the Port 2 of the VNA. The VNA records the real and imaginary part of S_{21} (at each point) which is the power ratio of the output to the input. The measured complex signal is processed in MATLAB to obtain its spatial FFT in k-space. The $N_{\parallel}$ spectrum plot (Power density v/s $N_{\parallel}$) obtained after transforming the FFT result in k-space to $N_{\parallel}$-space, for various external phase difference values (phase difference between the adjacent modules in the toroidal direction, $\Delta\phi$), is shown in Fig. 5.19.

In CST studio, the PAM launcher is modelled such that it launches RF power into an air box at the output. The RF signal across the centre of the waveguides of one of the poloidal sections at the launcher mouth is evaluated. It is then post-processed in MATLAB (as discussed in Section 5.2.1) to obtain the desired $N_{\parallel}$ spectrum as shown in Fig. 5.20.

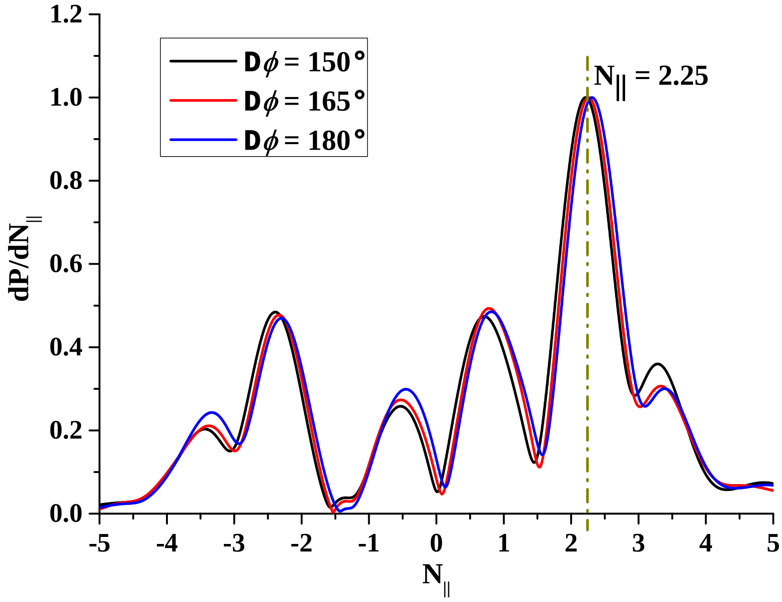

Figure 5.19: $N_{\|}$ spectrum plot obtained from measurements. Main peak $N_{\|}$ value of 2.25 is obtained for an external phase difference ($\Delta\phi$) of 165°.

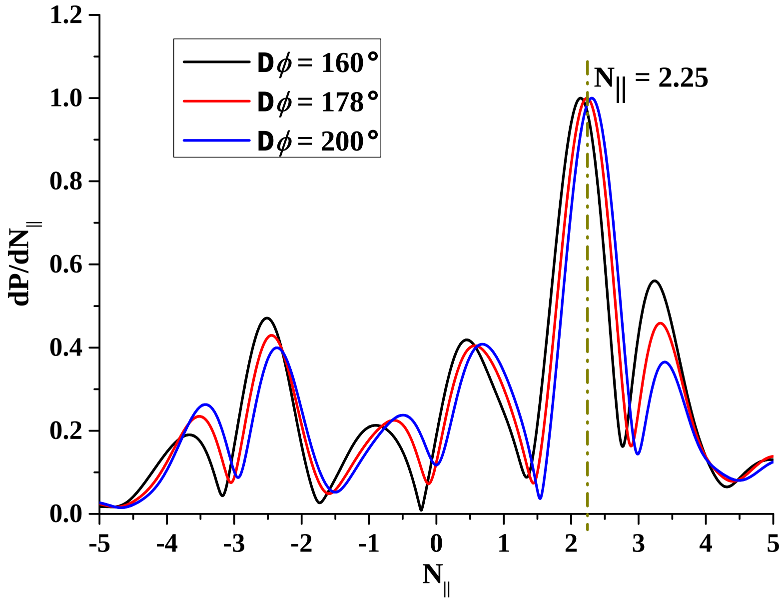

Figure 5.20: $N_{\|}$ spectrum plot obtained from CST studio. Main peak $N_{\|}$ value of 2.25 is obtained for an external phase difference ($\Delta\phi$) of 178°.

Further, the S-parameters obtained from the RF measurements in Section 5.1.3 are fed to the ALOHA coupling code as input. The subsequent $N_{\|}$ spectrum obtained is partially measured (S-parameters) and partially simulated (ALOHA) and is termed as "measured S-parameters-ALOHA" spectrum. Fig. 5.21 reports this $N_{\|}$ spectrum for different values of $\Delta\phi$.

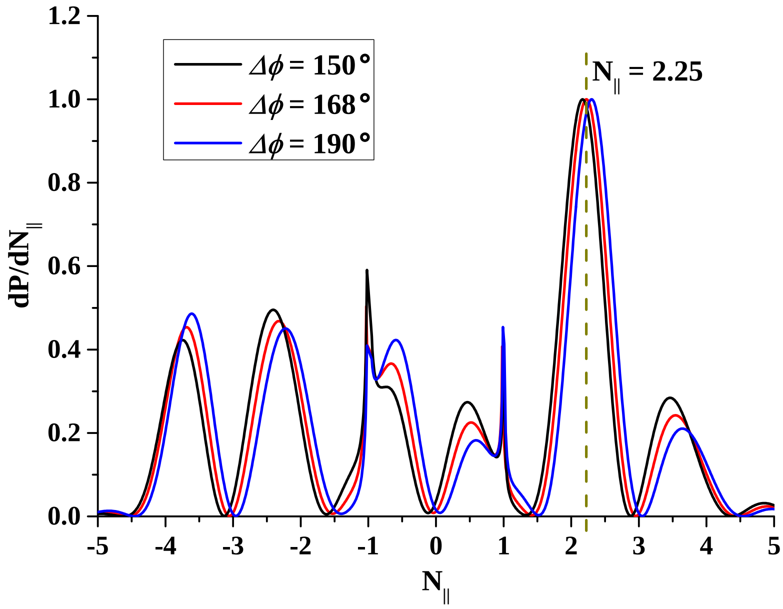

Figure 5.21: $N_{\|}$ spectrum plot obtained from measured S-parameters and ALOHA coupling code. Main peak $N_{\|}$ value of 2.25 is obtained for an external phase difference ($\Delta\phi$) of 168°.

It can be observed that the main peak $N_{\|}$ value of 2.25 is obtained for an external phase difference ($\Delta\phi$) of 165°, 178° and 168° from measurements (Fig. 5.19), CST studio (Fig. 5.20) and measured S-parameters-ALOHA (Fig. 5.21), respectively. The same is obtained for an analytical phase difference of 180° (or 170° from ALOHA simulations) as discussed in Chapter 3. There is a deviation in the required phase difference (to obtain $N_{\|}$ of 2.25) for all the four cases (ALOHA simulations, measurements, CST studio and measured S-parameters-ALOHA) from the analytical phase difference of 180°. This can be attributed to the different (small variation) mediums in which the RF power is launched in all the cases. The RF power is launched in open air surroundings during measurements while the air box used as the medium in CST studio simulations has perfectly matched boundary conditions. The medium modelled for ALOHA simulation has a linear density variation (see Section 3.4).

It can be observed that the value of the required external phase difference ($\Delta\phi$) and the profile of the $N_{\|}$ spectrum obtained from the measured S-parameters-ALOHA and the ALOHA simulation are similar since the medium used in both the cases are same. Also, the measured S-parameters used in the former are in close agreement with the simulated S-parameters used in the latter as discussed in Section 5.1.3.

There are additional minor peaks (side lobes) apart from the main peak in all the cases. The peaks, in the range of $N_{||}$ = -1 to 1, represent the fast waves while directivity of 75% (ideal, 65% obtained from ALOHA simulations) in the desired direction justifies the minor peaks on the negative side (in the opposite direction) of the $N_{||}$ spectrum. Also, the main peak $N_{||}$ value of the spectrum shifts to the right with the increase in the value of $\Delta\phi$ and is true for all the cases. Overall, the $N_{||}$ spectrum obtained in all the cases are in good agreement in terms of the required phase difference and its profile and further builds confidence in the performance of the launcher before installing it on to the tokamak.

The $N_{||}$ spectrum is measured/evaluated for all the three poloidal sections of the launcher. However, the results obtained are similar and are thus not reported here.

5.2.2 Measurement of 2D power spectrum

The measurement technique discussed above is used to obtain the 2D power spectrum at the mouth of the launcher. In this measurement, the probe scans the complete mouth of the PAM launcher and its scan path is explained with respect to Fig. 5.17. The probe is moved from point A to B and the signal received at the mouth during this movement is recorded. The complete path is scanned with a resolution of 5 μm (same as in Section 5.2.1). The probe is now returned back to point A and moved down by 1 mm to point C and the received signal is not recorded during this movement. The signal received by the probe during its movement from point C to point D is recorded, the probe returns back and the procedure continues until the complete mouth is scanned. The received signal is recorded (data is acquired) only when the probe moves in the +Z direction. Thus, a two-dimensional complex matrix of S_{21} in the YZ plane is obtained. A 2D FFT of this matrix is carried out in MATLAB to obtain the 2D power density spectrum in $k_{||}$ and $k_{\perp}$ space which is further transformed to $N_{||}$ and $N_{\perp}$ space. Fig. 5.22 shows the 2D power spectrum obtained from the measurements for an external phase difference ($\Delta\phi$) of 165° (for which the main peak $N_{\|}$ value is 2.25). For the sake of comparison, power spectrum obtained from the ALOHA simulations (for $\Delta\phi$ = 170°) and CST microwave studio (for $\Delta\phi$ = 178°) are shown in Fig. 5.23 and Fig. 5.24, respectively.

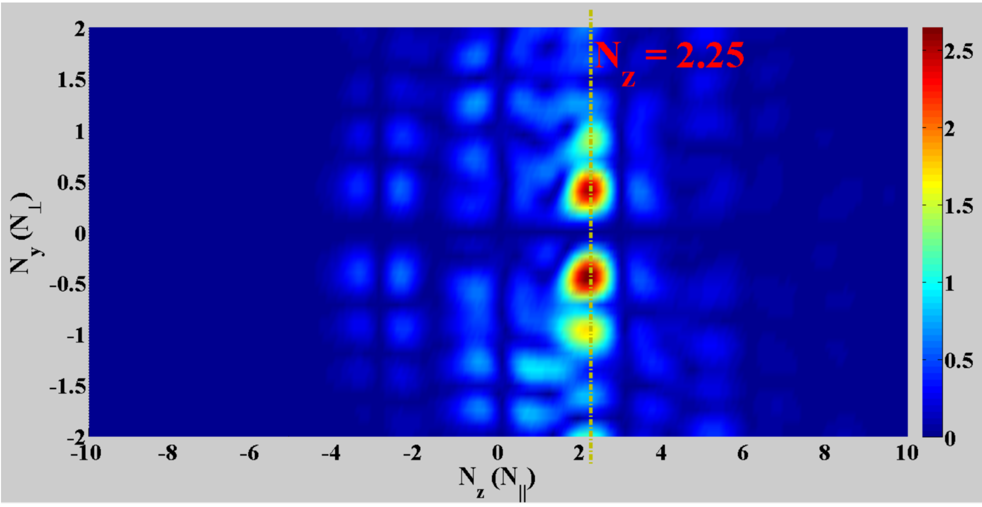

Figure 5.22: 2D power spectrum obtained from measurements.

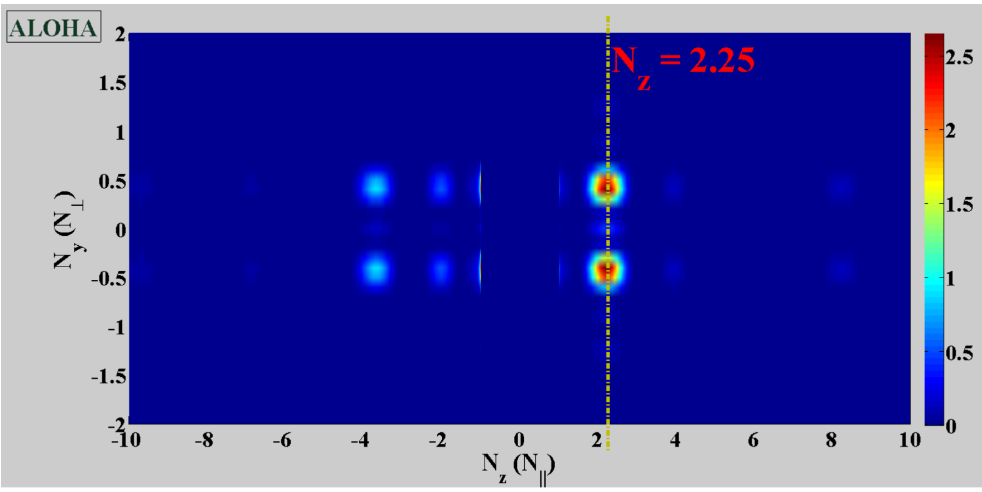

Figure 5.23: 2D power spectrum obtained from ALOHA simulations.

It can be observed that the major lobe is obtained at $N_z(N_{\|})$ = 2.25. The side lobe levels obtained during measurements decay on either side of N_z = 2.25 due to the non-ideal laboratory environment. The side lobe levels obtained are minimum in the case of ALOHA simulations as the medium is modelled to have a linear density variation which aids in the impedance matching of the medium with the launcher mouth. The side lobes are promi-

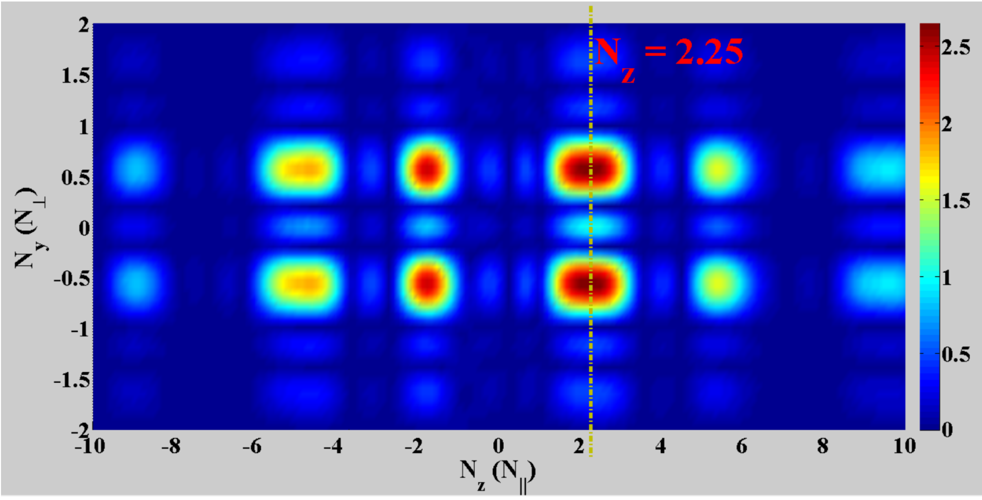

Figure 5.24: 2D power spectrum obtained from CST studio.

nent in CST studio results as the medium is modelled as a uniform air box resulting in an impedance mismatch.

The phase shift between the three poloidal sections is 180° (0°-180°-0°) because of the mode converter section as discussed in Chapter 3. Thus, analytically, this phase shift of 180° coupled with the periodicity of 91 mm (76 mm + 15 mm, the distance between the centres of two waveguides in the adjacent poloidal sections) results into a main peak $N_y(N_\perp)$ value of 0.45 (using the first part of Eq. 3.1). It is to be noted that, since the periodicity and phase shift used here is in the poloidal direction, the $N_\parallel(N_z)$ in Eq. 3.1 changes to $N_\perp(N_y)$. From Fig. 5.22, Fig. 5.23 and Fig. 5.24, it can be observed that the major lobes are obtained at N_y values of $\sim \pm 0.5$ which are in good agreement with the analytical values. Also, it confirms that the phase shift introduced by the mode converter section does not hamper the overall performance of the launcher.

5.2.3 Steering of waves (Directionality)

The relative phase shift between the adjacent active waveguides of the PAM launcher results in steering of the launched waves in the desired direction. The measurement technique discussed above helps in observing this phenomenon. The co-axial probe is moved across the centre of the output waveguides of one of the poloidal sections in +Z direction (same as in Section 5.2.1, see Fig. 5.17), thereby completing one set of reading. It is to be noted that, here, the probe is moved across the full range of translator (in the +Z direction, see Fig. 5.17) instead of just the width of the launcher mouth. The probe is then moved back to its starting position and also away from the launcher in the +X direction by 1 mm and the measurement is repeated in the +Z direction. The procedure continues until the full range of the translator in the +X direction is scanned. Thus, the data obtained form a 2D plane (XZ plane) when observed from the top. The real part of the S_{21} obtained is plotted with respect to the launcher position as shown in Fig. 5.25.

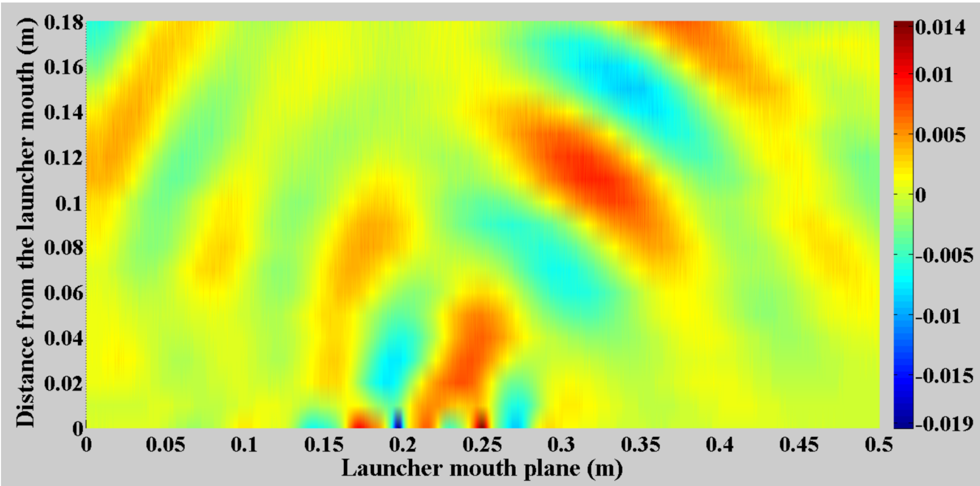

Figure 5.25: Measured S_{21} plot illustrating the steering of the waves in the desired direction.

Here, the launcher is placed on the x-axis from 0.14 m to 0.26 m. Also, the waves are scanned up to 180 mm in +X-direction away from the launcher mouth as shown on the y-axis. It can be observed that the power is steered to the right, thereby imparting momentum to the electrons in the anticlockwise direction. The plasma current would thus be driven in the opposite direction (clockwise) as desired.

5.3 Summary

This chapter presented the results obtained after carrying out measurements on the PAM launcher. The measurement results closely matched the ones obtained via simulations, indicating the correctness of the design. A new method to obtain the various parameters of the wave launched from the launcher was also proposed. Evaluation of these results indicated that the proposed launcher was functioning as desired, thus validating the design. However, the installation of this launcher onto the machine requires an RF window to be added at its input. This is because the RF lines feeding the launcher are pressurised while the launcher is in tokamak vacuum. The next chapter presents the design, fabrication and low and high power results of this RF window.

Chapter 6

RF Vacuum Window: Design, Development and Testing

As discussed in the previous chapter, the PAM launcher would be under tokamak UHV conditions. However, the transmission lines feeding RF power to the PAM launcher would be pressurised up to 3 bars (with dry nitrogen gas) to avoid RF breakdown during transmission. Thus, an RF vacuum window is required to mechanically isolate the UHV vacuum and the pressurised sections. Further, it should be transparent to microwaves, which implies that a low insertion loss (<0.1 dB) and high return loss (>35 dB) is needed. Since the window will handle a large amount of RF power (~125 kW) for duration up to 1 s, efficient thermal management would also be required. The RF windows with these specifications (125 kW at 3.7 GHz for 1 s) pose technical challenges and are not commercially available easily. Further, existing methods to develop a window warrant the use of multiple brazing cycles to fabricate it which increases the development cost and complexity. Hence, it is decided to undertake studies on the design and development of the RF vacuum window.

This chapter presents a novel design of a pill box type RF window. The novelty of the designed window is that it requires only one brazing cycle to be fabricated on account of improvements proposed in the mechanical design of the window without affecting its RF performance. The material selection, particularly in terms of loss tangent, dielectric constant and thermal conductivity, is carried out on the basis of its RF, thermal and mechanical performance. The RF and mechanical design, fabrication techniques and qualification tests determine the performance of the window at high power levels and thus, precise identification of the same is extremely important and challenging. Finally, the performance of the high power RF window is evaluated both at low and high power levels.

6.1 RF design and multiphysics analysis

6.1.1 Specifications and basic design

It is desired to design a pill box type RF vacuum window at a frequency of 3.7 GHz with major specifications outlined in Table 6.1.

Table 6.1: Desired specifications of the pill box type RF window.

Property	**Value**
Frequency and Bandwidth	3.7 GHz ± 10 MHz
Input RF power	125 kW, Up to 1 s
Return loss	>35 dB
Insertion loss	<0.1 dB
Input and Output port	WR284
Differential pressure	3 bars
UHV compatibility	Leak rate $< 5 \times 10^{-9}$ mbarl/s

A typical pill box type RF vacuum window consists of a low loss tangent dielectric disc of appropriate thickness as shown in Fig. 6.1. The input port of the window is connected to the pressurised transmission line while the output port serves as an input to the PAM launcher. These ports are standard WR284 rectangular waveguide ports. The window has four discontinuities along its length from the input to the output. The first discontinuity is the rectangular (input) to circular waveguide conversion. The diameter of the circular waveguide is chosen to be equal to the diagonal of the input rectangular waveguide. The mechanical isolation between the pressurised and UHV sides of the circular waveguide is provided by a ceramic disc. The transitions from the pressurised side of the circular waveguide to the ceramic disc and that from the ceramic disc to the UHV side of the circular waveguide are the second and third discontinuities, respectively. The circular to rectangular waveguide transition at the output is the fourth discontinuity in the structure.

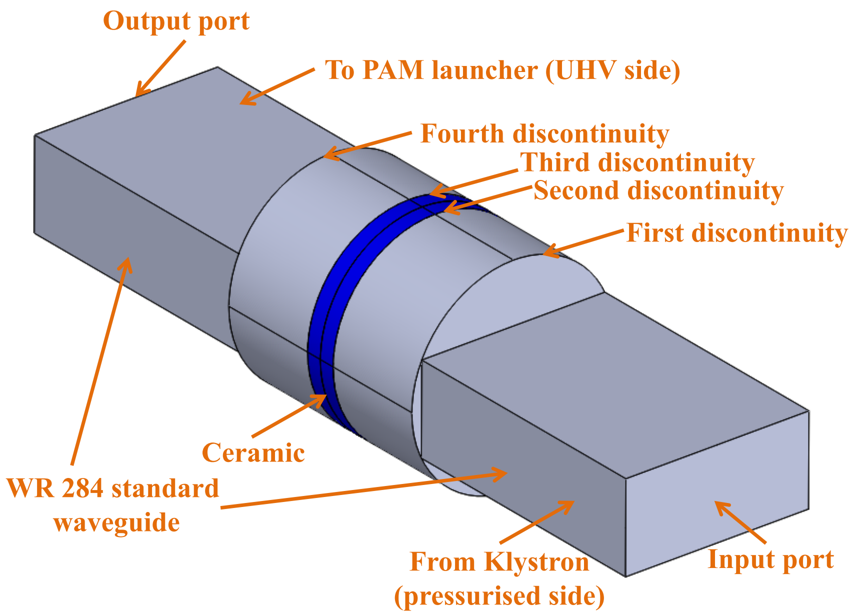

Figure 6.1: 3D structure of a pill box type RF vacuum window.

The design parameters of the window, such as the length of the circular section, thickness and position of the ceramic disc and the choice of material, govern the RF performance of the window. Generally, the impedance ($Z(l)$) of a lossless transmission line structure (here, RF window), having a characteristic impedance of Z_0, at a distance 'l' from the reference impedance Z_L is given by,

$$Z(l) = Z_0 \frac{Z_L + jZ_0 \tan \beta l}{Z_0 + jZ_L \tan \beta l} \tag{6.1}$$

where,

β is the phase constant (rad/m) and is given by ($2\pi/\lambda_g$).

For $l = \lambda_g/2$ (half of the guided wavelength), $\tan\beta l = 0$ and Eq. 6.1 becomes,

$$Z(l) = Z_L \tag{6.2}$$

This implies that the impedance on a transmission line repeats itself after a distance of $\lambda_g/2$. Thus, a ceramic disc having a thickness of $\lambda_g/2$ can be introduced in the window for mechanical isolation without affecting the overall RF impedance matching of it. However, this thickness needs to be further optimised by small values due to the presence of multiple modes in the ceramic. This argument is also true for the circular waveguide section. Thus, the length of the circular section without the ceramic and the thickness of the ceramic is typically half of their guided wavelengths ($L = \lambda_g/2$) for circular TE_{11} mode [109, 110, 132, 134] as shown in Fig. 6.2. The dielectric constant of the ceramic governs the guided wavelength in it and thereby determines the value of its thickness. For the circular waveguide section, the dielectric constant is 1 (vacuum or pressurised side). The symmetry of the overall structure is maintained by placing the ceramic at the centre of the circular waveguide.

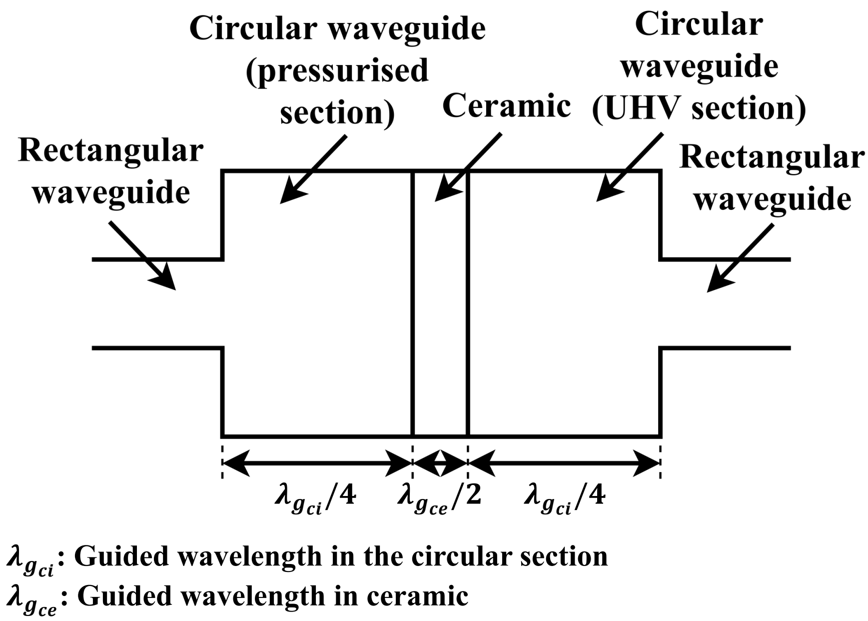

Figure 6.2: Schematic illustrating the typical dimensions and the ceramic placement in the window.

6.1.2 Choice of the material

A detailed analysis is carried for the choice of the ceramic material. The RF and thermal performance of the window is studied for three ceramic materials, namely, Beryllium Oxide (BeO), Aluminium Nitride (AlN) and Alumina (Al_2O_3). The properties of all the three materials under consideration are reported in Table 6.2.

Table 6.2: Properties of the three ceramic materials under study.

Property	**BeO**	**AlN**	**Al_2O_3**
Dielectric constant (ε_r)	7	9	9.7
Loss tangent ($\tan\delta$)	3×10^{-5}	1×10^{-3}	3×10^{-4}
Density (ρ) (kg/m^3)	2850	3300	3800
Specific heat capacity at constant pressure (C_p) (J/kgK)	1050	820	800
Thermal conductivity (k) (W/mK)	285	175	30
Coefficient of thermal expansion (μ) (/K)	9×10^{-6}	4.6×10^{-6}	8×10^{-6}
Young's modulus (Y) (GPa)	345	325	370
Poisson's ratio (ν)	0.26	0.22	0.22

The power dissipated in ceramic, P_{loss} (in Watts), for an input power of P_{in} can be evaluated as,

$$P_{loss} = P_{in}\frac{2\pi\sqrt{\varepsilon_r}\tan\delta L}{\lambda_{g_{ce}}} \tag{6.3}$$

where,

ε_r is the dielectric constant of the ceramic.

$\tan\delta$ is the loss tangent.

L is the length (thickness) of the ceramic (m).

$\lambda_{g_{ce}}$ is the guided wavelength of the ceramic (m).

As discussed in section 6.1.1, the thickness of the ceramic (L) is taken as $\lambda_g/2$. Using the values of the dielectric constant and loss tangent given in Table 6.2, the power dissipated in the ceramic materials is evaluated and reported in Table 6.3.

The average temperature rise (ΔT) of the ceramic (for 1 s of operation) due to the power dissipated in it is evaluated using Eq. 6.4,

$$\Delta T = \frac{P_{loss}}{\rho C_p V} \tag{6.4}$$

Table 6.3 reports the analytical values of the power dissipated and average temperature rise in the three ceramic materials, evaluated using Eq. 6.3 and Eq. 6.4, respectively.

Table 6.3: Analytical values of the power dissipated and average temperature rise in the three ceramic materials.

Material	**Power dissipated**	**Average temperature rise**
Al_2O_3	366.92 W	1.852°C
AlN	1178 W	6.433°C
BeO	31.17 W	0.135°C

It can be observed from Table 6.3, that the power dissipated and average temperature rise in AlN are maximum for 1 s of operation. Thus, AlN is further not considered in the designing of the RF window (without cooling). It is worth noting that AlN has a better thermal conductivity (see Table 6.2) as compared to that of Al_2O_3 and thus could be preferred for RF windows designed for CW operations (with cooling). BeO has the minimum power dissipation and average temperature rise values and thus can be preferred over Al_2O_3. However, the difference between the average temperature rise for Al_2O_3 and BeO is not significant for 1 s of operation. Also, Al_2O_3 is cheaper and easily available commercially as compared to BeO. Thus, Al_2O_3 is preferred in the design of the RF window discussed below.

6.1.3 Dimensions

For an alumina based RF window, the length of the circular section (without the alumina disc) and the thickness of the alumina disc turn out to be 50.48 mm and 13.04 mm, respectively (half of their guided wavelengths). The diameter of the alumina disc is equal to the diagonal of the rectangular waveguide that is 79.77 mm. The alumina disc available commercially had a thickness of 12.6 mm. Thus, the length of the circular section is required to be optimised in COMSOL Multiphysics to obtain the best RF impedance matching. A parametric scan of the length of the circular section is performed and the corresponding values of return loss (S_{11}) and insertion loss (S_{21}) obtained are plotted in Fig. 6.3. It can be observed that the best impedance matching is obtained for a circular section length of 81.9 mm. This length incorporates the thickness of the alumina disc as well.

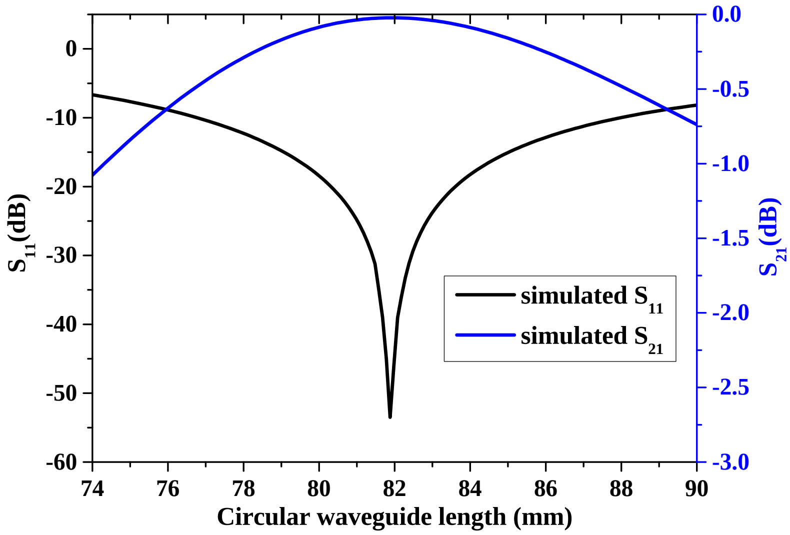

Figure 6.3: Change in the S-parameters of an alumina based RF window for varying length of the circular section (including the ceramic thickness of 12.6 mm).

6.1.4 Multiphysics analysis

The RF performance, RF breakdown, thermal and stress analysis constitute the Multiphysics analysis of the RF window. It is to be noted that even though the analyses are carried out for the complete window structure, plots reported henceforth are for specific components to highlight them. The RF performance of the window, in terms of E-field profile and RF losses, is evaluated using the RF module of COMSOL Multiphysics. The impedance boundary condition feature in COMSOL is used to resolve the skin depth in the metallic waveguide walls. A tetrahedral mesh size of $\lambda_g/10$ is used, where, λ_g is the guided wavelength in the respective material (here copper). An excitation of 125 kW of RF power in TE_{10} mode is applied at the input of the window. Fig. 6.4 illustrates the resultant peak electric field of 224 kV/m obtained on the alumina disc. The window provides a return loss of ~54 dB and an insertion loss of ~0.02 dB at the centre frequency of 3.7 GHz. The bandwidth (return loss > 25 dB) of the window is 20 MHz.

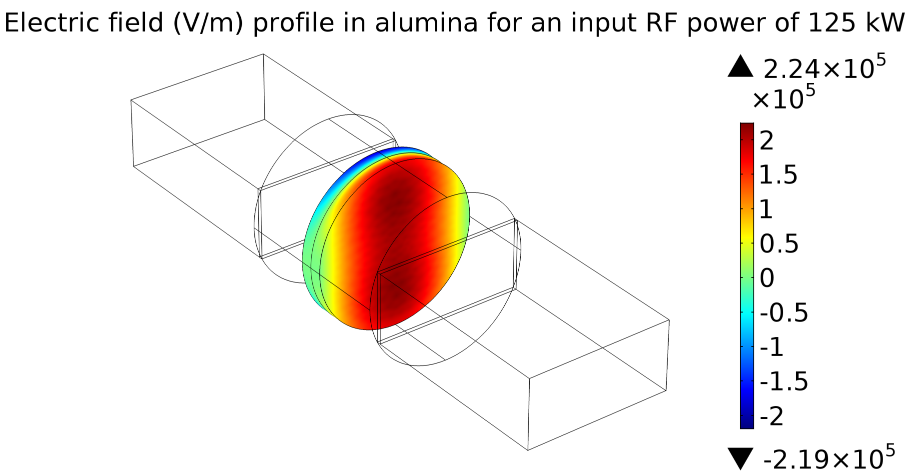

Figure 6.4: E-field (V/m) profile in alumina of the window for an input power of 125 kW.

The propagation of RF power through the window result in a surface loss of ~180 W in the waveguide metal walls and a volumetric power loss of ~450 W in the alumina disc as evaluated in COMSOL. The volumetric power loss obtained is in good agreement with the analytical value reported in Table 6.3.

The UHV environment on one side of the RF window and high E-fields in the alumina disc warrants the need for a multipaction analysis and evaluate the possibility of RF breakdown of the window for an input power of 125 kW and 150 kW. The Particle in Cell (PIC) solver of CST studio is used to evaluate the secondary electron growth in the window in response to the E-field. The window is modelled using an averaged version of Furman's Secondary Electron Yield (SEY) model. Fig. 6.5 shows the temporal evolution of secondary electrons in the RF window for an input RF power of 125 kW and 150 kW. The number of secondary electrons decreases with time indicating no electron avalanche. Thus, the window can be safely operated at the rated input RF power of 125 kW.

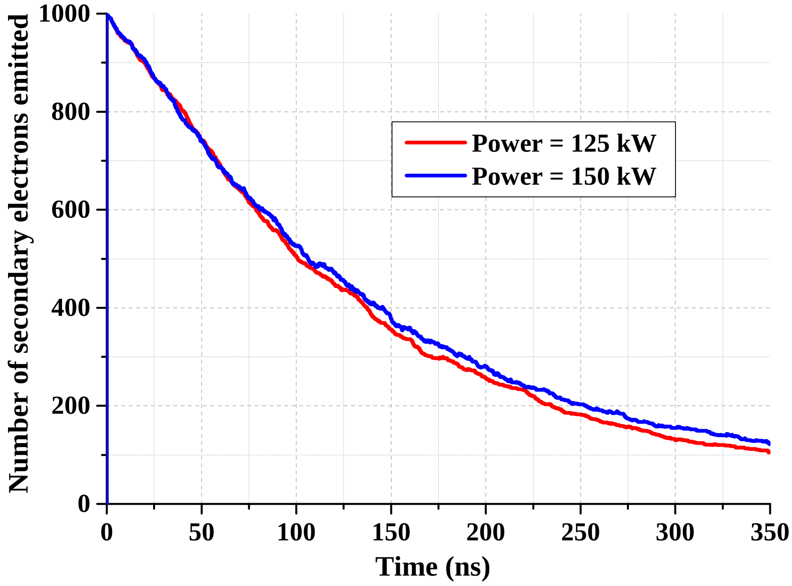

Figure 6.5: Number of secondary electrons emitted with time in the RF window for an input power of 125 kW and 150 kW.

The Heat Transfer module of COMSOL Multiphysics is used to evaluate the temperature profile in the RF window. The volumetric power loss and surface losses obtained earlier act as the input RF load and are coupled to the Heat Transfer module. The heat flux node is used to model the convection between the outer metallic surface of the waveguide and atmosphere. The peak temperature rise in the alumina disc, after 1 s of excitation, is 5.4°C and that in the waveguide structure is 1.6°C as shown in Fig. 6.6 and Fig. 6.7, respectively. A room temperature of 20°C is assumed during simulations.

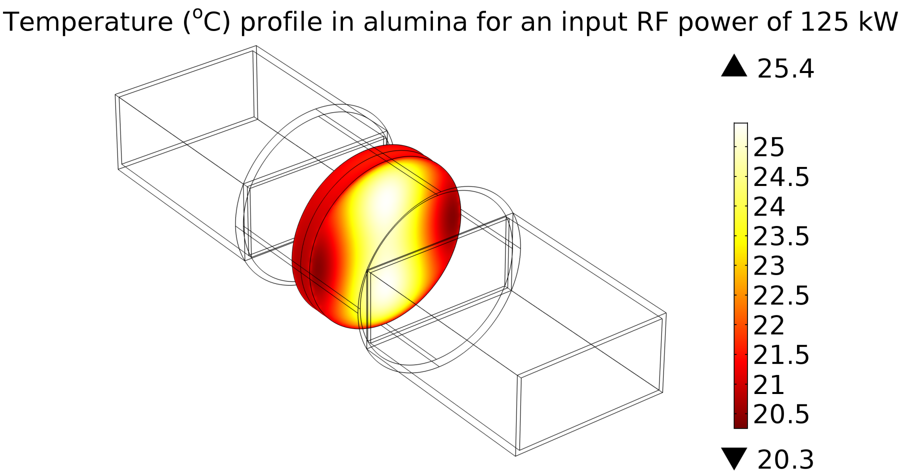

Figure 6.6: Temperature (°C) profile in the alumina disc for an input power of 125 kW.

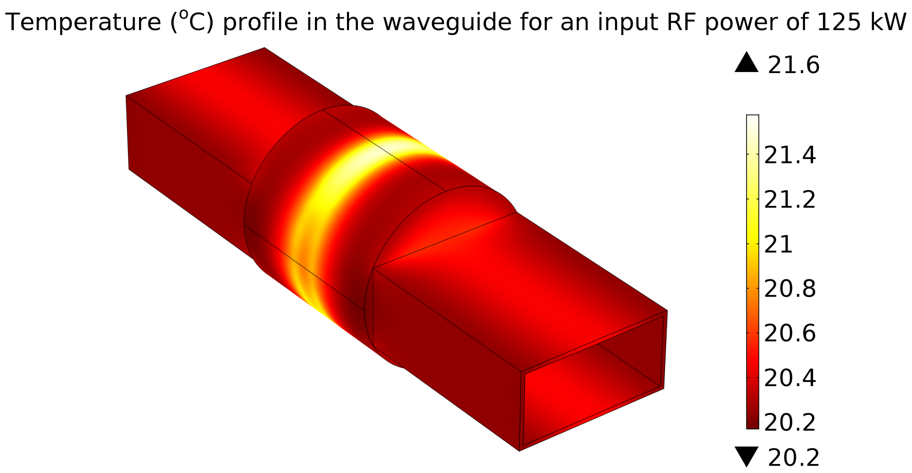

Figure 6.7: Temperature (°C) profile in the waveguide for an input power of 125 kW.

The window would be connected at the input of the PAM launcher which would launch RF power into the tokamak periodically. Thus, the RF window would be subjected to a number of 125 kW, 1 s pulses. It is important to know the duration after which the window can be operated again after one experimental pulse. Thus, the thermal analysis is carried out for a longer duration to evaluate the time required by the window to return to room temperature or reach a safe, steady-state temperature. The window is excited for 1 s and later it is subjected to convection. Fig. 6.8 depicts the peak temperature of the window versus time. There is a rise in the temperature of the window until 1 s and subsequently, the temperature starts decreasing once the RF power is switched OFF. Further, the peak temperature of the window returns back to a steady-state temperature after 30 seconds. Thus, the window can be operated again after 30 seconds of no excitation.

The two main sources of stress in the window are thermal load and the 3 bars of differential pressure across the alumina disc during operations. The Solid Mechanics module in COMSOL Multiphysics evaluates the thermal stress generated in the window due to the thermal load obtained from the Heat Transfer module. Meanwhile, the Boundary Load node is used to mimic the differential pressure across the alumina disc. The rectangular cross-sectional input and output of the window and the periphery of the alumina disc is subjected to a Fixed boundary condition. It is to be noted that First Principal stress is evaluated for brittle materials like alumina, while von Mises stress is evaluated for ductile

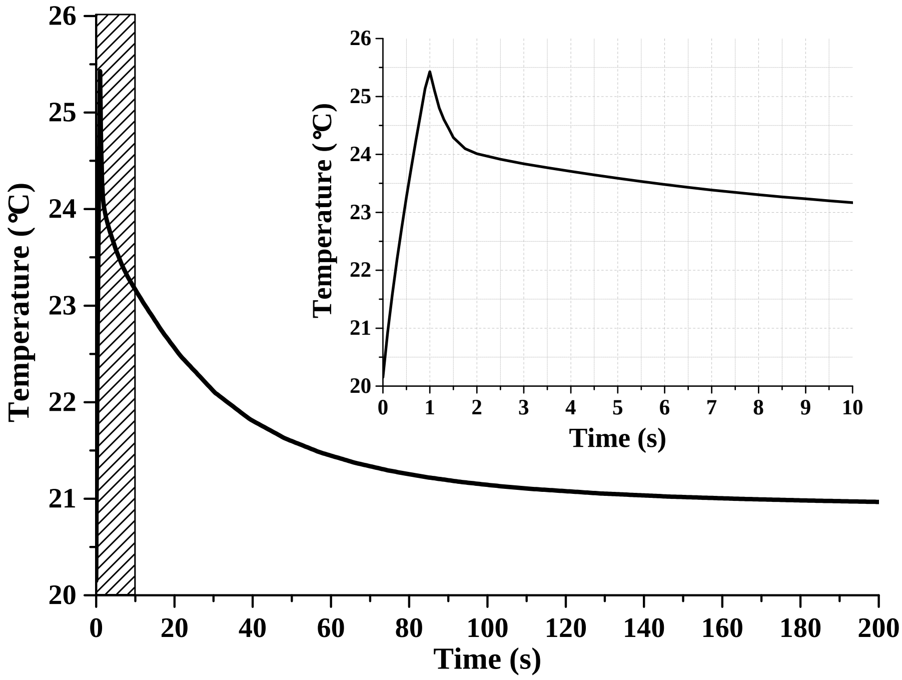

Figure 6.8: Peak temperature of the window with respect to time for 1 s of RF excitation followed by convection cooling. The inset figure is the zoomed-in version of the shaded region of the main figure. It illustrates the trend of the rise and fall in the temperature of the window.

materials like steel. The peak value of the First principal stress generated in the alumina disc due to these sources is ~13 MPa as shown in Fig. 6.9. This value is less than $(1/10)^{th}$ of the ultimate tensile strength of alumina that is 300 MPa. The deformation in the window due to this stress is ~0.83 μm as shown in Fig. 6.10. It is to be noted that the peak value of the von Mises stress generated in the metallic walls of the waveguide due to thermal load is ~12.3 MPa, which is much lower than the ultimate tensile strength of copper (210 MPa). The peak deformation generated in the waveguide is ~1.25 μm.

The peak value of the stress generated in the complete window structure suggests that it would operate in the elastic regime of the stress-strain curve thereby avoiding any permanent deformation. Further, the deformation generated is lower than the fabrication tolerance of 50 μm and thus would not affect the RF performance of the window.

The Multiphysics analysis confirms that the window does not require any cooling arrangements during high power operations.

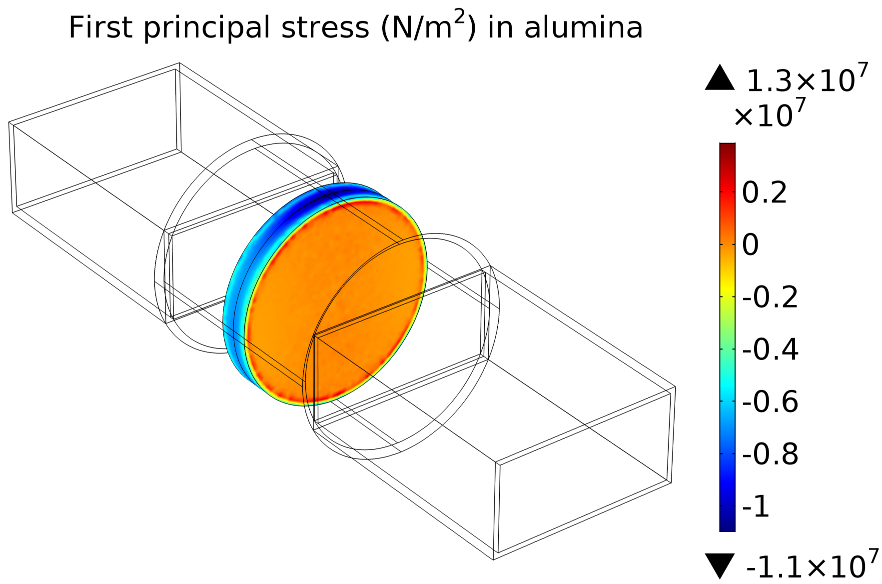

Figure 6.9: First principal stress (N/m^2) in the alumina disc due to thermal load and 3 bars of differential pressure.

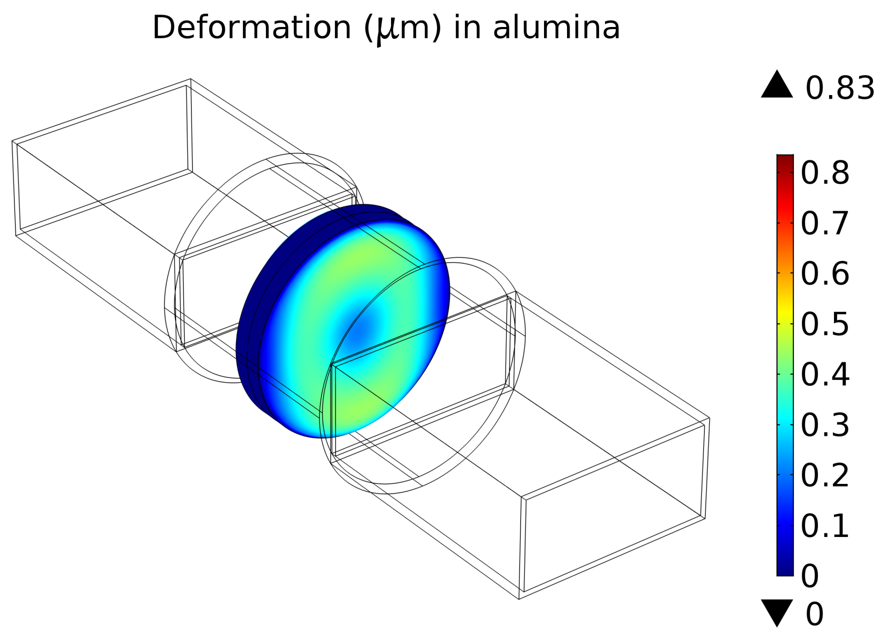

Figure 6.10: Deformation (μm) generated in the alumina disc.

6.2 Design, fabrication and cold test of the mock-up RF window

The RF performance of the basic design of the alumina based window is characterised using a mock-up window. This is done to build confidence in the design and further develop the actual prototype. The mock-up window is developed using an alumina disc, aluminium cylinder, copper rings and two aluminium flanges with standard WR284 slots. The aluminium cylinder is heated uniformly up to 80°C to allow its expansion radially. The inner diameter of the cylindrical structure is the same as the diameter of the ceramic disc that is 79.8 mm while its length is 77.2 mm. Since the coefficient of thermal expansion of aluminium (about 25 μm/m°C) is greater than that of the alumina (about 8 μm/m°C), the alumina disc can be push fitted inside the cylinder (at 80°C). The ceramic is prevented from moving further inside and held at the centre of the aluminium cylinder by a cylindrical SS block used as a stand at the bottom. The length of the circular waveguide section is varied by using thin copper rings of different thicknesses (0.1 mm, 0.2 mm, 0.5 mm and 1 mm). The circular to rectangular waveguide conversion at the input and output of the window is achieved by using flanges with rectangular WR284 slots. Fig. 6.11a, 6.11b and 6.11c show the aluminium cylinder with the alumina push-fitted at the centre of it, thin copper rings of different thicknesses and the rectangular slot flanges, respectively. The complete assembly of the mock-up window is shown in Fig. 6.12.

The cold test of the mock-up window is performed to measure its S-parameters using a Vector Network Analyser (VNA) as shown in Fig. 6.13.

Initially, the aluminium cylinder with alumina disc is connected to the rectangular slot flanges directly. The frequency response of the mock-up window, having a circular waveguide length of 77.2 mm, is not centred at the desired frequency of 3.7 GHz. The minimum of S_{11} is at a frequency higher than 3.7 GHz. The gradual and symmetrical addition of circular copper rings of different thicknesses on either side increases the overall length of the circular section. The frequency response of the mock-up window for different lengths of the circular waveguide section is reported in Fig. 6.14. It can be observed that the minimum of S_{11} shifts towards the left as the length of the circular waveguide increases and is at 3.7 GHz for a length of 81.6 mm.

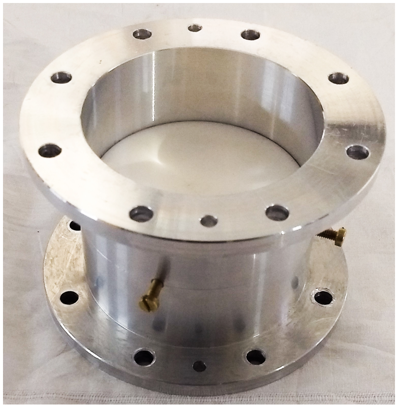

(a)

(b)

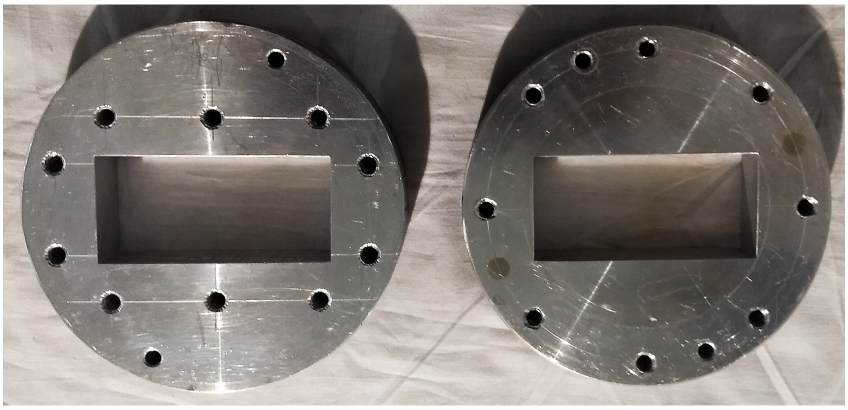

(c)

Figure 6.11: Components of the mock-up window, (a) Alumina push-fitted at the centre of the aluminium cylinder, (b) Thin copper rings of different thicknesses, (c) Flanges with rectangular slots.

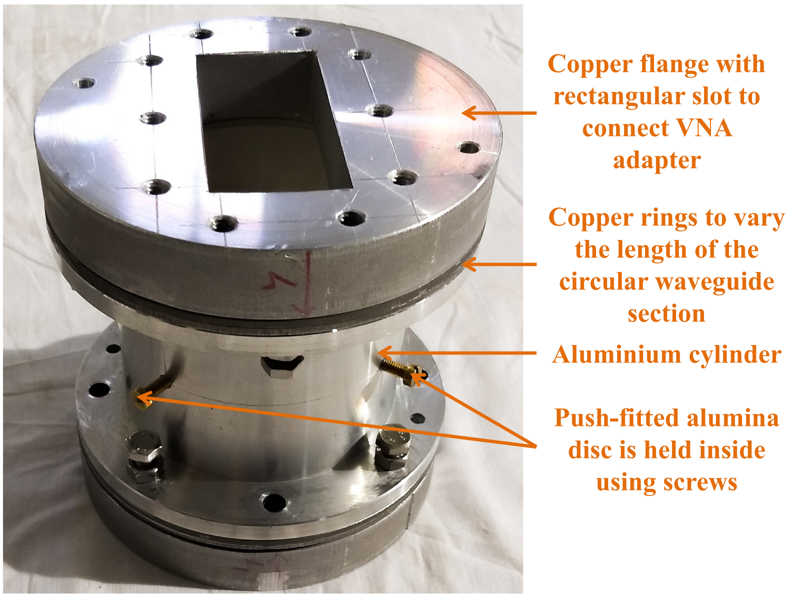

Figure 6.12: Complete assembly of the mock-up RF window.

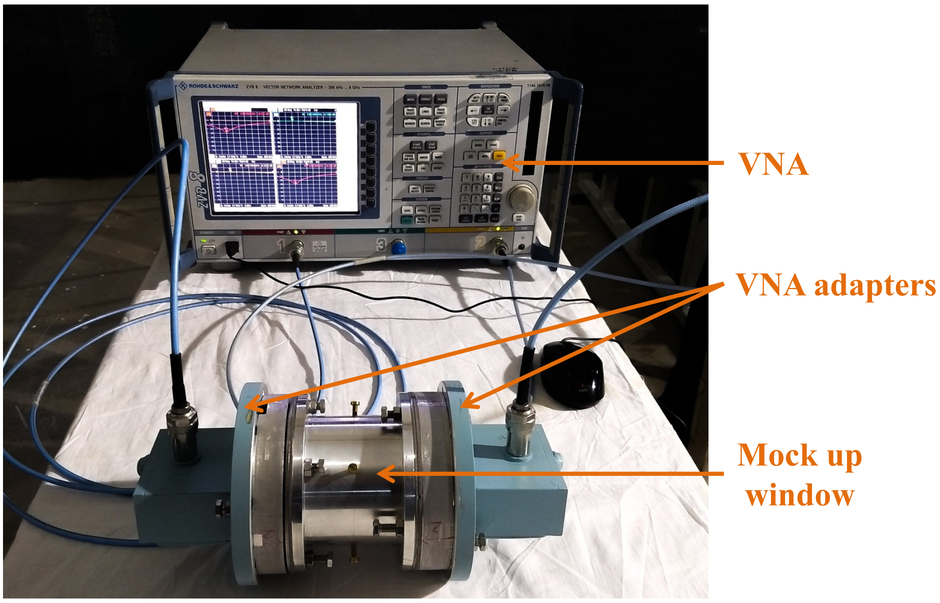

Figure 6.13: VNA characterisation of the mock-up window.

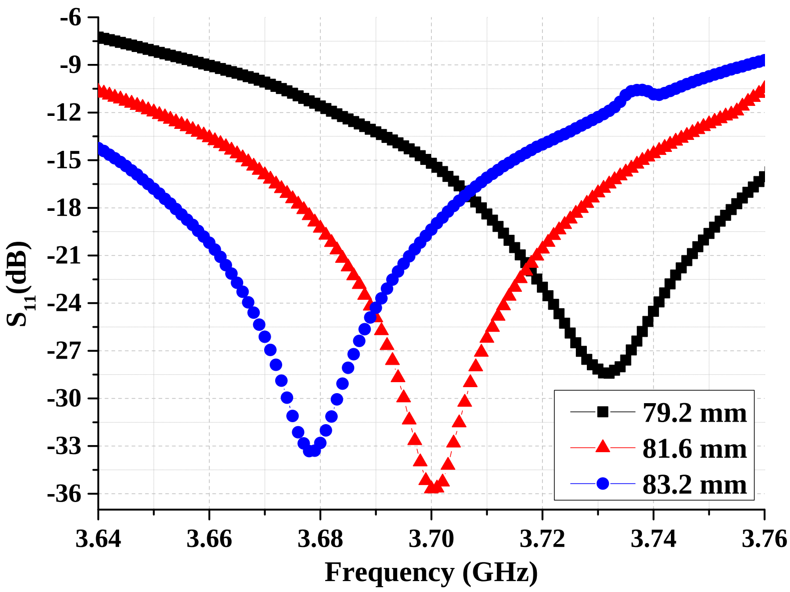

Figure 6.14: Frequency response of the mock-up window for different circular waveguide lengths.

The simulation and the mock-up measurement results are further compared based on their RF impedance matching and frequency response. The change in the S-parameters of the simulated design and the mock-up window, for varying lengths of the circular waveguide, is depicted in Fig. 6.15. The simulated design provides the best impedance matching for a circular waveguide length of 81.9 mm, while the mock-up window yields the best result for 81.6 mm.

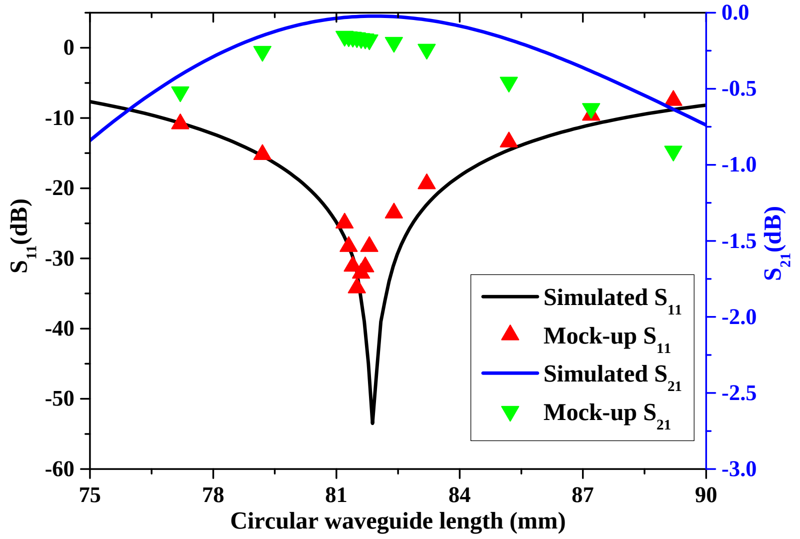

Figure 6.15: S-parameters of the simulated design and mock-up window for varying lengths of the circular waveguide section.

Fig. 6.16 shows the frequency response of the simulated design and the mock-up window for a circular waveguide length of 81.9 mm.

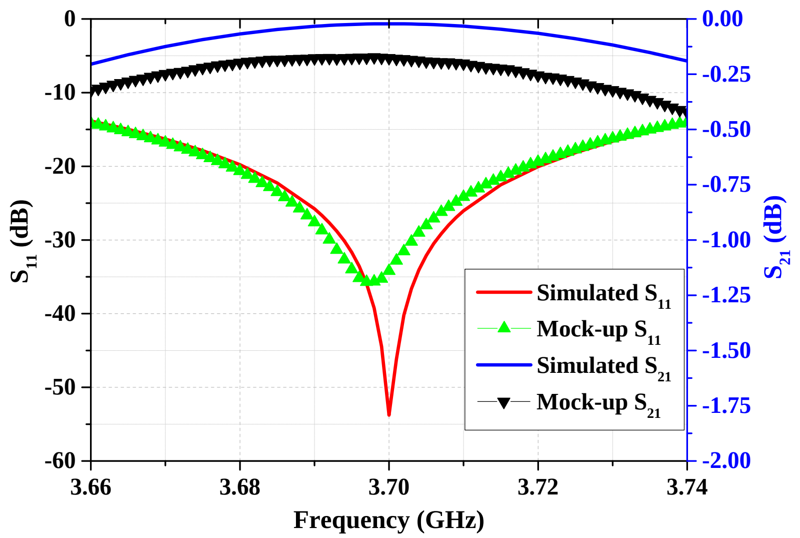

Figure 6.16: Frequency response obtained from simulations and mock-up window VNA measurements.

The return and insertion loss of the mock-up window are ~34 dB and ~0.18 dB, respectively. It can be observed that the simulated and the mock-up measurement results are in good agreement in terms of impedance matching at 3.7 GHz. However, the mock-up window has a poor insertion loss and thus, a lower return loss, as compared to the simulation results, due to poor mechanical joints between the aluminium cylinder, copper rings and the output flanges. The COMSOL simulations assume these joints to be ideal.

Thus, the VNA measurements of the mock-up window confirm the simulation results and thereby provides confidence for the development of the prototype RF vacuum window for high power operations.

6.3 Design, fabrication, low and high power test of the prototype RF window

A prototype high power RF vacuum window is fabricated using the vacuum brazing technique and the following components are required for its fabrication,

a An alumina disc having a metallised periphery.

b Copper cylinder.

c Brazing Filler Metal (BFM) (here CuSil).

d Circular to rectangular transitions (one with CF flange and the other with WR284 flange)

A 99.5% pure alumina disc of dimensions mentioned in section 6.2 is high temperature vacuum brazed at the centre of a 99.95% pure Oxygen Free High thermal Conductivity (OFHC) copper cylinder. The periphery of the alumina disc is coated with MolyManganese (MoMn) and Nickel (Ni), up to a thickness of 25 μm, so as to allow its brazing with the copper cylinder. Fig. 6.17 shows the alumina disc having a metallised periphery.

The inner diameter of the 50 mm long copper cylinder is same as the outer diameter of the alumina disc. A 0.1 mm step is machined around its inner periphery to hold the Brazing Filler Metal (BFM) during the brazing cycle (explained later). All the vacuum joints are brazed using CuSil (72% Silver and 28% Copper) as BFM.

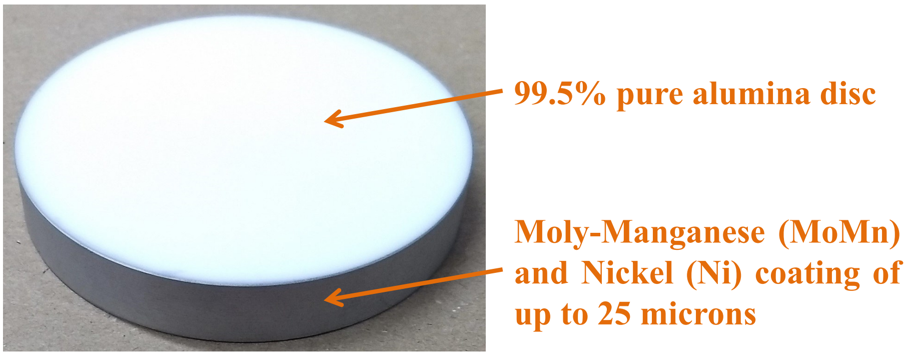

Figure 6.17: Alumina disc having a MoMn and Ni coating around its periphery.

Two circular to rectangular transitions are fabricated using SS304L material. The transition at the pressurised side of the window has a standard WR284 flange at the output and its circular waveguide is connected with the copper cylinder mechanically (Fig. 6.18). The circular to standard WR284 rectangular waveguide transition, on the vacuum side of the window, has a CF flange for a leak-proof vacuum joint (Fig. 6.19).

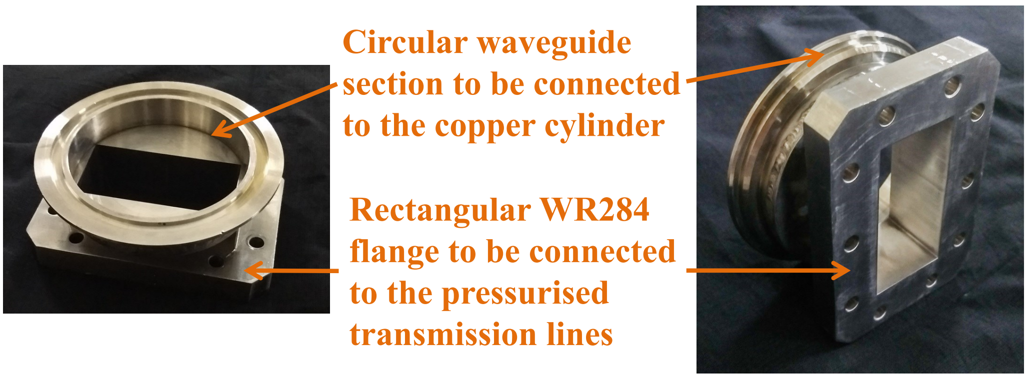

Figure 6.18: Circular to rectangular waveguide transition to be connected on the pressurised side of the window.

6.3.1 Novel mechanical design of the prototype RF window

In this thesis, a novel mechanical design of the RF window is proposed and implemented. In this design, an additional step section is machined at the bottom of the copper cylinder while a slot is made in the SS based circular to rectangular transition (with CF flange) as shown in Fig. 6.19. The BFM is sandwiched between the step (in the copper cylinder) and the slot (in the SS transition). At the peak temperature of the brazing cycle, this tight fit arrangement helps in holding the melted braze material in place. This special arrangement, along with the 0.1 mm step in the copper cylinder, facilitates efficient brazing of the Cu-SS and Cu-Al_2O_3 joints in a single brazing cycle. This method, as per the best of knowledge of the author, is demonstrated for the first time when compared to the open literature.

The length of the circular waveguide section of the transitions and that of the copper cylinder are adjusted such that the total length of the circular section of the prototype is the same as that of the mock-up design. The length of the rectangular waveguide section is decided as per the integration convenience. The placement of the transitions, copper cylinder and the alumina disc is illustrated in Fig. 6.20 through an exploded view of the prototype window.

It is intended to braze the alumina disc at the centre of the copper cylinder and thus, it is push fitted inside the cylinder at high temperature. CuSil strips and wires are inserted between them at the joint location. The additional step at the bottom of the copper cylinder (with the alumina disc) is push fitted inside the step slot of the SS transition with CuSil inserted between them. The whole assembly is placed over a steel stand so as to hold the alumina disc at the centre of the copper cylinder during brazing. SS deadweight is kept on the top of the alumina disc for its uniform movement. A titanium ring is placed around the periphery of the copper cylinder to restrict the radial expansion of the cylinder and thereby aid in holding the melted BFM between the alumina and the copper cylinder. Fig. 6.21 shows the complete brazing assembly ready to be placed in the high temperature vacuum brazing chamber.

The details of the brazing procedure, brazing cycle and several qualification tests like leak test, ultrasonic test and mechanical test conducted to ascertain the quality of the brazed joint are reported in the Appendix C.

Figure 6.19: OFHC copper cylinder and SS based circular to rectangular transition (with CF flange).

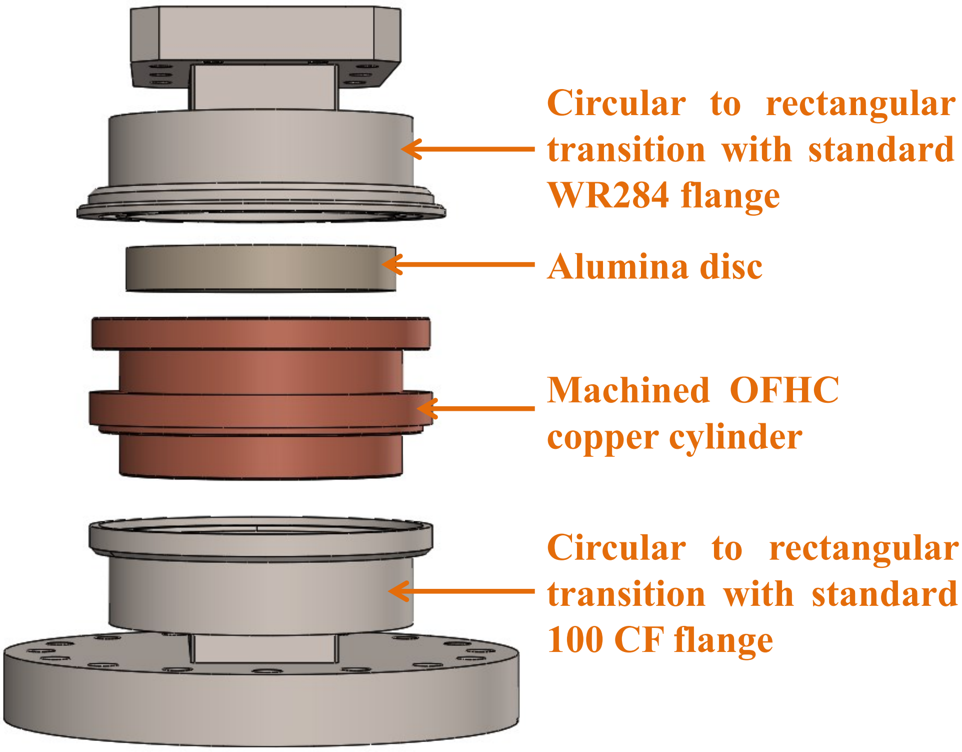

Figure 6.20: Exploded view of the prototype window setup.

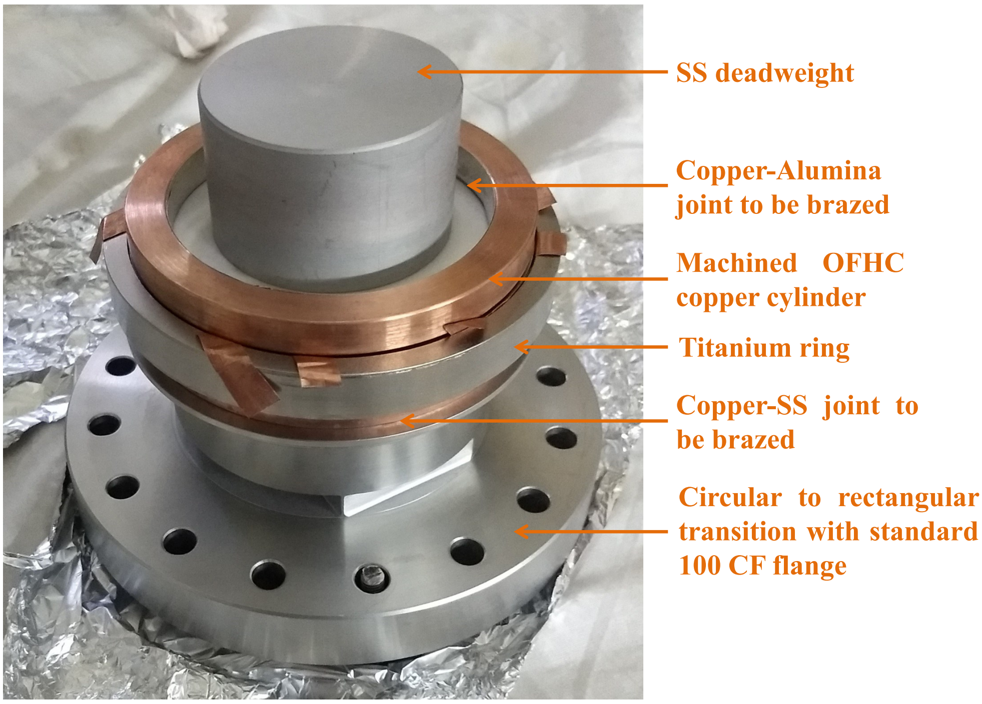

Figure 6.21: Complete assembly ready to be placed in the vacuum brazing chamber.

6.3.2 Cold test

The cold test of the brazed RF vacuum window is carried out using a VNA to qualify its performance at 3.7 GHz before operating it at high RF power. The rectangular to circular pressurised side transition is initially connected to the brazed assembly (centre copper cylinder and vacuum side transition) by mechanical joints. The length of the circular section is kept as that obtained from the mock-up window RF measurements and is 81.6 mm. It is observed that the frequency response, particularly S_{11} minimum, of the window is centred at a frequency which is to the left of the desired frequency of 3.7 GHz. The length of the circular section of the window is subsequently reduced in small steps by shaving-off the circular waveguide end of the transition using a sand paper. The frequency response (S_{11} minimum) gradually shifts to the right with a decrease in the length of the circular section and is finally centred at 3.7 GHz for a circular section length of 81.5 mm.

The frequency response of the RF window is shown in Fig. 6.22. The length of the circular section of the prototype window is slightly different from the simulated value because of the variation in the alumina disc properties as compared to those used during simulations, brazing and mechanical joint discontinuities, fabrication tolerances et cetera. However, the mock-up design and the prototype design are in close agreement. The measured return and insertion loss of the prototype window is ~36 dB and ~0.01 dB, respectively.

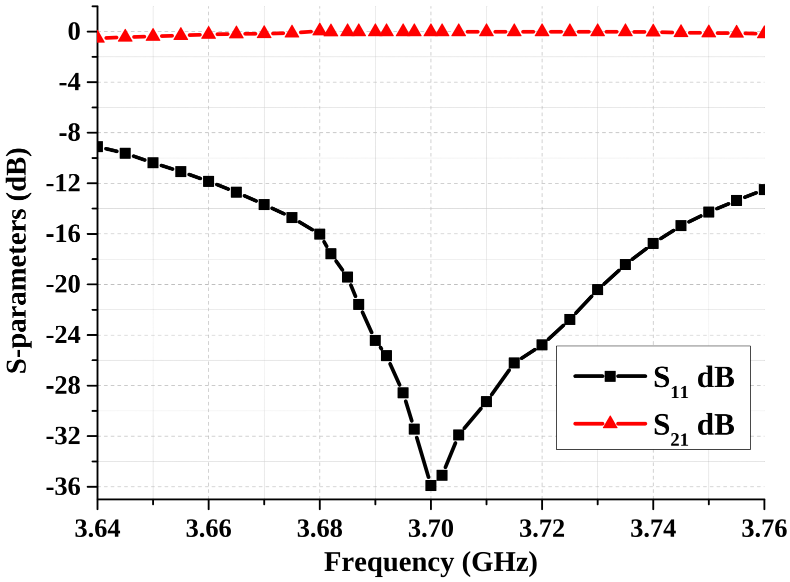

Figure 6.22: Frequency response of the RF window for circular section length of 81.5 mm.

6.3.3 High power test

The RF window is designed to operate at a frequency of 3.7 GHz and would be subjected to an input RF power of 125 kW for 1 s. Fig. 6.23 shows the block diagram of the test setup, while Fig. 6.24 shows the relative position of the infrared camera monitoring the RF window. The prototype RF window is connected to the 3.7 GHz, 0.5 MW rated, high power vacuum source, klystron, via high power isolators and directional couplers. The isolators (circulators with high power water loads) are used to protect the klystron from high power reflections while the couplers are used to measure the forward and reflected power levels during operations. The window is terminated by a high power water load. Arc detectors are placed at critical locations to detect RF breakdown. They generate a feedback signal to immediately stop the high power operations in the event of RF breakdown. An Infrared (IR) camera is placed in front of the RF window to measure the rise in the temperature at the periphery of the copper cylinder of the window, especially at the location of the alumina disc.

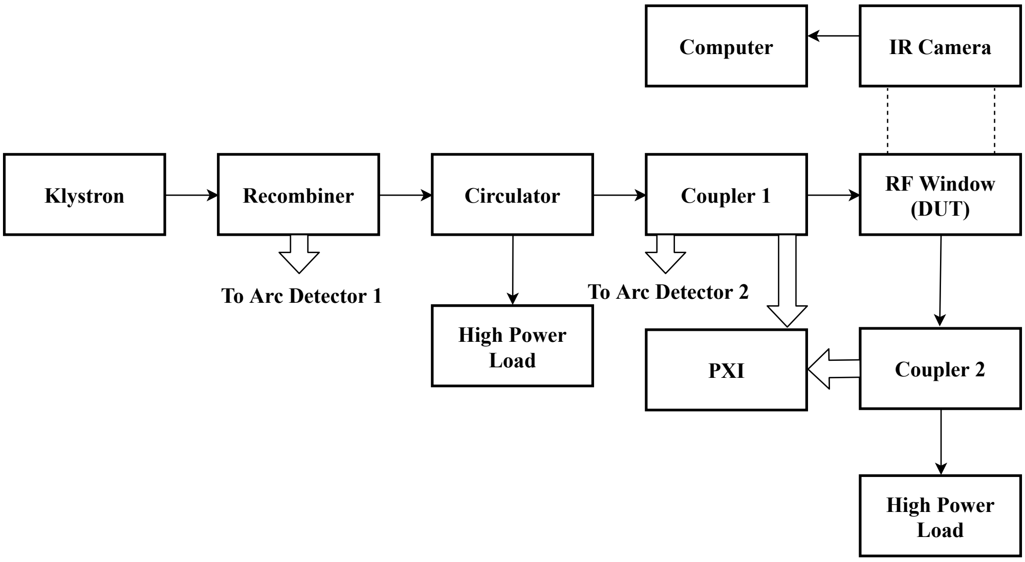

Figure 6.23: Schematic of the test setup used for high power testing of the RF window.

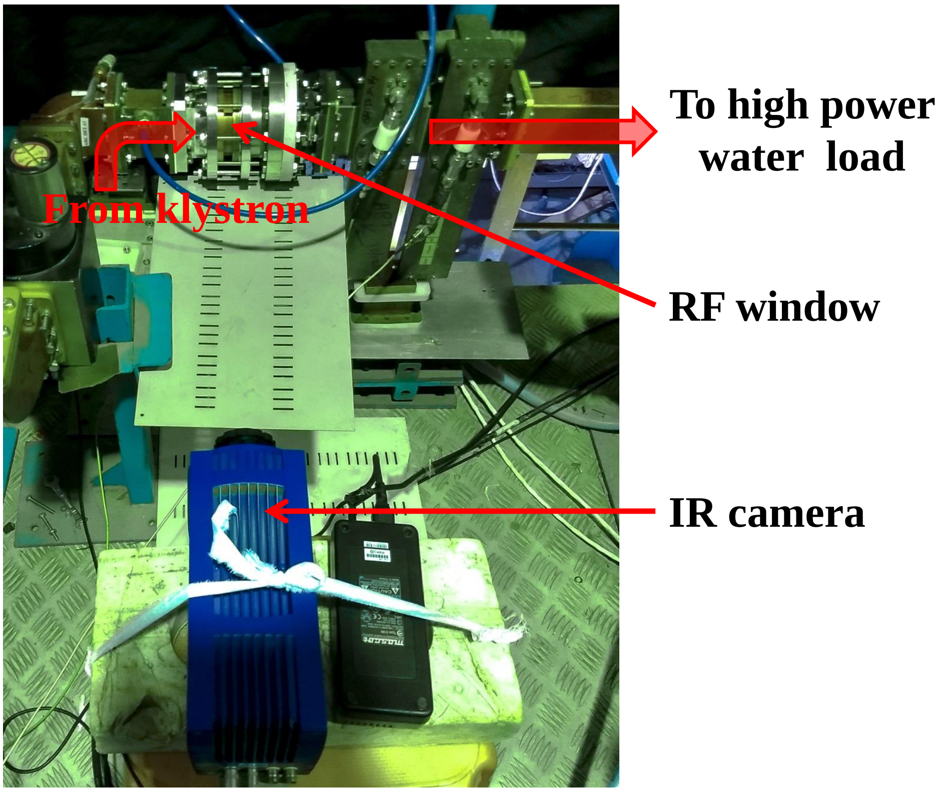

Figure 6.24: Placement of the IR camera in front of the RF window.

The window is tested for its high power performance; wherein, the RF power and its pulse length are gradually increased from 25 kW to 125 kW and 100 ms to 1 s, respectively. The window is initially excited with an input RF power of 25 kW for 100 ms. The power levels and the RF pulse length are gradually increased. The window is excited with its rated power of 125 kW for 1 s for a large number of shots. The RF breakdown and thermal performance of the window is observed for these shots. No RF breakdown is observed during the above qualification tests. Also, the reflected power measured by the use of directional coupler is very small. The window is further excited with an input RF power of 150 kW, 1 s. This power level is higher than the designed value by 20%.

The maximum power reflected by the combination of the RF window and the high power water load is measured at the input of the window and is ~4.5 kW. The power reflected by the window is ~2 kW since the high power water load has a known reflected power of ~2.5 kW. Thus, the window has a Voltage Standing Wave Ratio (VSWR) of 1:1.26, with a percentage reflected power of ~1.6. Fig. 6.25 shows typical high power test results for input excitations of ~110 kW, 500 ms and ~150 kW, 1 s.

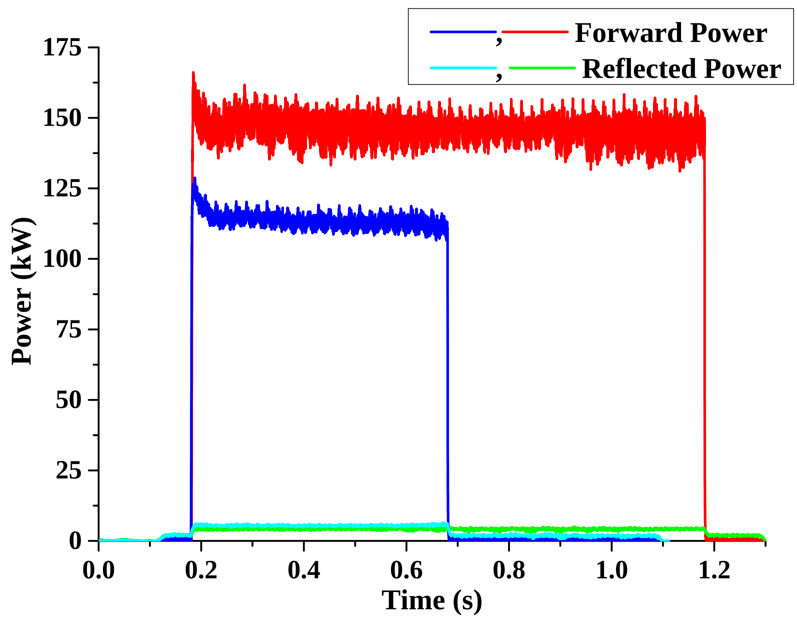

Figure 6.25: Typical high power test results of the window for input excitations of ~110 kW, 500 ms and ~150 kW, 1 s.

The IR camera is placed in front of the RF window to measure the rise in the temperature at the periphery of the copper cylinder. The front view of the RF window, which is a rectangular section of the copper cylinder enveloping the ceramic, is monitored. The temperature at various points on this rectangular section is recorded. The average temperature recorded for 125 kW RF power, 1 s shot is reported in Fig. 6.26. It is observed that the temperature rises for 1 s (duration of RF pulse excitation) and then starts decreasing due to convection cooling. The maximum rise in the temperature at the periphery of the window is ∼ 0.25°C which is in good agreement with the simulated result (Fig. 6.7).

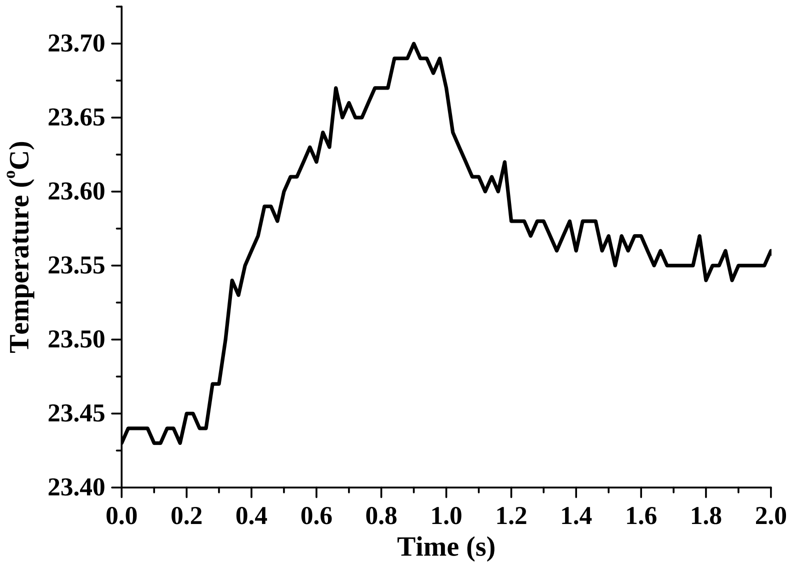

Figure 6.26: Average temperature of the window for 150 kW, 1 s shot.

Post the high power test, the prototype window is again subjected to the vacuum and pressurised qualification tests discussed in Appendix C. This is done to detect if any leaks are developed during the high power test. The window successfully passed the tests and yielded results similar to those obtained before the high power test. Thus, the RF window can handle 125 kW of RF power for 1 s while maintaining ∼3 bars of differential pressure across the alumina disc.

6.4 PAM launcher with RF window at the input

After the successful low and high power testing of the RF window, it is integrated with the PAM launcher, at its input, to evaluate their combined RF performance in terms of S-parameters. The combined structure has a return loss of ∼38 dB as shown in Fig. 6.27.

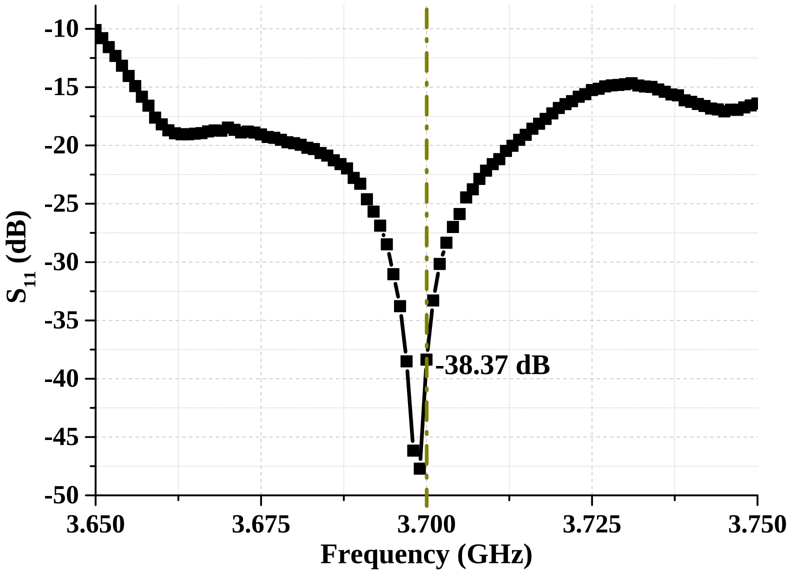

Figure 6.27: Return loss of the complete integrated launcher.

The input RF power is divided between the active waveguides equally ($|S_{21}|$ ~-8.2 dB ± 0.5 dB, (Fig. 6.28). The phase difference between the adjacent active waveguides is $\sim -90°$ as desired (Fig. 6.29).

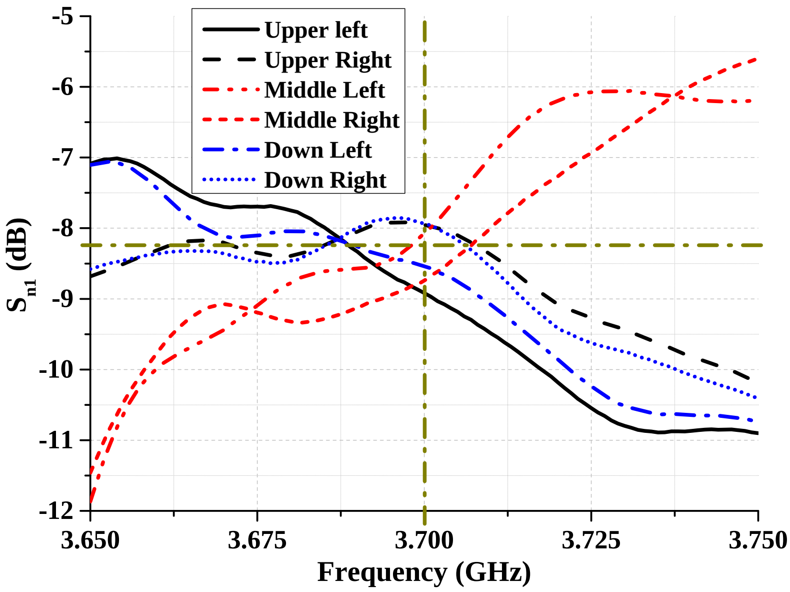

Figure 6.28: Power division between the active waveguides of the complete integrated launcher.

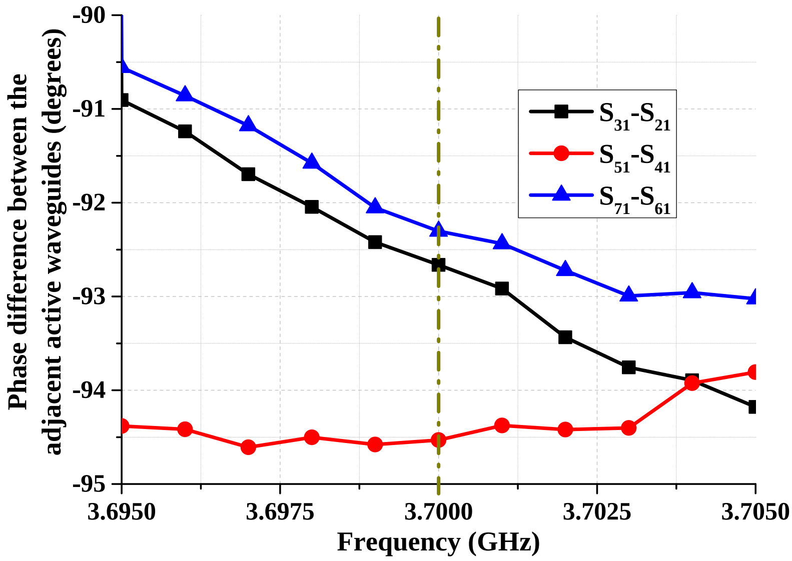

Figure 6.29: Phase difference between the adjacent active waveguides of the complete integrated launcher.

6.5 Summary

The design, Multiphysics analysis, development along with low and high power testing of a novel pill box type RF window is presented in this chapter. The novelty of the window lie in the addition of step in the mechanical design of the window to facilitate the brazing of two joints involving two dissimilar materials (metallised alumina and copper, SS304L and copper) in a single brazing cycle. The step was added in such a way that the RF functionality was not compromised. This addition led to a fifty percent reduction in the brazing efforts and its associated cost involved in developing the window. Exhaustive simulation studies were carried out to determine the best suitable ceramic material for the window. A mock-up model was built to evaluate the correctness of simulation, after which a prototype window was developed for high power tests. The window demonstrated excellent behaviour during high power pulsed measurements which reflect the correctness of the simulation model, mechanical design and fabrication protocols.

Chapter 7

Conclusion and Future Scope of Work

As the milestones for International Thermonuclear Experimental Reactor (ITER) at Cadarache are coming closer, it becomes important for member nations to be abreast and equipped with the developments in relevant technologies so as to rapidly capitalise on the results obtained from ITER. It was with this motivation that the objective of this thesis was to carry out studies on the design and development of the Passive Active Multijunction (PAM) launcher for the ADITYA –U tokamak.

Although PAM launchers have been designed, deployed and tested in a few tokamaks before, its design and performance vary from tokamak to tokamak on account of different port and plasma constraints. This thesis, therefore, presents the studies on the design and development of a PAM launcher for the ADITYA –U tokamak. Another focus of this thesis was to carry out studies relevant to the design and development of a high power pill box type RF vacuum window.

The salient contributions of this thesis are as follows:-

1 **Design, Development and testing of a PAM launcher:** The design, development and low power testing of a PAM launcher capable of handling 250 kW/1 s of RF power at 3.7 GHz are carried out. Due to the available port size, the launcher had

a smaller number of active and passive waveguides. The PAM concept was thus realised in a smaller size satisfactorily.

2 Low Power profile measurement technique: A new method to evaluate the performance of the PAM launcher, in air, at low power before installing it on the machine is proposed. This method gives the $N_{||}$ spectra; the power spectrum of the wave launched from the launcher and demonstrates the steering of the waves. The results obtained agreed excellently with simulation.

3 Design, Development, Low and High power testing of the RF window: A novel mechanical design of a pill box type RF vacuum window capable of handling 125 kW of RF power for 1 s at 3.7 GHz is proposed. Further, its Multiphysics analysis, fabrication and low and high power testing is carried out. The novel structure enables the brazing of two joints involving two dissimilar materials (metallised alumina and copper, SS304L and copper) in a single brazing cycle. Thus, there is a fifty percent reduction in the brazing efforts and costs involved in developing the window.

4 Novel Mode Converter design: A new mode converter structure is proposed which does not utilise a post to match the input. In this work, a few steps are added to the broader side of the mode converter (where the E-field is zero) at the output. This method reduces the concentration of the E-field locally near the post and thereby increases the power threshold for RF breakdown.

The salient characteristics of the developed PAM launcher and RF window which confirms its compatibility with the ADITYA –U tokamak are as follows:-

1 Parallel Refractive index ($N_{||}$): The developed PAM launcher can launch RF waves with a parallel refractive index ($N_{||}$) ranging from 1.875 to 2.625. This variation can be achieved by varying the external phase shift between the two toroidal modules. The central $N_{||}$ value of 2.25 is achieved when an external phase shift of 165° is applied. These measurements were reported in Chapter 5. The $N_{||}$ of the launched wave is found to be as desired and is consistent with various plasma parameters of the ADITYA –U tokamak

2 **Size of the port:** The cross-sectional dimension of the mouth of the PAM launcher after fabrication is 288 mm × 127 mm. This is consistent with the allocated ADITYA –U port size of 490 mm × 190 mm. Thus, the launcher can be installed with all the relevant diagnostics.

3 **Footprint:** The RF (Chapter 3) and mechanical (Chapter 4) design of the PAM launcher conforms to all the space constraints imposed by the support structure of the ADITYA –U tokamak. Fig. 7.1 shows the depiction of the PAM launcher connected to its tokamak port. The position of the PAM launcher in the tokamak along with various existing support structures can also be observed.

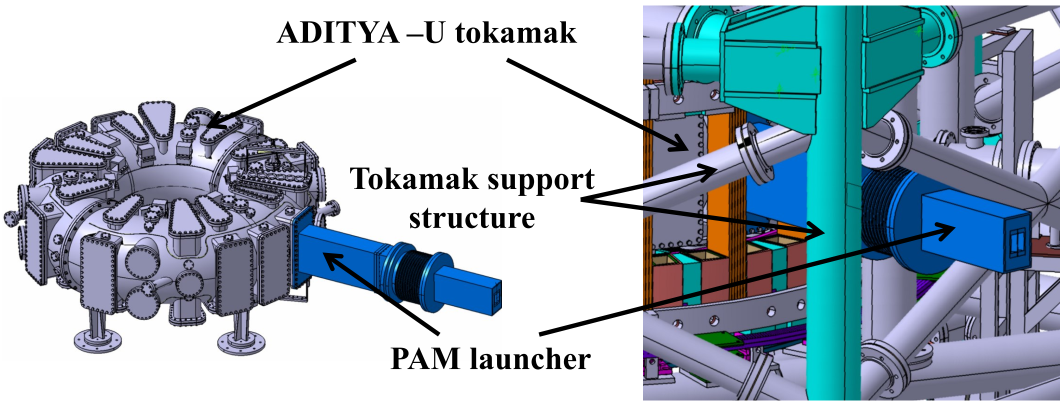

Figure 7.1: Position of the PAM launcher in the tokamak illustrating that the launcher conforms to all the space constraints.

4 **Disruption:** As elaborated in chapter 3, the PAM launcher was designed and further developed such that it could withstand the stress exerted on it due to thermal and plasma disruption effects. The total stress exerted on the launcher is ~53 MPa.

5 **HLD, Baking and UHV:** The complete PAM structure was tested for its leak rate (maximum leak rate < 1×10^{-9} mbarl/s), baking (up to a temperature of ~ 180°C) was employed to release the trapped gases and impurities and a vacuum level of

1.3×10^{-8} mbar was achieved. The leak rate obtained, maximum baking temperature applied and the vacuum level achieved satisfy the ADITYA –U tokamak's requirement before installation.

6 **RF vacuum window:** The fabricated window was able to withstand a differential pressure of 3 bars which it would encounter in real-time during high power operations. The HLD test of the window revealed a leak rate of less than 1.11×10^{-9} mbar-l/s confirming its UHV compatibility. The high power test of the window was conducted at 150 kW (20% higher than the design value of 125 kW) for 1 s. The design, development and all the qualification tests performed are elaborated in chapter 6

Future Scope of Work

1 **Investigation for CW operation:** The PAM launcher was designed for pulsed operation. In case the launcher is to be utilised for SST-1 tokamak (operating in CW mode for 1000 s), thermal, mechanical and plasma disruption studies would have to be carried out. The evaluation of the total stress acting on the launcher due to thermal load and plasma disruption would be important after the addition of cooling pipes at critical locations.

2 **Design of RF vacuum window for CW operation:** The use of a PAM launcher for SST-1 tokamak would warrant the need to design a pill box type RF vacuum window capable of operating in CW mode. During steady-state operation, the ceramic is usually unable to dissipate the heat away from its centre to periphery due to which it expands. This causes the ceramic to crack at various fixed boundaries. Thus, considerable research effort would have to be expended in selecting an appropriate ceramic material, cooling mechanism and thereby designing the RF window.

Appendix A

Benchmarking of Disruption Analysis in COMSOL Multiphysics

The disruption analysis evaluates the torque acting on the launcher system in the event of a sudden uncontrolled fall in the plasma current (plasma disruption). The PAM launcher system is a dimensionally non-standard system and thus, no empirical formulae are available to evaluate these forces theoretically. Thus, one has to rely on the 3D simulations performed on commercial software like COMSOL Multiphysics for its evaluation. However, benchmarking of the modelling done in the software is a must before using it for the actual simulations. A standard system (here, circular disc), whose empirical formulae required for the evaluation of the disruption forces are known, is used for benchmarking. The theoretical values of these forces can be evaluated, compared with the simulation results and the 3D simulations performed on COMSOL can thus be benchmarked.

An SS304L circular disc having a radius (r) and thickness (t) of 50 mm and 30 mm, respectively, is used for the analysis. The details of the modelling assumptions, boundary conditions and plasma current profile used for analysis in COMSOL are discussed in Chapter 3. The fall time of the plasma current (from 200 kA to 0) is assumed to be 1 ms. Thus, the corresponding frequency (f) would be 1 kHz. Further, the skin depth (δ) of the

SS304L plate having electrical conductivity (σ) of 1.4 $\times 10^6$ S/m is obtained using,

$$\delta = \frac{1}{\sqrt{\mu \pi f \sigma}} = 13.45\,\text{mm} \tag{A.1}$$

The penetration of fields into the plate is up to the skin depth of SS304L. With the perimeter of the plate being the length (l) and the product of the skin depth and radius being the area (A), the resistance (R) of the circular plate is evaluated using,

$$R = \frac{l}{\sigma A} = \frac{2\pi r}{\sigma \delta r} = 0.33\,\text{m}\Omega \tag{A.2}$$

Fig. A.1 shows the circular disc modelled in COMSOL Multiphysics with the disrupting plasma current and the toroidal magnetic field.

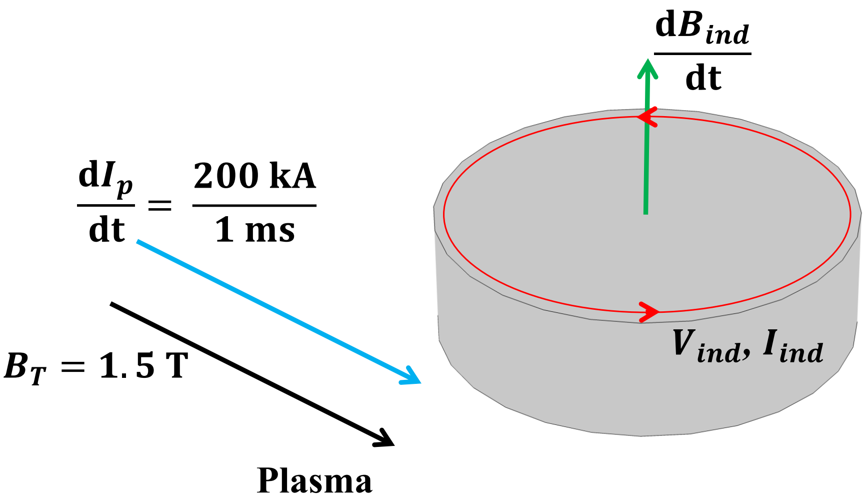

Figure A.1: A pictorial representation of time varying magnetic field, loop voltage and loop current induced on the circular disc.

In the event of plasma disruption, a time varying magnetic field ($\frac{dB_{ind}}{dt}$), indicated by the green arrow in Fig. A.1 is induced on the circular plate by Ampere's law. A loop voltage and hence a loop current is further induced. The loop voltage (V) induced in the circular plate in terms of flux linkage (ϕ) can be estimated using,

$$V = \left|\frac{d\phi}{dt}\right| \tag{A.3}$$

Substituting $\phi = BA$, we get,

$$V = A\left|\frac{\mathrm{d}B}{\mathrm{d}t}\right| \tag{A.4}$$

where,

A is the surface area of the plate (m^2) and is πr^2.

$\frac{\mathrm{d}B}{\mathrm{d}t}$ is the time varying induced magnetic field and can be substituted as $\frac{\mu_0}{2\pi r_1}\frac{\mathrm{d}I}{\mathrm{d}t}$

r_1 is the minimum distance between the plasma current and the circular plate.

$\frac{\mathrm{d}I}{\mathrm{d}t}$ is the change in the plasma current (plasma disruption).

Then Eq. A.4 becomes,

$$V = \pi r^2 \frac{\mu_0}{2\pi r_1}\frac{\mathrm{d}I}{\mathrm{d}t} \tag{A.5}$$

The minimum distance kept between the plasma current and the circular plate during modelling is $r_1 = 100\,\mathrm{mm}$. Thus, the induced voltage obtained using Eq. A.5 is 3.14 V and the induced loop current is evaluated as $I = V/R$ and is 9.5 kA. Further, the analytical value of the induced current density is evaluated using ($\boldsymbol{J} = I/A$) and is 1.2×10^6 A/m^2. Fig. A.2 shows the induced current density on the top plate of the circular disc obtained via COMSOL simulations.

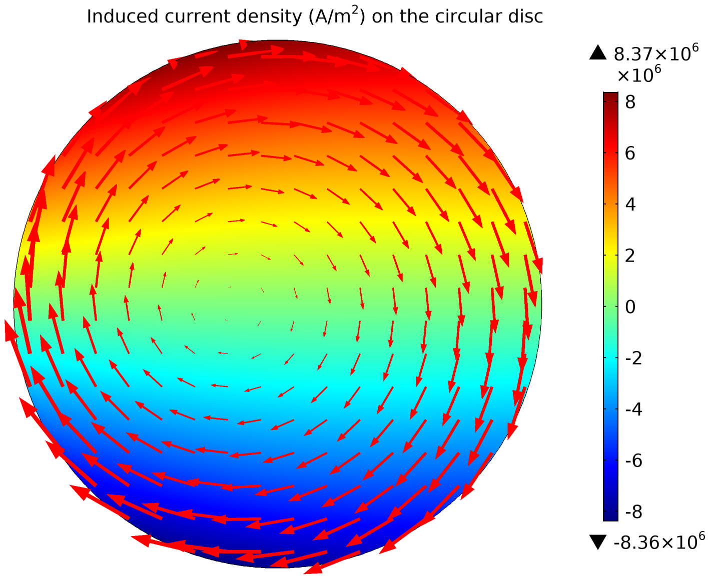

Figure A.2: Induced loop current density (A/m^2) on the top plate of the circular disc.

The peak value of the induced current density is 8.37×10^6 A/m^2. The order of the analytical and simulated value of the induced current density is in good agreement.

The induced current density ($\boldsymbol{J}$) crosses with the toroidal magnetic field ($\boldsymbol{B_T}$) of the tokamak and generates equal and opposite $\boldsymbol{J} \times \boldsymbol{B_T}$ disruption forces at the opposite ends of the circular disc. This phenomenon is illustrated in the schematic shown in Fig. A.3.

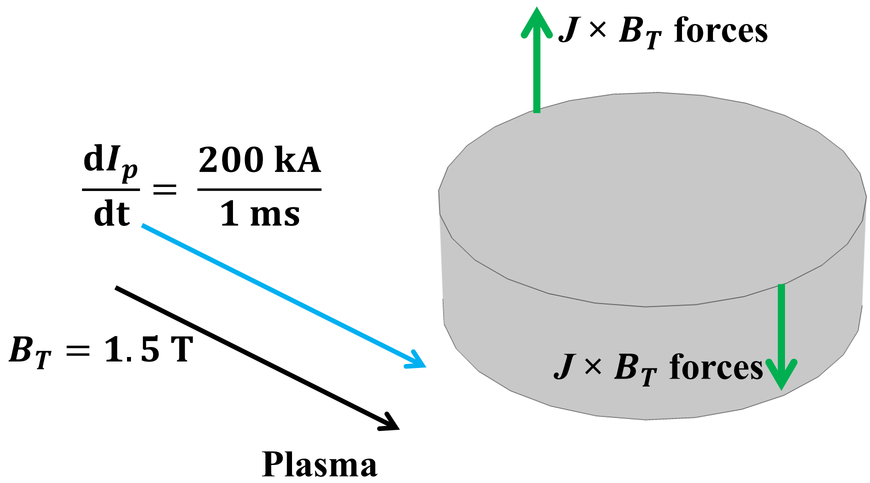

Figure A.3: A pictorial representation of the phenomenon of generation of equal and opposite disruption forces at the opposite ends of the circular disc.

The toroidal magnetic field of the tokamak is 1.5 T. Thus, the absolute value of the disruption forces is estimated as (JB) and is ~1.8×10^6 N/m^3. Fig. A.4 shows the $\boldsymbol{J} \times \boldsymbol{B_T}$ forces acting on the top plate of the circular disc. The peak value of this Lorentz force is 9.68×10^6 N/m^3.

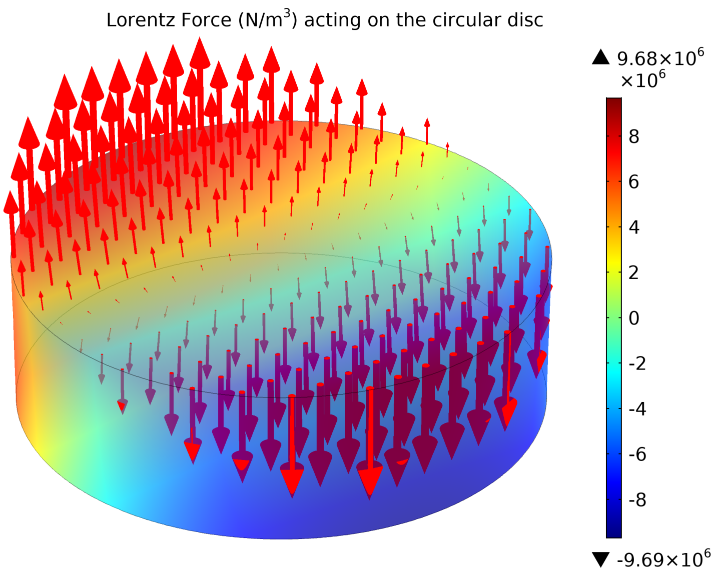

Figure A.4: $\boldsymbol{J} \times \boldsymbol{B_T}$ forces (N/m^3) acting on the top plate of the circular disc.

The order of the analytical and simulated values is in good agreement, thereby benchmarking the modelling of the disruption forces in COMSOL Multiphysics. This modelling is further used to evaluate the disruption forces acting on the PAM launcher and is discussed in Chapter 3.

Appendix B

Mechanical Drawings of the PAM Launcher

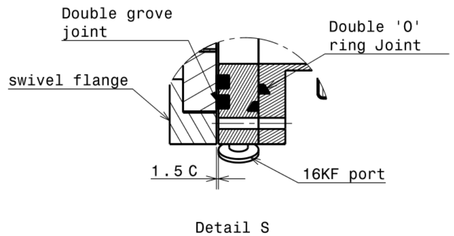

Detail S
Scale: 1:4

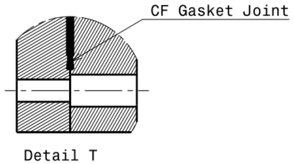

Detail T
Scale: 1:2

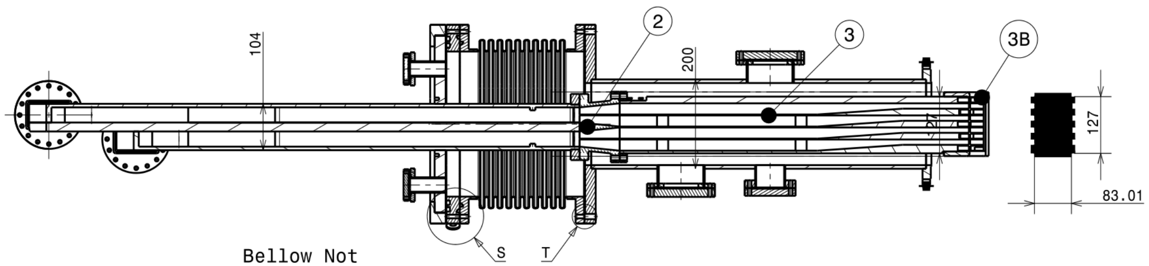

Bellow Not included in Vendor Scope of Work

Section view A-A

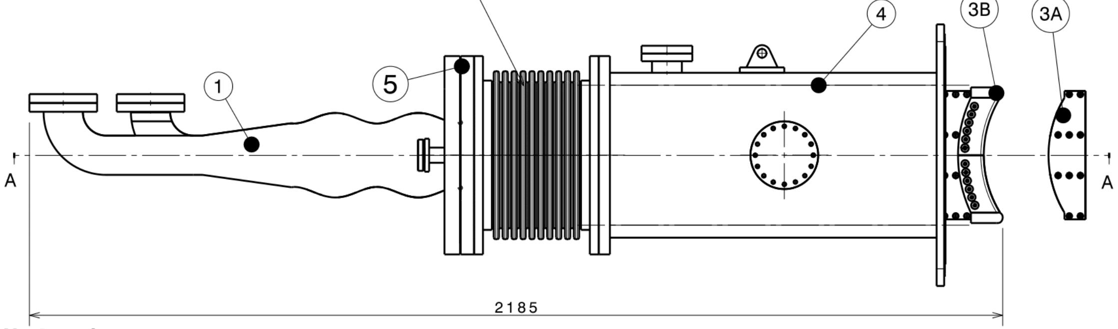

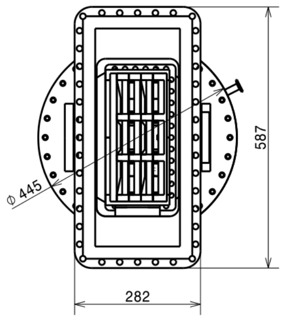

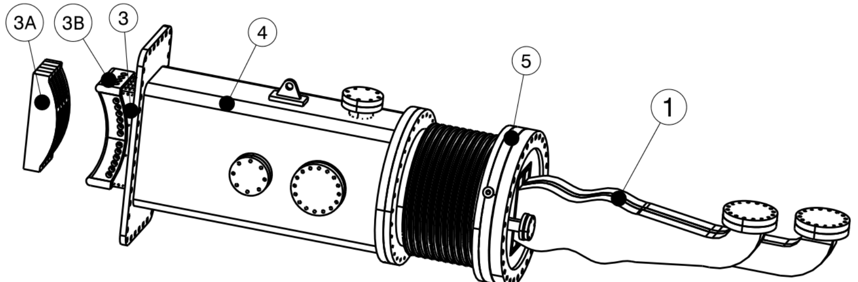

Isometric view

Free Issue Material (FIM):(1) Graphite block for tile fabrication (2)In place of Bellow an extension piece, Aluminium wire seals, Heating tapes, Thermocouples and dimmerstate shall be provided at the time of Helium leak testing and High Vacuum testing

NOTE-2:

(1) Front end component and Enclosure shall be checked for helium leak test (2) High Vacuum test shall be carried out for whole assembly with and without baking (3)Helium leak tighness of weld joints should be less than or equal to 1 x 10^-9 mbar liter per second. (4) Global leak rate should be less than 5x10^-9 mbar liter per second

Special Note:

Sliding support for End component assembly inside Enclosure has to be designed in due consultaion with IPR.

Sr. No.	ITEM NO.	Description	Qty.	Material	Remarks
12		Gasket CS 6Wx8H, ID342	04Nos.	VITON	
11		Gasket CS 6Wx8H, ID374	04Nos.	VITON	
10	--	O ring dia 6CS 382ID	04Nos.	VITON	
09	--	O ring dia 6CS 356ID	04Nos.	VITON	
08	-	Dowel pin Φ8x30LG	16 Nos	SS304L	
07	5	Intermediate flange	01	SS304L	Ref. Sheet 9 of 10
06	4	Enclosure	01	-----	Ref. Sheet 8 of 10
05	3B	Tile Assembly	01	----	Ref. Sheet 5, 6 & 7 of 10
04	3A	Test Block Assly	01	-----	
03	03	End Component Assly	01	-----	
02	02	Intermediate Taper Component	01	SS304L	Ref. Sheet 04 of 10
01	01	Front Component Assly	01	-----	Ref. Sheet 2 & 3 of 10

Note-1:

(1) All weld joint shall be TIG welded (2) Single pass welding shall be employed wherever possible to avoid trapping of gases between the weld joint (3) All weld shall be ground smooth and flushed with joining surfaces with convex curvature with adjoining wall (4) Use fixtures during welding, machining and heat treatment (5) All the inner surfaces and inner components surfaces shall have surface finish of 0.8 to 1.5microns (6) Enough care shall be taken to avoid damage (Dent and Scratches) during handling and storing of raw material, semi finished product and finish products (7) RT/UT shall be carried out on all the possible weld (8) All component which where seeing UHV shall be subjected to heat treatment at component stage as per approved procedure (9) After heat treatment component shall be subjected to electro polishing and ultrasonic cleaning as per approved procedure (10) All sharp corners(Except Inner component profile) shall be rounded off (11) Abrasive cleaning of surface exposed to vacuum is not allowed (12) During electropolishing the gasket seating portion of the CF flange shall be protected from by using suitable material

DRG.NO	▽ 8.25	▽▽ 1.6-8	▽▽▽ 0.025-1.6	▽▽▽▽ < 0.025
CO-ORDINATED BY				

MACHINING DEVIATIONS FOR NON-TOLERANCED DIMENSIONS

LENGTH IN mm OF SHORTER SIDE OF ANGLES				LENGTH OR DIA	UPTO 6	6-30	30-120	120-315
UPTO 10	10-50	50-120	OVER 120-400					
±1°	±0°-30'	±0°-20'	±0°-10'		±0.1	±0.2	±0.3	±0.5

REVISION COLUMN

REV	ZONE	DESCRIPTION	DATE	REMARKS	APPROVED BY

ASS'Y GROUP:			INSTITUTE FOR PLASMA RESEARCH BHAT, GANDHINAGAR-382 428.	
ALL DIMENSIONS ARE IN `mm' UNLESS OTHERWISE STATED				
SCALE	NTS	DATE	TITLE LAUNCHER ASSEMBLY	
DRAWN	SUKHDEV	08/02/2017		
CHECKED	PRP	08/02/2017	REF DRG NO:	REV 01
APPROVED			DRG.NO IPR/ADT/LH/UPG/001.A3	SHEET 01 OF 10

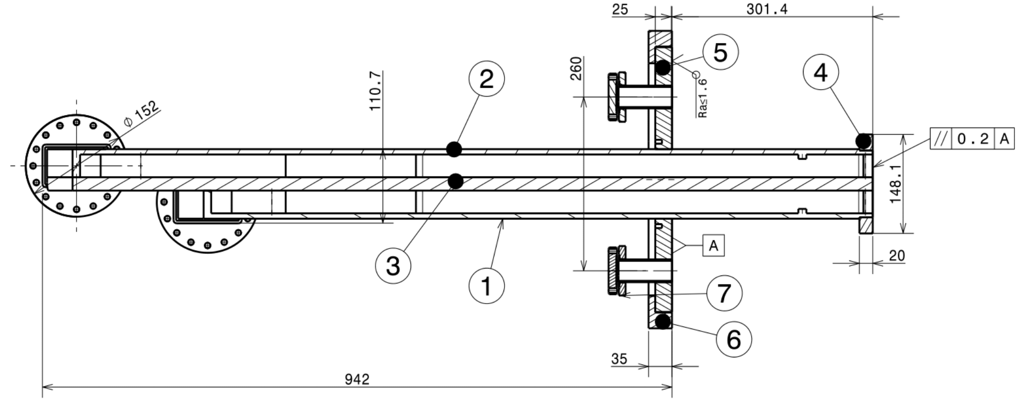

Section view B-B

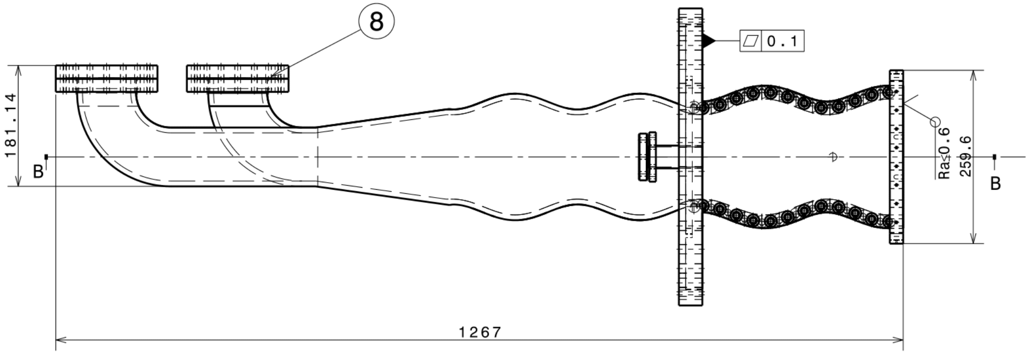

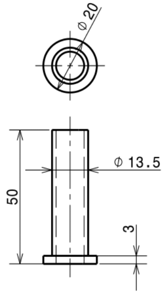

BUSH

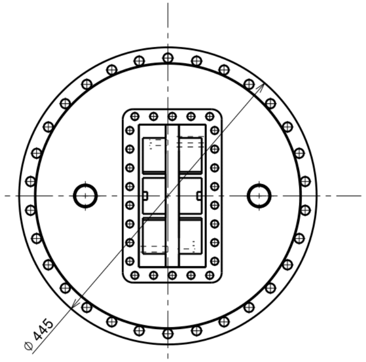

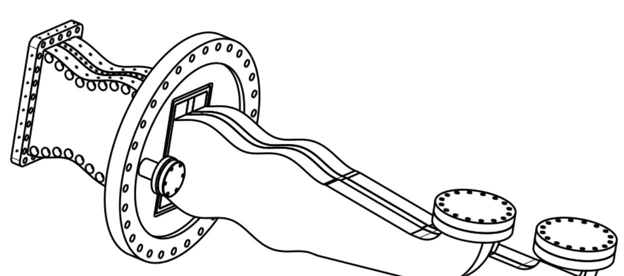

Isometric view

Note-3

At few locations, arrangement for wire clamps and thermocouple holes shall be made as per IPR requiremtns

**** Indicates nuts and bolts required slotting and drilling works as per Vacuum protocol for avoiding trapped volume

SR.NO	ITEM NO.	DESCRIPTION	MATERIAL	QUANTITY	REMARK
13		M10x35L Hex Bolts with spring washer	SS304L	50Nos	****
12	--	M8x40 Hex Bolts with spring washer	SS304L	24Nos.	****
11	--	Bush Φ20x50L	G10/CAST NYLONE	60Nos.	
10	--	M10x60L Hex bolts with plain washer, spring washer and nut	SS304L	60Nos.	****
09	--	M10x40L Socket Head Bolts with Spring Washer and Nuts	SS304L	75Sets	****
08	08	100CF Port With Blank Flange	SS 304L	02Nos.	
07	07	35CF Port With Blank Flange	SS 304L	02Nos.	
06	06	Swivel Flange	SS 304L	01No.	Ref. Sheet 3 of 10
05	05	Circular Flange-1	SS 304L	01No.	
04	04	Flange-1	SS 304L	01No.	
03	03	Intermediate plate	SS 304L	01No.	
02	02	Plate-2	SS 304L	01No.	
01	01	Plate-1	SS 304L	01No.	

Note-1:

(1) All weld joint shall be TIG welded (2) Single pass welding shall be employed wherever possible to avoid trapping of gases between the weld joint (3) All weld shall be ground smooth and flushed with joining surfaces with convex curvature with adjoining wall (4) Use fixtures during welding, machining and heat treatment (5) All the inner surfaces and inner components surfaces shall have surface finish of 0.8 to 1.5microns (6) Enough care shall be taken to avoid damage (Dent and Scratches) during handling and storing of raw material, semi finished product and finish products (7) RT/UT shall be carried out on all the possible weld (8) All component which where seeing UHV shall be subjected to heat treatment at component stage as per approved procedure (9) After heat treatment component shall be subjected to electro polishing and ultrasonic cleaning as per approved procedure (10) All sharp corners(Except Inner component profile) shall be rounded off (11) Abrasive cleaning of surface exposed to vacuum is not allowed (12) During electropolishing the gasket seating portion of the CF flange shall be protected from by using suitable material

NOTE-2:

(1) Helium leak tightness of weld joints should be less than or equal to 1 x 10^-9 mbar liter per second. (2)High Vacuum test shall be carried out for whole assembly with and without baking (3) Global leak rate should be less than 5x10^-9 mbar liter per second

DRG.NO	∇ 8.25	∇∇ 1.6-8	∇∇∇ 0.025-1.6	∇∇∇∇ < 0.025
CO-ORDINATED BY				

MACHINING DEVIATIONS FOR NON-TOLERANCED DIMENSIONS

LENGTH IN mm OF SHORTER SIDE OF ANGLES				LENGTH OR DIA	UPTO 6	6-30	30-120	120-315
UPTO 10	10-50	50-120	OVER 120-400		±0.1	±0.2	±0.3	±0.5
±1°	±0°-30'	±0°-20'	±0°-10'					

REVISION COLUMN

REV	ZONE	DESCRIPTION	DATE	REMARKS	APPROVED BY

ASS'Y GROUP:		
ALL DIMENSIONS ARE IN `mm' UNLESS OTHERWISE STATED		
SCALE	NTS	DATE
DRAWN	SUKHDEV	08/02/2017
CHECKED	PRP	08/02/2017
APPROVED		

INSTITUTE FOR PLASMA RESEARCH
BHAT, GANDHINAGAR-382 428.

TITLE
Front Component Assembly

REF DRG NO: | REV 01

DRG.NO IPR/ADT/LH/UPG/001.A3 | SHEET 02 OF 10

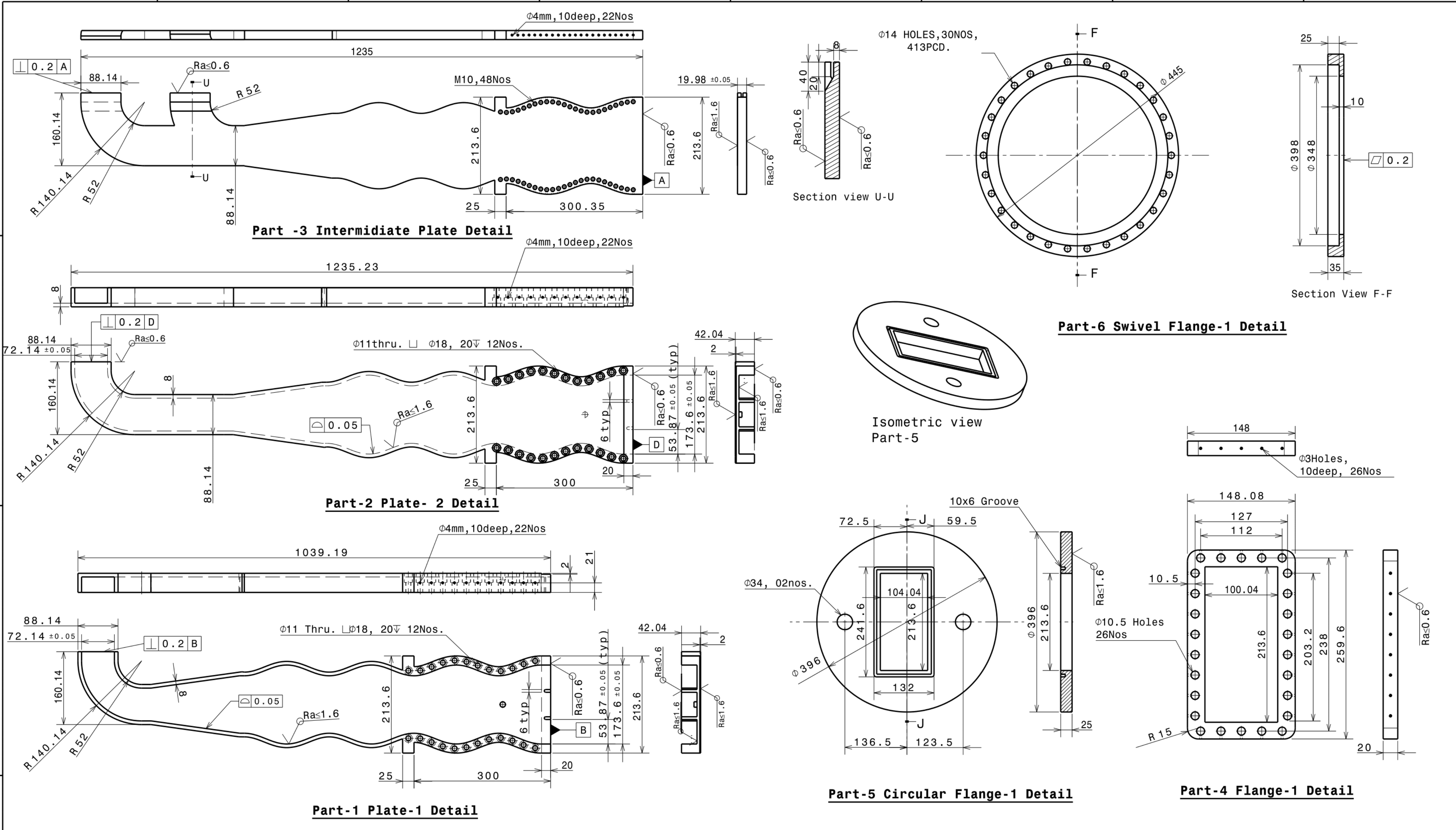

DRG.NO	▽ 8.25	▽▽ 1.6-8	▽▽▽ 0.025-1.6	▽▽▽▽ < 0.025
CO-ORDINATED BY				

MACHINING DEVIATIONS FOR NON-TOLERANCED DIMENSIONS

LENGTH IN mm OF SHORTER SIDE OF ANGLES				LENGTH OR DIA	UPTO 6	6-30	30-120	120-315
UPTO 10	10-50	50-120	OVER 120-400					
±1°	±0°-30'	±0°-20'	±0°-10'		±0.1	±0.2	±0.3	±0.5

REVISION COLUMN

REV	ZONE	DESCRIPTION	DATE	REMARKS	APPROVED BY

ASS'Y GROUP:		
ALL DIMENSIONS ARE IN `mm' UNLESS OTHERWISE STATED		
SCALE	NTS	DATE
DRAWN	SUKHDEV	08/02/2017
CHECKED	PRP	08/02/2017
APPROVED		

INSTITUTE FOR PLASMA RESEARCH

BHAT, GANDHINAGAR-382 428.

TITLE

COMPONENT DETAIL

REF DRG NO:		REV 01
DRG.NO	IPR/ADT/LH/UPG/001.A3	SHEET 03 OF 10

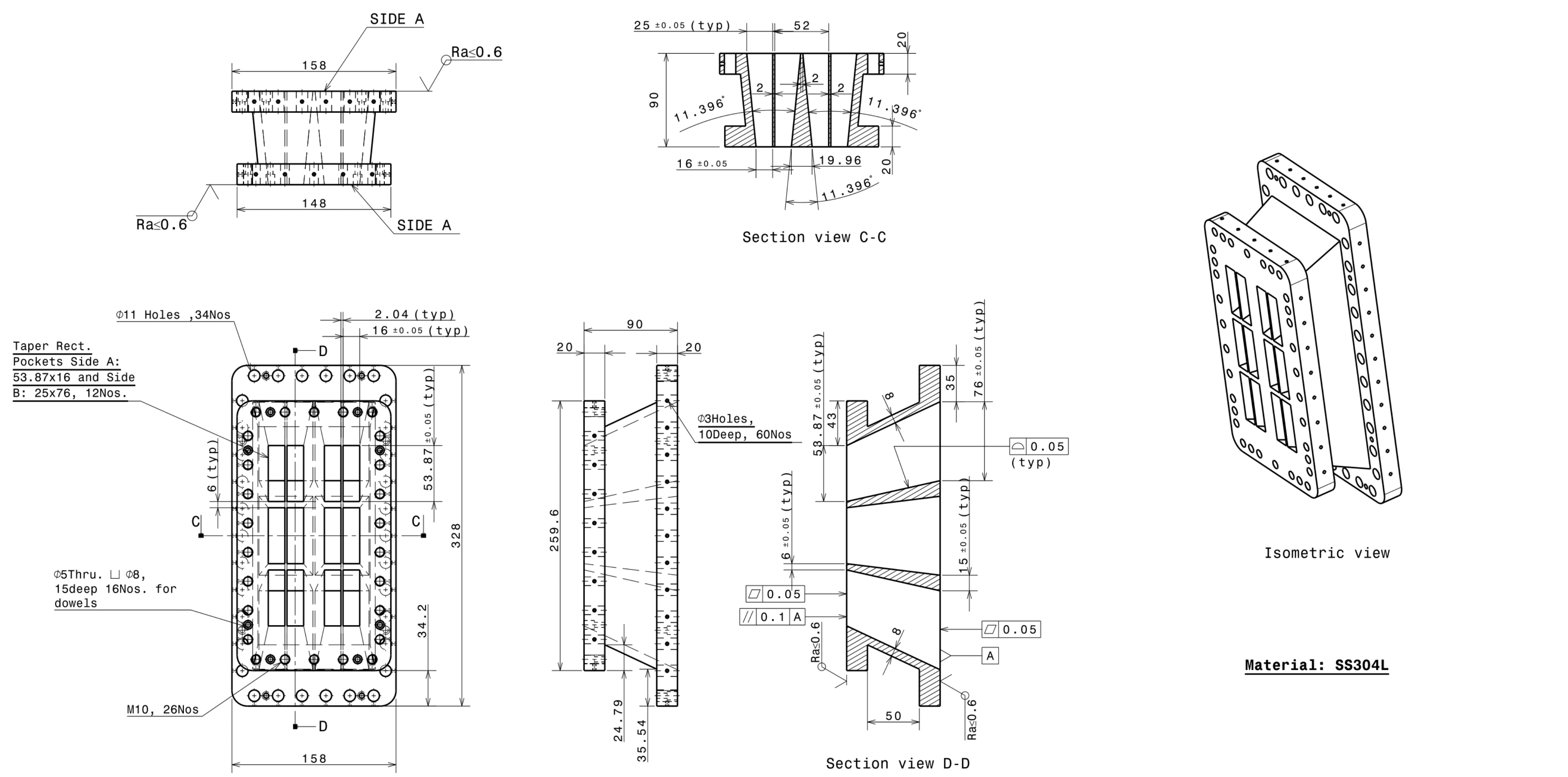

Material: SS304L

NOTE:-

1. All surface shall be free from scratches.
2. All sharp edges or corners (Except Inner Profile) shall be rounded off.
3. cleaning and passivation to be done as per approved procedure.
4. Electropolishing shall be done as per approved procedure

DRG.NO	∇ 8.25	∇∇ 1.6-8	∇∇∇ 0.025-1.6	∇∇∇∇ < 0.025
CO-ORDINATED BY				

MACHINING DEVIATIONS FOR NON-TOLERANCED DIMENSIONS

LENGTH IN mm OF SHORTER SIDE OF ANGLES				LENGTH OR DIA	UPTO 6	6-30	30-120	120-315
UPTO 10	10-50	50-120	OVER 120-400		±0.1	±0.2	±0.3	±0.5
±1°	±0°-30'	±0°-20'	±0°-10'					

REVISION COLUMN

REV	ZONE	DESCRIPTION	DATE	REMARKS	APPROVED BY

ASS'Y GROUP:		
ALL DIMENSIONS ARE IN `mm' UNLESS OTHERWISE STATED		
SCALE	NTS	DATE
DRAWN	SUKHDEV	08/02/2017
CHECKED	PRP	08/02/2017
APPROVED		

INSTITUTE FOR PLASMA RESEARCH

BHAT, GANDHINAGAR-382 428.

TITLE

INTERMIDIATE TAPER COMPONENT

REF DRG NO:		REV 01
DRG.NO	IPR/ADT/LH/UPG/001.A3	SHEET 04 OF 10

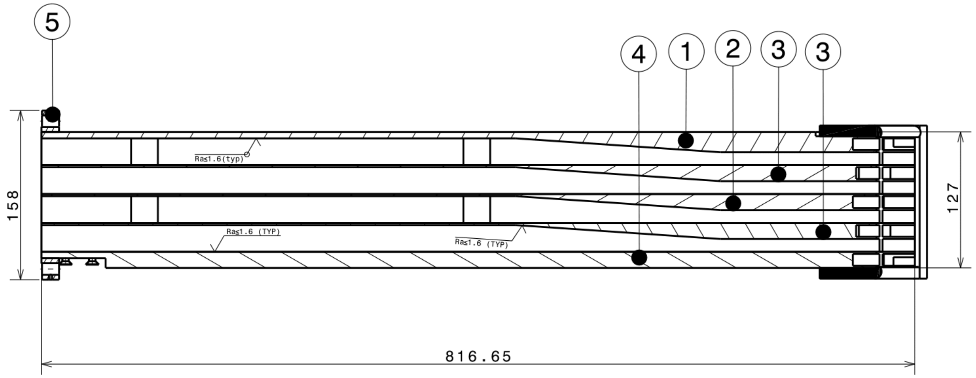

Section view E-E

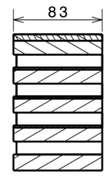

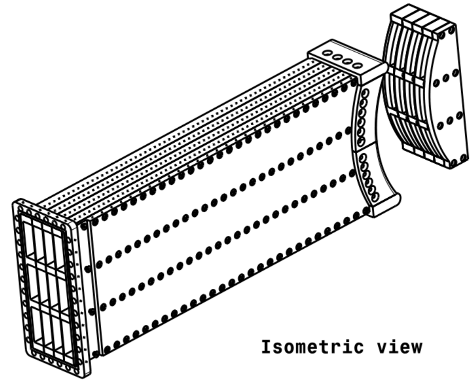

Isometric view

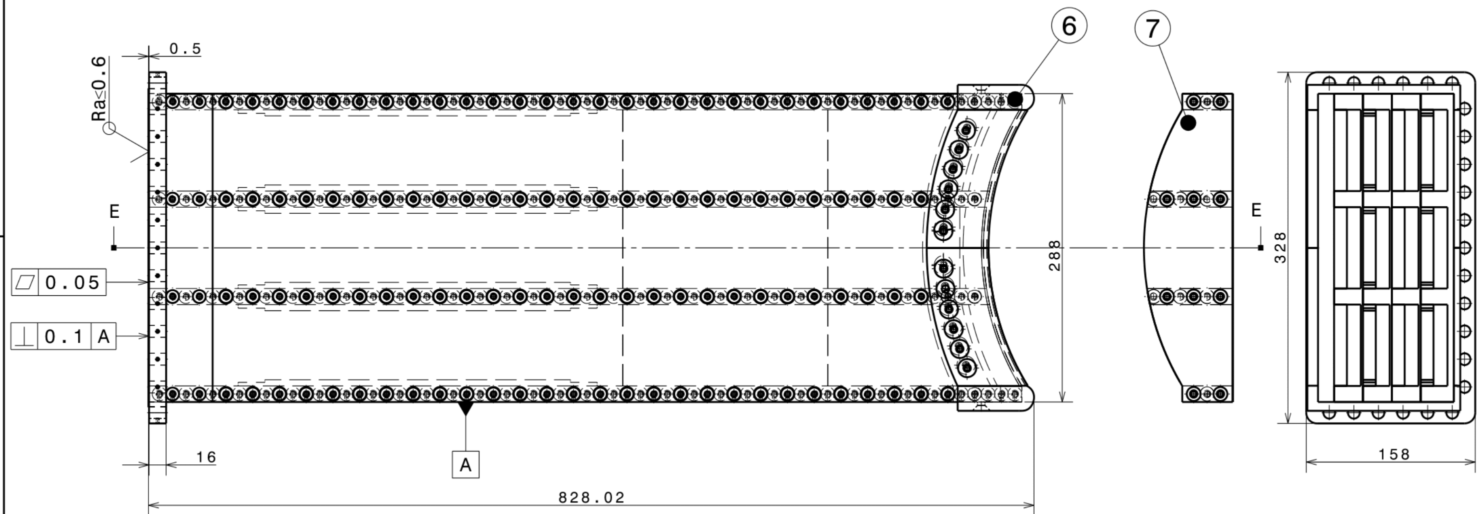

Free Issue Material(FIM): Graphite block shall be provided as a FIM for Tile assembly fabrication

**** Indicates nuts and bolts required slotting and drilling works as per Vacuum protocol for avoiding trapped volume

SR NO	PART NO	DESCRIPTION	MATERIAL	QTY	REMARK
10	--	M6x15L CSK BOLT	SS304L	20Nos.	****
09	--	M8x60L bolts with plain washer,spring washer and nut	SS 304L	24Nos.	****
08	--	M6x35L CSK BOLT	SS 304L	560Nos.	****
07	7	TEST BLOCK ASSEMBLY	SS 304L	01No	-
06	6	TILE ASSEMBLY	Graphite	01No	FIM
05	5	FLANGE	SS 304L	01No	-
04	4	PLATE-4	SS 304L	01No	-
03	3	PLATE-3	SS 304L	02Nos	-
02	2	PLATE-2	SS 304L	01No	-
01	1	PLATE-1	SS 304L	01No	-

Note: At few locations, arrangement for wire clamps and thermocouple holes shall be made as per IPR requiremtns

DRG.NO	▽ 8.25	▽▽ 1.6-8	▽▽▽ 0.025-1.6	▽▽▽▽ < 0.025
CO-ORDINATED BY				

MACHINING DEVIATIONS FOR NON-TOLERANCED DIMENSIONS

LENGTH IN mm OF SHORTER SIDE OF ANGLES				LENGTH OR DIA	UPTO 6	6-30	30-120	120-315
UPTO 10	10-50	50-120	OVER 120-400					
±1°	±0°-30'	±0°-20'	±0°-10'		±0.1	±0.2	±0.3	±0.5

REVISION COLUMN

REV	ZONE	DESCRIPTION	DATE	REMARKS	APPROVED BY

ASS'Y GROUP:

ALL DIMENSIONS ARE IN `mm' UNLESS OTHERWISE STATED

SCALE	NTS	DATE
DRAWN	SUKHDEV	08/02/2017
CHECKED	PRP	08/02/2017
APPROVED		

INSTITUTE FOR PLASMA RESEARCH

BHAT, GANDHINAGAR-382 428.

TITLE

END COMPONENT WITH TILE AND TEST BLOCK ASSEMBLY

REF DRG NO: | REV 01

DRG.NO IPR/ADT/LH/UPG/001.A3 | SHEET 05 OF 10

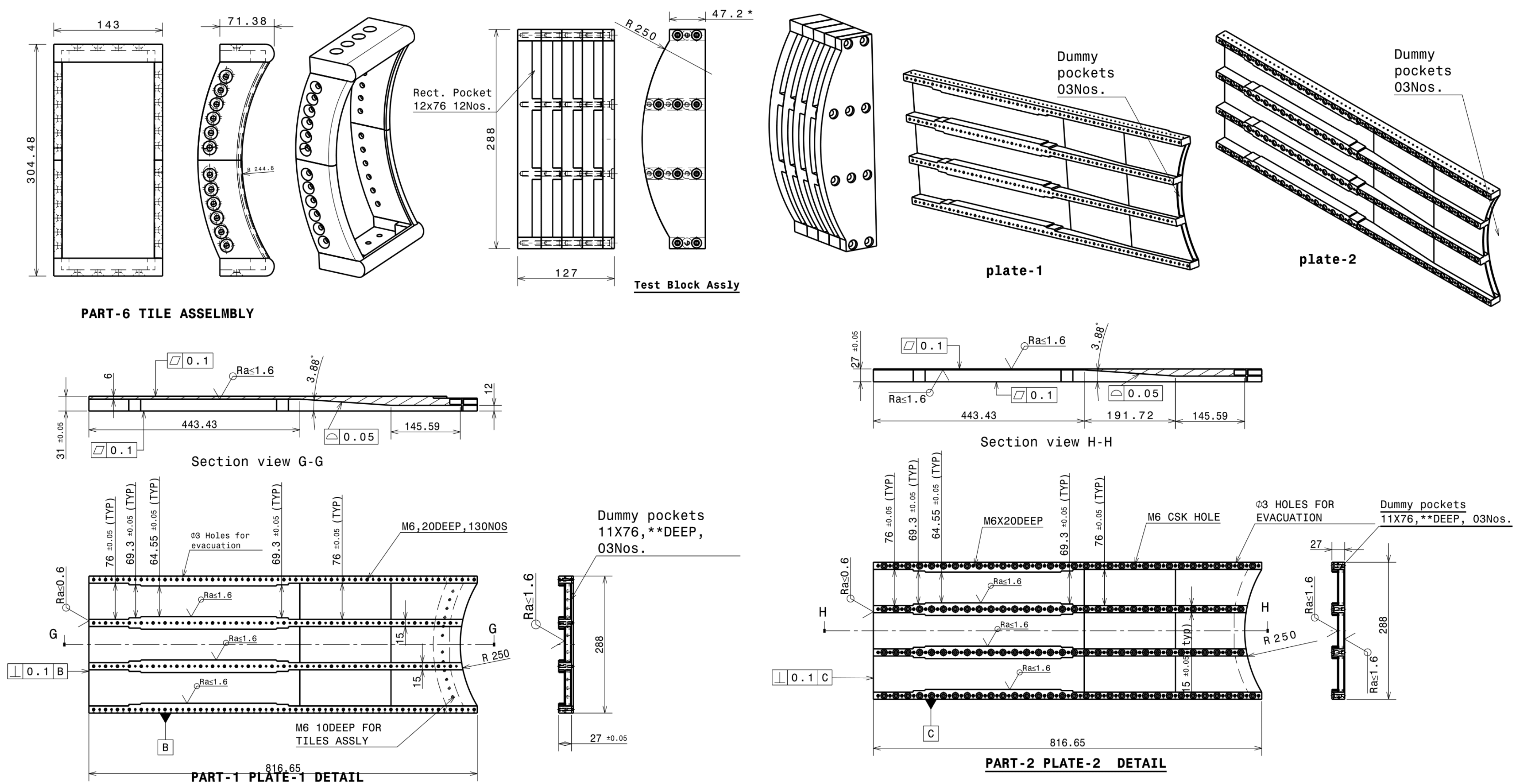

47.2* final length will be provided at the time of drawing approval
**Deep Exact dimension shall be provided at the time of Fab. drawing approval

NOTE:
1. All surface shall be free from scratches.
2. All sharp edges or corners (Except Inner Profile) shall be rounded off.
3. cleaning and passivation to be done as per approved procedure.
4. Electropolishing shall be done as per approved procedure

DRG.NO	∇ 8.25	∇∇ 1.6-8	∇∇∇ 0.025-1.6	∇∇∇∇ < 0.025
CO-ORDINATED BY				

MACHINING DEVIATIONS FOR NON-TOLERANCED DIMENSIONS

LENGTH IN mm OF SHORTER SIDE OF ANGLES				LENGTH OR DIA	UPTO 6	6-30	30-120	120-315
UPTO 10	10-50	50-120	OVER 120-400					
±1°	±0°-30'	±0°-20'	±0°-10'		±0.1	±0.2	±0.3	±0.5

REVISION COLUMN

REV	ZONE	DESCRIPTION	DATE	REMARKS	APPROVED BY

ASS'Y GROUP:		
ALL DIMENSIONS ARE IN `mm' UNLESS OTHERWISE STATED		
SCALE	NTS	DATE
DRAWN	SUKHDEV	08/02/2017
CHECKED	PRP	08/02/2017
APPROVED		

INSTITUTE FOR PLASMA RESEARCH
BHAT, GANDHINAGAR-382 428.

TITLE: Component and sub assembly details

REF DRG NO:	REV 01
DRG.NO IPR/ADT/LH/UPG/001.A3	SHEET 06 OF 10

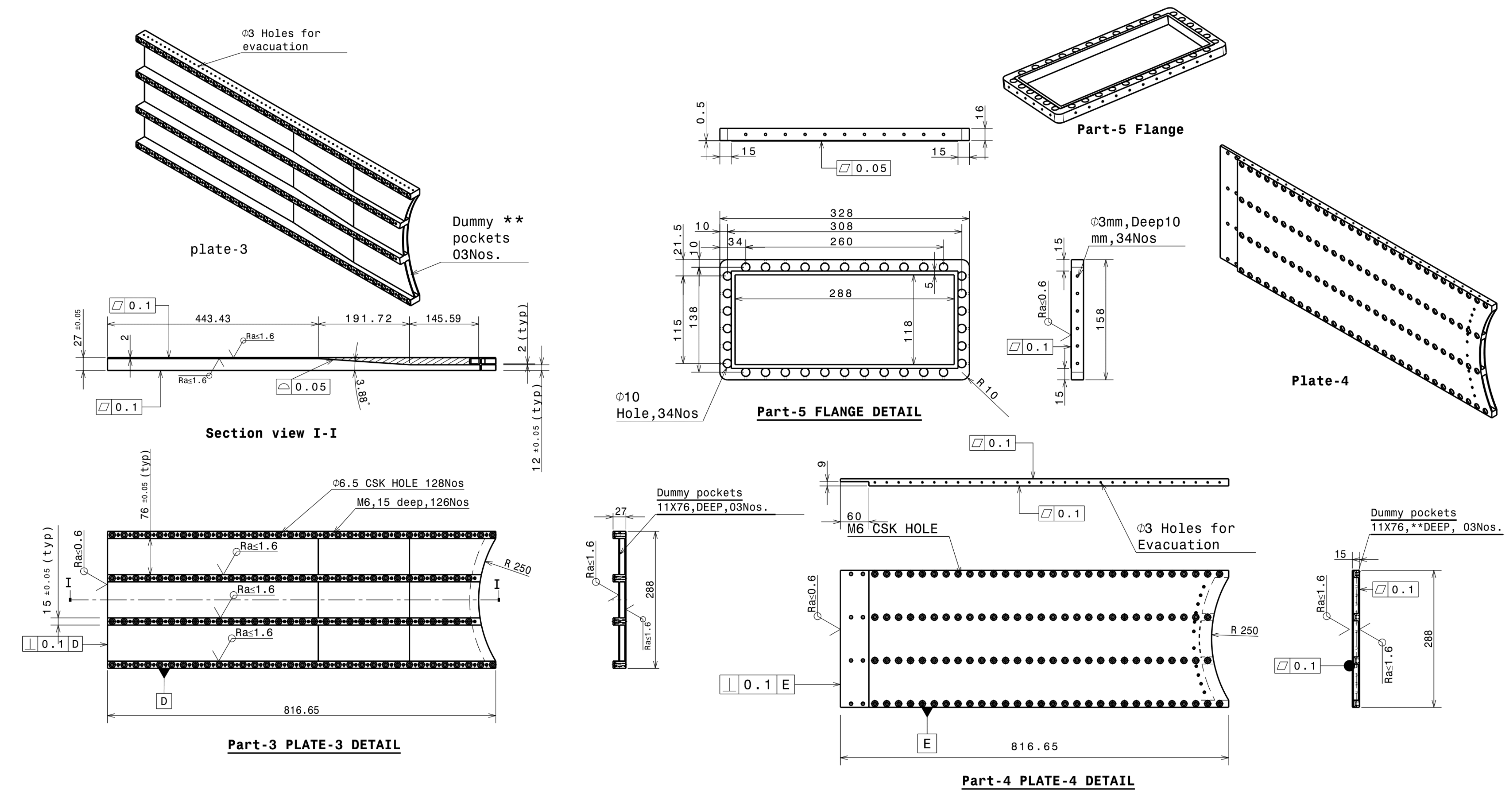

NOTE:

(1) Tolerance for Inner tapper rect. pockets dimension are +/-0.05mm.

** Indicates pocket deep shall be decided at the time of fab. drawing approval

DRG.NO	▽ 8.25	▽▽ 1.6-8	▽▽▽ 0.025-1.6	▽▽▽▽ < 0.025
CO-ORDINATED BY				

MACHINING DEVIATIONS FOR NON-TOLERANCED DIMENSIONS

LENGTH IN mm OF SHORTER SIDE OF ANGLES				LENGTH OR DIA	UPTO 6	6-30	30-120	120-315
UPTO 10	10-50	50-120	OVER 120-400		±0.1	±0.2	±0.3	±0.5
±1°	±0°-30'	±0°-20'	±0°-10'					

REVISION COLUMN

REV	ZONE	DESCRIPTION	DATE	REMARKS	APPROVED BY

ASS'Y GROUP:		
ALL DIMENSIONS ARE IN `mm' UNLESS OTHERWISE STATED		
SCALE	NTS	DATE
DRAWN	SUKHDEV	08/02/2017
CHECKED	PRP	08/02/2017
APPROVED		

INSTITUTE FOR PLASMA RESEARCH

BHAT, GANDHINAGAR-382 428.

TITLE

Component Details

REF DRG NO:		REV 01
DRG.NO	IPR/ADT/LH/UPG/001.A3	SHEET 07 OF 10

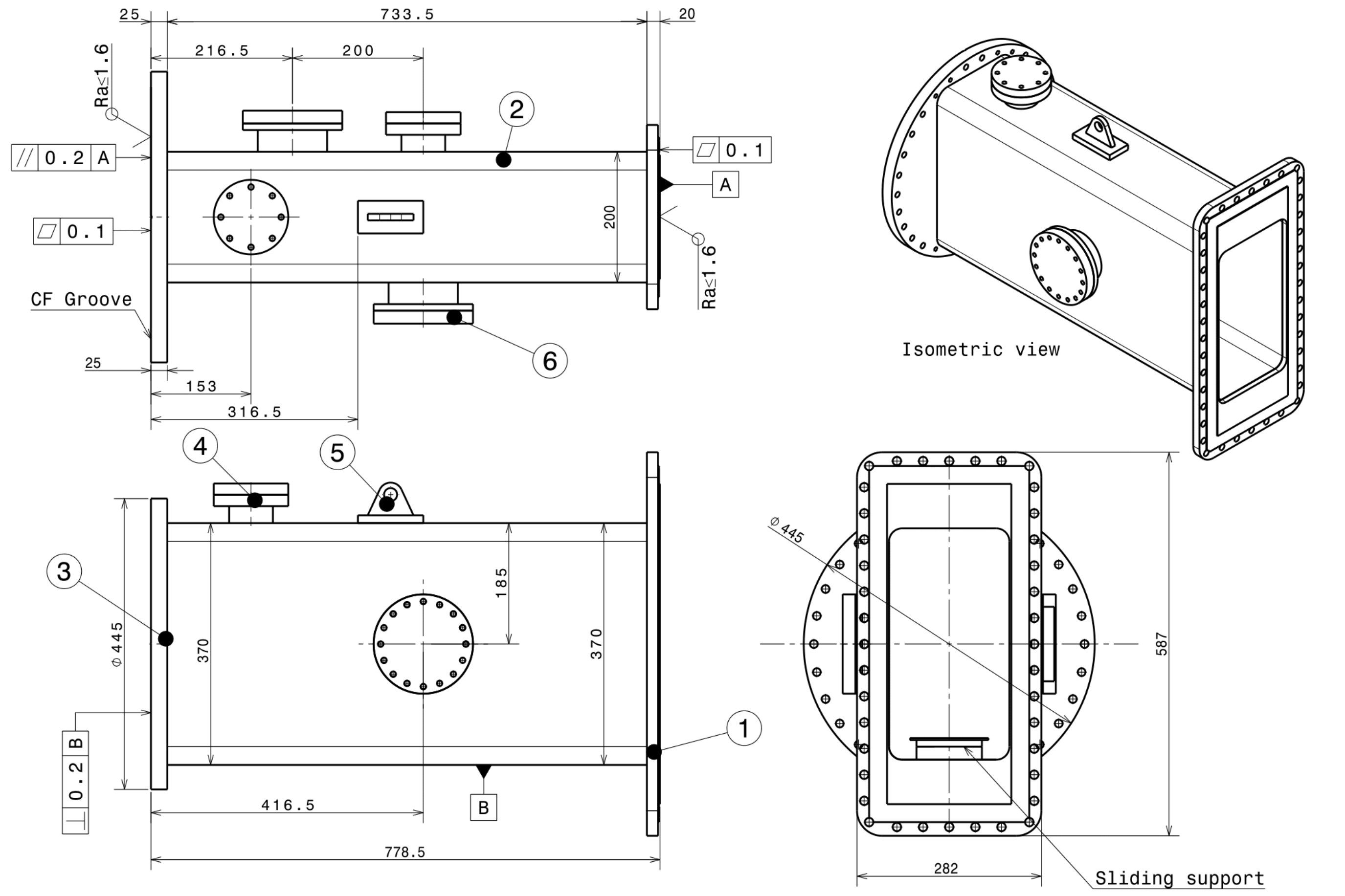

NOTE-2:

(1) Helium leak tightness of weld joints should be less than or equal to 1 x 10^-9 mbar liter per second.
(2)High Vacuum test shall be carried out for whole assembly with and without baking
(3) Global leak rate should be less than 5x10^-9 mbar liter per second

Special Note:
Sliding support for End component assembly inside Enclosure has to be designed in due consultaion with IPR.

Note:

(1) All weld joint shall be TIG welded (2) Single pass welding shall be employed wherever possible to avoid trapping of gases between the weld joint (3) All weld shall be ground smooth and flushed with joining surfaces with convex curvature with adjoining wall (4) Use fixtures during welding, machining and heat treatment (5) All the inner surfaces and inner components surfaces shall have surface finish of 0.8 to 1.5microns (6) Enough care shall be taken to avoid damage (Dent and Scratches) during handling and storing of raw material, semi finished product and finish products (7) RT/UT shall be carried out on all the possible weld (8) All component which where seeing UHV shall be subjected to heat treatment at component stage as per approved procedure (9) After heat treatment component shall be subjected to electro polishing and ultrasonic cleaning as per approved procedure (10) All sharp corners shall be rounded off (11) Abrasive cleaning of surface exposed to vacuum is not allowed (12) During electropolishing the gasket seating portion of the CF flange shall be protected from by using suitable material

SR NO	PART NO;	DESCIPTION	MATERIAL	QTY	REMARK
13	-	M12X60L Hex. bolt with plain washer, spring washer and nut	SS304L	40Nos.	-
12	-	M10X60L Hex. bolt with plain washer, spring washer and nut	SS304L	30Nos.	-
11	-	M8X55L Hex. bolt with plain washer, spring washer and nut	SS304L	48Nos.	-
10	-	CF gasket 398 OD	Soft Copper	02No.	-
09	-	Rect. Blank 282x587x20thk.	SS304L	01No.	-
08	-	100CF Gasket	Soft Copper	04Nos.	-
07	-	63CF Gasket	Soft Copper	04Nos.	-
06	6	100CF Port Assembly With Blank Flange	SS 304L	02Nos.	-
05	5	Lifting Plate Asly	SS 304L	01Nos.	-
04	4	63CF Port Assembly With Blank Flange	SS 304L	02Nos.	-
03	3	Circular Flange	SS 304	01No.	REF. Sheet 10 OF 10
02	2	Enclosure shell 8thk.	SS 304	01No.	-
01	1	Rectangular Flange	SS 304	01No.	REF. Sheet 10 OF 10

DRG.NO	▽ 8.25	▽▽ 1.6-8	▽▽▽ 0.025-1.6	▽▽▽▽ < 0.025
CO-ORDINATED BY				

MACHINING DEVIATIONS FOR NON-TOLERANCED DIMENSIONS

LENGTH IN mm OF SHORTER SIDE OF ANGLES				LENGTH OR DIA	UPTO 6	6-30	30-120	120-315
UPTO 10	10-50	50-120	OVER 120-400					
±1°	±0°-30'	±0°-20'	±0°-10'		±0.1	±0.2	±0.3	±0.5

REVISION COLUMN

REV	ZONE	DESCRIPTION	DATE	REMARKS	APPROVED BY

ASS'Y GROUP:

ALL DIMENSIONS ARE IN `mm' UNLESS OTHERWISE STATED

SCALE	NTS	DATE
DRAWN	SUKHDEV	08/02/2017
CHECKED	PRP	08/02/2017
APPROVED		

INSTITUTE FOR PLASMA RESEARCH
BHAT, GANDHINAGAR-382 428.

TITLE
ENCLOSURE

REF DRG NO:

REV 01

DRG.NO IPR/ADT/LH/UPG/001.A3

SHEET 08 OF 10

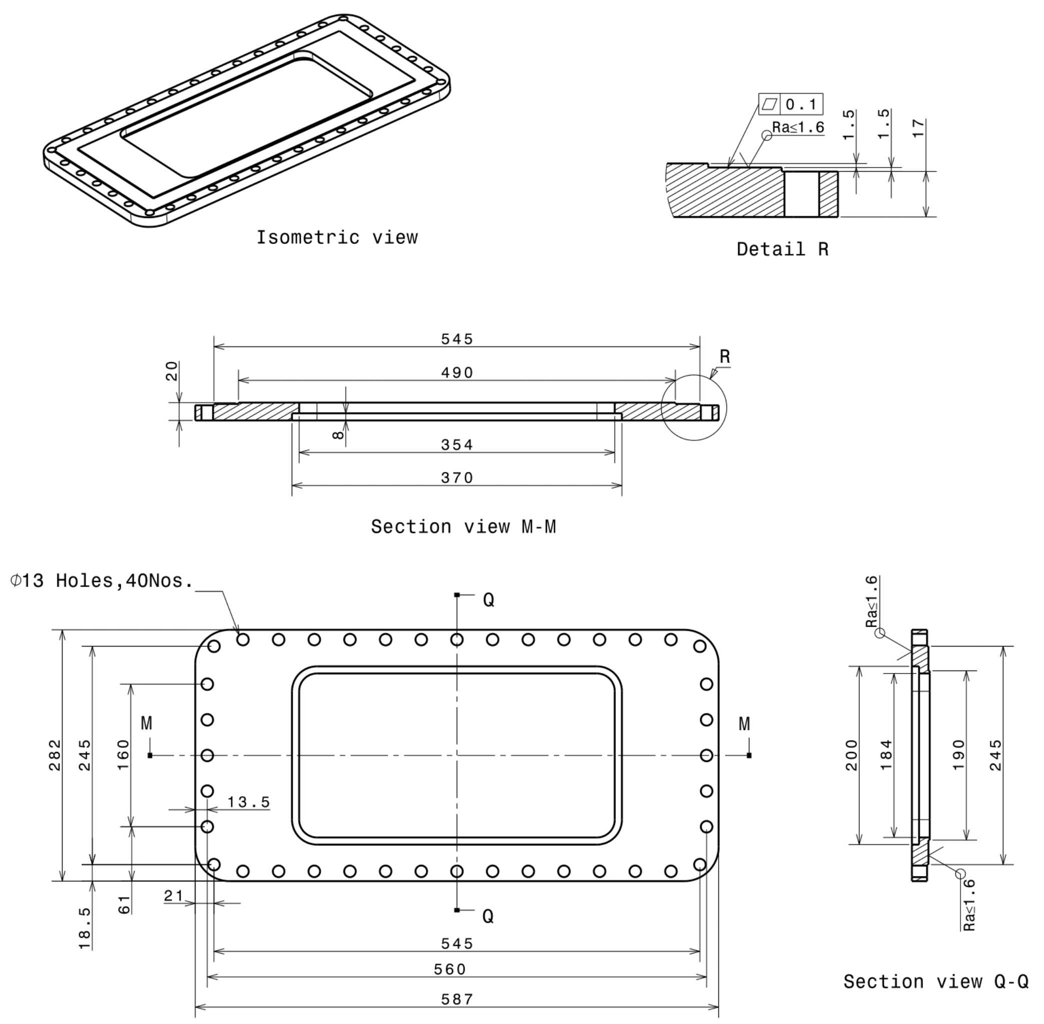

Part-1 Rectangular Flange Detail

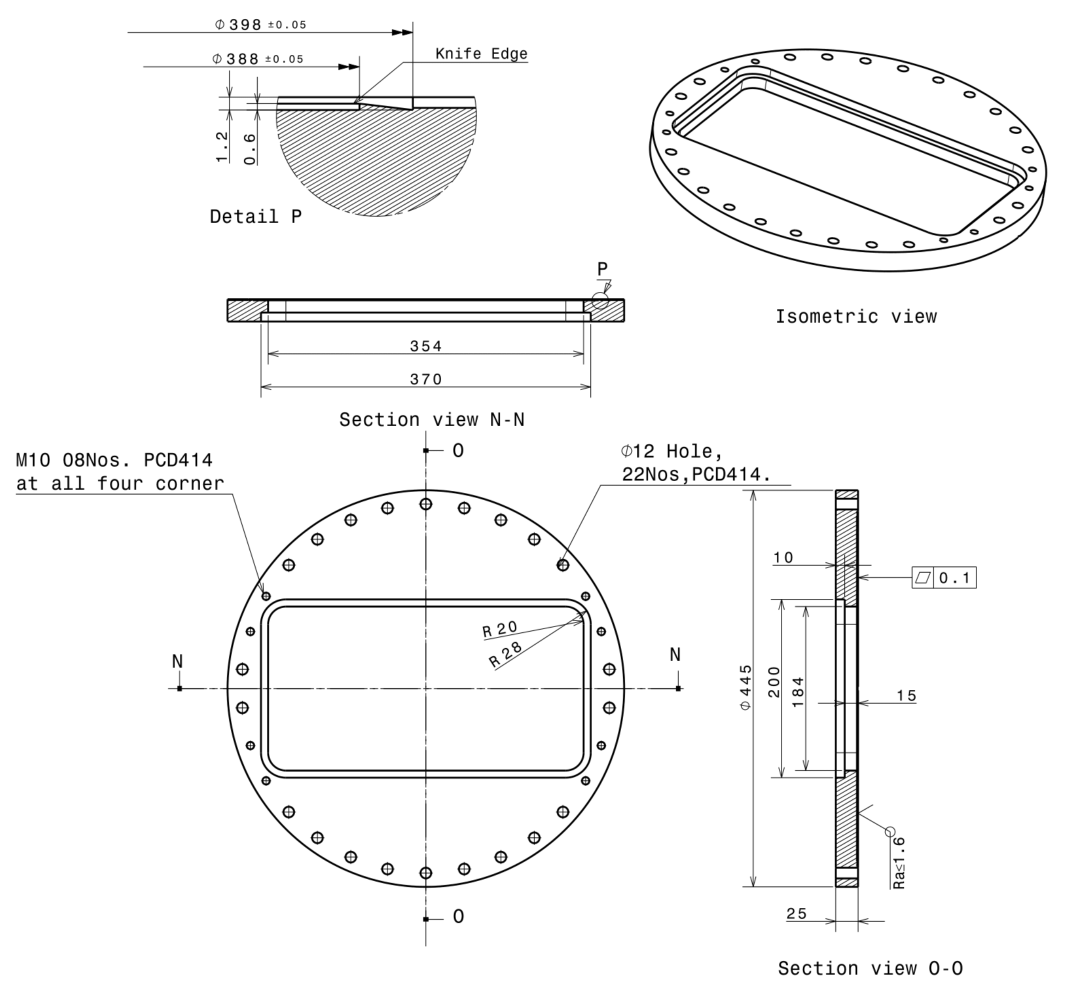

Part 3 Circular Flange Detail

Note:
1. All surface shall be free from scratches.
2. All sharp edges shall be rounded off.
3. cleaning and passivation to be done as per approved procedure.
4. Electropolishing shall be done as per approved procedure

DRG.NO	▽ 8.25	▽▽ 1.6-8	▽▽▽ 0.025-1.6	▽▽▽▽ < 0.025
CO-ORDINATED BY				

MACHINING DEVIATIONS FOR NON-TOLERANCED DIMENSIONS

LENGTH IN mm OF SHORTER SIDE OF ANGLES				LENGTH OR DIA	UPTO 6	6-30	30-120	120-315
UPTO 10	10-50	50-120	OVER 120-400		±0.1	±0.2	±0.3	±0.5
±1°	±0°-30'	±0°-20'	±0°-10'					

REVISION COLUMN

REV	ZONE	DESCRIPTION	DATE	REMARKS	APPROVED BY

ASS'Y GROUP:		
ALL DIMENSIONS ARE IN `mm' UNLESS OTHERWISE STATED		
SCALE	NTS	DATE
DRAWN	SUKHDEV	08/02/2017
CHECKED	PRP	08/02/2017
APPROVED		

INSTITUTE FOR PLASMA RESEARCH

BHAT, GANDHINAGAR-382 428.

TITLE

FLANGE DETAIL

REF DRG NO:		REV 01
DRG.NO	IPR/ADT/LH/UPG/001.A3	SHEET 09 OF 10

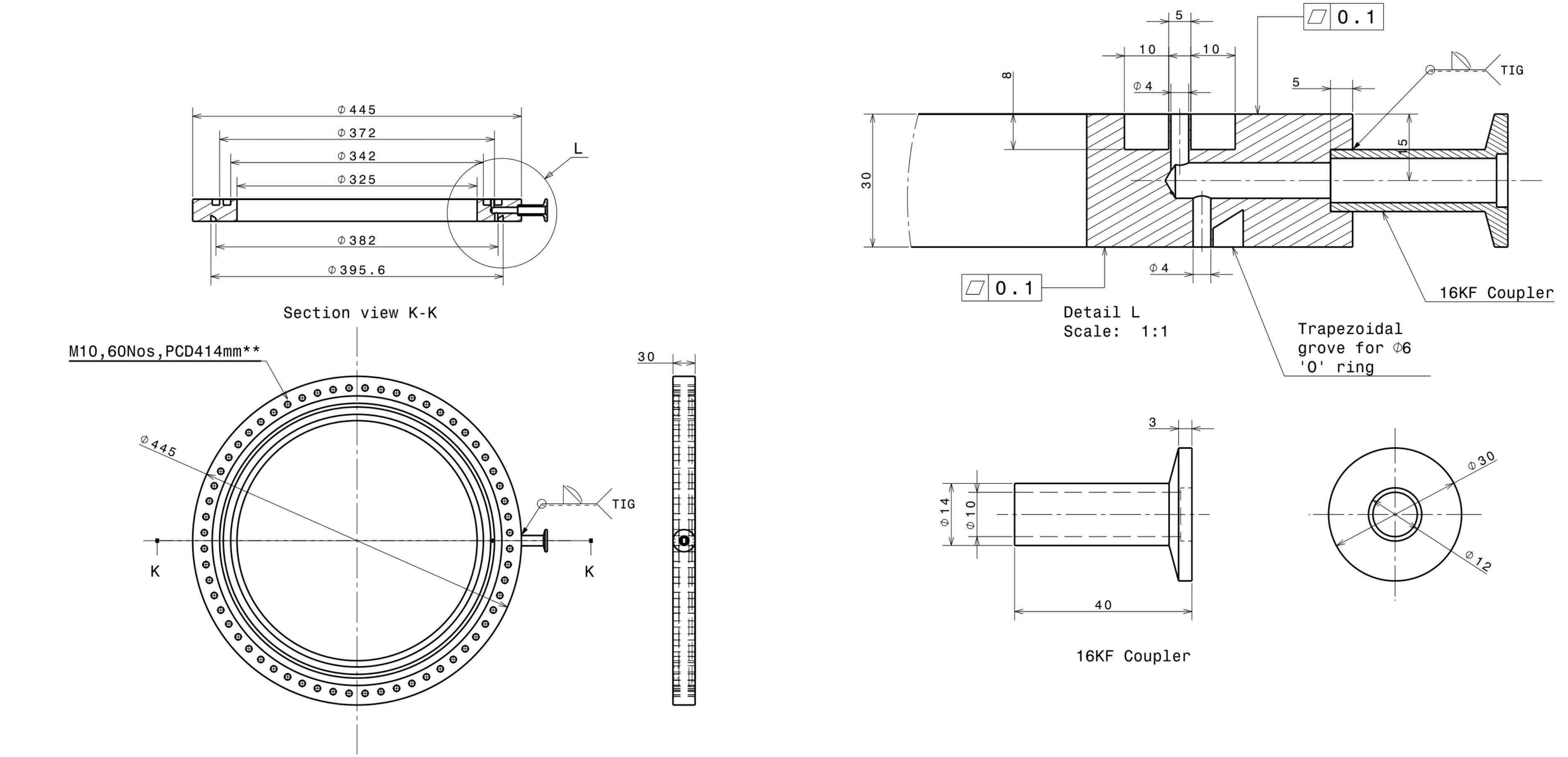

Note:
1. All surface shall be free from scratches.
2. All sharp edges shall be rounded off.
3. cleaning and passivation to be done as per approved procedure.
4. Electropolishing shall be done as per approved procedure

**Indicates holes should match with bellow flange

DRG.NO	▽ 8.25	▽▽ 1.6-8	▽▽▽ 0.025-1.6	▽▽▽▽ < 0.025
CO-ORDINATED BY				

MACHINING DEVIATIONS FOR NON-TOLERANCED DIMENSIONS

LENGTH IN mm OF SHORTER SIDE OF ANGLES				LENGTH OR DIA	UPTO 6	6-30	30-120	120-315
UPTO 10	10-50	50-120	OVER 120-400		±0.1	±0.2	±0.3	±0.5
±1°	±0°-30'	±0°-20'	±0°-10'					

REVISION COLUMN

REV	ZONE	DESCRIPTION	DATE	REMARKS	APPROVED BY

ASS'Y GROUP:		
ALL DIMENSIONS ARE IN `mm' UNLESS OTHERWISE STATED		
SCALE	NTS	DATE
DRAWN	SUKHDEV	08/02/2017
CHECKED	PRP	08/02/2017
APPROVED		

INSTITUTE FOR PLASMA RESEARCH

BHAT, GANDHINAGAR-382 428.

TITLE

Intermediate Flange

REF DRG NO:		REV 01
DRG.NO	IPR/ADT/LH/UPG/001.A3	SHEET 10 OF 10

Appendix C

Fabrication and Mechanical Tests

This appendix discusses the methodologies devised and precise techniques identified for the fabrication of the PAM section. Further, the results of the mechanical tests carried out to ensure its compatibility with the ADITYA –U tokamak are also reported. The brazing procedure employed for the brazing of multiple joints (metallised Al_2O_3-Cu and Cu-SS) of the RF vacuum window is explained in detail. The Ultrasonic test performed on these joints, the Helium Leak Detection (HLD) and sniffing test performed on either side of the window to qualify the brazed joints for their vacuum tightness are discussed.

C.1 Fabrication and Mechanical tests of the PAM launcher

This section discusses the fabrication scheme implemented and the procedure employed for the realisation of the PAM section. Further, the mechanical qualification tests carried out on the launcher is discussed in detail.

C.1.1 Stacking scheme of the PAM section

The PAM section is realised by stacking a total of five plates in a sequential manner. These plates have the waveguide profile scooped out of the thick SS304L plates. The details of these plates are as follows:

a The first type of plate (labelled as “A” for future reference), shown in Fig. C.1, is fabricated using the Vertical Milling Centre (VMC) machine. It has three C-sections (open waveguides), each having a 90° step phase shifter (refer Chapter 3 for design) followed by a tapered waveguide and a straight active waveguide section at the end. Each C-section pocket has a cross-sectional dimension of 76 mm × 25 mm and 76 mm × 12 mm at the input and output (cross-section of the active waveguide), respectively. A 22.5 mm deep passive waveguide pocket having a cross-section of 76 mm × 11 mm is machined out on the right of the active waveguide using the EDM spark technique. Further, it can be observed that plate “A” has alternate sunken through holes (even numbered holes) and tapped blind holes (odd numbered holes) to stack the adjacent plate with good metallic contact. It is to be noted that the terms “even” and “odd” are with respect to the first line array of holes marked in Fig. C.1. Also, there are holes on the top of the plate to release trapped gases between the bolt and the holes (sunken through or tapped blind types).

b The second type of plate, referred as “B” and shown in Fig. C.2, is fabricated with each C-section having a straight waveguide at the start of the plate instead of the step phase shifter (as in plate “A”). Again the straight waveguide is followed by a tapered and a straight active waveguide. Passive waveguide pockets are machined out on the right of the active waveguide. The dimensions of the C-section and that of the passive waveguides are the same as that of Plate A. It is to be noted that, in this plate, the first hole in the first line array is a sunken through hole (odd numbered) which matches with the first tapped blind hole of plate A. This enables a tight fit mechanical joint and further ensures good metallic contact between the plates.

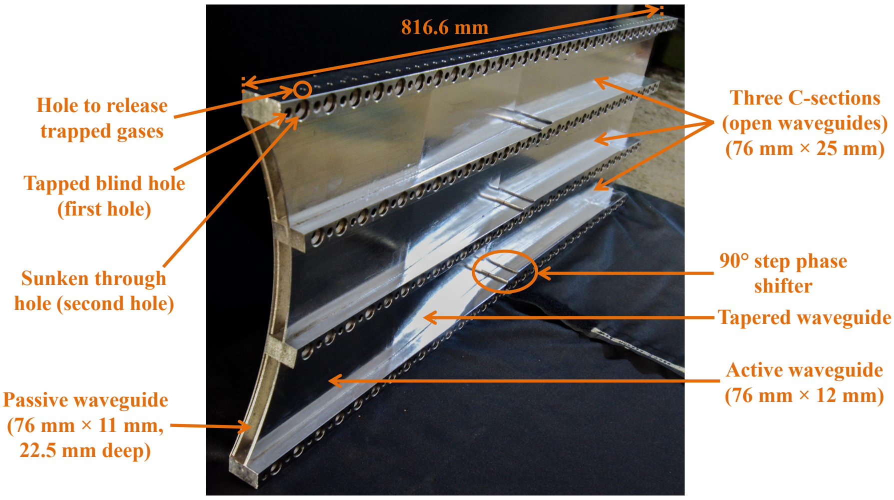

Figure C.1: 90° step phase shifter plate (Plate type A).

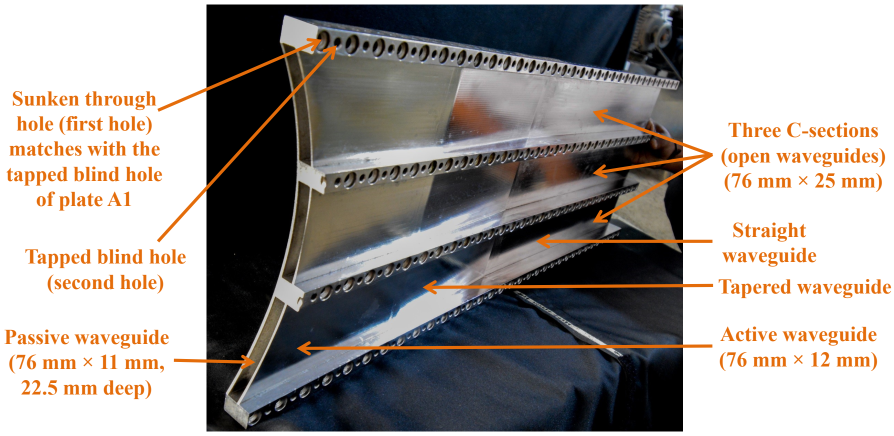

Figure C.2: Straight waveguide plate (Plate type B).

c The third type of plate (referred to as "C"), shown in Fig. C.3, is a covering solid plate with passive waveguide pockets at the mouth. It is used at the end of the stacking sequence.

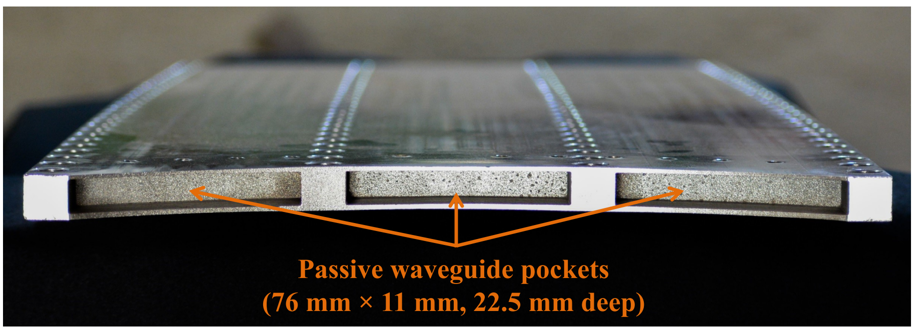

Figure C.3: Plate type C with passive waveguide pockets.

Initially, plate B1 (of type B) is bolted to plate A1 (of type A) such that all the sunken through holes of plate B1 and tapped blind holes of plate A1 are matched as shown in Fig. C.4a. B1 covers the three C-sections (open waveguides) of A1, thereby forming closed waveguides. The stacked combination of plates A1 and B1 forms one half of a module at the mouth of the launcher (Fig. C.4a) and the input to this half-module is formed on the other side (Fig. C.4b). Plate A1 is bolted to thick Mild Steel (MS) plate temporarily at the start of the stacking procedure to hold the bottom plate (A1) firmly during the procedure.

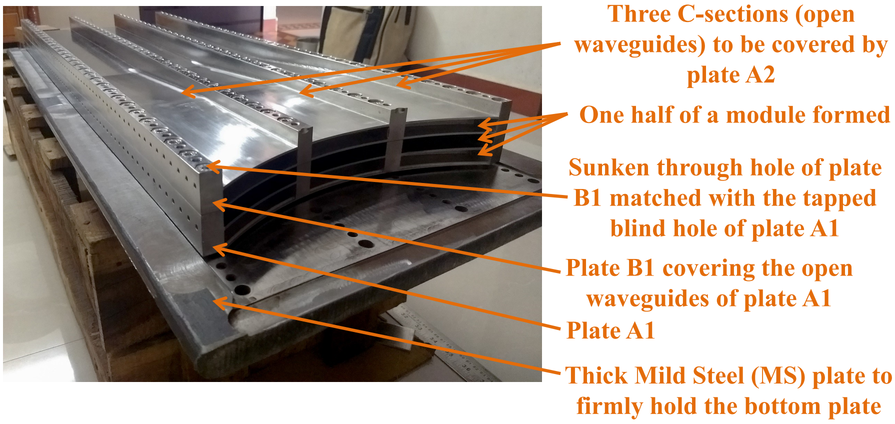

(a) Mouth side of the PAM section.

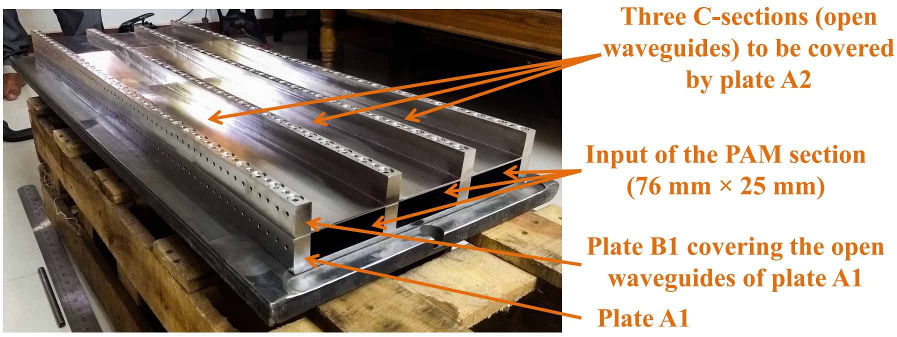

(b) Input side of the PAM section

Figure C.4: Stacked combination of plates A1 and B1.

Further, plate A2 is bolted to the above stacked combination of plates A1 and B1, thereby forming a stacked combination of A1-B1-A2 as shown in Fig. C.5a and Fig. C.5b. It is to be noted that the first sunken through hole of plate A2 is matched to the first tapped blind hole of plate B1 (which is already bolted to plate A1) and so on as shown in Fig. C.5a. This stacked combination forms a complete module (at the mouth) with one channel consisting of a step phase shifter and the other consisting of a straight waveguide.

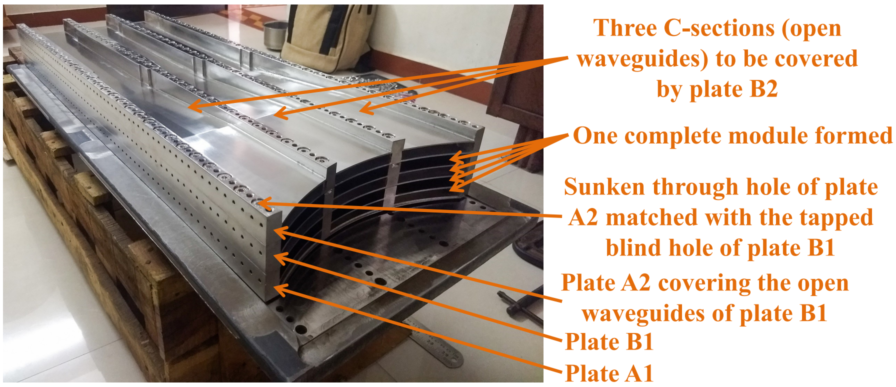

(a) Mouth side of the PAM section.

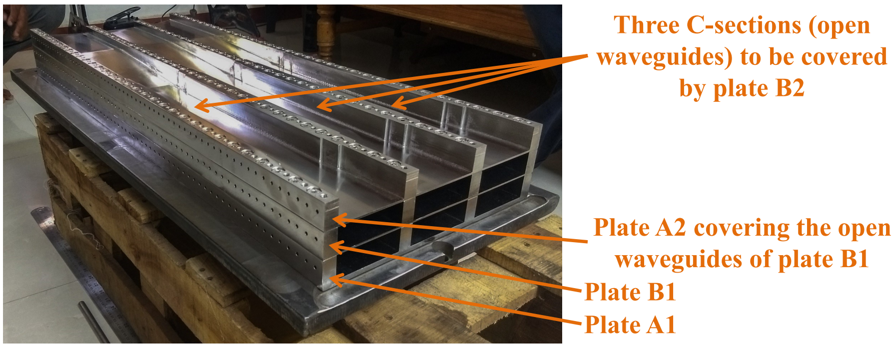

(b) Input side of the PAM section

Figure C.5: Stacked combination of plates A1, B1 and A2.

Further, plate B2 is added to the stack thereby forming A1-B1-A2-B2 as shown in Fig. C.6a and Fig. C.6b.

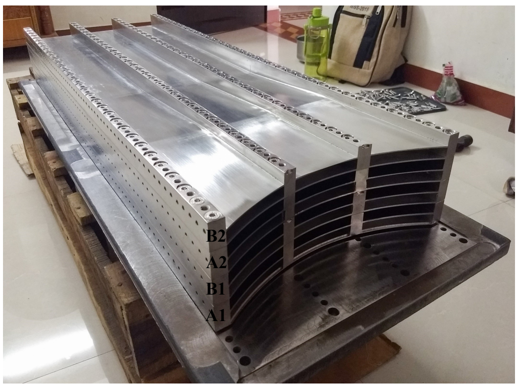

(a) Mouth side of the PAM section.

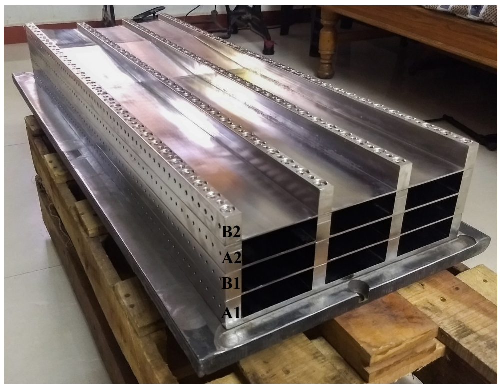

(b) Input side of the PAM section

Figure C.6: Stacked combination of plates A1, B1, A2, B2.

All the plates are bolted using customised M6 CSK bolts having a slot on its threading to allow the passage of trapped gases outside the assembly through the holes on top of the plate (see Fig. C.1)

Finally, Plate C is bolted to cover the complete assembly, thereby forming two toroidal modules and three poloidal sections. The input side of the PAM section has 12 waveguide pockets, each having a cross-section of 76 mm × 25 mm, as shown in Fig. C.7. The output of the tapered divider section is connected to this input. The launcher mouth formed on the other side has 15 passive waveguide pockets, 12 active waveguides and its surface is contoured to the plasma surface (poloidal radius = 250 mm) so as to geometrically match the two surfaces as shown in Fig. C.8.

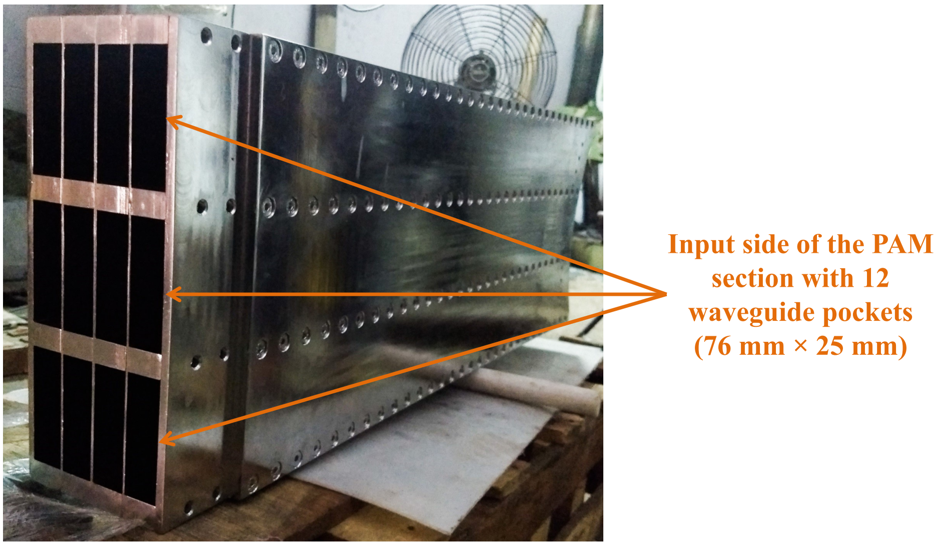

Figure C.7: Input side of the PAM section.

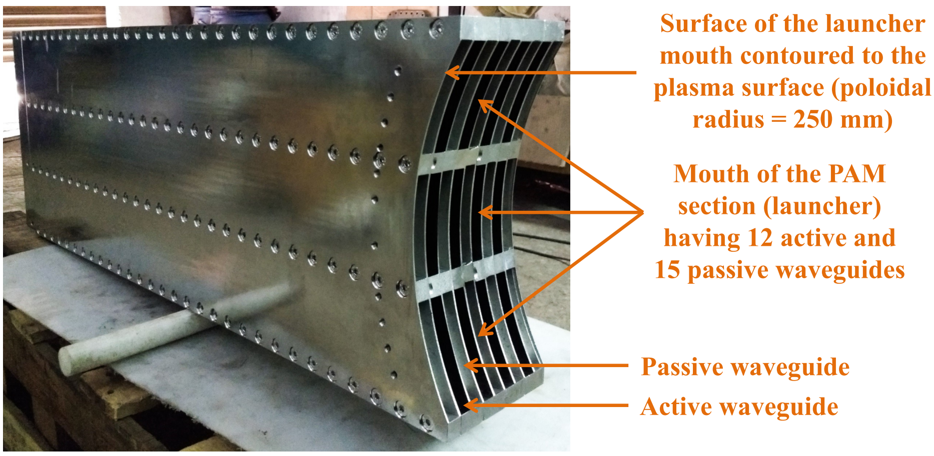

Figure C.8: Mouth of the PAM section.

C.1.2 Mechanical Qualification tests of the PAM launcher

C.1.2.1 Dimensional qualification test

One of the most important mechanical qualification tests, post fabrication, is the dimensional qualification test. The fabrication of the launcher is carried out precisely to meet all the dimensional tolerances and surface finish requirements and the tests performed to confirm the same are discussed in this subsection.

A dimensional qualification test is carried out; wherein, the critical dimensions of all the components of the launcher individually and that of the launcher as a whole are measured. All the dimensions are required to be within the tolerance limit of $\pm 50\,\mu$m. A typical test is carried out for the tapered divider as shown in Fig. C.9 and its corresponding results are further reported in detail.

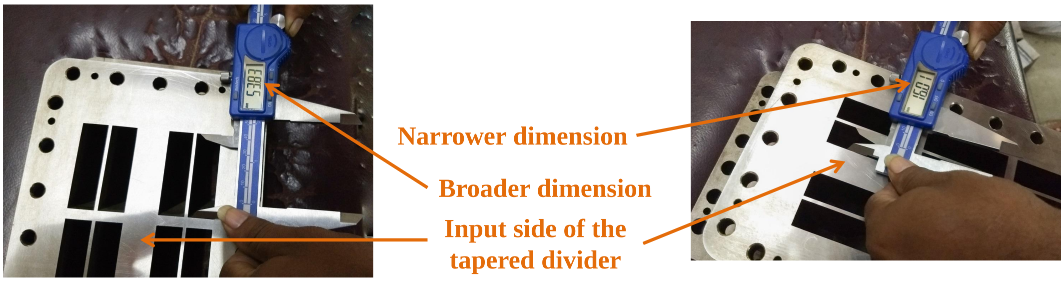

Figure C.9: Measurements carried out at the input side of the tapered divider. Broader dimension (designed value = 53.87 mm) (left), Narrower dimension (designed value = 16 mm) (right).

The critical dimensions of the tapered divider are that of the 12 rectangular cross-sections at the input and output of the divider as shown in Fig. 4.5 (Chapter 4). The 12 input pockets of the tapered divider, results of which are reported below, have a designed cross-section of 53.87 mm × 16 mm. Each cross-sectional dimension (broader or narrower) of the tapered divider is measured at three locations (top, middle and bottom of the pocket) to determine the deviations introduced because of the machining techniques as shown in Fig. C.10. Also, the input pockets, numbered for the ease of plotting the measurement results, are illustrated.

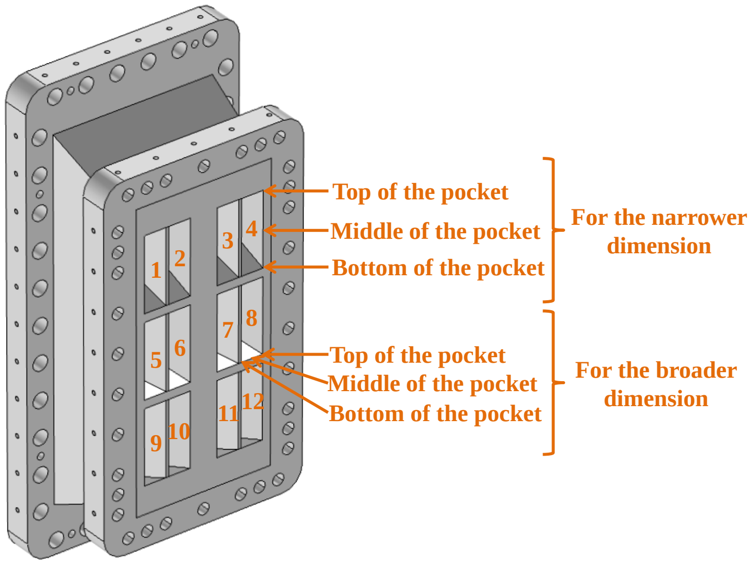

Figure C.10: Input side of the tapered divider illustrating the numbering and position of the top, middle and bottom of the pockets.

The measurement results for the broader and the narrower dimension are shown in Fig. C.11a and Fig. C.11b, respectively. The x-axis represent the pocket numbers and the y-axis represent the dimensions in mm. For each pocket, there are three measurement values corresponding to the three locations of measurement (top, middle and bottom). Horizontal dash-dot lines mark the tolerance limit of ±50 microns and the measurements suggest that dimensions are within this limit.

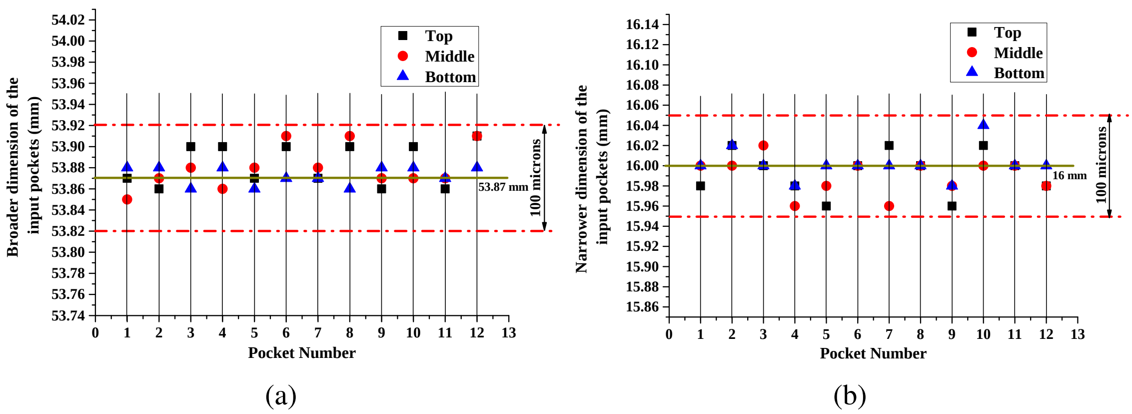

Figure C.11: Measurement results for the (a) broader dimension and (b) narrower dimension of the tapered divider.

Similar dimensional checks are performed for all the components of the launcher and of the integrated launcher and are found to be within the tolerance limit.

The surface finish of the inner surfaces of the components is critical in obtaining a low insertion loss and avoiding local E-field concentration and hence the RF breakdown. It is desired to obtain three delta surface finish (lower than the skin depth of around 7 μm) on the inner surfaces. A surface finish test is thus performed using a roughness meter. A typical test result obtained for the test performed on the launcher mouth inner surface is shown in Fig. C.12. It can be observed that the meter shows a reading of Ra (arithmetic mean deviation of the assessed profile) as 0.25 μm corresponding to the three delta finish.

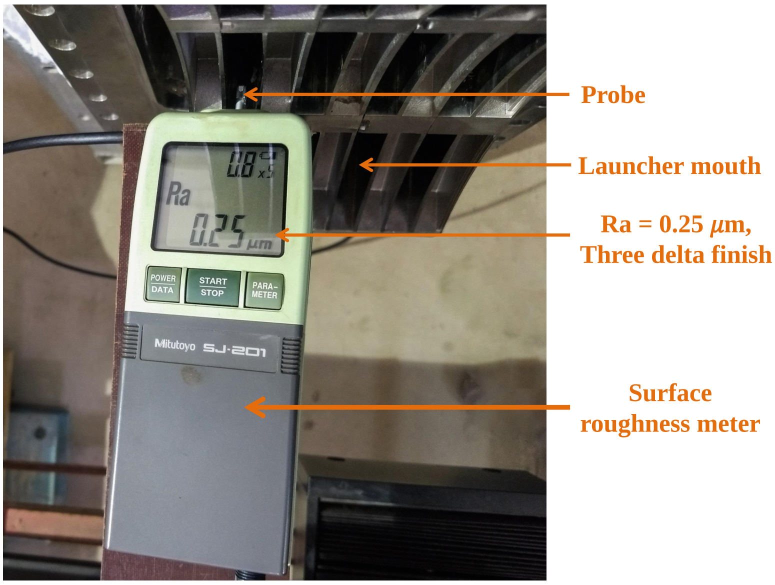

Figure C.12: Surface finish measurement of the inner surface of the launcher mouth using a roughness meter.

Similar surface finish measurements are performed at various locations in the inner profile of the launcher and are found to be satisfying the required criteria.

C.1.2.2 Baking cycle, Helium Leak Detection (HLD) and Vacuum test

The launcher is to be operated in the Ultra High Vacuum (UHV) environment of the tokamak. Thus, the baking of the complete launcher followed by the Helium Leak Detection (HLD) test and vacuum test is carried out.

Initially, the complete system is baked to remove any moisture, trapped gases, et cetera and tested for leaks (maximum leak rate $< 1 \times 10^{-9}$ mbar-l/s), if any. The bellow used in the PAM launcher is the same that was earlier used in the GRILL launcher (installed earlier on the ADITYA tokamak). The bellow is tested for any leaks (maximum leak rate $< 1 \times 10^{-9}$ mbar-l/s) in a standalone manner. It is mimicked by a cylindrical extension during the testing of the complete structure to avoid any damages to it. The specifications of the accessories used during these tests are reported in Table C.1.

Table C.1: Specifications of the accessories used during the Baking Cycle, Helium Leak Detection (HLD) and Vacuum test.

Component	**Make/Model/Specifications**
Helium Leak Detector	PIFEFFER HLT260
Calibrator	5.7×10^{-7} mbar-l/sec. Calibration date: 9^{th} Oct. 2018.
Turbo Molecular Pump	PIFEFFER TMU 521P n = 49980 rpm, f = 833 Hz, S(N2):520 l/s.
Rotary Vacuum Pump	DUO 10 Pumping speed: $10\,m^3$/hr
Ionisation Gauge	Granville-Philips 356 Range: 1×10^{-9} mbar to atm

The PAM launcher is large and complex. The detection of leaks in the complete structure during the vacuum test, at once, is very difficult. Thus, a three-stage vacuum test is carried out to qualify the structure sequentially. In the first stage, the PAM and the tapered divider sections along with the enclosure are tested. The mode converter section is not included in this stage. After the successful qualification of the first stage, the PAM and tapered divider sections are removed and the mode converter section is connected to the enclosure. The complete PAM structure is tested for its vacuum after the successful testing of the first two stages. The same procedure is followed to carry out the vacuum tests in all the three stages. Thus, the procedure pertaining to the final stage is discussed below.

The schematic of the setup employed for the vacuum test of the PAM launcher is illustrated in Fig. C.13. The complete structure (System Under Test (SUT)) is initially assembled and connected to the Turbo Molecular Pump (TMP) for the vacuum test. The pumping speed of the TMP employed is 520 l/s. A vacuum valve is used to switch between the connection of the TMP to the rotary pump (during pumping) or the HLD setup (during leak tests). An ionization gauge is connected to the system to monitor the vacuum level in the system. The TMP is appropriately water cooled using a Cooling unit while the gauge is cooled using a fan. Initially, the gases inside the launcher are pumped out using the Turbo Molecular Pump (TMP) via the rotary pump. Further, the rotary pump is disconnected and the TMP is connected to the Helium Leak Detection (HLD) setup and the system is tested for leaks if any.

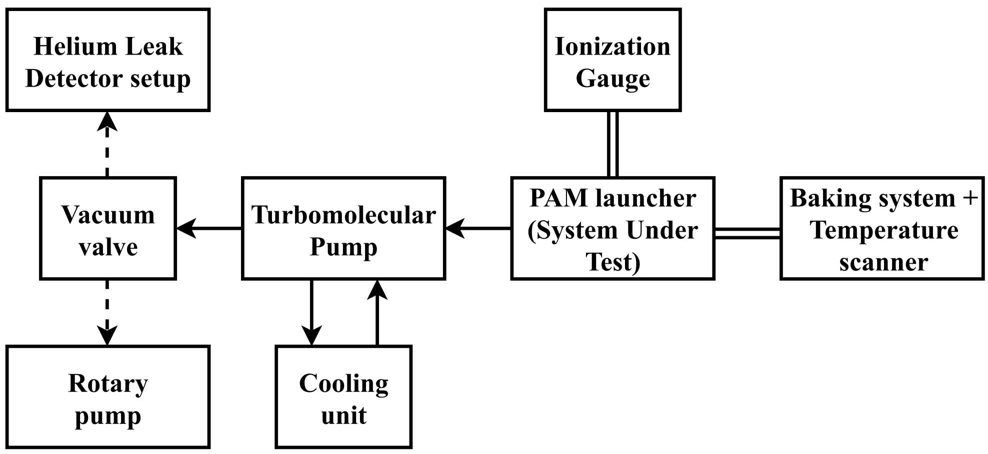

Figure C.13: Schematic illustrating the setup employed for the vacuum test of the PAM launcher.

After ensuring that the leak rate is below the desired threshold of 1×10^{-9} mbar-l/s, the system is baked at ∼180°C (maximum) for a 40 hours baking cycle to remove the trapped gases. The whole system under test is wrapped with baking tapes and special cloth for uniform heating. The schematic of the electronic setup used for baking of the launcher is shown in Fig. C.14. Variable autotransformers (Variacs) are used to pass current through the baking tapes resulting into the heating of the tapes and hence the system. Resistance Temperature Detectors (RTD's) are placed at various locations on the structure to detect the temperature of the structure at any instant. A temperature scanner is used to monitor the temperature detected by the RTD's. The temperature required to be maintained during the complete baking cycle is manually set using a computer. The computer also logs the temperature detected by each RTD at every second. A relay system is connected to the computer which detects the change in the set temperature and correspondingly switches the state of the variacs.

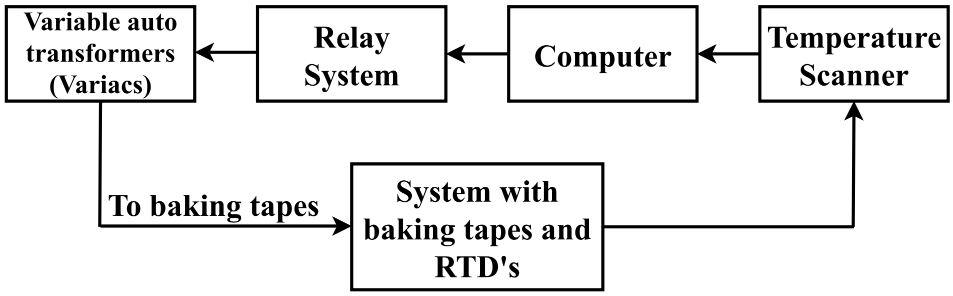

Figure C.14: Schematic illustrating the electronic setup used for baking.

The baking cycle and the procedure employed to achieve the desired vacuum are discussed below. The system is initially at room temperature of ~30°C. The heating phase of the baking cycle is 450 minutes long, wherein the desired temperature is increased by 15°C in every 45 min. The system is allowed to uniformly heat up to the desired temperature in this 45 min window. At every step, the impurities are released and the vacuum level keeps degrading. These impurities are pumped out via the TMP. The system is maintained at 180°C for 24 hours for the removal of maximum impurities. In the process of baking, various leaks, which are otherwise not detectable, open up and the vacuum level drops further. The cooling phase is initiated after 24 hours (after the vacuum reaches its lowest possible level and becomes constant). The cooling steps are the same as the heating steps (15°C in 45 min) until the system reaches 50°C. After the system reaches 50°C, the variacs are completely turned off and natural cooling is employed. The vacuum level rises during cooling and the best vacuum level is achieved after continuously pumping for several days post the baking cycle. Once the system is completely cooled, the tapes are removed and HLD is employed to detect any leaks generated during baking. Appropriate measures are taken to remove the leaks. Several baking cycles are run and TMP pumping is employed for several days. Fig. C.15 shows the launcher system connected to the TMP, rotary pump and various other accessories required for the vacuum test, while Fig. C.16 shows that a vacuum level of 1.3×10^{-8} mbar is achieved.

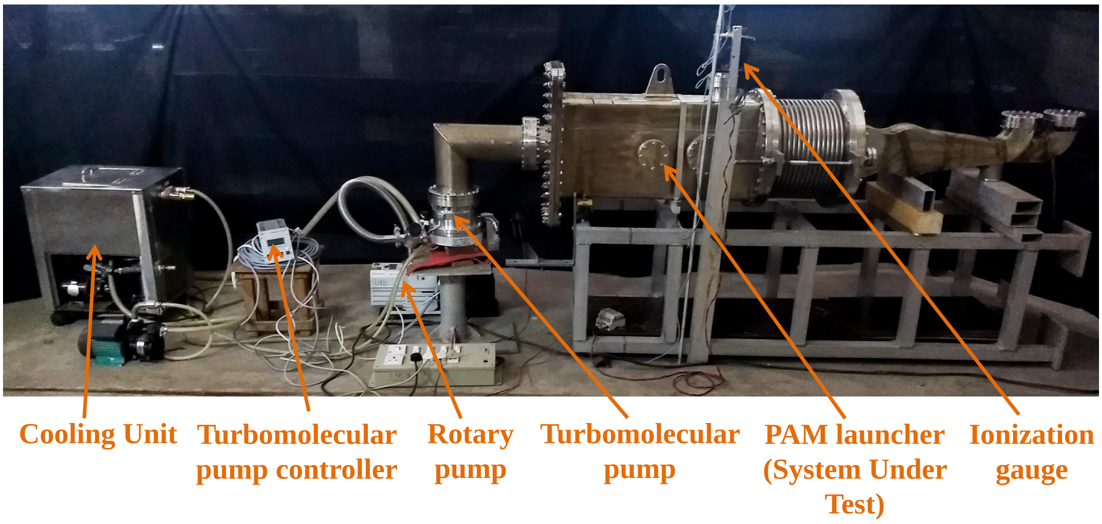

Figure C.15: Baking and vacuum setup.

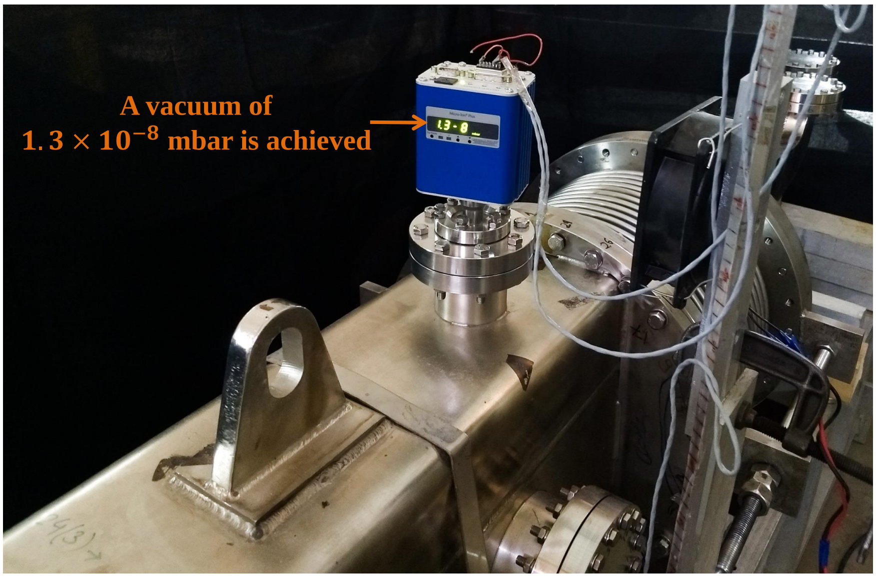

Figure C.16: Vacuum level of 1.3×10^{-8} mbar is achieved.

C.1.2.3 DC isolation test

It is important to isolate the ground of the tokamak and that of the RF during tokamak operations. Thus, a DC break is provided between the port flange and the RF input using the double O-ring flange (discussed in Chapter 4). The isolation between the two grounds is tested using an Insulation Resistance Tester (Megohmmeter) and an isolation resistance of 36.7 MΩ is obtained for a voltage of 2.5 kV as shown in Fig. C.17.

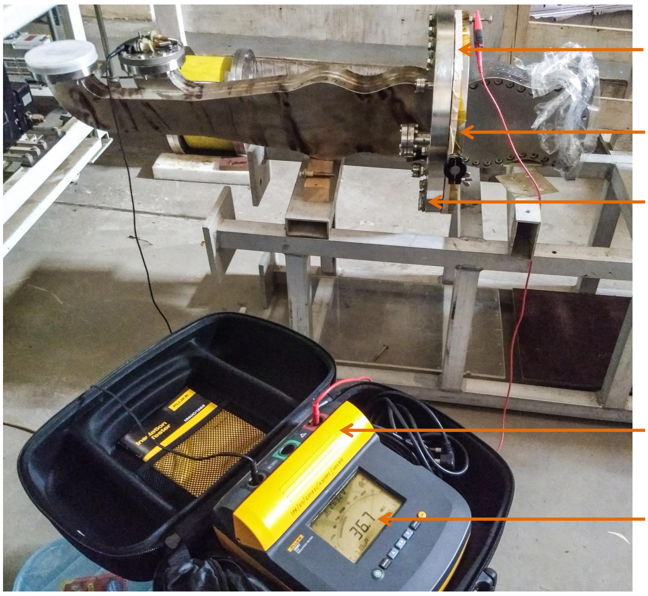

Figure C.17: Isolation test conducted on the two sides (port flange side and the RF input side) of the double O-ring flange .

C.2 Fabrication and Mechanical Tests of the RF vacuum window

The RF and mechanical design of the pill box based RF vacuum window was discussed in Chapter 6. This section further elaborates on the fabrication and qualification process of the window by detailing the brazing process and mechanical tests carried out.

C.2.1 Brazing of the RF vacuum window

A high temperature vacuum brazing technique is employed for the joining of the alumina disc at the centre and the rectangular to circular transition on one end of the copper cylinder using CuSil as the BFM. The following procedure is carried out for the precise and successful brazing of the joints.

C.2.1.1 Cleaning of the brazing assembly components

The components to undergo brazing are cleaned so as to maintain dirt free brazing surfaces. Any form of contamination in the brazing surfaces can lead to flaws, cracks or defects in the brazed joint. The brazing assembly comprises of the copper cylinder, alumina disc, SS based circular to rectangular transition, CuSil and a SS stand.

All the components are baked in the vacuum furnace at 200°C for ~4 hours to remove any form of dirt, moisture and external contamination. Each component is later treated individually in an ultrasound bath using isopropyl alcohol for 10 minutes. The OFHC copper cylinder and CuSil is etched in 10% hydrochloric acid solution while the SS transition and stand are etched in Kroll's reagent. All the components are later cleaned using isopropyl alcohol.

The window is further assembled as detailed in Chapter 6, Section 6.3.1, so that it can be brazed using the brazing cycle outlined next.

C.2.1.2 Vacuum brazing cycle

The brazing assembly is placed inside the vacuum chamber which is evacuated using a rotary pump followed by a Turbo Molecular Pump (TMP) to achieve a vacuum of $\sim 5 \times 10^{-5}$ mbar. The assembly is heated above the liquidus of the BFM (780°C for CuSil) and below the solidus of the base metal in a high vacuum environment. The BFM, in liquid form, gets uniformly distributed between the surfaces to be brazed. At the Cu-alumina joint, it is held in position due to the 0.1 mm step machined at the inner periphery of the copper cylinder and capillary action, while at the Cu-SS joint, the tight fit arrangement holds the liquid BFM. The choice of the brazing cycle is critical in obtaining a strong leak-proof brazed joint and is shown in Fig. C.18. The temperature is maintained at 750°C (below the liquidus of CuSil) for 60 minutes to uniformly heat the complete assembly and avoid temperature gradients across it. A peak temperature of 830°C is finally achieved.

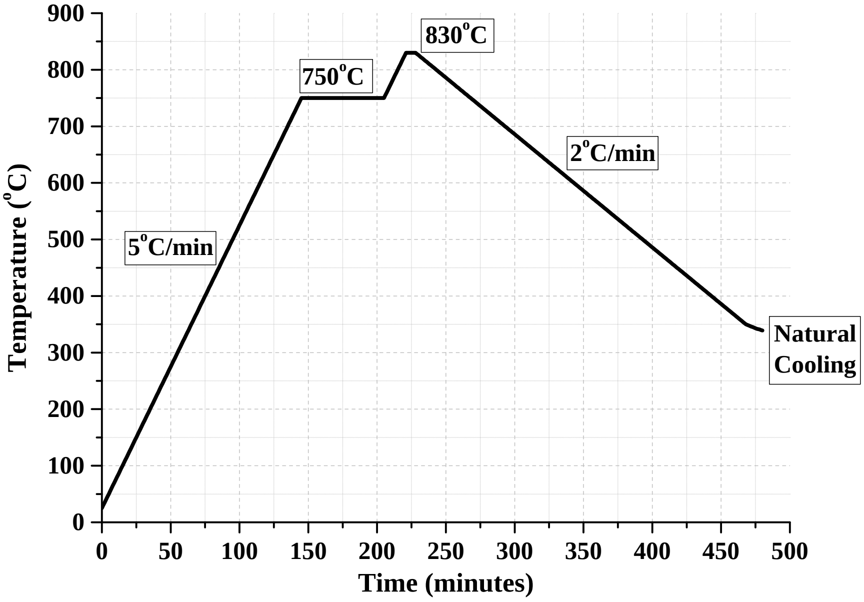

Figure C.18: Brazing cycle loaded in the vacuum chamber.

The complete assembly post brazing, as shown in Fig. C.19, is cleaned using acetone. It can be observed that there is no spill over of the braze material from the joint locations.

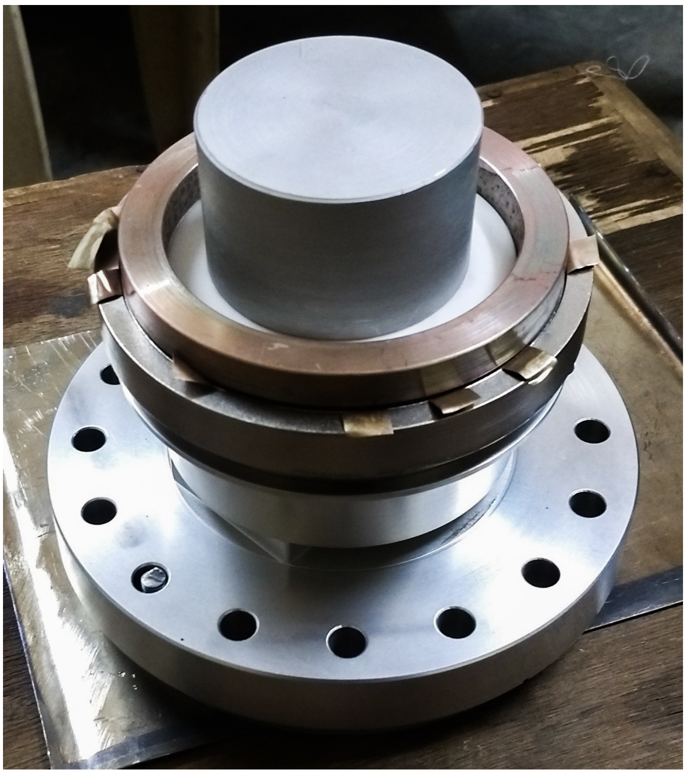

Figure C.19: Complete brazed assembly.

C.2.2 Mechanical Qualification tests of the RF vacuum window

Post brazing, it is important to perform mechanical qualification tests on the brazed joints to determine their strength and check the vacuum tightness of the window. An Ultrasonic test, Helium Leak Detection and Sniffing test, performed on the brazed assembly, is explained below in detail.

C.2.2.1 Ultrasonic test

The brazed joints in the window assembly are required to be well bonded. Any form of de-bonding would result in leaks when the window is subjected to a differential pressure of ~4 bars. The Ultrasonic Testing (UT) method [135–137] is used to qualify the brazed Copper-Alumina (Cu-Al_2O_3) joint. A Normal Beam Pulse-echo immersion C-scan technique is employed using a 20 MHz, 3.16 mm diameter probe. The test is performed on the periphery of the window at the Copper-Alumina (Cu-Al_2O_3) joint location as shown in Fig. C.20. The probe is moved around the outer periphery and over the complete thickness of the alumina disc. Thus, a circular ring of 12.6 mm thickness is scanned. The ring, opened up for the sake of plotting, forms a rectangle of 12.6 mm height and its length, in terms of degrees (angle of the ring), is 360°.

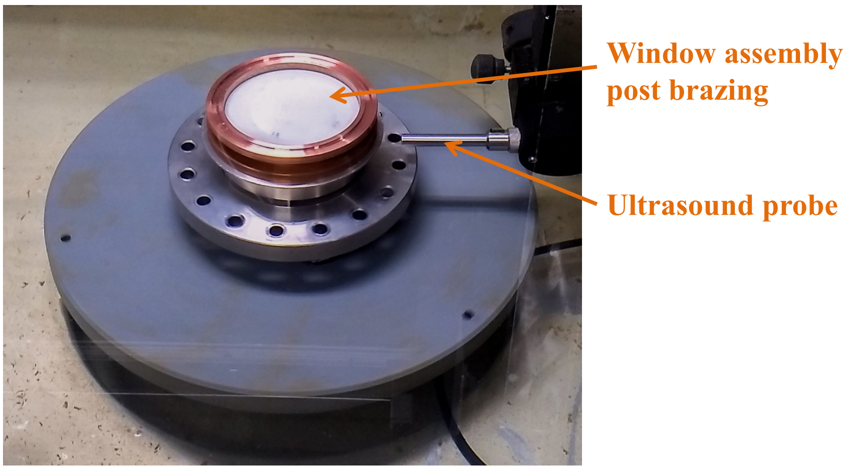

Figure C.20: Ultrasonic test performed on the brazed joint.

The rectangular C scan plot obtained from the Ultrasonic test is shown in Fig. C.21. The perimeter of the ceramic in degrees is plotted on the x-axis while the thickness of the ceramic is along the y-axis. The big grey areas in the plot signify that the joint is perfect. The comparatively smaller blue, yellow and red spots signify that the joint has isolated de-bonding. This de-bonding would not result in any leak when the window is subjected to a differential pressure of ~4 bars.

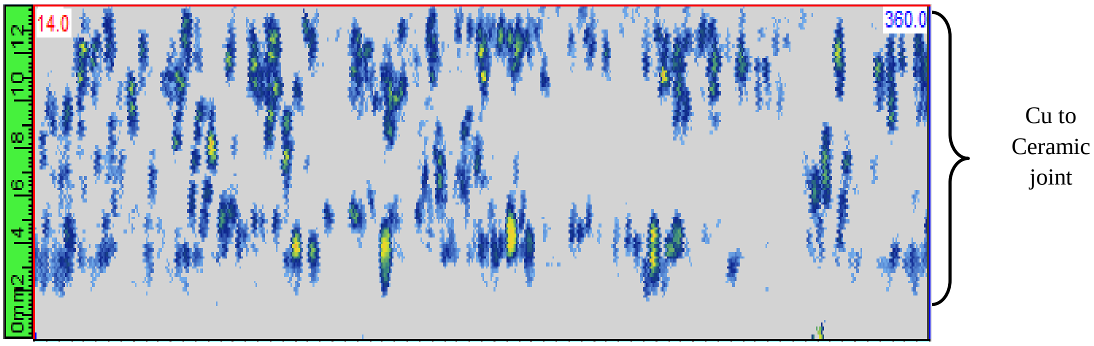

Figure C.21: C-scan plot obtained after the UT test.

C.2.2.2 Helium Leak detection and Sniffing Test

The window, with brazed Cu-Al_2O_3 and Cu-SS joints, is required to operate under UHV on one side of the alumina disc and ~3 bars pressure on the other side. The Helium Leak Detection (HLD) and Sniffing tests are carried out to validate the brazed joints for their UHV and pressure performance. Fig. C.22 shows the vacuum side of the assembly connected to the HLD machine to measure the leak rate. The HLD machine is operated in the vacuum mode and the maximum leak rate obtained on the opposite (pressurised) side is less than 1.11×10^{-9} mbar-l/sec. The HLD test, thus, confirms that the window is UHV leak tight and can be operated in UHV conditions.

The pressurized side of the assembly is now filled with Helium gas (up to 4 bars, with 1 bar pressure on the other side and thus a pressure difference of 3 bars across alumina). A sniffing probe is used to sniff out any leak from the opposite (vacuum) side. This is done in the sniff mode of the HLD machine as shown in Fig. C.23. A maximum leak rate

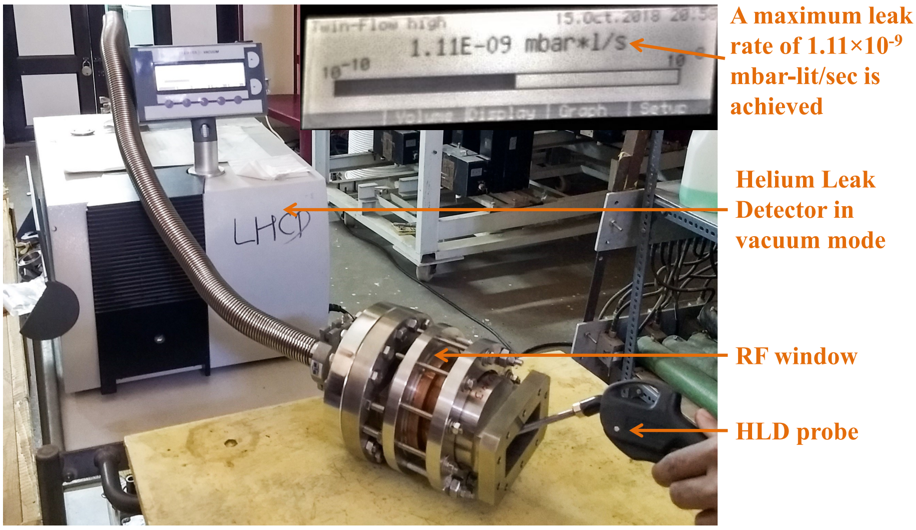

Figure C.22: HLD test performed on the window.

of 4.6 × 10^{-7} mbar-l/sec is obtained. This ensures that the window has no leaks and can withstand 3 bars of differential pressure.

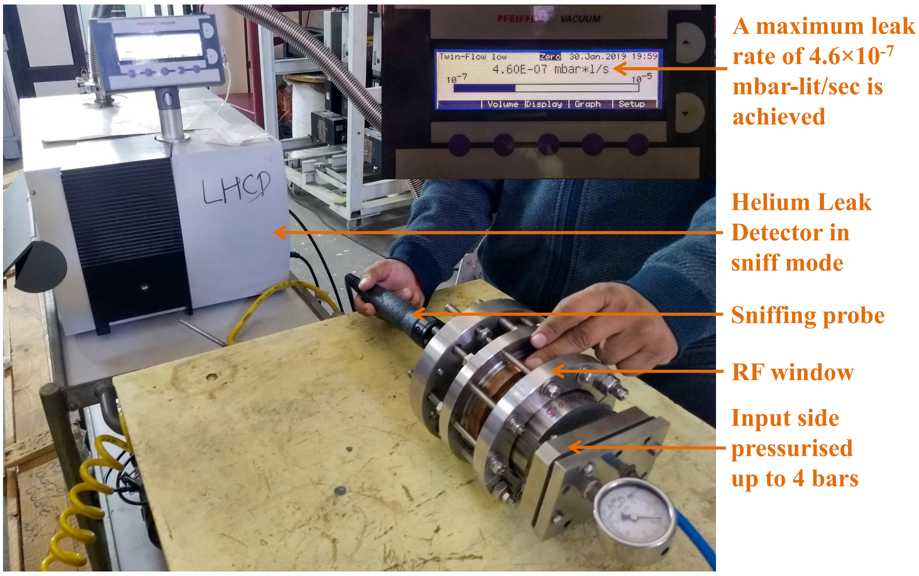

Figure C.23: Sniffing test performed on the window.

Appendix D

Design, Development and Testing of Test Kits

As discussed in Chapter 5, the waveguide pockets of the input and output of the PAM section and the output of the mode converter section have non-standard rectangular dimensions. Thus, specially customised test kits are required for RF characterisation of individual PAM components and the complete PAM launcher. These test kits would transform the non-standard rectangular waveguide dimensions to standard WR284 rectangular waveguide dimensions. Further, they aid in the integration of the VNA adapters during RF measurements. This appendix discusses the design, development and RF characterisation of these test kits. The S-parameters obtained during the RF characterisation are further used for post-processing (see Appendix E) to obtain the S-parameters of the PAM launcher components.

Two specially customised test kits; namely, Mode converter test kit and PAM test kit, are designed and developed. The details of each are discussed below.

D.1 Mode converter test kit

The PAM launcher design is such that the output of the mode converter section is connected to the input of the PAM section via the tapered divider. Thus, the mode converter test kit can be used during the RF characterisation of the mode converter section (at the output) and during that of the PAM section + tapered divider (at the input). The output of the mode converter section, for one toroidal module, is a 3×1 vector of non-standard rectangular waveguide pockets each having a cross-sectional dimension of 53.87 mm $\times$ 34.04 mm. Further, these pockets are separated by a septa thickness of 6 mm only. Thus, the output of the mode converter section cannot be connected directly to the standard WR284 VNA adapters. A specially customised Mode converter test kit is thus designed and developed.

Fig. D.1 shows the input side of the mode converter test kit. The input waveguide pockets and the input flange of the test kit matches with the output waveguide pockets and the output flange of the mode converter section, respectively.

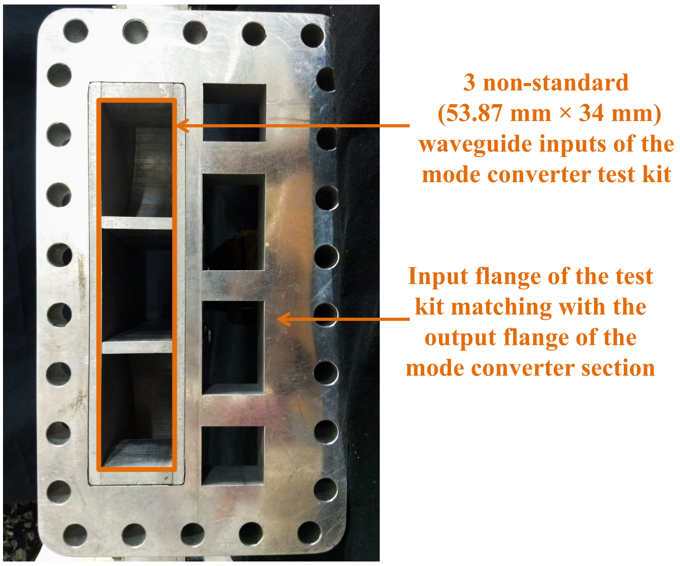

Figure D.1: Input side of the mode converter test kit illustrating the non-standard waveguide inputs.

Fig. D.2 shows the top view of the mode converter test kit. It can be observed that the bend arms translate the three inputs of the test kit to three different directions, thereby aiding in the integration of the VNA adapters at the output. Further, the step transformers at the output of each arm transform the non-standard cross-section of the input waveguide to standard WR284 waveguide cross-section at the output.

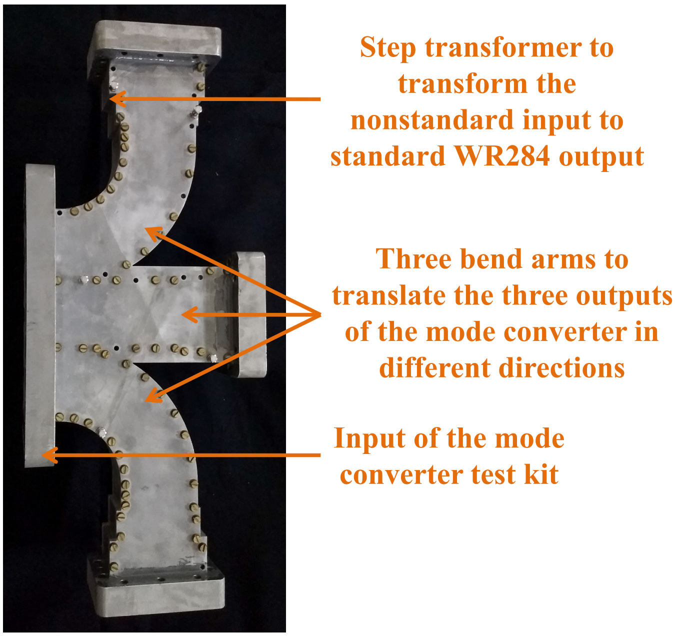

Figure D.2: Top view of the mode converter test kit.

The mode converter test kit is designed and its RF performance is evaluated using COMSOL Multiphysics. Further, the test kit is fabricated using a plate-fit mechanism. It is important to measure the S-parameters of the mode converter test kit so that the S-parameters of the individual PAM components can be evaluated during post-processing (see Appendix E). The input of the mode converter test kit is non-standard and cannot be connected to VNA adapters directly. Thus, two such test kits are fabricated and connected back-to-back by their input flanges to measure the S-parameters as shown in Fig. D.3. It can be observed that each arm now has WR284 waveguide cross-sections at both ends to connect the adapters. By this configuration, the S-parameters obtained are that of the combination of the two test kits. The S-parameters of the individual test kit can be obtained from the measured S-parameters using the procedure discussed in Appendix E.

The return loss of the test kits is required to be high (>30 dB) so that the return loss measurement of the PAM components is not affected by the use of them. The frequency

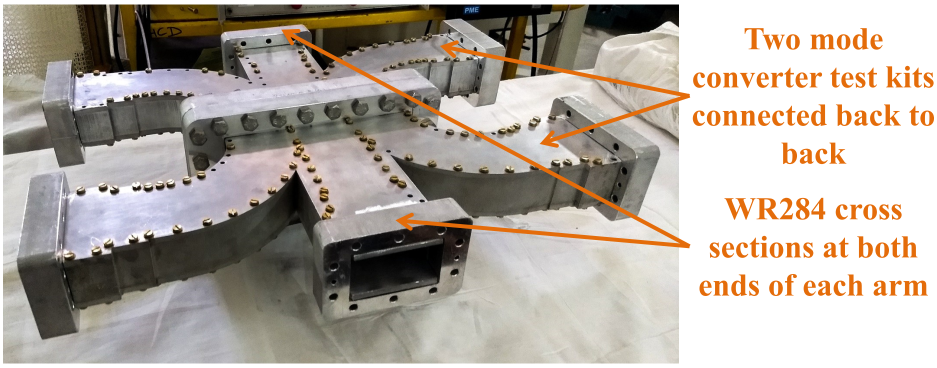

Figure D.3: Two mode converter test kits connected back-to-back for RF characterisation.

response (S_{11}) obtained for one of the arms of the individual test kit is shown in Fig. D.4. It can be observed that the return loss at 3.7 GHz is ~48.4 dB. The return loss obtained for the other two arms is also greater than 45 dB.

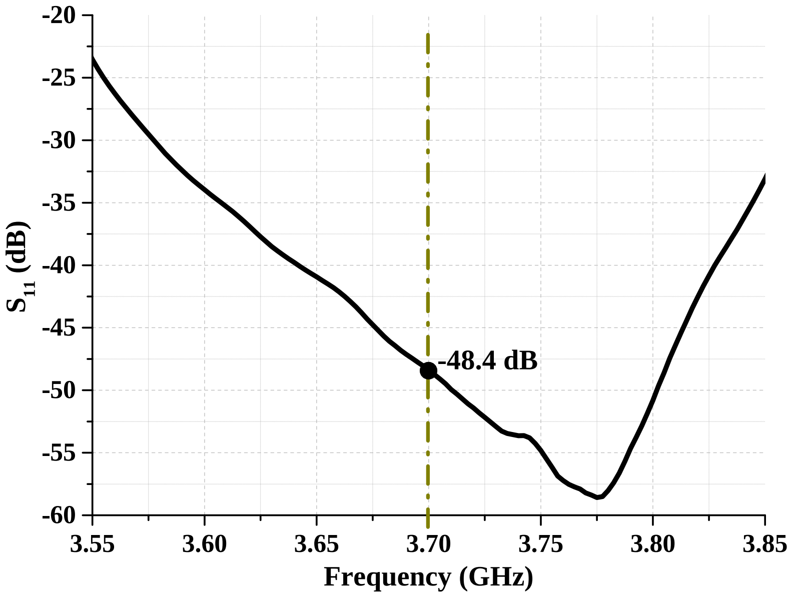

Figure D.4: Frequency response of one of the arms of the mode converter test kit.

It is to be noted that any phase shift added by the test kit to the final measurement result of the PAM components is nullified during post-processing as discussed in Appendix E.

D.2 PAM test kit

The output of the PAM section (mouth of the PAM launcher) is a curved surface having an array of non-standard rectangular active (76 mm × 12 mm) and passive (76 mm × 11 mm) waveguides juxtaposed together as shown in Fig. 4.3 (Chapter 4). One input of the PAM launcher transmits power to a single toroidal module, which consists of a 3×2 array of active waveguides. The adjacent active waveguides are separated by passive waveguides by a septa thickness of 2 mm only. The VNA adapters cannot be connected to such a curved surface, which has non-standard waveguide dimensions.

The curved surface of the mouth of the PAM launcher is transformed to a flat surface using its counterpart obtained during fabrication as shown in Fig. 5.7 and discussed in Chapter 5. The passive waveguides at the output of the counterpart are blocked since they do not receive RF power from the PAM input. Further, special holes are drilled onto the flat surface of the counterpart. A specially customised PAM test kit is designed and developed such that it can be installed onto this flat surface through these holes. Thus, the mouth of the PAM launcher is connected to its counterpart. The PAM test kit is now connected to the launcher-counterpart combination as shown in Fig. 5.8 in Chapter 5. The PAM test kit aids in the RF characterisation of one toroidal module of the PAM launcher and the PAM section at a time.

Fig. D.5 shows the input side of the PAM test kit. The input waveguide pockets and the flange holes of the test kit matches with the flat surface waveguide pockets and the specially drilled holes of the counterpart.

Fig. D.6 shows the top view of the PAM test kit. It can be observed that the bend arms translate the inputs of the test kit to different directions, thereby aiding in the integration of the VNA adapters at the output. Further, the step transformers at the output of each arm transform the non-standard input waveguide cross-section to standard WR284 waveguide cross-section at the output.

The PAM test kit is designed and its RF performance is evaluated using COMSOL Multiphysics. Further, it is fabricated using Computer Numerical Control (CNC) machining. It is important to measure the S-parameters of the PAM test kit so that the S-parameters of the PAM section and the PAM launcher can be evaluated (see Appendix E).

Figure D.5: Input side of the PAM test kit illustrating the non-standard waveguide inputs.

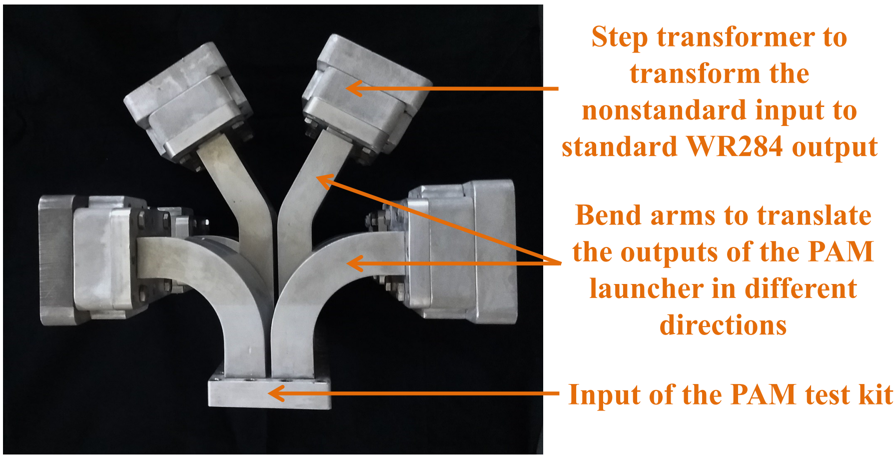

Figure D.6: Top view of the PAM test kit.

The input cross-section of each of the PAM test kit waveguides is non-standard and cannot be connected to VNA adapters directly. Thus, two such test kits are fabricated and connected back-to-back by their input flanges to measure the S parameters as shown in Fig. D.7. It can be observed that each arm now has WR284 waveguide cross-sections at both ends to connect the adapters. By this configuration, the S-parameters obtained are that of the combination of the two test kits. The S-parameters of the individual test kit can be obtained from these measured S-parameters using the methodology discussed in Appendix E.

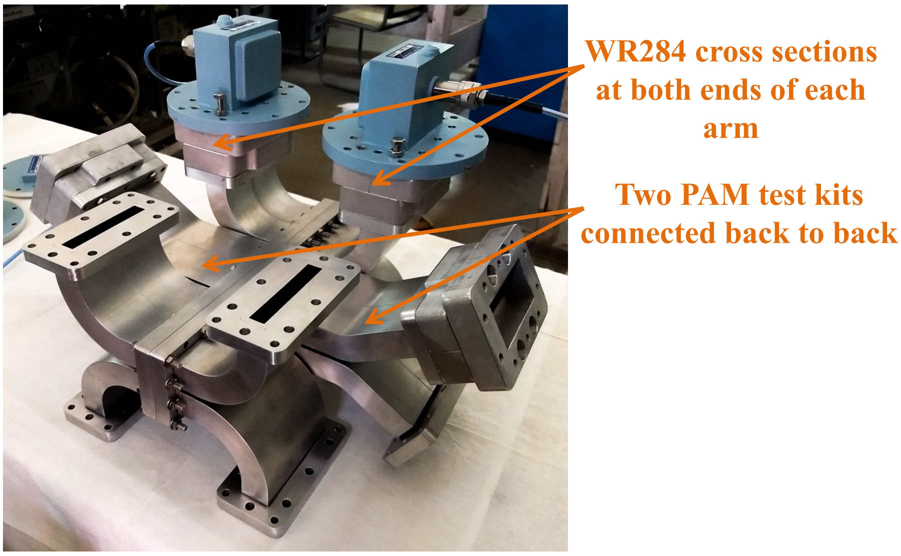

Figure D.7: Two PAM test kits connected back-to-back for RF characterisation.

The frequency response (S_{11}) obtained for one of the arms of the individual test kit is shown in Fig. D.8. It can be observed that the return loss at 3.7 GHz is ~53.9 dB. The return loss obtained for the other two arms is also greater than 47 dB.

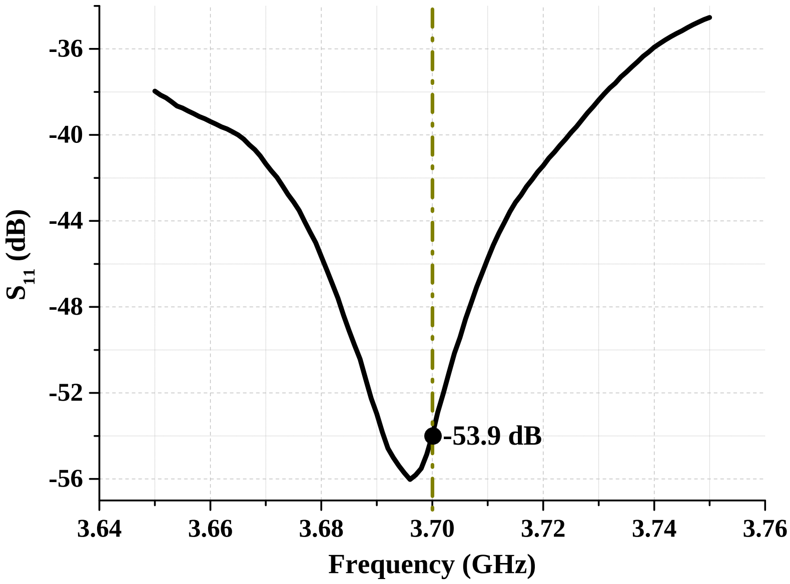

Figure D.8: Frequency response of the mode converter test kit.

It is to be noted that any phase shift added by the test kit to the final measurement result of the PAM launcher is nullified during post-processing as discussed in Appendix E.

Appendix E

Post-processing Methodology for Low Power RF Measurement Results

The RF performance of the PAM launcher is characterised by measuring its S-parameters using a Vector Network Analyser (VNA). The S-parameters of the individual launcher components and that of the complete PAM launcher are measured using specially customised test kits (PAM test kit and Mode converter test kit) as discussed in Chapter 5. Thus, the measured S-parameters are the combined S-parameters of the launcher component and the test kit used. The post-processing methodology used in obtaining the S-parameters of the launcher component from the measured combined S-parameters is discussed in this appendix. It is to be noted that the design, development and S-parameters measurement of the test kits are discussed in Appendix D.

The S-parameters measurement of the mode converter (complete PAM) requires the use of the mode converter test kit (PAM test kit) at its output. The mode converter test kit and PAM test kit are connected at the input and the output of the PAM section, respectively, for its measurement. Thus, based on the use of the test kit at the input, output or both, the following two (of the possible three) configurations are used and are further discussed.

E.1 System Under Test (SUT) with test kit at its output

The S-parameters measurement of the mode converter and that of the complete PAM launcher falls under this category. Fig. E.1 shows the cascade configuration of SUT and the test kit at the output. The notations $[S]_{SUT}$, $[S]_{TK}$, $[T]_{SUT}$ and $[T]_{TK}$ represent the S and T parameters of the SUT and the test kit. $[S]_{comb}$, $[T]_{comb}$ represent the combined S and T parameters, respectively. It is desired to obtain $[S]_{SUT}$.

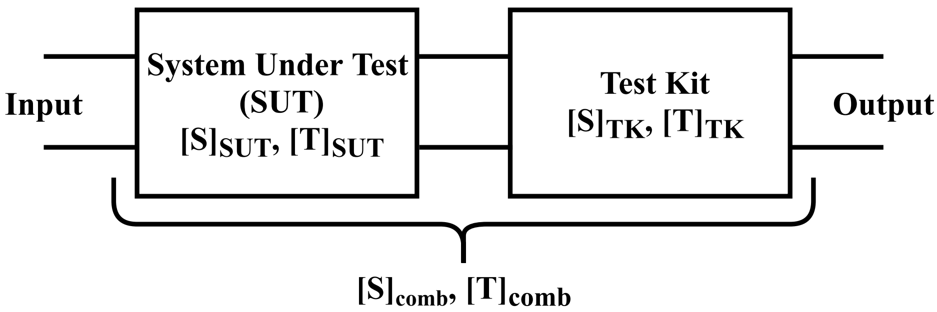

Figure E.1: Cascade configuration of the System Under Test (SUT) and test kit at the output.

The measured S-parameters of the combined structure and that of the test kit can be converted to their corresponding T-parameters using [132],

$$\begin{aligned}
A &= \frac{(1+S_{11})(1-S_{22})+S_{12}S_{21}}{2S_{21}} \\
B &= Z_0\frac{(1+S_{11})(1+S_{22})-S_{12}S_{21}}{2S_{21}} \\
C &= \frac{1}{Z_0}\frac{(1-S_{11})(1-S_{22})-S_{12}S_{21}}{2S_{21}} \\
D &= \frac{(1-S_{11})(1+S_{22})+S_{12}S_{21}}{2S_{21}}
\end{aligned} \tag{E.1}$$

where,

Z_0 is the characteristic impedance.

The combined T-parameters for a cascade configuration shown in Fig. E.1 can be written in terms of its components as,

$$[T]_{comb} = [T]_{SUT}\,[T]_{TK} \tag{E.2}$$

Taking the inverse of T-parameters of the test kit on both sides, we obtain the T-parameters of the SUT as,

$$[\mathrm{T}]_{\mathrm{SUT}} = [\mathrm{T}]_{\mathrm{comb}} \left([\mathrm{T}]_{\mathrm{TK}}\right)^{-1} \tag{E.3}$$

This $[\mathrm{T}]_{\mathrm{SUT}}$ can again be converted to the desired S-parameters of the SUT ($[\mathrm{S}]_{\mathrm{SUT}}$) using [132],

$$\begin{aligned} S_{11} &= \frac{A + B/Z_0 - CZ_0 - D}{A + B/Z_0 + CZ_0 + D} \\ S_{12} &= \frac{2\,(AD - BC)}{A + B/Z_0 + CZ_0 + D} \\ S_{21} &= \frac{2}{A + B/Z_0 + CZ_0 + D} \\ S_{22} &= \frac{-A + B/Z_0 - CZ_0 + D}{A + B/Z_0 + CZ_0 + D} \end{aligned} \tag{E.4}$$

It is to be noted that though the above T to S and S to T parameters transformation equations are for two port networks, these equations can be further translated to multiport networks. The above procedure is implemented in MATLAB to obtain the S-parameters of the mode converter and the complete PAM launcher.

E.2 System Under Test (SUT) with test kits at its input and output

The S-parameters measurement of the PAM section falls under this category. Fig. E.2 shows the cascade configuration of SUT and test kits at the input as well as at the output. The notations $[\mathrm{S}]_{\mathrm{SUT}}$, $[\mathrm{S}]_{\mathrm{TKi}}$, $[\mathrm{S}]_{\mathrm{TKo}}$, $[\mathrm{T}]_{\mathrm{SUT}}$, $[\mathrm{T}]_{\mathrm{TKi}}$ and $[\mathrm{T}]_{\mathrm{TKo}}$ represent the S and T parameters of the SUT, input and output test kits. $[\mathrm{S}]_{\mathrm{comb}}$, $[\mathrm{T}]_{\mathrm{comb}}$ represent the combined S and T parameters, respectively.

The measured S-parameters of the complete structure and that of the test kits at the input and output can be converted to their corresponding T-parameters using Eq. E.1. The combined T-parameters for a cascade configuration shown in Fig. E.2 can be written in

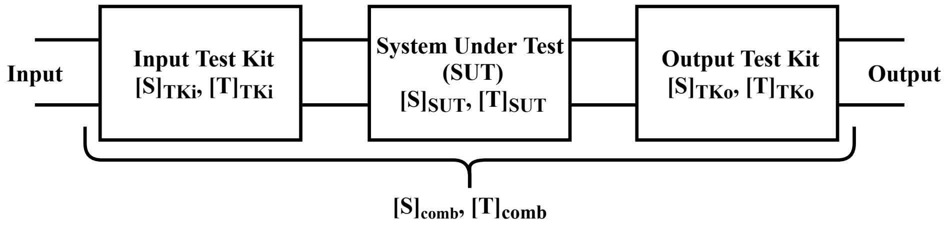

Figure E.2: Cascade configuration of the System Under Test (SUT) and test kits at the input and the output.

terms of its components as,

$$[\mathrm{T}]_{\mathrm{comb}} = [\mathrm{T}]_{\mathrm{TKi}}\,[\mathrm{T}]_{\mathrm{SUT}}\,[\mathrm{T}]_{\mathrm{TKo}} \tag{E.5}$$

Pre-multiplying both sides by the inverse of T-parameters of the input test kit and post-multiplying by the inverse of T-parameters of the output test kit, we obtain the T-parameters of the SUT as,

$$[\mathrm{T}]_{\mathrm{SUT}} = ([\mathrm{T}]_{\mathrm{TKi}})^{-1}\,[\mathrm{T}]_{\mathrm{comb}}\,([\mathrm{T}]_{\mathrm{TKo}})^{-1} \tag{E.6}$$

This $[\mathrm{T}]_{\mathrm{SUT}}$ can be converted to the desired S-parameters of the SUT ($[\mathrm{S}]_{\mathrm{SUT}}$) using Eq. E.4. The above procedure is implemented in MATLAB to obtain the S-parameters of the PAM section.

Bibliography

[1] P. K. Sharma et al. “Commissioning of 3.7 GHz LHCD system on ADITYA tokamak and some initial results”. In: *Fusion Engineering and Design* 82.1 (2007), pp. 41–53.

[2] M. H. Li et al. “Design of a PAM launcher and comparative analysis with the old FAM launcher for 2.45 GHz LHCD system on EAST”. In: *Fusion Engineering and Design* 147 (2019), p. 111250.

[3] V. P. Ridolfini et al. “LHCD and coupling experiments with an ITER-like PAM launcher on the FTU tokamak”. In: *Nuclear Fusion* 45.9 (2005), pp. 1085–1093.

[4] Gia Tuong Hoang et al. “A lower hybrid current drive system for ITER”. In: *Nuclear Fusion* 49.7 (2009), p. 075001.

[5] A. Ekedahl et al. “Validation of the ITER-relevant passive-active-multijunction LHCD launcher on long pulses in Tore Supra”. In: *Nuclear Fusion* 50.11 (Sept. 2010), p. 112002.

[6] J. H. Belo. “An ITER-relevant passive active multijunction launcher for lower hybrid current drive in JET-grade plasmas”. In: *Nuclear Fusion* 51.8 (July 2011), p. 083017.

[7] J. Kim et al. “Design of mid-plane passive active multijunction antenna for 5 GHz KSTAR LHCD system”. In: *Fusion Engineering and Design* 123 (2017), pp. 299–302.

[8] Yogesh M. Jain et al. "RF design of Passive Active Multijunction (PAM) launcher for LHCD system of ADITYA -Upgrade tokamak". In: *Fusion Engineering and Design* 134 (2018), pp. 109–117.

[9] Yogesh M. Jain, P. K. Sharma, and H. V. Dixit. "Multiphysics analysis of the Passive Active Multijunction (PAM) launcher for LHCD system of ADITYA - Upgrade tokamak". In: *Fusion Engineering and Design* 147 (2019), p. 111225.

[10] F. F. Chen. *Introduction to Plasma Physics and Controlled Fusion*. Second edition. New York: Plenum Press, 1984.

[11] X. Litaudon. "JET Program for Closing Gaps to Fusion Energy". In: *IEEE Transactions on Plasma Science* 44.9 (2016), pp. 1481–1488.

[12] S. Ciattaglia et al. "The Frascati Tokamak Upgrade machine: plant and operation status". In: *Fusion Technology*. Oxford: Elsevier, 1997, pp. 973–976.

[13] D. Frigione et al. "High density operation on Frascati Tokamak Upgrade". In: *Nuclear Fusion* 36.11 (Nov. 1996), pp. 1489–1499.

[14] Y. Camenen et al. "Experimental observations and modelling of intrinsic rotation reversals in tokamaks". In: *Plasma Physics and Controlled Fusion* 59.3 (Jan. 2017), p. 034001.

[15] J. Chung et al. "Considerations of the q-profile control in KSTAR for advanced tokamak operation scenarios". In: *Review of Scientific Instruments* 89.10 (2018), p. 10D112.

[16] S. T. Wu et al. "The R&D progress of the EAST (HT-7U) superconducting tokamak". In: *20th IEEE/NPSS Symposium on Fusion Engineering*. 2003, pp. 646–651.

[17] J. P. Qian et al. "Equilibrium properties on the EAST superconducting tokamak". In: *Journal of Plasma Physics* 75.3 (2009), pp. 337–344.

[18] K. Tomabechi et al. “ITER conceptual design”. In: *Nuclear Fusion* 31.6 (June 1991), pp. 1135–1224.

[19] D. Guilhem et al. “Implications of the TORE-SUPRA WEST-Project on Radio Frequency Additional Heating Systems”. In: *IEEE Transactions on Plasma Science* 42.3 (2014), pp. 879–884.

[20] C. Bourdelle et al. “WEST Physics Basis”. In: *Nuclear Fusion* 55.6 (May 2015), p. 063017.

[21] S. J. Kilpatrick et al. “Characterization of the Tokamak Fusion Test Reactor plasma edge by Langmuir-calorimeter probes”. In: *Journal of Vacuum Science & Technology A* 4.3 (1986), pp. 1817–1821.

[22] R. S. Granetz et al. “Alcator C-Mod Status, Recent Accomplishments, and Future Plans”. In: *21st IEEE-NPS Symposium on Fusion Engineering SOFE*. 2005, pp. 1–6.

[23] K. Kurihara. “Current Status of Experimental Study and Device Modifications in JT-60U”. In: *21st IEEE/NPS Symposium on Fusion Engineering SOFE*. 2005, pp. 1–6.

[24] P. Decool et al. “JT-60SA TF Magnet Joints Developments and Prequalification”. In: *IEEE Transactions on Applied Superconductivity* 22.3 (2012), pp. 4202504–4202504.

[25] S. Ishida. “7 - JT-60U”. In: *Magnetic Fusion Energy*. Woodhead Publishing, 2016, pp. 167–214.

[26] I. Bandyopadhyay and S. P. Deshpande. “Plasma position control in SST1 tokamak”. In: *Pramana* 55.5-6 (2000), pp. 741–750.

[27] S. Pradhan et al. “The first experiments in SST-1”. In: *Nuclear Fusion* 55.10 (June 2015), p. 104009.

[28] P. K. Sharma et al. “Recent Activities on SST-1 and ADITYA -U Tokamaks”. In: *Plasma and Fusion Research* 13 (2018), pp. 3502100–3502100.

[29] R. L. Tanna et al. “Overview of operation and experiments in the ADITYA -U tokamak”. In: *Nuclear Fusion* 59.11 (June 2019), p. 112006.

[30] S. Glasstone and RH. Lovberg. *Controlled Thermonuclear Reactions: An Introduction to Theory and Experiment*. van Nostrand Princeton, 1960.

[31] J. Raeder et al. *Kontrollierte Kernfusion: Grundlagen ihrer Nutzung zur Energieversorgung*. Stuttgart: Teubner-Studienbucher: Physik, 1981.

[32] *Appraisal of Resources and Costs of Critical Chemical Elements Used in Fusion, AEA/CS/ZJ/16401091/P01*. Tech. rep. Culham: AEA Technology National Environment Technology Centre, 1994.

[33] J. Raeder et al. *Safety and Environmental Assessment of Fusion Power (SEAFP): Report of the SEAFP Project.* Tech. rep. Brussels: European Commission DGXII, Fusion Programme. EURFUBRU XII-217/95, 1995.

[34] I. Cook et al. “Safety and Environmental Impact of Fusion”. In: *European Fusion Development Agreement* (2001).

[35] T. Hamacher and AM. Bradshaw. “Fusion as a Future Power Source: Recent Achievements and Prospects”. In: *18^{th} World Energy Congress*. 2001.

[36] P. K. Kaw. “Fusion power, who needs it?!” In: *Current Science* 65.1 (1993), pp. 20–25.

[37] A. Beiser. *Perspectives of Modern Physics*. McGraw-Hill series in fundamentals of physics. McGraw-Hill, 1969.

[38] L. Spitzer. “The Stellarator Concept”. In: *The Physics of Fluids* 1.4 (1958), pp. 253–264.

[39] R. A. Ellis, L. P. Goldberg, and J. G. Gorman. “Loss of Charged Particles in a Stellarator During Ohmic Heating”. In: *The Physics of Fluids* 3.3 (1960), pp. 468–473.

[40] R. F. Post. “The magnetic mirror approach to fusion”. In: *Nuclear Fusion* 27.10 (Oct. 1987), pp. 1579–1739.

[41] W. H. Bennett. “Magnetically Self-Focussing Streams”. In: *Phys. Rev.* 45.12 (June 1934), pp. 890–897.

[42] A. S. Bishop and U.S. Atomic Energy Commission. *Project Sherwood: The U.S. Program in Controlled Fusion*. Addison-Wesley books in Nuclear Science and Metallurgy. Addison-Wesley Publishing Company, 1958.

[43] D. D. Ryutov, M. S. Derzon, and M. K. Matzen. “The physics of fast *Z* pinches”. In: *Review of Modern Physics* 72.1 (Jan. 2000), pp. 167–223.

[44] V. P. Smirnov. “Tokamak foundation in USSR/Russia 1950–1990”. In: *Nuclear Fusion* 50.1 (Dec. 2009), p. 014003.

[45] John Wesson. *Tokamaks*. Third edition. Oxford University Press, 2004.

[46] *Tokamak Principle*. URL: https://www.euro-fusion.org/news/detail/detail/News/tokamak-principle/.

[47] *Tokamaks Around the World*. URL: www.tokamak.info.

[48] D. Bora. “SST and ADITYA tokamak research in India”. In: *Brazilian Journal of Physics* 32 (Mar. 2002), pp. 193–216.

[49] P. K. Sharma. “Advances In LHCD System For SST-1 Tokamak”. In: *Fusion Science and Technology* 65.1 (2014), pp. 103–119.

[50] P. K. Sharma et al. “High Power CW Testing of 3.7-GHz Klystron for SST1 LHCD System”. In: *IEEE Transactions on Plasma Science* 42.9 (2014), pp. 2298–2308.

[51] K. Ikuta. “On Steady Tokamaks with Relativistic Electrons”. In: *Japanese Journal of Applied Physics* 11.11 (Nov. 1972), pp. 1684–1685.

[52] N. J. Fisch. “Confining a Tokamak Plasma with RF-Driven Currents”. In: *Physical Review Letters* 41.13 (Sept. 1978), pp. 873–876.

[53] N. J. Fisch. “Current generation in tokamaks by phased injection of pellets”. In: *Nuclear Fusion* 24.3 (Mar. 1984), pp. 378–386.

[54] P. M. Bellan. “Physical model of current drive by ac helicity injection”. In: *The Physics of Fluids* 27.8 (1984), pp. 2191–2192.

[55] J. M. Finn and T. M. Antonsen. “Anomalous current penetration and oscillating current drive in tokamaks”. In: *The Physics of Fluids* 30.8 (1987), pp. 2450–2456.

[56] N. J. Fisch. “Theory of current drive in plasmas”. In: *Review of Modern Physics* 59 (1 Jan. 1987), pp. 175–234.

[57] T. H. Stix. *The Theory of Plasma Waves*. McGraw-Hill advanced physics monograph series. McGraw-Hill, 1962.

[58] T. H. Stix. *Waves in Plasmas*. American Institute of Physics, 1992.

[59] J. P. Freidberg. *Plasma Physics and Fusion Energy*. Cambridge University Press, 2007.

[60] P. Lallia. “A LHR heating slow wave launching structure suited for large toroidal experiments”. In: *Proceedings of Second Topical Conference on RF Plasma Heating, Paper C3*. 1974.

[61] M. Brambilla. “Slow-wave launching at the lower hybrid frequency using a phased waveguide array”. In: *Nuclear Fusion* 16.1 (Feb. 1976), pp. 47–54.

[62] V. Krapchev and A. Bers. “Waveguide array excitation of lower hybrid fields in a tokamak plasma”. In: *Nuclear Fusion* 18.4 (Apr. 1978), pp. 519–527.

[63] A. Bers and K. S. Theilhaber. “Three-dimensional theory of waveguide-plasma coupling”. In: *Nuclear Fusion* 23.1 (Jan. 1983), pp. 41–48.

[64] O. Hurtak and J. Preinhaelter. “The theory of long waveguide structures radiating lower hybrid waves into a plasma”. In: *IEEE Transactions on Plasma Science* 20.4 (1992), pp. 425–431.

[65] O. Hurtak. “Aperiodically-phased multijunction sections as components of large launching structures for LHCD”. In: *Plasma Physics and Controlled Fusion* 32.8 (Aug. 1990), pp. 623–636.

[66] M. A. Irzak and O. N. Shcherbinin. “Theory of waveguide antennas for plasma heating and current drive”. In: *Nuclear Fusion* 35.11 (Nov. 1995), pp. 1341–1356.

[67] V. E. Golant. “Plasma Penetration near the Lower Hybrid Frequency”. In: *Soviet Physics Technical Physics* 16.12 (June 1972), pp. 1980–1988.

[68] K. K. Ambulkar et al. “Measurement of LHCD antenna position in Aditya tokamak”. In: *Journal of Physics: Conference Series* 208 (Feb. 2010), p. 012025.

[69] Ph. Bibet and J. Belo. “JET Passive Active Multijunction Lower Hybrid Launcher”. In: *Plasma Physics and Fusion Technology* 37.21 (2005).

[70] J. H. Belo et al. “ITER-like PAM launcher for Tore Supra’s LHCD system”. In: *Fusion Engineering and Design* 74.1 (2005), pp. 283–288.

[71] Y. S. Bae et al. “Launcher study for KSTAR 5 GHz LHCD system”. In: *Journal of the Korean Physical Society* 49 (2006), pp. S314.

[72] R. W. Motley and W. M. Hooke. “Active-passive waveguide array for wave excitation in plasmas”. In: *Nuclear Fusion* 20.2 (Feb. 1980), pp. 222–224.

[73] T. K. Nguyen and D. Moreau. “Compact launching structures for lower hybrid waves”. In: *Fusion Technology*. Pergamon, 1982, pp. 1381–1386.

[74] T. K. N’Guyen, G. Rey, and D. Moreau. “A 4 waveguide multijunction antenna for L.H.H. in PETULA”. In: *13^{th} Symposium on Fusion Technology*. Varese, Italy, 1984, pp. 663–668.

[75] IP. Gladkovskii et al. “Interaction of electromagnetic waves with a toroidal plasma”. In: *Soviet Physics Technical Physics* 18 (Feb. 1974), p. 1029.

[76] C. Gormezano et al. “Lower-hybrid-heating data on the Wega experiment revisited, using ion-stochastic-heating and electron-Landau-damping theories”. In: *Nuclear Fusion* 21.9 (Sept. 1981), pp. 1047–1065.

[77] M. I. Petelin et al. “Quasi-optical diffraction grill for excitation of lower-hybrid waves in tokamaks”. In: *Plasma Physics and Controlled Fusion* 38.4 (Apr. 1996), pp. 593–610.

[78] R. Borghi et al. “Quasi-optical grill launching of lower-hybrid waves for a linearly increasing plasma density”. In: *IEEE Transactions on Plasma Science* 26.4 (1998), pp. 1330–1338.

[79] J. Preinhaelter et al. “Proposals of quasi-optical grills for ITER and NSTX tokamaks”. In: *26th EPS Conference on Controlled Fusion and Plasma Physics*. Vol. 23. Maastricht, Netherland, June 1999, pp. 1601–1604.

[80] T. Yamamoto et al. “Experimental Observation of the rf-Driven Current by the Lower-Hybrid Wave in a Tokamak”. In: *Physical Review Letters* 45.9 (Sept. 1980), pp. 716–719.

[81] S. C. Luckhardt et al. “Generation of RF-Driven Currents by Lower-Hybrid-Wave Injection in the Versator-II Tokamak”. In: *Physical Review Letters* 48.3 (Jan. 1982), pp. 152–155.

[82] X. Litaudon et al. “Lower hybrid wave coupling in TORE SUPRA through multijunction launchers”. In: *Nuclear Fusion* 32.11 (Nov. 1992), pp. 1883–1898.

[83] G. Kuang et al. “Lower hybrid current drive experiments and improved performance on the HT-7 superconducting tokamak”. In: *Nuclear Fusion* 39.11Y (Nov. 1999), pp. 1769–1774.

[84] Y. Peysson and Tore Supra Team. “High power lower hybrid current drive experiments in the Tore Supra tokamak”. In: *Nuclear Fusion* 41.11 (Nov. 2001), pp. 1703–1713.

[85] V. P. Ridolfini and M. L. Apicella. “Experimental test of an ITER-like Passive Active Multijunction Lower Hybrid RF launcher on the FTU tokamak”. In: *31st EPS Conference on Plasma Physics*. Vol. 28G. P-2.105. London, 2004, pp. 1–4.

[86] F. Mirizzi et al. “PAM, multijunction and conventional LHCD grills: Operational experience on FTU”. In: *Fusion Engineering and Design* 82.5 (2007), pp. 751–757.

[87] A. Ekedahl et al. “Long Pulse operation with the ITER-Relevant LHCD Antenna in Tore Supra”. In: *AIP Conference Proceedings* 1406.1 (2011), pp. 399–406.

[88] M. Preynas et al. “Coupling characteristics of the ITER-relevant lower hybrid antenna in Tore Supra: experiments and modelling”. In: *Nuclear Fusion* 51.2 (Jan. 2011), p. 023001.

[89] B. Ding et al. “Recent Results of LHCD Experiments in EAST”. In: *Plasma Science and Technology* 13.2 (Apr. 2011), pp. 153–156.

[90] M. Preynas et al. “Experimental characterization and modelling of non-linear coupling of the lower hybrid current drive power on Tore Supra”. In: *Nuclear Fusion* 53.1 (Jan. 2013), p. 013012.

[91] S. Puri and M. Tutter. “Accessibility to the Lower Hybrid Resonance”. In: *Plasma Physics and Fusion Technology* 4.12 (1973), pp. 438–442.

[92] C. D. Boley. “GRILL: A code to calculate the spectrum of lower hybrid waves launched by a Brambilla waveguide array”. In: *Fusion Power Program* (1980), pp. 1–26.

[93] M. Porkolab. “Survey of Lower Hybrid Experiments”. In: *IEEE Transactions on Plasma Science* 12.2 (1984), pp. 107–117.

[94] F. Alladio et al. "Density limit for lower hybrid wave-electron interaction and minority hydrogen absorption in FT". In: *Nuclear Fusion* 24.6 (June 1984), pp. 725–731.

[95] C. Gormezano and D. Moreau. "Lower hybrid wave coupling in the Wega Tokamak". In: *Plasma Physics and Controlled Fusion* 26.3 (Mar. 1984), pp. 553–564.

[96] J. E. Stevens et al. "Lower hybrid experiments on PLT using grills with various $N_{\|}$ spectral widths". In: *Nuclear Fusion* 28.2 (Feb. 1988), pp. 217–230.

[97] N. Akaoka et al. "Recent results of LH experiments on the JT-60 tokamak". In: *Plasma Physics and Controlled Fusion* 32.11 (Nov. 1990), pp. 853–867.

[98] F. X. Soldner et al. "Profile control with lower hybrid waves on ASDEX". In: *Nuclear Fusion* 34.7 (July 1994), pp. 985–1016.

[99] M. Sakamoto et al. "Current profile control and improvement of current drive efficiency by combined lower hybrid waves in TRIAM-1M". In: *Nuclear Fusion* 40.3Y (Mar. 2000), pp. 453–459.

[100] J. Hosea et al. "The LHCD launcher for Alcator C-Mod–Design, construction, calibration and testing". In: *Fusion Engineering and Design* 74.1 (2005), pp. 479–483.

[101] D. Bora et al. "Design criteria and current status of LHCD system on SST1 machine". In: *Fusion Engineering and Design* 82.2 (2007), pp. 141–152.

[102] M. Pain et al. "The hyperguide: a new concept of lower hybrid launcher". In: *Fusion Engineering and Design* 22.3 (1993), pp. 251–256.

[103] Y. Ikeda et al. "Simple multijunction launcher with oversized waveguides for lower hybrid current drive on JT-60U". In: *Fusion Engineering and Design* 24.3 (1994), pp. 287–298.

[104] X. Litaudon and D. Moreau. "Coupling of slow waves near the lower hybrid frequency in JET". In: *Nuclear Fusion* 30.3 (Mar. 1990), pp. 471–484.

[105] Ph. Bibet, X. Litaudon, and D. Moreau. *Principle of a'retro reflecting' or 'back-fire' LH antenna. A robust efficiently cooled launching structure for LH waves in reactor grade plasmas*. Tech. rep. IAEA Technical Committee Meeting on RF Launchers for Heating and Current Drive JAERI-Conf 94-001, 1994, pp. 98–103.

[106] P. Bibet, X. Litaudon, and D. Moreau. "Conceptual study of a reflector waveguide array for launching lower hybrid waves in reactor grade plasmas". In: *Nuclear Fusion* 35.10 (Oct. 1995), pp. 1213–1223.

[107] J. Hillairet et al. "ALOHA: an Advanced LOwer Hybrid Antenna coupling code". In: *Nuclear Fusion* 50.12 (Nov. 2010), p. 125010.

[108] J. Hillairet et al. "RF modeling of the ITER-relevant lower hybrid antenna". In: *Fusion Engineering and Design* 86.6 (2011), pp. 823–826.

[109] D. Pal et al. "Design and testing of RF window for a high power klystron". In: *European Journal of Advances in Engineering and Technology* 1.2 (2014), pp. 29–34.

[110] J. Hillairet et al. "Design and tests of 500 kW RF windows for the ITER LHCD system". In: *Fusion Engineering and Design* 94 (2015), pp. 22–30.

[111] C. Wang et al. "Development of RF Window for 3.7 GHz LHCD System on HL-2A". In: *Fusion Science and Technology* 73.4 (2018), pp. 539–544.

[112] Yogesh M. Jain et al. "Design and multiphysics analysis of a high power RF window for LHCD system of tokamaks". In: *Progress in Electromagnetics Research Symposium-Fall (PIERS-FALL)*. Singapore, 2017, pp. 2888–2894.

[113] M. Neubauer et al. "High power RF window design for the PEP-II B factory". In: *4th European Particle Accelerator Conference (EPAC 94)*. SLAC. 1994, pp. 2033–2035.

[114] M. Neubauer et al. "High-power RF window and coupler development for the PEP-II B factory". In: *Proceedings Particle Accelerator Conference*. Vol. 3. 1995, pp. 1803–1805.

[115] F. Mirizzi et al. “The test of a PAM launcher on FTU: The first step toward the LHCD launcher for ITER”. In: *Fusion Engineering and Design* 74.1 (2005), pp. 237–242.

[116] K. Rustomji et al. “Mimicking Electromagnetic Wave Coupling in Tokamak Plasma with Fishnet Metamaterials”. In: *Scientific reports* 8.1 (2018), pp. 1–7.

[117] J. Hillairet et al. “Design and testing of a 5 GHz TE_{10}–TE_{30} mode converter mock-up for the lower hybrid antenna proposed for ITER”. In: *Fusion Engineering and Design* 87.3 (2012), pp. 275–280.

[118] Wang Xiao-Jie et al. “Design of a TE_{10}–TE_{30} rectangular mode converter for 4.6 GHz LHCD launcher in the experimental advanced superconducting tokamak”. In: *Chinese Physics Letters* 26.2 (2009), p. 025202.

[119] X. Litaudon. “Etude théorique et expérimentale du couplage de l’onde hybride dans Tore-Supra et jet au moyen d’antennes à multijonctions”. PhD thesis. 11284, Aix-Marseille, 1990.

[120] X. Bai et al. “Coupling optimization experiment on HL-2A based on Passive Active Multijunction antenna for 3.7 GHz Lower Hybrid system”. In: *42nd EPS Conference on Plasma Physics*. Lisbon, Portugal, 2015, pp. 3–6.

[121] Bo Lu et al. “Development of the 3.7 GHz LHCD system on HL-2A”. In: *Journal of the Korean Physical Society* 65.8 (2014), pp. 1243–1246.

[122] F. Mirizzi et al. “Experiment with the PAM launcher for FTU”. In: *20th IEEE/NPSS Symposium on Fusion Engineering*. 2003, pp. 512–515.

[123] D. Milanesio et al. “Benchmark of coupling codes (ALOHA, TOPLHA and GRILL3D) with ITER-relevant Lower Hybrid antenna”. In: *Fusion Engineering and Design* 86.6 (2011).

[124] M. Brambilla. “Waveguide launching of lower hybrid waves”. In: *Nuclear Fusion* 19.10 (Oct. 1979), pp. 1343–1357.

[125] H. V. Dixit et al. “Design of the 3.7 GHz, 500 kW CW circulator for the LHCD system of the SST-1 tokamak”. In: *Fusion Engineering and Design* 119 (2017), pp. 51–60.

[126] N. F. Kovalev. “Wave transformation in multi-mode waveguide with corrugated walls”. In: *Izv. VUZov, Radiofizika* 11 (1968), pp. 783–786.

[127] R. Dusseaux, P. Chambelin, and C. Faure. “Analysis of rectangular waveguide H-plane junctions in nonorthogonal coordinate system”. In: *Progress In Electromagnetics Research* 28 (2000), pp. 205–229.

[128] Hans-Georg Unger. “Circular waveguide taper of improved design”. In: *Bell System Technical Journal* 37.4 (1958), pp. 899–912.

[129] MA. Furman and MTF. Pivi. “Probabilistic model for the simulation of secondary electron emission”. In: *Physical review special topics-accelerators and beams* 5.12 (2002), p. 124404.

[130] URL: https://www.cst.com/products/cstps.

[131] R. Woo. *Final report on RF voltage breakdown in coaxial transmission lines*. Jet Propulsion Laboratory, California Institute of Technology, 1970.

[132] D. M. Pozar. *Microwave Engineering*. Fourth edition. John Wiley & Sons, Inc., 2012, pp. 1–732.

[133] R. Pinsker et al. “Comparison of coupling to 5 GHz lower hybrid waves and 0.5 GHz helicon waves”. In: *AIP Conference Proceedings*. Vol. 1689. 1. AIP Publishing LLC. 2015, pp. 1–4.

[134] S. Y. Liao. *Microwave Devices and Circuits*. Prentice Hall of India Private Limited, 1990.

[135] J. Krautkrämer and H. Krautkrämer. *Ultrasonic testing of materials*. Springer Science & Business Media, 2013.

[136] GA. Gordon, S. Canumalla, and B. R. Tittmann. “Ultrasonic C-scan imaging for material characterization”. In: *Ultrasonics* 31.5 (1993), pp. 373–380.

[137] G. Corneloup, J. Moysan, and IE. Magnin. “Ultrasonic image data processing for the detection of defects”. In: *Ultrasonics* 32.5 (1994), pp. 367–374.

Thesis Highlight

Name of the Student: Jain Yogesh Mithalalji

Name of the CI/OCC: Institute for Plasma Research **Enrolment No.:** ENGG06201504001

Thesis Title: Design, Development and Characterisation of a Passive Active Multijunction RF Launcher Compatible with ADITYA –Upgrade Tokamak.

Discipline: Engineering Sciences **Sub-Area of Discipline:** Plasma Sciences

Date of viva voce: February 5, 2021.

In this thesis work, a Passive Active Multijunction (PAM) RF launcher compatible with the ADITYA -Upgrade tokamak and capable of launching 250 kW for 1 second at 3.7 GHz has been designed, developed and tested. The PAM concept has thus been realised for a small size launcher system satisfactorily. The launcher has been designed and analysed for its plasma coupling, RF, thermal, stress and RF breakdown performance using Advanced LOwer Hybrid Antenna (ALOHA) and COMSOL Multiphysics. Post fabrication, a novel measurement technique has been developed wherein the performance of the wave launched by the launcher, in air, can be evaluated without installing the launcher onto the tokamak (Figure 1). The measured results were in good agreement with the simulation results.

Furthermore, the mode converter section, because of the matching post, acts as a bottleneck with regards to the power handling capacity of the complete launcher system. Thus, a novel mode converter has been designed wherein a few steps are added to the broader dimension of the waveguide (where the E-field is zero) near the output. This method reduces the concentration of the E-field locally, thereby increasing the power threshold for RF breakdown.

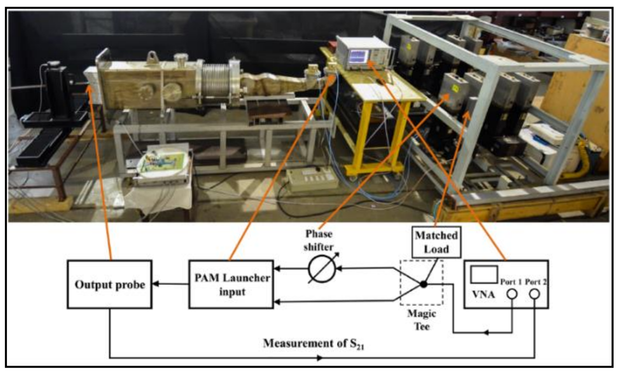

Figure 1. Profile measurement of the wave launched by the launcher illustrating the complete PAM launcher.

A 3.7 GHz, 125 kW pill box type RF vacuum window has been designed, developed and tested for its low and high power performance. The window acts as a mechanical isolation between the Ultra High Vacuum environment of the tokamak and 3 bars pressurized transmission lines. The pill box window has a novel mechanical structure, keeping the RF performance intact, that enables brazing of two joints involving two dissimilar materials (metallised alumina and copper, SS304L and copper) in a single brazing cycle. Thus, the overall brazing effort and resources, required for the fabrication of the window, are reduced by a factor of two.

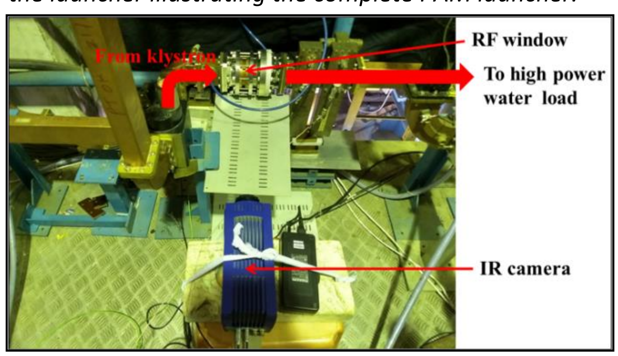

Figure 2. High power testing of the RF vacuum window.

Thus, a complete launcher system capable of launching 250 kW for 1 second at 3.7 GHz has been designed, developed and tested for its mechanical and RF performance and is ready to be installed onto the tokamak for fusion experiments.